

ARL-TR-334  
NASA Contractor Report 194446

0

# Composite Matrix Experimental Combustor

Final Technical Report

AD-A280 344

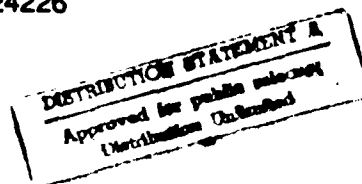
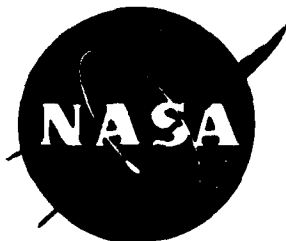


Marc D. Paskin  
Allison Gas Turbine Division  
General Motors Corporation  
Indianapolis, Indiana

April 1994

DTIC QUALITY INSPECTED 2

Prepared for  
Lewis Research Center  
Under Contract NAS3-24226



94-18611



94 6 075

REPORT DOCUMENTATION PAGE			Form Approved OMB No. 0704-0188	
<small>Public reporting burden for this collection of information is estimated to average 1 hour per response, including the time for reviewing instructions, searching existing data sources, gathering and maintaining the data needed, and completing and reviewing the collection of information. Send comments regarding this burden estimate or any other aspect of this collection of information, including suggestions for reducing this burden, to Washington Headquarters Services, Directorate for Information Operations and Reports, 1215 Jefferson Davis Highway, Suite 1204, Arlington, VA 22202-4302, and to the Office of Management and Budget, Paperwork Reduction Project (0704-0188), Washington, DC 20503.</small>				
1. AGENCY USE ONLY (Leave blank)	2. REPORT DATE April 1994	3. REPORT TYPE AND DATES COVERED Final Contractor Report		
4. TITLE AND SUBTITLE Composite Matrix Experimental Combustor		5. FUNDING NUMBERS WU- NAS3-24226		
6. AUTHORS Marc D. Paskin		8. PERFORMING ORGANIZATION REPORT NUMBER EDR 16346		
7. PERFORMING ORGANIZATION NAME(S) AND ADDRESS(ES) Allison Gas Turbine Division General Motors Corporation P. O. Box 420 Indianapolis, IN 46206-0420		10. SPONSORING/MONITORING AGENCY REPORT NUMBER NASA CR-194446 ARL-TR-334		
9. SPONSORING/MONITORING AGENCY NAME(S) AND ADDRESS(ES) National Aeronautics and Space Administration Lewis Research Center Cleveland, OH 44135-3191		11. SUPPLEMENTARY NOTES Project Manager, Waldo A. Acosta, U.S. Army Vehicle Propulsion Directorate, Lewis Research Center, Cleveland, OH 44135 (216) 433-3393		
12a. DISTRIBUTION/AVAILABILITY STATEMENT Unclassified - Unlimited Subject Category 07		12b. DISTRIBUTION CODE		
13. ABSTRACT (Maximum 200 words) A joint Army/NASA program was conducted to design, fabricate, and test an advanced, reverse-flow, small gas turbine combustor utilizing a compliant metal/ceramic (CMC) wall cooling concept. The objectives of this effort were to develop a design method (basic design data base and analysis) for the CMC cooling technique and then demonstrate its application to an advanced cycle, small, reverse-flow combustor with 3000°F burner outlet temperature (BOT). The CMC concept offers significant improvements in wall cooling effectiveness resulting in a large reduction in cooling air requirements. Therefore more air is available for control of BOT pattern in addition to the benefits of improved efficiency, reduced emissions, and smoke levels. Task 1 of the program defined component materials and localized design of the composite wall structure in conjunction with development of basic design models for the analysis of flow and heat transfer through the wall. Task 2 required implementation of the selected materials and validated design model during combustor preliminary design. Detail design of the selected combustor concept and its refinement with 3-D aerothermal analysis were completed in Task 3. Task 4 covered detail drawings, process development and fabrication, and a series of burner rig tests. Burner rig tests covered characterization of cold flow pressure drop, lean blowout and ignition mapping, steady-state performance throughout the operating range including the milestone 3000°F BOT as well as two series of simulated cyclic thermal shock tests at high point BOT conditions of 2700°F (32 total cycles) and 3000°F (68 total cycles). Rig test results have demonstrated the benefits and viability of the CMC concept, meeting or exceeding the aerothermal performance and liner wall temperature characteristics of similar lower temperature-rise combustors, achieving 0.15 pattern factor at 3000°F BOT, while utilizing approximately 80% less cooling air than conventional, film-cooled combustion systems.				
14. SUBJECT TERMS Combustor, Compliant Layer, Liner Cooling, Gas Turbine, Thermal Barrier Coating, Ceramics		15. NUMBER OF PAGES		
		16. PRICE CODE A04		
17. SECURITY CLASSIFICATION OF REPORT Unclassified	18. SECURITY CLASSIFICATION OF THIS PAGE Unclassified	19. SECURITY CLASSIFICATION OF ABSTRACT Unclassified	20. LIMITATION OF ABSTRACT	

### GENERAL INSTRUCTIONS FOR COMPLETING SF 298

The Report Documentation Page (RDP) is used in announcing and cataloging reports. It is important that this information be consistent with the rest of the report, particularly the cover and title page. Instructions for filling in each block of the form follow. It is important to stay within the lines to meet optical scanning requirements.

**Block 1. Agency Use Only (Leave Blank).**

**Block 2. Report Date.** Full publication date including day, month, and year, if available (e.g. 1 Jan 88). Must cite at least the year.

**Block 3. Type of Report and Dates Covered.** State whether report is interim, final, etc. If applicable, enter inclusive report dates (e.g. 10 Jun 87 - 30 Jun 88).

**Block 4. Title and Subtitle.** A title is taken from the part of the report that provides the most meaningful and complete information. When a report is prepared in more than one volume, repeat the primary title, add volume number, and include subtitle for the specific volume. On classified documents enter the title classification in parentheses.

**Block 5. Funding Numbers.** To include contract and grant numbers; may include program element number(s), project number(s), task number(s), and work unit number(s). Use the following labels:

C - Contract	PR - Project
G - Grant	TA - Task
PE - Program Element	WU - Work Unit Accession No.

**Block 6. Author(s).** Name(s) of person(s) responsible for writing the report, performing the research, or credited with the content of the report. If editor or compiler, this should follow the name(s).

**Block 7. Performing Organization Name(s) and Address(es).** Self-explanatory.

**Block 8. Performing Organization Report Number.** Enter the unique alphanumeric report number(s) assigned by the organization performing the report.

**Block 9. Sponsoring/Monitoring Agency Name(s) and Address(es).** Self explanatory.

**Block 10. Sponsoring/Monitoring Agency Report Number.** (If known)

**Block 11. Supplementary Notes.** Enter information not included elsewhere such as: Prepared in cooperation with...; Trans. of ...; To be published in.... When a report is revised, include a statement whether the new report supersedes or supplements the older report.

**Block 12a. Distribution/Availability Statement.** Denotes public availability or limitations. Cite any availability to the public. Enter additional limitations or special markings in all capitals (e.g. NOFORN, REL, ITAR).

DOD - See DoDD 5230.24, "Distribution Statements on Technical Documents."  
DOE - See authorities.  
NASA - See Handbook NHB 2200.2.  
NTIS - Leave blank.

**Block 12b. Distribution Code.**

DOD - Leave blank.  
DOE - Enter DOE distribution categories from the Standard Distribution for Unclassified Scientific and Technical Reports.  
NASA - Leave blank.  
NTIS - Leave blank.

**Block 13. Abstract.** Include a brief (Maximum 200 words) factual summary of the most significant information contained in the report.

**Block 14. Subject Terms.** Keywords or phrases identifying major subjects in the report.

**Block 15. Number of Pages.** Enter the total number of pages.

**Block 16. Price Code.** Enter appropriate price code (NTIS only).

**Blocks 17. - 19. Security Classifications.** Self-explanatory. Enter U.S. Security Classification in accordance with U.S. Security Regulations (i.e., UNCLASSIFIED). If form contains classified information, stamp classification on the top and bottom of the page.

**Block 20. Limitation of Abstract.** This block must be completed to assign a limitation to the abstract. Enter either UL (unlimited) or SAR (same as report). An entry in this block is necessary if the abstract is to be limited. If blank, the abstract is assumed to be unlimited.



**Allison**

JJC:T94-630  
June 8, 1994

NASA Lewis Research Center  
21000 Brookpark Road  
Cleveland, OH 44135

Attention: Mr. Waldo Acosta, MS 49-1

Subject: **NAS3-24226**  
**Final Report**

Reference: Your letter dated February 28, 1994

Attached is the approved final report for your acceptance. A DD Form 250 is included for your signature as required by contract. Please execute and return as evidence of final acceptance.

If you have any questions, please do not hesitate to call me, telephone (317) 230-3252.

Very truly yours,

Marc Paskin  
Senior Research Engineer, T14

/cjm

Attachments

cc: See Distribution List (attached)

# NAS3- 24226 Distribution List

Recipient	# of copies
NASA Lewis Research Center Attn.: Waldo Acosta MS 49-1 21000 Brookpark Road Cleveland, OH 44135	20
NASA Lewis Research Center Attn.: Wayne Girard MS 500-305 21000 Brookpark Road Cleveland, OH 44135	1
NASA Lewis Research Center Attn.: Library MS 60-3 21000 Brookpark Road Cleveland, OH 44135	2
NASA Lewis Research Center Attn.: Report Control Office MS 60-1 21000 Brookpark Road Cleveland, OH 44135	1
NASA Lewis Research Center Attn.: Robert Bill MS 77-12 21000 Brookpark Road Cleveland, OH 44135	1
NASA Lewis Research Center Attn.: Peter Meitner MS 77-12 21000 Brookpark Road Cleveland, OH 44135	1
NASA Lewis Research Center Attn.: Richard Niedzwiecki MS 77-10 21000 Brookpark Road Cleveland, OH 44135	1
NASA Lewis Research Center Attn.: Valerie Lyons MS 77-10 21000 Brookpark Road Cleveland, OH 44135	1
NASA Lewis Research Center Attn.: Robert Tacina MS 77-10 21000 Brookpark Road Cleveland, OH 44135	1
NASA Lewis Research Center Attn.: Peter Batterton MS 86-1 21000 Brookpark Road Cleveland, OH 44135	1

NASA Center for Aerospace Information Attn.: Accession Branch P. O. Box 8757 Baltimore, MD 21240-0757	25
Technetics Corporation Attn.: <del>David Day</del> <i>Barry W. Sauer</i> 1600 Industrial Drive DeLand, FL 32724	2
Director Aviation Applied Technology Directorate (ATCOM) Attn.: Technical Library Bldg. 401 Ft. Eustis, VA 23604-5577	1
Director Advanced Systems Research Analysis Office (ATCOM) Attn.: AMSAT-R-NR (Library) MS 219-3 Ames Research Center Moffett Field, CA 94035-1000	1
Commander US Army Aviation and Troop Command Attn.: AMSAT-R-N 4300 Goodfellow Boulevard St. Louis, MO 63120-1798	1
Commander US Army Aviation and Troop Command Attn.: AMSAT-B-DSL (Ms. Feng) 4300 Goodfellow Boulevard St. Louis, MO 63120-1798	2
Commander US Army Belvoir RD&E Center Attn.: SATBE-ZT (Mr. Zusman) Ft. Belvoir, VA 22060-5606	1
Director US Army Research Laboratory Attn.: AMSRL-OP-CI-AD (Technical Library) 2800 Powder Mill Road Adelphi, MD 20783-1145	1
Director Turbopropulsion Lab Code AA/SF Naval Postgraduate School Monterey, CA 93943-5000	1

Mr. Thomas M. Sebestyen 1  
US DOE  
1000 Independence Avenue  
Washington, DC 20585

Director 1  
US Army Research Laboratory  
Attn.: AMSRL-OP-CI-AD (Technical Publishing)  
2800 Powder Mill Road  
Adelphi, MD 20783-1145

AMSAA 1  
Attn.: AMXSY-MP (H. Cohen)  
Aberdeen Proving Ground, MD 21005-5071

Defense Technical Information Center 1  
Attn.: DDTC-DDA  
Cameron Station Bldg. 5  
Cameron, VA 22304-6145

Commander 1  
US Army Tank-Automotive Command  
Attn.: AMSTA-RGE (Dr. R. Munt)  
Warren, MI 48397-5000

Dr. Donald Dix 1  
Director, Advance Technology  
ODDR&E(AT)  
Room 3D1089, The Pentagon  
Washington, DC 20301-3080

Director 1  
Army Research Office  
Attn.: AMXRO-EN (Dr. R. Singleton)  
P. O. Box 12211  
Research Triangle Park, NC 27709-2211

Department Head 1  
Department of Civil & Mechanical Eng.  
United States Military Academy  
West Point, NY 10996-1792

Commander 1  
Southwest Research Institute  
US Army Fuels & Lubricants Research Laboratory  
P. O. Drawer 28510  
San Antonio, TX 78284

Director 1  
US Army Research Laboratory  
Attn.: AMSRL-OP-CI-AD (Records Mgt)  
2800 Powder Mill Road  
Adelphi, MD 20783-1145

## TABLE OF CONTENTS

<u>Section</u>	<u>Title</u>	<u>Page</u>
I	Summary .....	1
II	Introduction .....	2
III	Task 1—Materials Selection and Micro Design .....	5
	3.1 Literature Review: Selection of CMC Materials .....	5
	3.1.1 Compliant Layer Material .....	5
	3.1.2 Bond Coat and Substrate Material .....	5
	3.1.3 Thermal Barrier Coating .....	6
	3.2 Isolated Segment Flow and Heat Transfer Characterization .....	6
	3.2.1 Flow Model Development .....	6
	3.2.1.1 Experimental Apparatus .....	7
	3.2.1.2 Data Analysis and Correlation .....	8
	3.2.2 Two-Dimensional Finite Difference Heat Transfer Model Development .....	15
	3.2.2.1 Heat Transfer Test Specimens .....	15
	3.2.2.2 Heat Transfer Characteristics of the Brunsbond Pad .....	15
	3.2.2.3 Complete Micro (Isolated Segment) Design Model .....	19
	3.2.2.4 Heat Transfer Model Experimental Verification .....	22
	3.3 Results of Thermal Stress and Micro Structural Life Prediction .....	25
IV	Task 2—Preliminary (Macro) Combustor Design .....	28
	4.1 Preliminary Design Study—Early Concept Combustion System .....	28
	4.2 Preliminary Mechanical Design Effort .....	30
V	Task 3—Final Combustor Design .....	32
	5.1 Empirical Design .....	32
	5.2 Micro Design of the CMC Wall and Determination of the Overall Coolant Distribution .....	34
	5.3 Determination of Overall Combustor Aerothermal Design .....	42
	5.4 Micro-Macro Heat Transfer Correspondences .....	43
	5.5 Final Verification: 3-D Aerothermal and Heat Transfer Analysis .....	45
	5.6 Final Mechanical Design and Detail Drawings .....	56
VI	Task 4—Fabrication and Testing .....	74
	6.1 Fabrication .....	74
	6.2 Testing .....	80
	6.2.1 Description of Test Facility and Capability .....	80
	6.2.2 Test Procedures .....	84
	6.2.3 Test Plan .....	85
	6.2.4 Test Results and Analysis .....	88
	6.2.4.1 BU1 .....	90
	6.2.4.2 BU2 .....	100
	6.2.4.3 BU3 .....	106
	6.2.4.4 BU4 .....	115
	6.2.4.5 BU5 .....	125
VII	Summary and Recommendations .....	140
	References .....	142



# TABLE OF CONTENTS (cont)

<u>Section</u>	<u>Title</u>	<u>Page</u>
Appendix A	.....	A-1
Appendix B	.....	B-1

Accession For		<input checked="" type="checkbox"/>
DTIC GRA&I		<input type="checkbox"/>
DTIC TAB		<input type="checkbox"/>
Unannounced		
Justification		
By		
Distribution		
Availability Codes		
Avail and/or		
Special		
Dist		
A-1		

# LIST OF FIGURES

Figure	Title	Page
1	Army/NASA compliant metal/ceramic experimental combustor program .....	1
2	Schematic of compliant metal/ceramic isolated wall segment.....	3
3	Experience curve for liner cooling flow requirements for CMC and film-cooled combustors.....	4
4	Schematic of radial flow specimens.....	8
5	Schematic of thermal effectiveness rig.....	9
6	Thermal effectiveness rig.....	10
7	Correlation of Brunsbond flow characteristics .....	11
8	Comparison of measured and calculated flow characteristics of CMC test specimens—0.062 in. thick pad .....	13
9	Comparison of measured and calculated flow characteristics of CMC test specimens—0.127 in. thick pad .....	14
10	Schematic of verification test specimen A .....	16
11	Thermal effectiveness and matrix dimensionless temperature gradient data from heat transfer characteristics specimen .....	17
12	Thermal conductivity for 1/16 in. H-875 35% density Brunsbond pad, through the plane thickness.....	18
13	Finite difference heat transfer model.....	20
14	Verification specimen A porous pad metal temperature data .....	23
15	Verification specimen B porous pad metal temperature data .....	23
16	Comparison of calculated and measured porous pad temperatures of specimen B.....	25
17	General layout of concept 1 CMC combustor.....	29
18	Basic design features.....	34
19	CMC material temperature versus radius from 2-D finite difference heat transfer analysis.....	36
20	CMC combustor cooling circuit design and cooling airflow distribution.....	36
21	Micro heat transfer predictions for a single segment—tile #5: outer liner .....	37
22	Micro heat transfer model predictions for a single segment—tile #1: outer liner .....	37
23	Micro heat transfer model predictions for a single segment—tile #2: inner liner .....	38
24	Micro heat transfer model predictions for a single segment—tile #6: inner liner .....	38
25	Micro heat transfer model predictions for a single segment—row #7 at transition inlet.....	39
26	Micro heat transfer model predictions for a single segment—row #8 at transition upper center.....	39
27	Micro heat transfer model predictions for a single segment—row #10 at transition outlet.....	40
28	CMC segment temperature versus ceramic thickness—tile #3: outer liner .....	40
29	CMC liner tile #3 temperature versus radius—restricted flow scenario: 50% blockage .....	41
30	CMC combustor predicted airflow distribution at design point, before rework .....	43
31	Macro heat transfer model predictions for wall temperatures—outer liner .....	44
32	Macro heat transfer model predictions for wall temperatures—inner liner .....	44
33	Macro-micro heat transfer model predictions—outer liner .....	45
34	Macro-micro heat transfer model for wall temperatures—inner liner .....	46
35	Inner wall grid and orifice arrangement, i-k plane.....	47
36	Outer wall grid and orifice arrangement, i-k plane.....	47

# LIST OF FIGURES (cont)

Figure	Title	Page
37	Dome grid in the j-k plane .....	48
38	COM3D velocity vectors, i-j plane, k=16, fuel nozzle centerline .....	48
39	COM3D velocity vectors, j-k plane, i=17, primary jets .....	49
40	COM3D velocity vectors, j-k plane, i=31, dilution jets .....	49
41	Temperature contours from COM3D, i-j plane, k=16, fuel nozzle centerline .....	50
42	Temperature contours from COM3D, j-k plane, i=2, dome .....	50
43	Temperature contours from COM3D, j-k plane, i=17, primary jets .....	51
44	Temperature contours from COM3D, j-k plane, i=24, primary zone .....	51
45	Temperature contours from COM3D, j-k plane, i=31, dilution zone .....	52
46	Fuel-air ratio contours from COM3D, i-j plane, k=16, fuel nozzle centerline .....	52
47	Fuel-air ratio contours from COM3D, j-k plane, i=17, primary jets .....	53
48	Unburned fuel contours from COM3D, i-j plane, k=16, fuel nozzle centerline .....	53
49	Army/NASA compliant metal/ceramic combustor 3-D microvolume heat transfer analysis 3000°F BOT design point .....	55
50	CMC combustor detailed drawings of the combustion liner .....	57
51	CMC combustor detailed drawings of the combustion liner .....	59
52	CMC combustor detailed drawings of the combustion liner .....	61
53	CMC combustor detailed drawings of the combustion liner .....	63
54	CMC combustor detailed drawings of the combustion liner .....	65
55	CMC combustor detailed drawings of the outer transition liner (OTL) .....	67
56	CMC combustor detailed drawings of the outer transition liner (OTL) .....	69
57	CMC combustor detailed drawings of the outer transition liner (OTL) .....	71
64	Inner and outer liner—substrate and Brunsbond only .....	78
65	Brunsbond surface and staggered seam .....	78
66	Inner liner—ready for TBC application .....	79
67	Outer liner—ready for TBC application .....	79
68	Detail of thermocouple installation at critical ceramic/Brunsbond interface .....	80
69	Inner liner—after TBC application .....	81
70	Completed CMC combustor—before test .....	81
71	Completed CMC combustor with OTL—before test .....	82
72	Advanced reverse-flow full-scale small combustor test rig .....	83
73	Single-cycle illustration for throttle excursions of cyclic tests 1 to 3 .....	84
74	Army/NASA CMC combustor predicted and measured pressure drop versus corrected flow .....	92
75	CMC combustor after 1989 BU1 thermal paint test .....	93
76	CMC combustor after 1989 BU1 thermal paint test, view of dome .....	93
77	CMC combustor after 1989 BU1 thermal paint test, view of OTL .....	94
78	Measured pattern factor as a function of temperature rise, BU1 .....	94
79	Measured radial profile—BU1 .....	95
80	CMC combustor—BU1 idle point circumferential temperature trace .....	95
81	CMC combustor—BU1 MCP point circumferential temperature trace .....	97
82	Predicted wall temperature contours for CMC 2458°F BOT test point—outer wall .....	98
83	Predicted wall temperature contours for CMC 2458°F BOT test point—inner wall .....	99
84	CMC OTL—pressure loss versus corrected flow .....	99
85	Installed CMC combustor pretest for 1992 series (BU2) testing .....	101
86	2800°F BOT thermal paint test (BU2, 8/27/92), circumferential BOT trace .....	102
87	2800°F BOT thermal paint test (BU2, 8/27/92) radial temperature profile .....	102
88	CMC combustor after 8/27/92, 2800-F BOT thermal paint test—liner .....	103

# LIST OF FIGURES (cont)

Figure	Title	Page
89	CMC combustor after 8/27/92, 2800-F BOT thermal paint test—liner.....	103
90	CMC combustor after 8/27/92, 2800-F BOT thermal paint test—outer transition liner (OTL).....	104
91	CMC combustor after 8/27/92, 2800°F BOT thermal paint test—outer transition liner (OTL).....	104
92	CMC combustor predicted airflow distribution at design point—after rework.....	105
93	CMC combustor lean blowout characteristics .....	107
94	CMC combustor ignition characteristics.....	107
95	CMC combustor after 9/25/92 3000°F BOT steady-state performance test— liner .....	108
96	CMC combustor after 9/25/92 3000-F BOT steady-state performance test—OTL ..	108
97	2400°F BOT steady-state performance (9/25/92); circumferential temperature trace—T/C probe cooling air on.....	109
98	2400°F BOT steady-state performance (9/25/92); radial temperature profile, T/C probe cooling air on.....	110
99	2400°F BOT steady-state performance (9/25/92); circumferential temperature trace—T/C probe cooling air off.....	110
100	2400°F BOT steady-state performance (9/25/92); radial temperature profile— T/C probe cooling air off.....	111
101	Comparison of 1989/1992 radial profile data .....	111
102	2800°F BOT steady-state performance (9/25/92)—circumferential temperature trace.....	112
103	2800°F BOT steady-state performance (9/25/92)—radial temperature profile.....	113
104	3000°F BOT steady-state performance (9/25/92)—circumferential temperature trace.....	113
105	3000-F BOT steady-state performance (9/25/92)—radial temperature profile.....	114
106	CMC combustor after 9/29/92 2700°F BOT cyclic shock test—liner.....	115
107	CMC combustor after 9/29/92 2700°F BOT cyclic shock test—OTL.....	116
108	2700°F cyclic testing, initial scan (9/29/92)—circumferential temperature trace.....	116
109	2700°F cyclic testing, initial scan (9/29/92)—radial temperature profile .....	117
110	2700°F cyclic testing, final scan (9/29/92)—circumferential temperature trace.....	117
111	2700°F cyclic testing, final scan (9/29/92)—radial temperature profile.....	118
112	Army/NASA CMC combustor thermal shock test—2700°F BOT high point operating condition versus cycle.....	119
113	Army/NASA CMC combustor thermal shock test—2700°F BOT high point pressure drop versus corrected flow.....	119
114	Army/NASA CMC combustor thermal shock test—2700°F BOT high point effective flow areas versus number of cycles.....	120
115	Army/NASA CMC combustor thermal shock test—2700°F BOT high point, ceramic/Brunsbond interface, outer barrel .....	120
116	Army/NASA CMC combustor thermal shock test—2700°F BOT high point, ceramic/Brunsbond interface, inner barrel .....	121
117	Army/NASA CMC combustor thermal shock test—2700°F BOT high point, ceramic/Brunsbond interface, OTL .....	121
118	Army/NASA CMC combustor thermal shock test—2700°F BOT high point metal/Brunsbond interface, outer barrel.....	122
119	Army/NASA CMC combustor thermal shock test—2700°F BOT high point, metal/Brunsbond interface, inner barrel.....	122

# LIST OF FIGURES (cont)

Figure	Title	Page
120	Army/NASA CMC combustor thermal shock test—2700°F BOT high point, metal/Brunsbond interface, OTL.....	123
121	Army/NASA CMC combustor thermal shock test—2700°F BOT high point, metal cold side, outer barrel .....	123
122	Army/NASA CMC combustor thermal shock test—2700°F BOT high point, metal cold side, inner barrel .....	124
123	Army/NASA CMC combustor thermal shock test—2700°F BOT high point, metal cold side, effusion cooled dome .....	124
124	Army/NASA CMC combustor thermal shock test—2700°F BOT high point, metal cold side, OTL .....	125
125	3000°F BOT cyclic testing, initial scan (10/02/92)—circumferential temperature trace.....	126
126	3000°F BOT cyclic testing, initial scan (10/02/92)—radial temperature profile..	126
127	3000°F BOT cyclic testing, repeat point (10/02/92)—circumferential temperature trace.....	127
128	3000°F BOT cyclic testing, repeat point (10/02/92)—radial temperature profile.....	127
129	3000°F BOT cyclic testing, final scan after 30 cycles (10/02/92)—circumferential temperature trace.....	128
130	3000°F BOT cyclic testing, final scan after 30 cycles (10/02/92)—radial temperature profile.....	128
131	Army/NASA CMC combustor thermal shock test—3000°F BOT high point operating condition versus cycle.....	129
132	Army/NASA CMC combustor thermal shock test—3000°F BOT high point pressure drop versus corrected flow.....	130
133	Army/NASA CMC combustor thermal shock test—3000°F BOT high point effective flow area versus number of cycles.....	130
134	Army/NASA CMC combustor thermal shock test—3000°F BOT high point, ceramic/Brunsbond interface, outer barrel .....	131
135	Army/NASA CMC combustor thermal shock test—3000°F BOT high point, ceramic/Brunsbond interface, inner barrel .....	131
136	Army/NASA CMC combustor thermal shock test—3000°F BOT high point, ceramic/Brunsbond interface, OTL .....	132
137	Army/NASA CMC combustor thermal shock test—3000°F BOT high point, metal/Brunsbond interface, outer barrel.....	132
138	Army/NASA CMC combustor thermal shock test—3000°F BOT high point, metal/Brunsbond interface, inner barrel.....	133
139	Army/NASA CMC combustor thermal shock test—3000°F BOT high point, metal/Brunsbond interface, OTL.....	133
140	Army/NASA CMC combustor thermal shock test—3000°F BOT high point, metal cold side, outer barrel .....	134
141	Army/NASA CMC combustor thermal shock test—3000°F BOT high point, metal cold side, inner barrel .....	134
142	Army/NASA CMC combustor thermal shock test—3000°F BOT high point, metal cold side, dome .....	135
143	Army/NASA CMC combustor thermal shock test—3000°F BOT high point, metal cold side, OTL .....	135
144	CMC combustor after 10/02/92 3000°F BOT cyclic shock test—liner .....	136
145	CMC combustor after 10/02/93 3000°F BOT cyclic shock test—OTL.....	137
146	CMC combustor outer wall after 10/02/93 3000°F BOT cyclic shock test.....	137

# LIST OF FIGURES (cont)

Figure	Title	Page
147	CMC combustor inner wall after 10/02/93 3000°F BOT cyclic shock test.....	138
148	Post 3000°F BOT cyclic shock test—dome distortion.....	138
149	Post 3000°F BOT cyclic shock test—damaged fuel nozzle.....	139

# LIST OF TABLES

Table	Title	Page
I	Combustor design conditions.....	3
II	Preliminary design study—concept 1 combustor design parameters.....	30
III	Preliminary design study—concept 2 combustor design parameters.....	31
IV	Fundamental parameters for final design.....	33
V	Summary of results from 3-D performance code prediction.....	54
VI	EPS 7101 required wall coupons for fabrication quality control.....	75
VII	CMC combustor fabrication effort: description, sequence, and split of processing operations.....	77
VIII	Matrix of test conditions for CMC combustor.....	86
IX	Burner wall temperature thermocouple locations.....	87
X	Steady-state, thermal paint, ignition, and LBO performance measurements for CMC combustor.....	87
XI	Cyclic testing program for CMC combustor.....	88
XII	Fuel nozzle location and immersion depths.....	90
XIII	Summary of Army/NASA CMC combustor steady-state performance.....	91
XIV	Comparison between measured and predicted wall temperature levels (°F), MCP operating condition.....	96
XV	Results of 1-D heat transfer analysis of outer transition liner.....	100
XVI	Fuel nozzle location and immersion depth, BU2.....	101

# NOMENCLATURE

$A_e$	slot exit area
$A_g$	gas side surface area
$A_t$	exit slot turn area
$C_{pc}$	specific heat of coolant
$C/H$	carbon to hydrogen ratio by weight
$D_h$	hydraulic diameter
$f/a$	fuel to air ratio
$G_c$	specific mass flow rate
$h'$	volumetric heat transfer coefficient
$h_c$	coolant side heat transfer coefficient
$h_{eq}$	equivalent heat transfer coefficient (Equation 16)
$h_g$	gas side heat transfer coefficient
$k_c$	thermal conductivity of coolant
$k_g$	thermal conductivity of gas
$k_m$	matrix thermal conductivity
$k_{PAD}$	porous pad thermal conductivity
$k_{ss}$	thermal conductivity of stainless steel
$k_d$	dump head loss factor
$k_t$	turning head loss factor
$l_b$	mean beam length
$L$	cell side length
$\dot{m}$	mass flow per unit thickness
$p_1$	upstream pressure or pressure at radius $R_1$
$p_2$	downstream pressure or pressure at radius $R_2$
$p_{gs}$	liner static gas pressure
$Pr_c$	Prandtl number of coolant
$Pr_g$	Prandtl number of gas
$Q$	rate of heat flow
$q''_{rad}$	radiative heat flux
$q''_{rad,TBC}$	radiative heat flux in presence of thermal barrier coating
$r$	radial coordinate
$R_1$	radius at station 1
$R_2$	radius at station 2
$R$	gas constant
$T_B$	backplate surface temperature
$T_c$	coolant temperature
$T_g$	gas temperature
$T_H$	flame temperature
$T_i$	thermal barrier coating/porous pad interface temperature
$T_s$	thermal barrier coating surface temperature
$\bar{T}_w$	average wall temperature
$T_{CC}$	coolant temperature at entrance of porous pad
$T_{CH}$	coolant temperature at exit of porous pad
$T_{ci}$	coolant inlet temperature
$T_{co}$	coolant outlet temperature
$T_{SC}$	matrix surface temperature on coolant inlet side
$T_{SH}$	matrix surface temperature at coolant exit side
$T_{WH}$	surface temperature on gas side



$U$	overall heat transfer coefficient (Equation 19)
$V_c$	coolant velocity
$V_e$	coolant exit velocity
$V_g$	gas velocity
$V_t$	velocity of coolant at turn
$W_c$	coolant flow rate
$x$	surface distance from dome
$z$	through-the-wall coordinate

#### Greek

$\alpha, \beta$	porous pad flow coefficients
$\alpha_w$	wall absorptivity
$\epsilon_H$	flame emissivity
$\eta_t$	matrix thermal effectiveness (Equation 6)
$\theta_f(o)$	dimensionless fluid temperature (Equation 10)
$\theta_T(o)$	dimensionless matrix temperature (Equation 7)
$\mu_c$	coolant viscosity
$\mu_g$	gas viscosity
$\rho$	density
$\rho_c$	coolant density
$\rho_g$	gas density
$\sigma$	Stephan-Boltzman constant
$\tau$	porous matrix thickness
$\tau_{PAD}$	pad thickness
$\tau_{TBC}$	thermal barrier coating thickness

#### Mixed

$\Delta P_{exit}$	pressure drop across exit of specimen
$\Delta P_{inlet}$	pressure drop across inlet of specimen
$\Delta P_{PAD}$	pressure drop across porous pad
$\Delta P_T$	total pressure drop across combustor wall
$\Delta V$	incremental volume
$\Delta z$	incremental distance through the wall
$\Delta z_{ss}$	stainless steel cover sheet thickness
$\Delta z_{PAD}$	incremental distance through the pad

## FOREWORD

This final technical report describes the work for a program carried out by the Allison Gas Turbine Division, General Motors Corporation, Indianapolis, IN, under Army/NASA Contract NAS3-24226, "Composite Matrix Experimental Combustor." Messrs. M. D. Paskin and H. C. Mongia served as Allison Gas Turbine Division program managers. The Army/NASA technical monitor is Mr. Waldo Acosta, Vehicle Propulsion Directorate (ARL), Lewis Research Center.

Contract NAS3-24226 was jointly funded by the National Aeronautics and Space Administration (NASA) and the U.S. Army Vehicle Propulsion Directorate (ARL), Lewis Research Center, Cleveland, Ohio.

## I. SUMMARY

A joint Army/NASA program was conducted to design, fabricate, and test an advanced, reverse-flow, small gas turbine combustor utilizing a compliant metal/ceramic (CMC) wall cooling concept. The objectives of this effort were to develop a design method (basic design data base and analysis) for the CMC cooling technique and then demonstrate its application to an advanced cycle, small, reverse-flow combustor with 3000°F burner outlet temperature (BOT). Figure 1 summarizes the features of the CMC concept as well as the potential payoffs associated with its application. The CMC concept offers significant improvements in wall cooling effectiveness resulting in a large reduction in cooling air requirements. Therefore more air is available for control of burner outlet temperature pattern in addition to the benefits of improved efficiency, reduced emissions, and smoke levels. The program was divided into four tasks. Task 1 defined component materials and localized design of the composite wall structure in conjunction with development of basic design models for the analysis of flow and heat transfer through the wall. Task 2 required implementation of the selected materials and validated design models during combustor preliminary design. Detail design of the selected combustor concept and its refinement with 3-D aerothermal analysis were completed in Task 3. Task 4 covered detail drawings, process development and fabrication, and a series of burner rig tests. Burner rig tests covered characterization of cold flow pressure drop, lean blowout and ignition mapping, steady-state performance throughout the operating range including the milestone 3000°F BOT design conditions listed in Table 1, as well as two series of simulated cyclic thermal shock tests at high point BOT conditions of 2700°F (32 total cycles) and 3000°F (68 total cycles). Rig test results have demonstrated the benefits and viability of the CMC concept—meeting or exceeding the aerothermal performance and liner wall temperature characteristics of similar lower temperature-rise combustors, achieving 0.15 pattern factor at 3000°F BOT, while utilizing approximately 80% less cooling air than conventional, film-cooled combustion systems.

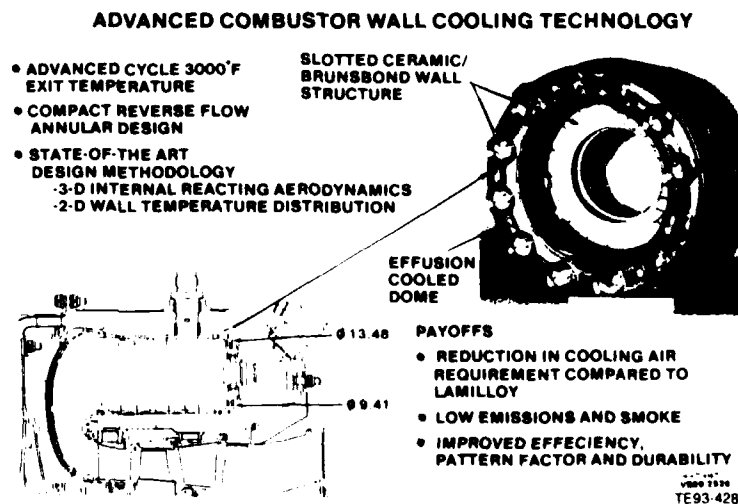


Figure 1. Army/NASA compliant metal/ceramic experimental combustor program.

## II. INTRODUCTION

Throughout the gas turbine industry, research effort is being directed at improving the performance, emissions, and reliability of gas turbine engines while reducing the specific fuel consumption. Higher cycle efficiencies can be realized if the cycle pressure ratio and turbine inlet temperatures are raised along with increasing individual component efficiencies. The higher operating pressure and temperatures require that a greater portion of the combustor throughflow air be used for burning the fuel in the primary zone, thus leaving less air for cooling the liner walls.

Conventional wall cooling methods (e.g., film cooling) are incapable of providing satisfactory durability without using excessive amounts of cooling air, which, in turn, severely restricts air available for temperature pattern control. Engine envelope demands further exacerbate the situation by requiring foldback (reverse-flow) combustor designs, which reduce engine length and weight but contain an inherently large combustor surface area-to-volume ratio. Therefore, to meet one of the most critical needs of future small gas turbine engine designs (Ref 1), advanced wall cooling schemes are required to minimize cooling air requirements.

Many advanced cooling schemes have been developed in recent years (Ref 2) and include enhanced convection film cooling techniques such as etched convective channels, impingement, multiple discrete holes (effusion), and transpiration (Lamilloy®) cooling. In addition, there has been a recent rapid growth in research and development effort aimed at introducing ceramics into gas turbine engines.

Ceramic coatings are used extensively as thermal barriers in gas turbine engines. High temperature ceramic coatings protect the metal substrate from the combined effects of temperature and oxidizing-corrosive environment. The effectiveness of a ceramic thermal barrier increases with ceramic thickness and porosity. Ceramic coating thicknesses, however, have been limited to 0.010-0.030 in. in environments where rapid thermal excursions subject the ceramic to severe thermal shock.

One of the most effective cooling schemes, however, is the CMC concept developed in a number of preliminary demonstrations by a joint U.S. Army/NASA-Lewis Research Center combustor research program (Ref 3, 4, and 5). This cooling scheme uses a sintered metal fiber structure between a thick ceramic thermal barrier coating (TBC) and a high temperature alloy substrate as shown in Figure 2. The intermediate fiber metal pad is designed to yield at relatively low levels of stress, thereby absorbing the differential expansion which develops between the metal substrate and ceramic as the material is heated. Fiber metal strain isolators are compliant, low modulus porous materials that are able to compensate for the differential movement of coating and backing during thermal cycling. The strain isolator is a relatively flexible component of the system that yields elastically to reduce the stress applied to the ceramic coating. Using fiber metal strain isolators allows ceramic coatings to be applied 0.060-0.100 in. thick without spalling during thermal cycling. This thermal barrier design approach offers superior properties because the fiber metal strain isolator in itself is an excellent insulator.

For the current CMC application, the ceramic is divided into nominally square tiles forming the inside surfaces of the combustor inner, outer, and transition liners. Each ceramic square is fed cooling air from a substrate orifice, allowing air to enter the porous compliant layer and convectively cool the ceramic backside. Slots between tiles allow the coolant flow to exit through the combustion chamber.

Current film cooling technology addresses small turbine engine cycles operating with moderate pressure ratios and BOTs less than 2500°F. The CMC combustor is designed for an advanced engine cycle with a 19:1 pressure ratio and 3000°F BOT. Table I provides design conditions for the CMC combustor.

---

\* Lamilloy is a registered trademark of the General Motors Corporation.

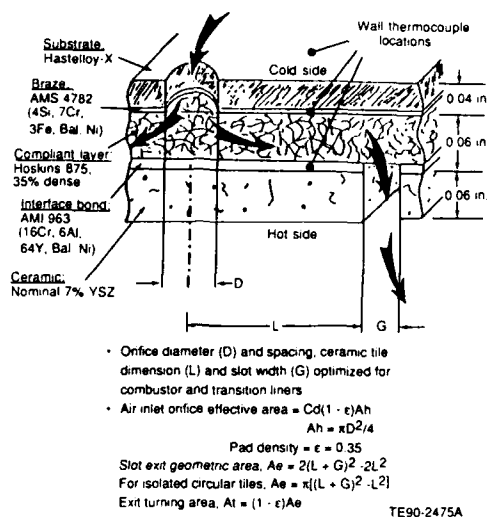


Figure 2. Schematic of compliant metal/ceramic isolated wall segment.

Table I.  
Combustor design conditions.

	CMC combustor
Wa (liner flow, lb/s)	7.940
P3 (inlet pressure, psi)	271
T3 (inlet temperature, °F)	895
Wf (fuel flow, lb/hr)	1008
F/A (fuel/air ratio)	0.03526
Wcorr (corrected flow, lb/sec)	0.696
Temperature rise (°F)	2105
Burner outlet temperature (°F)	3000
Liner pressure drop (%)	5

Figure 3 shows average coolant flux (total cooling airflow rate divided by combustor surface area) versus combustor inlet pressure. The experience curve for conventional film cooling was obtained from Ref 6. At the severe conditions of the design point, the CMC offers more than 80% reduction in the required coolant flux compared to conventional film cooling.

This report describes the CMC combustor development program to investigate utilization of the CMC concept in a full-scale, reverse-flow, small annular combustor. The main objectives of this program are : (1) the development of materials and design methodology, (2) full-scale design, and (3) fabrication and testing for steady-state performance and cyclic durability. As described in the remainder of the report,

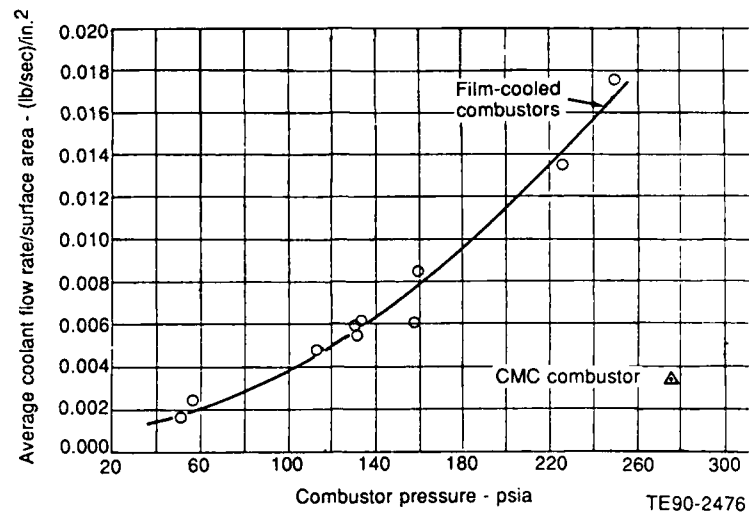


Figure 3. Experience curve for liner cooling flow requirements for CMC and film-cooled combustors.

the program's main objectives have been achieved. The following sections will describe in detail the four major tasks of the program:

- Task 1—Materials Selection and Micro Design
- Task 2—Preliminary Combustor Design
- Task 3—Final Combustor Design
- Task 4—Fabrication and Testing

### III. TASK 1—MATERIALS SELECTION AND MICRO DESIGN

#### 3.1 LITERATURE REVIEW: SELECTION OF CMC MATERIALS

Task 1 effort centered on a literature review and materials selection along with subsequent isolated segment flow and heat transfer characterization. Also part of this phase was a stress analysis for maximum in-plane and through-the-plane stresses and deflection. Results from Task 1 included choice of optimum materials, identification of various construction techniques, and the development of tools for isolated segment design.

Selection of materials to be used during design analysis phases of the program were made using the most current sources of information. Experience combined with the latest results available from government agencies sponsoring work in the area of thermal barrier coating (TBC) development supplemented a review of the open literature.

Materials used in the design and fabrication of the CMC combustor walls are given in Figure 2.

##### 3.1.1 Compliant Layer Material

Materials research communication with NASA-Lewis Research Center amplified on their work and the implication of findings to the program. NASA was involved in designing turbine vane airfoils from sintered metal fiber of a composition identical to that proposed for the strain isolator pad of the CMC combustor.

The strain isolator (compliant metal layer) is made from Hoskins 875, an alloy with a FeCrAl composition chosen for excellent long-term oxidation resistance in thermal environments to 1800°F. The Hoskins 875 alloy wire was found to be the most oxidation-resistant material available for the CMC application. The compliant layer or sintered metal fiber pad (also referred to as porous pad) is available commercially as Brunsbond® sheet. The 0.06 in. thickness chosen for the compliant layer was based on providing the required compliancy to minimize wall stress in the substrate and ceramic layers with consideration of minimizing the total combustor wall thickness. It was also realized that loss of post-sintering formability with Brunsbond pad much thicker than 0.06 in. could impede the combustor fabrication process. Brunsbond pad is typically manufactured in densities of 35-45%. A density of 35% was chosen for the CMC combustor to provide sufficient mechanical strength. Due mainly to the porosity, the sintered fiber metal pad also provides excellent thermal insulation, comparable to the ceramic.

##### 3.1.2 Bond Coat and Substrate Material

The bond coat chosen for the interface between ceramic TBC and the metal compliant layer was AMI 963. AMI is high chromium content NiCrAlY composition found to provide exceptional oxidation resistance at high temperatures in a variety of gas turbine applications. To ensure full coverage and best bond performance, the bond coating is applied to an above surface thickness (in addition to a 2-3 fiber diameter penetration into the compliant layer) of 0.005 to 0.007 in. Attachment of the compliant layer to the metal substrate is carried out with nickel braze alloys such as AMS 4782. These materials have been fully developed for high temperature applications where Hoskins 875 is brazed to nickel, iron, or cobalt base superalloy components. For the CMC combustor, based on past successful experience, the metal substrate material was chosen as Hastelloy-X.

---

\* Brunsbond is a trademark of Technetics Corporation, Deland, Florida.

### 3.1.3 Thermal Barrier Coating

Research at NASA and the gas turbine industry over many years has identified zirconia ( $ZrO_2$ ) as one of the most suitable materials for plasma-flame sprayed thermal barrier coatings (Ref 7). Zirconia is well suited as a TBC due to its properties of low thermal conductivity, high melting temperature (3900°F), and good thermal shock resistance. The major development effort for zirconia TBCs over the years has centered on phase stabilization of the crystal structure through the use of additives such as MgO, CaO, Al<sub>2</sub>O<sub>3</sub>, and Y<sub>2</sub>O<sub>3</sub> (yttria).

Early thermal barrier work at NASA utilized zirconia powder prereacted with 12 weight-percent yttria stabilizer (12-YSZ) with good results. Subsequent investigations indicated that appreciably better performance was possible with stabilized zirconia of only 8 weight-percent (w/o) yttria. Allison has followed NASA's lead in this regard and has used 8-YSZ in a variety of applications with considerable success.

NASA's recent work has indicated that, in some instances, zirconia stabilized with even less yttria (6 w/o) performs better than other compositions. The data base for the 6-YSZ is less developed than for 8-YSZ or 12-YSZ.

The choice of material for the ceramic layer also considered work at Allison using 6-8 w/o yttria-stabilized zirconia powder obtained from the supplier in hollow particle form (YSZ-HP). This material has been sprayed using a gun in which powder can be introduced into the plasma at: (1) the throat of the nozzle for longest residence time and maximum heating, (2) a location external to the nozzle which provides further control over the extent to which a powder is heated and melted, and (3) both locations simultaneously (co-spray), which enables the creation of various structures.

Coatings prepared at Allison using solid particle 8-YSZ powder injected at the nozzle throat and 6-8 w/o hollow particle YSZ-HP injected external to the nozzle exit have proven to be outstanding performers in comparative thermal shock/thermal fatigue tests.

Consideration of all sources and information surveyed suggests the choice for the ceramic layer of the thermal barrier system should reflect a compromise. In view of the past history of good results obtained with 8-YSZ by both NASA and Allison and the recent interest of NASA in 6-YSZ, the selection of 7-YSZ was made.

## 3.2. ISOLATED SEGMENT FLOW AND HEAT TRANSFER CHARACTERIZATION

This section deals with the experimental determination of the flow and heat transfer characteristics of the CMC system, the formulation and verification of a heat exchange model of the system, and finally a study of parameters affecting the heat transfer performance of the system at typical combustor operating conditions. A detailed account of this effort was also published in Ref 25.

### 3.2.1 Flow Model Development

A basic requirement for developing the design methodology for the CMC system was the experimental investigation of flow characteristics of the three layer wall system along with formulation and verification of a flow model. Total pressure loss behavior for flow through the CMC wall structure must consider the following series of flow resistances: (1) flow through the coolant orifice in the substrate, (2) flow entering and transpiring through the fiber metal compliant layer (porous or strain isolator pad), and (3) flow turning and exiting through slots formed in the ceramic TBC.



### 3.2.1.1 Experimental Apparatus

Bench scale test specimens used in flow and heat transfer model verification experiments consisted of the following:

- porous pad only
- porous pad with clamped plastic disks and rings to simulate the coolant feed orifice and exit slots
- heat transfer samples consisting of porous pad with brazed Inconel 600 substrate, eloxed (electric discharge machining or EDM) to produce a hole representing the coolant orifice (brazed to the other side of the porous pad were a stainless steel outer ring and inner disk to represent the coolant exit slot)

All test specimens were circular with a 2 in. diameter to fit the Allison flow and thermal effectiveness rig.

A total of four Brunsbond porous pad configurations were subjected to cold flow testing to determine the pad-only flow characteristics. The disk specimens, all made from Hoskins 875 material of 0.005 in. nominal diameter wire, had the following specifications:

- pad specimen No. 1—50% density, 0.040 in. thick
- pad specimen No. 2—30% density, 0.101 in. thick
- pad specimen No. 3—35% density, 0.062 in. thick
- pad specimen No. 4—35% density, 0.127 in. thick

The data necessary to verify the flow/pressure drop calculation procedure was obtained using pad specimens 1 and 4 contained within an assembly to simulate the CMC flow network. These radial flow assemblies consisted of: a 0.25 in. thick plastic inlet disk containing a 3/16 in. diameter inlet hole, a porous pad disk, and a 0.25 in. thick plastic cover sheet containing a 1/8 in. annulus exit slot. Actually, the cover sheet consisted of two pieces: an outer ring, 2 in. in outer diameter, and an inner disk, 0.75 in. in outer diameter. A schematic of the radial flow assembly is shown in Figure 4 along with pertinent dimensions. All pieces were assembled using double-sided tape at the interfaces between plastic sheets and the porous pad. In addition, a clamp held the inner disk of the cover sheet in place. Additional clamping of the complete assembly was afforded by the rig clamping rings. Cold flow data, consisting of inlet and exit pressure, air temperature, and mass flow rate, were obtained on the inlet disk (inlet hole) only, inlet disk/porous pad/outer cover sheet ring subassembly, and the complete assembly (Figure 4). Reduced data from the component cold flow testing, plotted as effective area (ACd) versus pressure ratio, are provided in Appendix A.

All tests of the measurement of the flow and heat transfer characteristics of specimens as well as tests to be used in the verification of the thermal design model used the existing Allison thermal effectiveness rig. This rig has been used for a number of years to obtain the flow and heat transfer characteristics of Lamilloy. A schematic of the thermal effectiveness rig is shown in Figure 5. A photo of the rig is shown in Figure 6. The discussion that follows describes the rig as it is used to obtain heat transfer information. However, it should be noted that cold flow specimen testing likewise uses the same set-up except that the heat source is inactive.

The heat source used is a six-element quartz light powered by a Thermac temperature controller and power regulator that is used in the power regulator mode. The cooling air supply is the Allison shop air system. As shown schematically in Figure 5, a circular test specimen (outer diameter equal to 2 in.) is clamped between two rings with the upstream ring attached to the air supply plenum that directs the cooling air to the specimen. The downstream ring faces the quartz light. To prevent radiation from the quartz light from overheating the specimen clamping rings and other rig hardware, a water-cooled plate has been placed between the light and the specimen such that only the specimen is irradiated. During rig operation, shop air enters the air supply plenum and from there flows through the test spec-

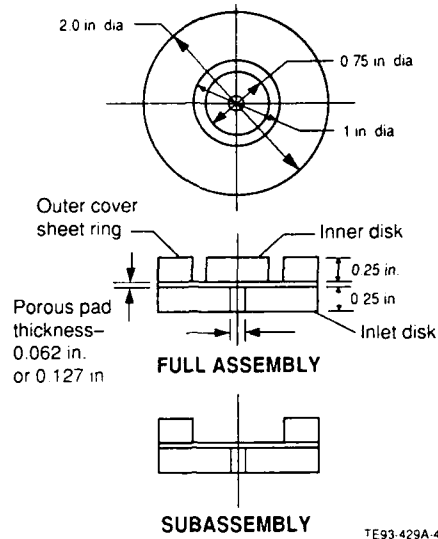


Figure 4. Schematic of radial flow specimens.

imen. The air exits the system through gaps located between the water-cooled plate and the quartz light. The specimen hot side surface temperature is measured by thermocouples with the leads brought out through the gap left between the specimen clamping ring and the water-cooled plate. The temperature of the specimen backface is also measured by thermocouples with the leads brought out through instrumentation ports built into the air supply plenum. The cooling air inlet temperature and pressure are measured by thermocouples and static pressure taps located in the air supply plenum. The temperature of the cooling air leaving the specimen is measured by an aspirated thermocouple that can be traversed across the downstream face of the specimen. The cooling airflow rate is measured by a thin plate orifice located upstream of the air supply plenum.

### 3.2.1.2 Data Analysis and Correlation

The pad-only (Brunsbond) flow data were correlated in terms of the dimensionless parameters originally suggested by Green (Ref 8) for flow through compact porous media. The macroscopic model developed by Green related the difference in pressure across a porous wall to the specific flow rate,  $G_c$ . The relationship is quadratic in  $G_c$ , the linear term representing the viscous shear contribution to the pressure drop and the second order term accounting for inertial momentum loss effects. Two empirical constants, which must be experimentally determined for a given porous matrix, appear in the final momentum equation. Thus

$$\frac{(P_1^2 - P_2^2)g}{\mu_c^2 (2RT_c)} = \alpha \left( \frac{G_c}{\mu_c} \right) + \beta \left( \frac{G_c}{\mu_c} \right)^2 \quad (1)$$

Equation 1 can be rearranged to establish a straight line relationship,

$$\frac{(P_1^2 - P_2^2)g}{\mu_c G_c (2RT_c)} = \alpha + \beta \left( \frac{G_c}{\mu_c} \right) \quad (2)$$

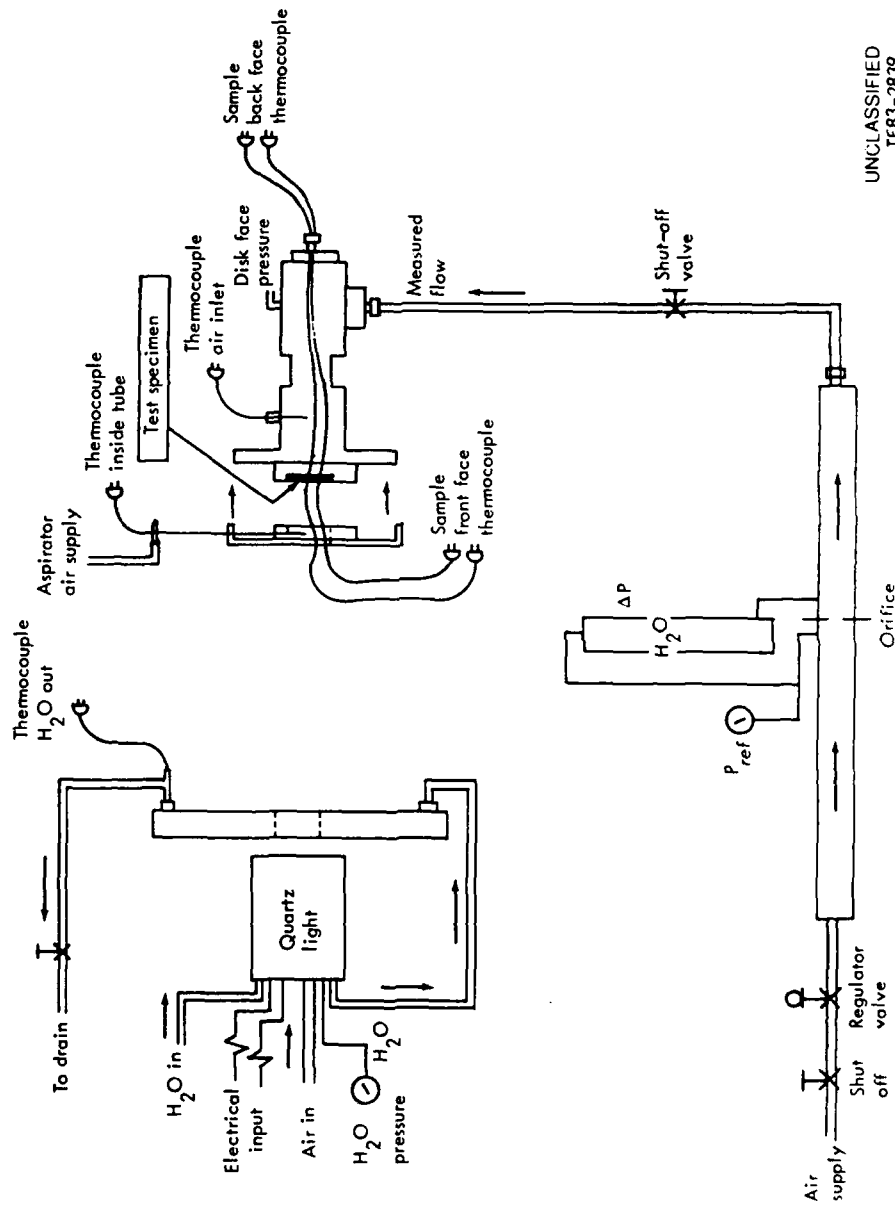


Figure 5. Schematic of thermal effectiveness rig.

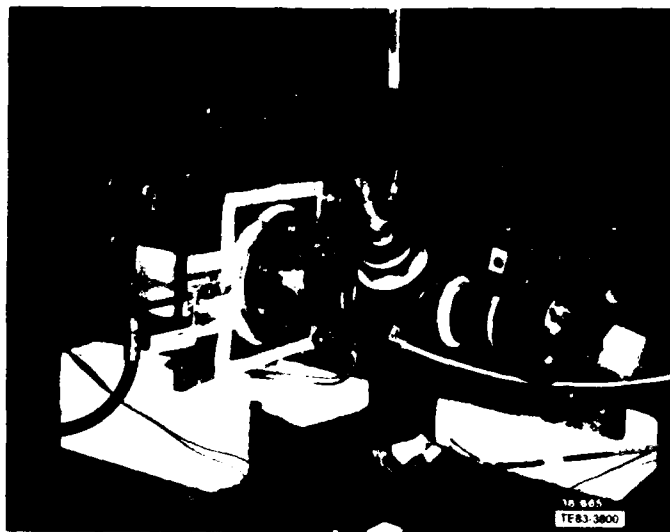


Figure 6. Thermal effectiveness rig.

In equation (2),  $G_c$  is defined as the specific flow or flow rate per unit area of porous pad in the units of  $\text{lbm/sec in.}^2$ . In addition:

- $\mu_c$  = coolant viscosity,  $\text{lbm/sec in.}$
- $T_c$  = coolant temperature,  $^{\circ}\text{R}$
- $\bar{R}$  = gas constant
- $\tau$  = pad thickness, in.
- $g$  = gravitational constant
- $P_1$  and  $P_2$  = upstream and downstream pressure in  $\text{lb/in.}^2$

Inspection of Equation 2 reveals that the resistance coefficients,  $\alpha$  and  $\beta$ , are determined as the intercept and slope, respectively, of each straight line correlation.

Figure 7 shows the pad flow data for the four specimens in terms expressed by Equation 2. Note that for flow data correlated in these terms, the lower flowing specimens have the greater slopes. Thus it would be anticipated that specimen 1 (50% density, 50% open) would have the greatest slope (highest flow resistance) followed by specimens 3 and 4 (35% density, 65% open) and finally by specimen 2 (30% density, 70% open). Examination of Figure 7 shows the data of specimen 1 and indicates that it is the more resistive but the data for the remaining specimens with densities of 30% and 35% and pad thicknesses of 0.062 and 0.127 in. reveals no significant differences in flow characteristics. The main conclusion reached from the data is that the porous pad flow characteristics should be measured to determine  $\alpha$  and  $\beta$  for a given design system and selected porous pad configuration.

The flow calculation model for the flow specimens (full assemblies) consisted of the sum of three individual resistances in series: the inlet hole loss, the pad loss, and the exit slot loss. It should be noted that in the actual combustor design, a segment of the CMC wall will be in the form of a square rather than the circular geometry of the flow and heat transfer test specimens. To accommodate this difference, the flow and heat transfer analyses were made for a circular geometry of the same area as the

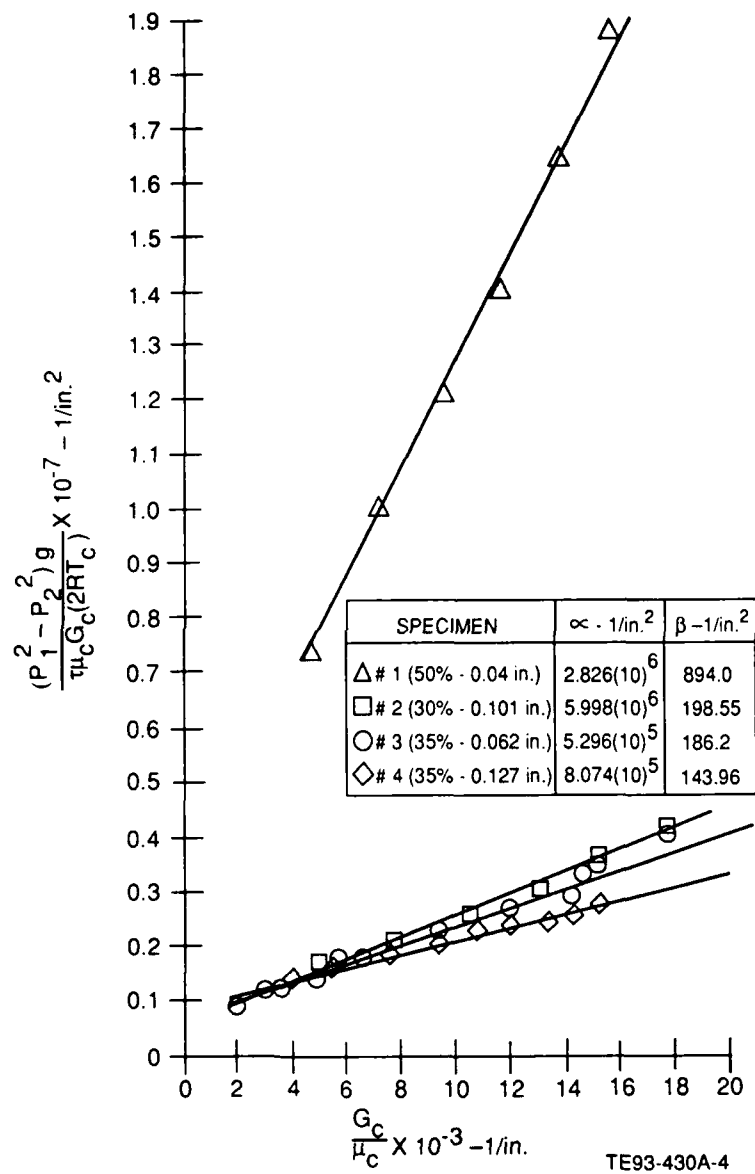


Figure 7. Correlation of Brunsbond flow characteristics.

square cell. That is, for a square segment of side length  $L$ , the radius of the circular (computational) segment was  $R_2 = L/\sqrt{\pi}$ . Figure 1 provides a definition of several important parameters used in the flow model and referred to in the discussion that follows. In equation form the flow model is expressed as:

$$\Delta P_T = \Delta P_{\text{inlet}} + \Delta P_{\text{pad}} + \Delta P_{\text{exit}} \quad (3)$$

A coefficient of discharge for the inlet hole/pad blockage was determined from the data to be 0.665 for pressure ratios up to 1.30. The effective area of the inlet hole was defined in Figure 2.

The flow/pressure drop characteristic of the pad was calculated using Green's equation (equation 2) but written in cylindrical coordinates (Ref 9),

$$\frac{(P_1^2 - P_2^2)}{T_c} = C_1 \dot{m} \alpha + C_2 \beta \dot{m}^2 \quad (4)$$

where

$$C_1 = \frac{\bar{R}}{\pi} \ln \frac{R_2}{R_1}$$

$$C_2 = \frac{\bar{R}}{2\pi^2} \left( \frac{R_2 - R_1}{R_2 R_1} \right)$$

and  $\dot{m}$  is the mass flow rate per unit thickness. The flow coefficients,  $\alpha$  and  $\beta$ , were taken from the correlation of the pad-only cold flow data.

For the exit slot loss, the pressure drop was calculated as the sum of a turning loss with a head loss factor of 0.125 and an area equal to 0.65 times the geometric slot area plus a dump loss with a head loss factor of 1 with an area equal to the slot area. In equation form the flow/pressure drop for the exit is expressed as:

$$\Delta P_{\text{exit}} = K_t \frac{1}{2} \rho V_t^2 + K_d \frac{1}{2} \rho V_e^2 \quad (5)$$

where

$$V_t = W_c / \rho A_t \text{ and } V_e = W_c / \rho A_e$$

Calculations showed that the exit loss was negligible due to the relatively large area of the exit slot.

Having established the flow calculation model, it remained to compare cold flow data from the full assembly flow specimen (Figure 4) to results from the model. However, realizing the risk of altering the flow characteristics of the CMC wall structure introduced by the actual combustor fabrication process, cold flow data was also obtained for heat transfer verification specimens A and B and compared to model predictions and data for the full assembly flow specimens.

Specimens A and B consisted of 0.062 in. porous pad with an Inconel 600 substrate brazed to the pad. A 0.1875 in. inlet orifice was cut into the Inconel 600 substrate. The specimens were completed by brazing on a 0.025 in. thick stainless steel outer ring and inner disk to form the 0.125 in. wide annular cooling air exit slot. Figure 10 provides a schematic of specimen A. Specimens A and B differed only in the length of the flow path and thermocouple placement. Specimen A had a 0.75 in. diameter center disk while specimen B had a 1.25 in. diameter center disk.

Figures 8 and 9 display the cold flow data for the subassembly and full assembly flow specimens (refer to Fig. 2) as well as specimens A and B. The data are presented as reduced cold flow data in the form of a flow factor and plotted versus the pressure ratio across the assemblies. In the plots,  $W$  is the mass flow rate through the specimens,  $T_c$  is the air temperature, and  $P_u$  and  $P_d$  are the upstream and downstream pressures, respectively.

Examination of Figures 8 and 9 shows that the inlet loss due to the inlet hole and blockage of the pad (subassembly data) is essentially the same for both pad thicknesses, whereas the flow for the full assembly is a strong function of pad thickness.

The calculated flow/pressure drop characteristics for the full assemblies are compared to the data on Figures 8 and 9. Differences between calculated and measured flow are, at a given pressure ratio, at most only 7% and, in general, much less. The implication of this close comparison is that the pad flow coefficients,  $\alpha$  and  $\beta$ , as determined from a cold flow test on the pads with flow in the specimen axial direction, can be used to define the flow/pressure drop relationship where flow is in the radial (edgewise) direction.

Also shown in Figure 8 are the cold flow data from heat transfer verification specimen A. Specimen A had the same nominal geometry as the full assembly specimen with 0.062 in. pad so that a direct comparison can be made. As can be seen, specimen A's cold flow characteristics are much lower than the full assembly flow specimen.

The material from which specimen A was made was received with a backplate brazed to the pad with the amount of braze material and extent of braze wicking into the pad unknown. In addition, when brazing the cover sheet ring and disk in place, it was necessary to subject specimen A to the braze process five times before an acceptable assembly was obtained. It is felt that the braze wicking could be significant, thus accounting for all or a portion of the reduced flow characteristics.

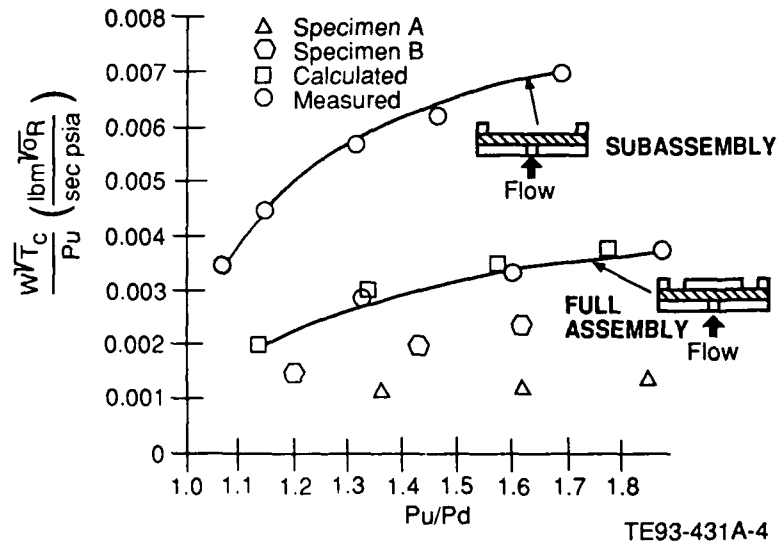


Figure 8. Comparison of measured and calculated flow characteristics of CMC test specimens—0.062 in. thick pad.

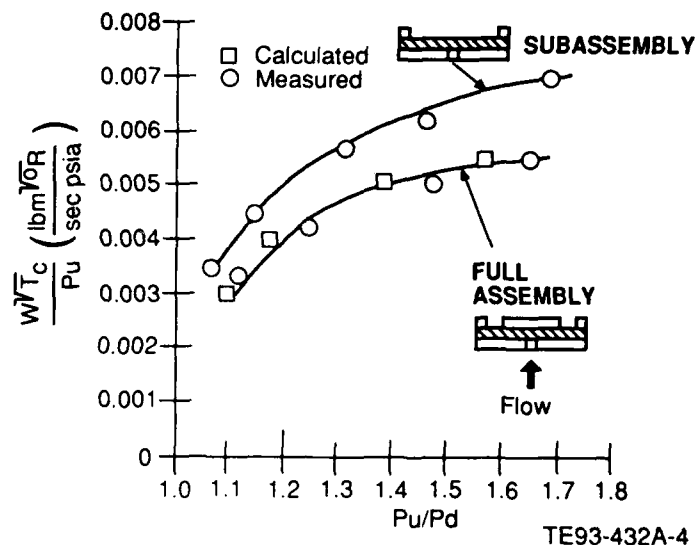


Figure 9. Comparison of measured and calculated flow characteristics of CMC test specimens—0.127 in. thick pad.

In addition to specimen A's flow data, the cold flow data for specimen B are also shown in Figure 8. As discussed previously, specimens A and B differed only in flow-path length. The additional pressure drop associated with the longer flow path of specimen B is small because most of the overall pressure drop occurs at the lower radius. Therefore, the specimen A and B flow data can be compared. The braze material found in the inlet hole of specimen A was not present in specimen B. Moreover, specimen B was only subjected to one braze cycle when attaching the cover sheet inner disk. The cold flow data of specimen B show that this specimen is less restrictive than specimen A. However, specimen B's data still lies below the flow model suggesting that the braze wicking still presents a problem.

The low flow situation of specimens A and B implies that development work is necessary so that the flow characteristics of the CMC system, as manufactured, will approach that of the radial flow specimens. If the extent of braze wicking can be determined, the pad thickness can be increased to restore the specified flow path height. A basic assumption made in the remaining portion of the investigation where flow rate calculations were required was that the analytical model is applicable or that the actual flow rate through the CMC system can be restored too close to the analytical value by fabrication modifications.

The probable cause for the flow restriction is related to the specimen fabrication procedure. Discussion with the manufacturer has also revealed that about a 50% reduction in flow area can be expected above the as-manufactured open area of the Brunsbond pad. The further restriction is probably due to braze wicking, introduction of impurities, ceramic spray penetration, and/or crushing of the Brunsbond pad.

The three terms of the flow model (Equation 3) were coded into program CMFLO3 to calculate the unknown pressures at the inlet and exit of the Brunsbond pad along with the mass flowrate through the segment. Input consists of cycle conditions, porous pad specification, and geometry of the compliant matrix segment. In light of the cold flow data given for specimens A and B in Figure 8, the program was coded with a 50% correction factor to account for flow restrictions. The corrected program was used in design calculations to size cooling orifices and determination of the final cooling airflow distribution.



Some general conclusions can be drawn by the application of the flow model to the design conditions and typical geometry of an isolated segment (i.e., individual tile element) of the CMC combustor. Calculations indicate that for the 5% liner pressure drop design condition, 63% of the overall pressure drop (3.15%) occurs across the combination of inlet orifice and surface blockage introduced by the porous pad. The remaining 37% of the total pressure loss (1.85%) occurs from pad inlet to porous pad outlet. The turning and dump loss from the coolant exit loss is found to be negligible. The loss distribution remains the same for a 3% liner total pressure drop, a value considered typical for future CMC combustor designs.

Because the inlet orifice accounts for the majority of loss and thus provides the flow distribution, the small change in loss through the porous pad will consequently lead to small relative changes in velocity distribution and convective heat removal.

Therefore, by reducing the liner pressure drop from 5% to 3% for future designs, it is expected that the cooling effectiveness of the CMC wall structure will remain relatively insensitive.

### 3.2.2 Two-Dimensional Finite Difference Heat Transfer Model Development

The heat transfer model developed for an isolated segment of the CMC wall, designated EJ8D, consists of a finite difference approximation of the heat transfer occurring within a circular element of the wall structure. The nodal network of the 2-D model represents coolant and material temperatures as a function of radial location from the inlet orifice. In the actual combustor design, an isolated segment of the CMC wall (see Figure 2) was in the form of a square rather than the circular geometry used in the finite difference model and model verification test specimens.

#### 3.2.2.1. Heat Transfer Test Specimens

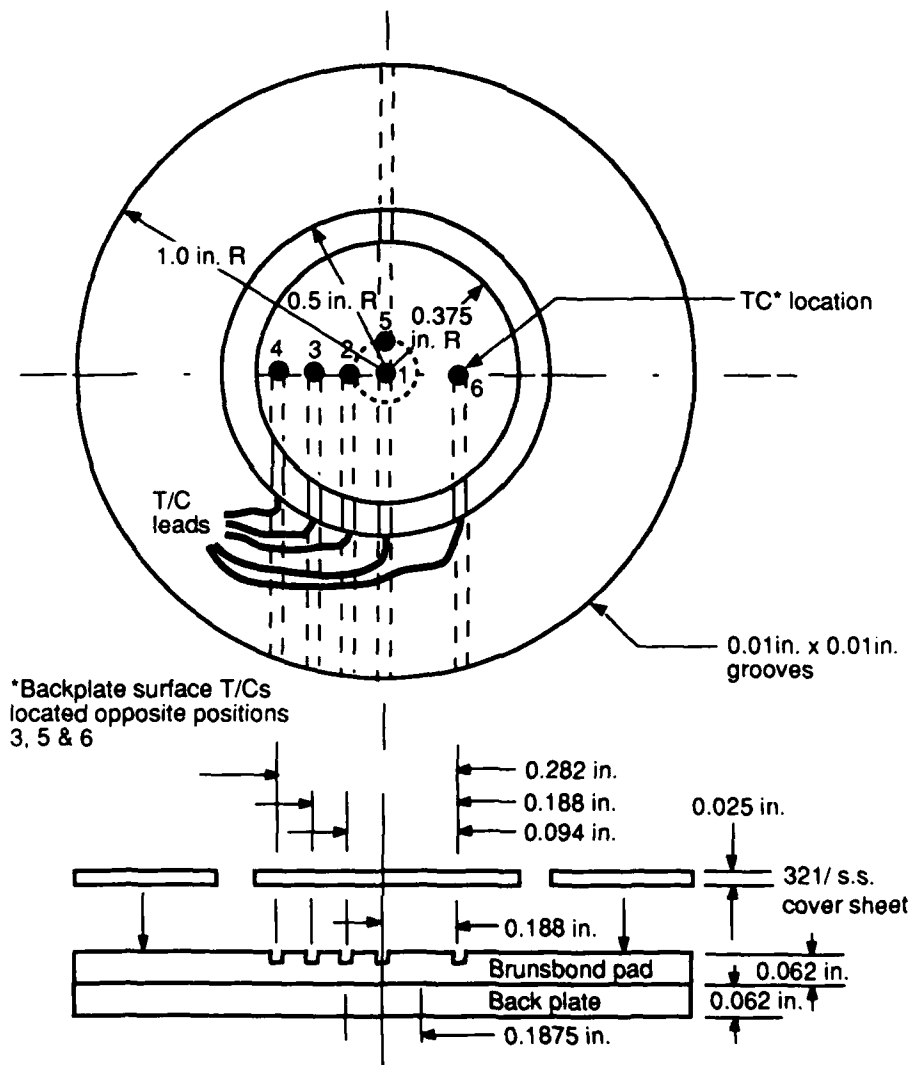
Pad specimen 1, previously described, was used to obtain an internal heat transfer characterization of the Brunsbond material. The necessary data required to establish this characterization are the cold ( $T_{SC}$ ) and hot ( $T_{SH}$ ) side surface temperature, the coolant inlet temperature ( $T_{ci}$ ), and the coolant outlet temperature ( $T_{CH}$ ). The cold and hot side surface temperatures were measured by an array of thermocouples. Grooves, 0.01 in.<sup>2</sup> in cross section, were cut into the pad using an end mill and blade. Closed tip chromel/alumel thermocouples were mounted in the grooves and fastened by laser welding the thermocouple tip to the pad wire. Also at a location removed from the tip, the thermocouple sheath was laser welded to the pad wire.

The verification specimens (previously described) were fabricated from material supplied by Technet-ics Corp. As received, the material was approximately 2 by 4 in., 0.062 in. thick, 35% density pad with a 0.068 in. Inconel 600 plate brazed to the pad. Two specimens 2 in. in diameter were cut from this material. As shown schematically in Figure 10, a 0.1875 in. diameter hole was eloxed through the Inconel 600 backplate of each specimen. Grooves were cut in the pad and thermocouples were mounted in the same manner as for the heat transfer characteristic specimen. The completed assembly was formed by brazing a 0.025 in. thick stainless steel outer ring and inner disk. Braze tape 0.005 in. thick was used in the braze process.

The two specimens differed only in length of active cooling and thermocouple placement. Specimen A had a 0.75 in. diameter center disk while specimen B had a 1.25 in. diameter center disk. For both specimens, a 0.125 in. wide annular cooling air exit slot was formed by the outer ring and inner disk.

#### 3.2.2.2 Heat Transfer Characteristics of the Brunsbond Pad

Knowledge of the internal (matrix) heat transfer characteristics of the Brunsbond pad is required as an input to the design system. The coolant temperature rise through the matrix (thermal effectiveness)



\*Backplate surface T/Cs  
located opposite positions  
3, 5 & 6

TE93-433 -4

Figure 10. Schematic of verification test specimen A.

and the metal temperature gradient across the structure in the direction of coolant flow are the most useful parameters. These principal test results of interest (i.e., coolant dimensionless temperatures rise and matrix dimensionless temperature gradients) were analyzed using a one-dimensional porous wall thermal exchange model to evaluate the mean matrix-to-coolant heat transfer coefficient.

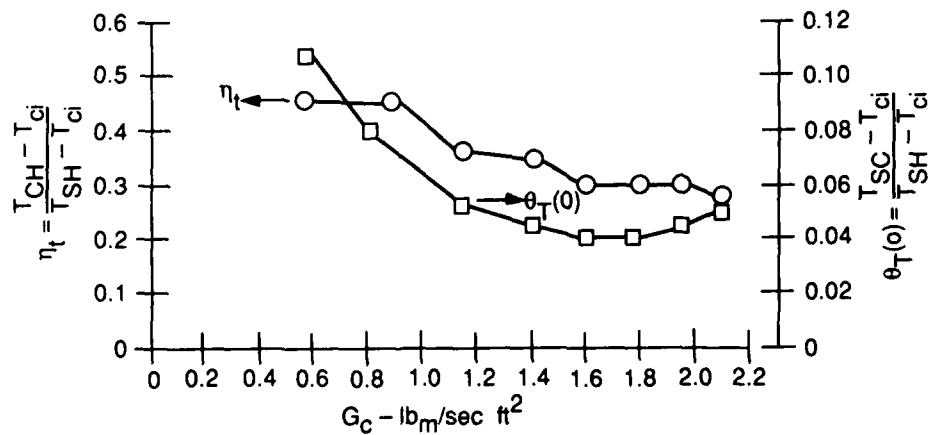
Figure 11 displays the thermal effectiveness ( $\eta_t$ ) and matrix dimensionless temperature gradient ( $\theta_T(o)$ ) versus the specific coolant flow rate obtained during testing. The thermal effectiveness compares the actual heat transfer rate to the maximum possible heat transfer rate that would be realized if the coolant temperature reached the wall temperature, viz,

$$\eta_t = \frac{T_{CH} - T_{ci}}{T_{SH} - T_{ci}} \quad (6)$$

The matrix dimensionless temperature gradient ( $\theta_T(o)$ ) is defined as:

$$\theta_T(o) = \frac{T_{SC} - T_{ci}}{T_{SH} - T_{ci}} \quad (7)$$

In Equations (6) and (7), the hot and cold side matrix temperatures are the average of the five and four thermocouples measuring these surface temperatures. The coolant outlet temperature is the average of three readings taken across the instrumented region of the specimen. The trends exhibited by these data are, in general, what would be anticipated—a decreasing of the parameter with increasing specific flow rate. Two of the  $\theta_T(o)$  values at the highest specific flow rates do not follow the anticipated trend. This is attributed to the uncertainty in the measurement of small temperature difference occurring at high flow rates. It should also be noted the low value of  $\theta_T(o)$  which is a direct result of the low conductivity of the pad.



TE93-434 -4

Figure 11. Thermal effectiveness and matrix dimensionless temperature gradient data from heat transfer characteristics specimen.

The porous wall model used to evaluate the mean matrix-to-coolant heat transfer coefficient was taken from Ref 10. The assumptions made in deriving the governing equations were:

- one dimensional heat transfer and fluid flow with heat flux in the opposite direction to fluid flow
- heat transfer by gas conduction is neglected
- constant property values and heat transfer coefficient

The result of Ref 10 which is used for data reduction is that:

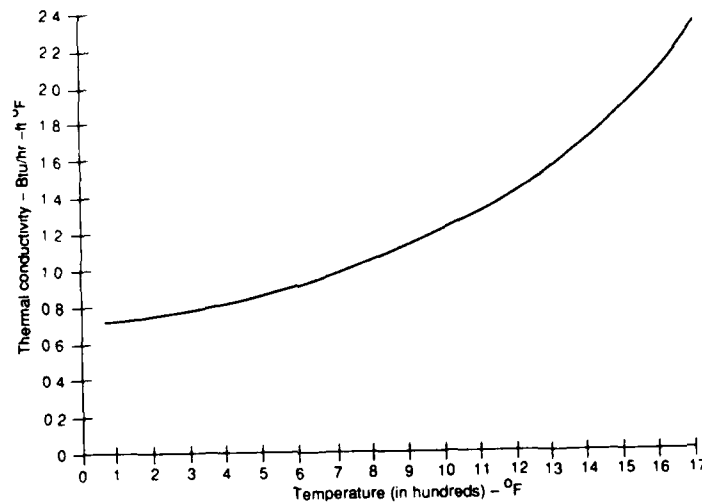
$$\eta_t = (B[e^{r_1} - e^{r_2}])^{-1}([1 - \theta_T(o)e^{r_2}]r_1e^{r_1} - [1 - e^{r_1}\theta_T(o)]r_2e^{r_2}) \quad (8)$$

where

$$r_1 = \frac{A}{2}(1 - \sqrt{1 + 4(B/A)}), \quad r_2 = \frac{A}{2}(-1 - \sqrt{1 + 4(B/A)})$$

$$A = \frac{h't}{G_c C_p c}, \quad B = \frac{G_c C_p c \tau}{k_m}$$

For a given configuration, the parameters  $\eta_t$ ,  $\theta_T(o)$ ,  $G_c$ ,  $C_p c$ , and  $t$  are known and the volumetric heat transfer coefficient,  $h'$ , can be evaluated from Equation 8 by iteration if the thermal conductivity,  $k_m$ , of the matrix is known. The pad thermal conductivity was taken from Ref 11. Figure 12 displays the pad thermal conductivity versus temperature.



TE93-435-4

Figure 12. Thermal conductivity for 1/16 in. H-875 35% density Brunsbond pad, through the plane thickness.

Applying Equation 8 to the data yields the results shown in Equation 9. The resulting least squares linear fit of the data yielded the expression:

$$h' = 276.96 G_c^{0.8298} \quad (9)$$

where  $G_c$  has the units of  $\text{lbm/hr ft}^2$  and  $h'$ ,  $\text{Btu/hr ft}^3 \text{ }^\circ\text{F}$ .

Another parameter which was calculated was the dimensionless fluid temperature rise up to the backface of the specimen. This parameter is denoted as  $\theta_f(o)$  and is given by:

$$\theta_f(o) = \frac{T_{CC} - T_{ci}}{T_{SH} - T_{ci}} = (B[e^{r_2} - e^{r_1}])^{-1} ([1 - \theta_T(o)e^{r_2}]r_1 - [1 - \theta_T(o)e^{r_1}]r_2) \quad (10)$$

Four of the data points yielded the result that  $\theta_f(o) > \theta_t(o)$  which implies that the coolant temperature at the backface is greater than the backface matrix temperature or that heat transfer is from the fluid to the matrix rather than the opposite which is the expected result. These unexpected results were felt to be due to inaccurate matrix metal or coolant outlet temperatures and, therefore, were not included in the fit of the data.

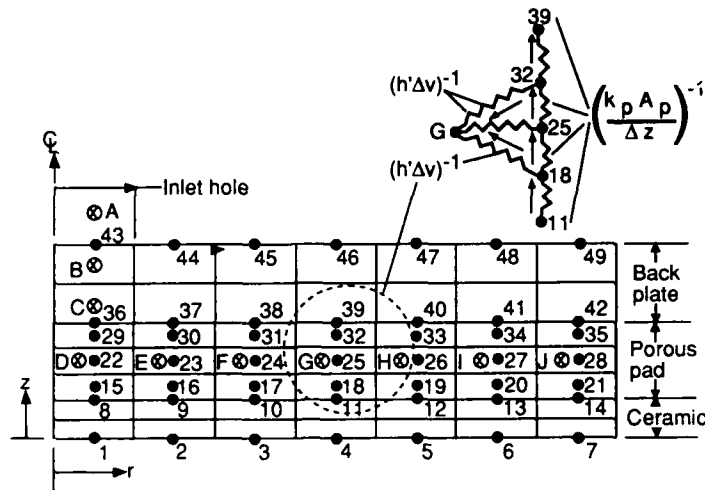
Attempts to correlate  $h'$  in terms of a Nusselt versus Reynolds number type of relationship were not made since the internal surface area to volume ratio and characteristic length could only be determined by further testing which was beyond the scope of the present program. Likewise, property values are, strictly speaking, only those that occurred during the test. Use of equation (9) will yield conservative values of  $h'$  at combustor operating condition since actual property values would, at the higher temperature levels, produce higher heat transfer coefficients.

### 3.2.2.3 Complete Micro (Isolated Segment) Design Model

The 2-D heat transfer model (EJ8D) is shown in Figure 13. This model consists of a finite difference approximation of the heat transfer occurring within an isolated segment of CMC wall structure. The isolated segment is represented by 49 nodes with each node representing the material contained within the node boundaries. Conduction is modeled in both the  $r$  and  $z$  directions. Material thermal conductivity is allowed to vary with temperature or direction. The coolant circuit is simulated by 10 fluid nodes A through J. The temperatures of the entire network of nodes were solved for by using an explicit finite difference technique. A description of this technique is found in Ref 12.

It is important to note the simulation of heat flow in the  $z$  direction as well as the heat flow from the pad nodes to the coolant. Shown in Figure 13 is an example of this heat flow simulation where the connectivity of nodes is shown in terms of resistances (resistance =  $1/\text{conductance}$ ). Heat flowing from the ceramic first passes through a portion of the pad by conduction (from node 11 to 18) and then a portion of the heat (from node 18 to G) is picked up by the coolant. In the actual case, heat would flow from the ceramic Brunsbond interface directly into the coolant; therefore, in the finite difference model an approximation is made. The remaining heat flow in the  $z$  direction must pass through successive pad resistances before flowing into the coolant. The coolant node represents the average temperature of the coolant at a particular radial location.

Boundary conditions for the 2-D heat transfer model consisted of: (1) a hot side driving temperature and heat transfer coefficient, (2) coolant side heat transfer coefficient, (3) coolant flow rate, and (4) backplate side ambient temperature and heat transfer coefficient.



TE93-436 -4

Figure 13. Finite difference heat transfer model.

In summary, the following elements comprise the complete isolated segment analysis/design method for the CMC system:

- The heat transfer model consisted of the finite difference model as shown in Figure 13 with the nodal conductances modified to reflect variations of the specific geometry being examined.
- The thermal conductivity of the porous pad in both the radial (r) and through-the-wall (z) directions was that shown in Figure 12.
- The Brunsbond pad internal volumetric heat transfer coefficient was calculated using Equation 9.
- The inlet hole flow/pressure drop was calculated using a coefficient of discharge of 0.665 with an area equal to the inlet hole free area multiplied by 1 minus the porous pad density.
- The porous pad flow/pressure drop was calculated using Equation 4 with the flow coefficients  $\alpha$  and  $\beta$  taken from the experimental data shown in Figure 7.
- The cell exit slot pressure loss was calculated using Equation 5.
- The thermal conductivity of the thermal barrier coating (TBC) used was 0.87 Btu/hr ft °F and invariant with temperature over the range of 1700°F to 3600°F (Ref 13).

For design study, the system pressure drop ( $\Delta P/P$ ), thickness of porous pad ( $\tau_p$ ), thickness of thermal barrier coating (TBC), and cell size (L) were varied. The boundary conditions of radiation heat flux, gas-to-wall convective heat transfer coefficient and temperature, and backplate to ambient heat transfer coefficient and temperature were calculated at conditions consistent with combustor operating conditions.

The radiation heat flux was calculated in the case of the TBC-coated walls using Ref 14

$$q''_{\text{rad, TBC}} = \sigma(0.5) \epsilon_H T_H^{1.5} (T_H^{2.5} - T_{WH}^{2.5}) \quad (11)$$

and for the metal cover sheet using Ref 15

$$q''_{\text{rad}} = \sigma \frac{(1 + \alpha_w)}{2} \epsilon_H T_H^{1.5} (T_H^{2.5} - T_{WH}^{2.5}) \quad (12)$$

with  $\alpha_w = 0.9$

The flame emissivity,  $\epsilon_H$ , was calculated using Ref 16

$$\epsilon_H = 1 - \exp(-39000 P_{gs} \Lambda \sqrt{f/a} l_b T_H^{1.5}) \quad (13)$$

where

$P_{gs}$  = gas static pressure in atmospheres  
 $\Lambda$  = luminosity factor  
 $f/a$  = fuel-to-air ratio  
 $l_b$  = mean length in feet = hydraulic diameter for an annular combustor

The luminosity factor,  $\Lambda$ , was calculated by Ref 17

$$\Lambda = 0.0691 (C/H - 1.82)^{2.71} \quad (14)$$

where  $C/H$  is the fuel carbon/hydrogen ratio by weight. For this study,  $\Lambda$  had a value of 3.

The gas-to-wall convective heat transfer coefficient was calculated using the turbulent flat plate equation modified for temperature dependent properties as suggested in Ref 18.

$$h_g = 0.0295 \frac{k_g}{x} \left( \frac{\rho_g V_g x}{\mu_g} \right)^{0.8} Pr_g^{0.6} \left( \frac{T_{WH}}{T_g} \right)^{-0.25} \quad (15)$$

where the thermal properties  $k$ ,  $\mu$ , and  $Pr$  are evaluated at the gas temperature and  $x$  (surface distance) is measured in this case from the combustor dome plane. For inclusion into the finite difference model, the radiation heat flux (from Equations 11 or 12) and the gas-to-wall convective heat transfer coefficient were combined into an equivalent heat transfer coefficient by the relationship

$$h_{eq} = \frac{h_g(T_g - T_{WH}) + q''_{\text{rad}}}{(T_g - T_{WH})} \quad (16)$$

The backplate-to-ambient heat transfer coefficient was calculated using the turbulent pipe flow equation (Ref 19)

$$h_c = 0.023 \frac{k_c}{D_h} \left( \frac{\rho_c V_c D_h}{\mu_c} \right)^{0.8} Pr_c^{0.333} \quad (17)$$

It should be noted that the gas temperature next to the wall,  $T_g$ , has been assumed to be equal to the average flame temperature,  $T_h$ , having a value close to that of stoichiometric. Assuming the near stoichiometric gas temperature to define the convective heat load accounts for the possibility that a "hot" streak could occur next to the combustor wall.

It should also be noted that in the actual combustor design a "cell" of the CMC system will be in the form of a square rather than circular as was the case with the verification samples and the finite dif-

ference model. To accommodate this difference, the flow calculations and heat transfer analysis were made for a circular geometry fully encompassing the square cell. That is, for a square cell having a side length of  $L$ , the radius of the circular (computational) cell was  $R_2 = L/\sqrt{2}$ . Basing the flow calculations on this radius ( $R_2$ ) is conservative in that the longest flow path is used. However, the actual flow and heat transfer occurring within the square cell will not be symmetric and, therefore, the analysis based on a circular cell will only be approximate.

The established design methodology for an isolated segment of the CMC wall structure was subsequently applied in a study of the parameters affecting the temperature distribution of the CMC system at typical combustor operating conditions. In this study, the temperature of the TBC ( $T_s$ ), the TBC/porous pad interface temperature ( $T_i$ ), and the substrate surface temperature ( $T_b$ ) distributions were plotted versus radius of the isolated segment. The following conclusions were made from this investigation:

- For a fixed cell length, the TBC thickness has the greatest effect on the maximum temperature attained by the TBC surface and the temperature difference across the TBC as compared to the effects produced by  $\Delta P/P$  or  $\tau_{PAD}$ .
- For a fixed cell length, the maximum temperature attained by the TBC/porous pad interface is affected more by changes in  $\tau_{PAD}$  as compared to changes in  $\Delta P/P$  or  $\tau_{TBC}$ .
- For a fixed cell length, the radial temperature distribution (but not level) of  $T_{TBC}$ ,  $T_i$ , and  $T_b$  are virtually unaffected by changes of  $\tau_{TBC}$ ,  $\tau_{PAD}$ , and  $\Delta P/P$ .
- The greatest changes in maximum temperature and temperature distribution of  $T_s$ ,  $T_i$ , and  $T_b$  are made by changes in cell length.

The expected result was obtained that since there is a greater resistance to heat flow with the TBC, a lower interface ( $T_i$ ) temperature is attained than with a Hastelloy X cover sheet.

#### 3.2.2.4 Heat Transfer Model Experimental Verification

Having established the CMC isolated segment (micro) design method, experimental verification tests were carried out to validate the 2-D heat transfer model.

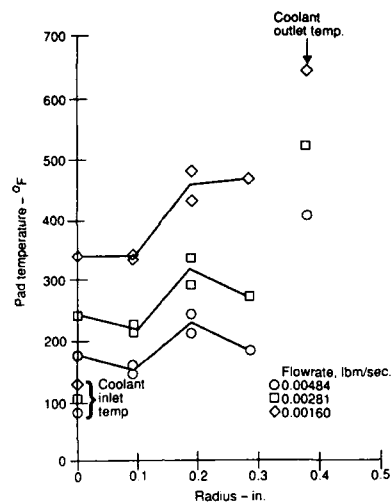
The verification specimens described previously and shown in Figure 10 were tested in the thermal effectiveness rig to obtain near cover sheet/porous pad interface temperature data. Thermocouples imbedded in the porous pad measured pad temperature approximately 0.01 in. from the interface. Testing was accomplished over a range of mass flow ratios at essentially constant heat flux. Figures 14 and 15 show the thermocouple data for three flow rates. The flow rates shown represent the range of flow rates plus a midrange value. The data for specimen A shows a leveling off or decreasing temperature trend with increasing radius. The expected trend of increasing temperature with radius is exhibited by the data of specimen B. Since it is important to the data reduction to obtain a realistic average temperature, it was decided to use only specimen B's data for the verification of the heat transfer model.

Boundary conditions for the model consisted of: (1) a hot side driving temperature and heat transfer coefficient, (2) coolant side heat transfer coefficient, (3) coolant flow rate, and (4) backplate side ambient temperature and heat transfer coefficient. The methods for obtaining these parameters are described in the following paragraphs.

The method used to establish a gas side heat transfer coefficient,  $h_g$ , for the finite difference model (refer to Figure 13) simulation of the rig test is based on a simple heat balance on the specimen, i.e.,

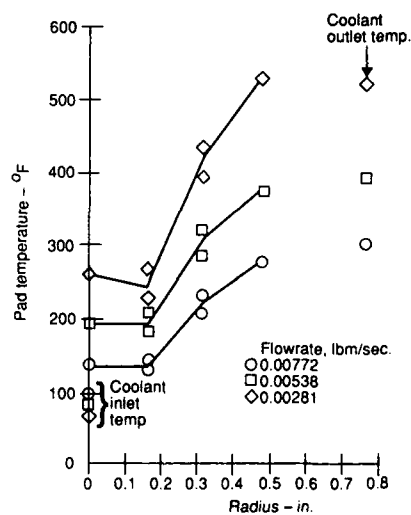
$$Q = UA_g (T_g - \bar{T}_w) = W_c C_{p_c} (T_{co} - T_{ci}) \quad (18)$$





TE93-437-4

Figure 14. Verification specimen A porous pad metal temperature data.



TE93-438-4

Figure 15. Verification specimen B porous pad metal temperature data.

where

$$U = \left[ \frac{1}{h_g} + \frac{\Delta Z_{ss}}{K_{ss}} + \frac{\Delta Z_{PAD}}{K_{PAD}} \right]^{-1}$$

or

$$U = \frac{W_c C_{p_c} (T_{co} - T_{ci})}{A_g (T_g - T_w)} = \left[ \frac{1}{h_g} + \frac{\Delta Z_{ss}}{K_{ss}} + \frac{\Delta Z_{PAD}}{K_{PAD}} \right]^{-1} \quad (19)$$

$U$ , the overall conductance, is from the heat source to the location of test specimen thermocouples and  $\Delta Z_{PAD}$  is the distance into the pad to this location ( $= 0.010$  in.).

The value of  $h_g$  can be calculated once a value of  $T_g$  is selected since all other parameters are measured or are known. The driving temperature,  $T_g$ , was selected at an arbitrary high value so that regardless of the wall temperature calculated by the model, the correct value of  $Q$  would be reproduced. The average wall temperature  $\bar{T}_w$ , was determined by integrating the curve of measured wall temperature versus radius.

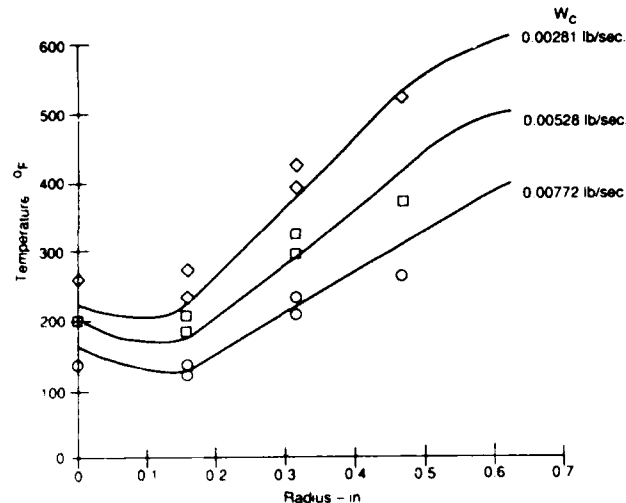
The coolant side heat transfer coefficient was calculated from the relationships between volumetric heat transfer coefficient,  $h'$ , and the specific flow rate,  $G_c$  (Equation 9). The measured flow rate during the test divided by the average geometric flow area of a node was used to determine the local value of  $G_c$ . The coolant inlet temperature was taken as the value indicated by the thermocouple placed over the inlet hole. Local coolant temperatures were calculated as part of the node network.

The backplate-to-ambient fluid heat transfer coefficient was set at a value of  $5 \text{ Btu/hr ft}^2 \text{ } ^\circ\text{F}$  which is consistent with a low flow or free convection case. The ambient fluid temperature was set equal to the measured plenum air temperature.

The model and boundary condition calculation technique previously described was applied to the conditions obtained during testing of specimen B. The calculated temperatures of the porous pad at a location 0.01 in. into the pad are compared to the measured temperatures in Figure 16. The correlation between calculated and measured temperatures appears to be good with radial distance and throughout the range of flow rates. A maximum difference of  $55^\circ\text{F}$  occurs between calculated and measured temperatures with the calculated value being high. It should be noted that to obtain the decreasing trend of temperature from a radius of zero to approximately 0.15 in., it was necessary to reduce the volumetric heat transfer coefficient calculated for the first porous pad node. This lower heat transfer coefficient, it is argued, is due to the lower velocities occurring in this near stagnation region. The factor by which the volumetric heat transfer coefficient was lowered was determined for the midrange flow rate case and held constant for the high and low flow rate cases.

The influence of two additional parameters on the correlation of calculated specimen temperatures with the measured data were examined prior to the selection of the final verification analysis method. These two parameters were: (1) the porous pad thermal conductivity in the  $r$  direction and (2) the backplate ambient heat transfer coefficient.

As was stated previously, the porous pad thermal conductivity was taken from Ref 11. These values are for the thermal conductivity in the  $z$  direction (parallel to the thickness direction) and according to Ref 13 the thermal conductivity of the pad in the  $x$ - $y$  plane (parallel to the sheet dimension) is different. To ascertain the influence of the anisotropic thermal conductivity on calculated specimen tempera-



TE93-439 -4

Figure 16. Comparison of calculated and measured porous pad temperatures of specimen B.

tures, a case was run using the model where the pad thermal conductivity in the z and r directions were allowed to be different. Since there was no published data on the thermal conductivity of the pad in the x-y direction (or radial direction in the model) a value corresponding to that of Inconel 600 material was used. Using this value represents a conservative value as regards radial conduction.

The results of this study compared the metal temperatures of the isotropic thermal conductivity case to those of the anisotropic thermal conductivity case. The flow rate selected for these cases corresponds to the lowest of the range tested. The low flow rate was selected since the conduction effects would be relatively more important than in the higher flow rate cases. Examination of these temperature distributions shows very little effect due to the anisotropic thermal conductivity, particularly when it is recalled that the r direction thermal conductivity has been set to a value one order of magnitude larger than the z direction value. Due to this small influence, the value of thermal conductivity in both the z and r directions are set equal to the porous pad thermal conductivity for the final verification analysis.

It should also be noted that since the information required to evaluate the amount of heat conducted along the backplate (i.e., specimen edge/rig clamping ring temperature) was not known, further work to correlate the backplate wall temperatures was not attempted. Rather, the final heat transfer model established by the verification process was that which yielded the best reproduction of the critical porous pad temperature distribution and coolant temperature rise. As a consequence the final heat transfer yielded an overpredicted specimen backplate wall temperature.

### 3.3 RESULTS OF THERMAL STRESS AND MICRO STRUCTURAL LIFE PREDICTION

This section provides a brief description of a parametric study (Ref 20) carried out to assess the thermal stress and deflection characteristics of an isolated segment of the CMC wall structure. The goal of this work was an attempt to predict the structural life of the CMC system for various design configurations.

For the CMC system, the critical failure modes of the material in the combustor can be summarized as follows:

- substrate (i.e. metal support or backing): low cycle fatigue and buckling
- compliant layer/ceramic interface: delamination at the braze joint and oxidation/corrosion of the compliant layer material
- ceramic layer: low cycle fatigue, spalling and cracking

Data that was available at the time of the study for material strengths for each of the materials in the CMC system were as follows:

- Strength at 0.2% yield for 310 stainless steel, used in the study for the substrate layer, is approximately 25 ksi. For Hastelloy-X, the yield strength is 42 ksi at 1000°F.
- For the compliant layer or Brunsbond; data for Hoskins 875, 35% dense, indicated the inplane 0.2% yield strength at 70°F is 4.6 ksi and at 1500°F 0.85 ksi. Linear interpolation to 1000°F puts the strength at 2.16 ksi reducing to 1.90 ksi at 1100°F.
- Wide variation was found in the quoted bend strength of yttria stabilized zirconia. The ceramic, at the high end was found to have a strength of 17 ksi at 1832° F reducing to 10 ksi at 2192°F. More abundant data supported a bend strength of 1-4 ksi at 2000°F for ceramics with an approximate density of 4.5 gm/cubic centimeter.

Results from the isolated segment heat transfer design study, reported previously, were used in the analysis of thermal stress and deflection produced by the corresponding temperature fields. Baseline design for the parametric was defined with a 0.375 in. diameter inlet, 0.042 in. thick substrate of 310 stainless, 0.062 in. thick compliant layer of Hoskins 875 wire, 5 mils in diameter with 35% solid pad density, and plasma sprayed Zirconia thermal barrier 0.040 in. thick.

The analysis was performed using a 20 node solid finite element model (STRATA/SOLID). The ceramic and Brunsbond pad layers having 18 elements each and the metal substrate layer having 34 elements. The composite section was modeled as a quarter section and as a complete segment. The complete segment was analyzed for one case to compare with the results of the quarter section model. Results were the same and the quarter section model was used for all subsequent geometries.

Results were generated for maximum tensile and compressive normal stresses both in the plane of the material and perpendicular to the plane. The stresses perpendicular to the plane of the material are considerably less than within the plane; typically by an order of magnitude.

Output from the finite element model was in the form of isostress plots for the various geometries and deflection data. Data from the isostress plots were reduced to obtain max in-plane and normal-to-plane stresses for each of the three wall layers (ceramic, Brunsbond, and substrate) versus tile segment side length, ceramic thickness, Brunsbond thickness, and pressure drop.

Conclusions from the overall analysis were given as follows:

- The 1.0 in. length segment has significantly lower in-plane stresses than the 2.0 in. length segment for the metal 310SS layer (35 ksi versus 83 ksi). The ceramic and Brunsbond pad have lower stresses but not of the same magnitude in reduction as the 310SS. The ceramic max in-plane stress was reduced from 21 ksi to 16.5 ksi for the change from 2.0 in. to 1.0 in. length segment. The Brunsbond pad maximum stress was reduced from 4.25 ksi to 2.8 ksi for the 2.0 in. to 1.0 in. length segment change.
- For the baseline geometry, the 0.02 in. thick ceramic CMC segment has lower in-plane stresses for all layers of CMC materials compared to the 0.06 in. thick ceramic composite segment.

- For the baseline geometry, the 0.085 in. thick brunsbond pad CMC segment has lower in-plane stresses for all layers of CMC material compared to the 0.040 in. thick Brunsbond pad composite segment.
- Percent pressure drop of cooling air seems to have little effect on max in-plane stresses on the baseline geometry for the 2% to 4% range. The metal 310SS in-plane stress has largest reduction of stress from 38 ksi to 32 ksi for 2% versus 4% pressure drop.
- The maximum in-plane stresses on the Brunsbond pad for all conditions analyzed were above the interpolated 0.2% yield strength of 1.90 ksi at 1100°F and 2.16 ksi at 1000°F.
- The maximum in-plane stress on the metal 310SS layer was below the 25 ksi 0.2% yield strength only for the baseline geometry with 0.085 in. thick Brunsbond pad.
- A plastic analysis was not performed to see what effect yielding of material would have on stress distribution since STRATA would not allow plastic analysis on the Brunsbond pad with anisotropic properties.
- Location of maximum inplane tensile stress, the component which appears to be durability limiting, has maximums in the ceramic and in the compliant layer occurring on the axis of the cooling sector, at their respective cold side interfaces. Maximum in the substrate metal occurred at the edge of the coolant inlet hole, aligned with an edge bisector, and at the hot side interface except when the pad thickness was altered.
- Thermal deflection at the corners of the cooling sector amount to 0.003 in to 0.005 in. in the plane of the material regardless of composite layer or dimensions. Normal to the plane the deflections are negligible for the lower stress designs to a positive (toward the cold surface) 0.003 in. - 0.005 in., for example with the baseline.

With stress, temperature, and material limitations taken into account the best of the parametric study design (0.020 ceramic thickness) exceeds the material limits in all three layers. Further concluded from the parametric is that improvement in the design could be obtained by reducing the ceramic thickness, increasing the substrate strength by changing material, and/or changing the thickness.

Although the finite element model analysis did evaluate maximum in-plane and normal-to-plane stresses and deflections, the results were deemed inconclusive due to the many weaknesses of the method which included the following:

- lack of operational experience
- ceramics not well characterized
- material characterization beyond current program scope
- use of available material data

Subsequently, predicted cycle life of the CMC structure based on thermally induced stresses was omitted from the program with approval of the NASA Technical Monitor. Combustor predicted life cycle goals were replaced with goals comparing overall cooling performance directly with other high performance candidates, i.e. Lamilloy or effusion. For oxidation life considerations of the Brunsbond pad, a ceramic/Brunsbond interface temperature design limit of 1750°F was set.

#### IV. TASK 2—PRELIMINARY (MACRO) COMBUSTOR DESIGN

In Task 2, the selected materials and micro-segment flow and heat transfer characterization from the Task 1 effort were implemented for a preliminary design study of a complete combustion system utilizing the CMC wall structure. The initial macro design phase of the program encompassed two sets of cycle conditions that provided input conditions for an investigation that included the following:

- empirical and simple 1-D design analysis
- aerothermal design optimization studies utilizing Allison's air distribution and three-dimensional (3-D) internal flow analysis models
- development and utilization of algorithms for one-dimensional (1-D) and pseudo 3-D macro heat transfer models for predicting CMC wall temperatures in the axial and axial/tangential combustor directions
- an ongoing investigation of combustor construction techniques
- preparation of conceptual layout drawings to examine the fundamental mechanical design constraints and provide geometric input to the aerothermal modeling effort

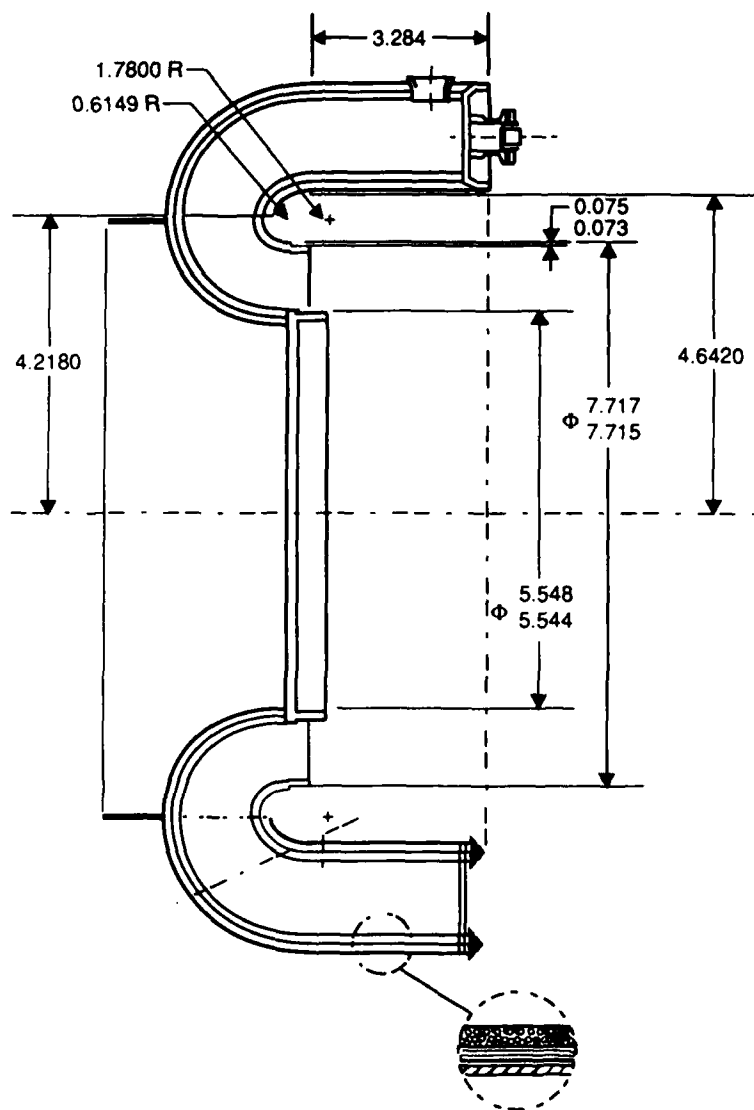
Although the level of technical specification provided during Task 2 effort was extensive, only an overview description is provided in this report. This is because the final, selected cycle conditions (Table I) were chosen near the completion of Task 2 effort and many of the mechanical and aerothermal design results of Task 2 effort are not directly applicable to the final combustor configuration. However, during preliminary combustor design, the gross mechanical features of the combustion system were selected and the iterative aerothermal analysis provided valuable insight to the performance characteristics and wall temperature distribution of the CMC combustion system. The final CMC combustor design, fabrication, and testing are described in Sections V and VI. In addition, since Task 2 effort included development of the macro heat transfer codes used in the final detailed design, as well as utilization of Allison's aerothermal design codes, a description of the macro design codes is referred to the reader and provided in Appendix B.

##### 4.1 PRELIMINARY DESIGN STUDY—EARLY CONCEPT COMBUSTION SYSTEM

The preliminary design effort resulted in the selection of the early CMC combustor configuration based on Allison's advanced, small reverse-flow combustor development program, which was active at the time and subsequently paralleled the CMC combustor program. The CMC program relied on this development effort by following its lead in regard to cycle conditions and overall flowpath. The concept 1 combustor is a compact, annular, reverse-flow design incorporating a single row of primary combustion air holes and a single row of dilution air holes, on both the inside and outside liners. The selected design dimensions were compatible with the existing Allison single-burner rig facility. Figure 17 shows a cross-section of the combustor along with major dimensions. The CMC concept is used in construction of the inner and outer liner walls as well as the outer transition liner. The dome was cooled with Lamilloy and contained twelve (12) piloted, air blast fuel nozzles each surrounded by an axial swirler. Design conditions, for the 3000°F burner outlet temperature case, and preliminary design parameters for the concept 1 design are given in Table II.

The concept 1 cycle conditions were used along with the combustor flowpath dimensions to prepare boundary conditions for a full combustor aerothermal analysis of the concept 1 system. Results from this effort included COM3D 3-D combustor performance code output for operation at 2240°F and 3000°F BOT. Subsequent to this analysis, the 1-D macro heat transfer code, WALLTEMP, was used to optimize the cooling flow distribution.

COM3D results for gas temperature and  $f/a$  ratio distribution in the combustor were applied to the WALLTEMP heat transfer study which investigated the effects of variations in liner percentage of cooling air, ceramic thickness, and inlet gas temperature. Conclusions from this study for the cycle and design conditions given in Table II suggested a ceramic thickness of 0.05 to 0.06 inch was optimal and



TE83-3805 -4

Figure 17. General layout of concept 1 CMC combustor.

Table II.  
Preliminary design study—concept 1 combustor design parameters.

Wa (liner flow, lb/s)	5.029
P3 (inlet pressure, psi)	203
T3 (inlet temperature, °F)	812
Wf (fuel flow, lb/hr)	645
F/A (fuel/air ratio)	0.0356
Wcorr (corrected flow, lb/s)	0.570
Temperature rise (°F)	2188
Burner outlet temperature (°F)	3000
Liner pressure drop (%)	3.0
Vref (reference velocity, ft/s)	25.7
Tau (residence time, msec)	10.63
Aref (liner reference area, sq in.)	65.3
L/H (liner aspect ratio)	2.05
Theta (aerodynamic loading parameter, lb/sec-cu ft)	0.039
HRR (heat release rate, Btu/hr-cu ft-atm)	6.92E10+6
Vol (combustor volume, cu ft)	0.124

that inlet gas temperatures shouldn't exceed 900°F to meet Brunsbond/ceramic interface temperature goals. Four major flow split modifications were also investigated to minimize cooling air requirements and obtain a uniform wall temperature profile. Plots of wall temperature at the ceramic surface, Brunsbond/ceramic interface, Brunsbond/substrate interface, and substrate surface versus axial location in the combustor were generated with the objective of achieving a relatively flat profile to minimize temperature gradients in the axial direction.

Additional aerothermal analysis were subsequently carried out along with CMC wall temperature predictions when revised cycle conditions became available. Design effort was refocused on a combustion system with design conditions shown in Table III. For the new cycle, baseline BOT was 2398°F and the target BOT was 3000°F.

In addition to the design point cycle conditions, the basic geometric envelope of the system was modified to the latest small combustor technology development program configuration. Heat transfer parameters were re-directed to the baseline design and layout drawings initiated. For comparative purposes, modifications to the baseline airflow distribution were initiated to minimize wall temperature gradients. Soon after this effort was initiated, the final selection of cycle design conditions was announced, and as described in Section V, the final CMC combustor design was carried out.

#### 4.2 PRELIMINARY MECHANICAL DESIGN EFFORT

Concurrent with the preliminary aerothermal design effort was an ongoing investigation of liner construction techniques. Investigation of the best methods to make gaps or slots in the CMC material was pursued by starting a limited test program. Gaps need to be created in the ceramic coating and Brunsbond pad for two major reasons. First, holes in the outer metal substrate allow cooling air to flow through the strain isolator pad which, in turn, must pass through the ceramic coating for effective combustion chamber cooling. A slot appears to be the best choice for this. Secondly, differences between the thermal expansion coefficients of the ceramic coating and the metal substrate require relative motion between the two materials. The slot allows relative movement between the ceramic and metal substrate. This minimizes failures of the ceramic coating during radial growth of the combustor, when a hoop stress is created. The techniques investigated for forming the slots include masking with a room



Table III.  
Preliminary design study—concept 2 combustor design parameters.

	Concept 2 baseline
Wa (liner flow, lb/s)	6.384
P3 (inlet pressure, psi)	213.0
T3 (inlet temp., °F)	791
Wf (fuel flow, lb/hr)	631.0
F/A (fuel/air ratio)	0.02746
Wcorr (corr. flow, lb/s)	0.684
Temperature rise (°F)	1607.0
Burner outlet temp. (°F)	2398.0
Liner pressure drop (%)	3.6
Vr (ref. velocity, ft/s)	27.44
Residence time (msec)	12.15
Ref. area (sq in.)	72.91
Length (in.)	4.0
Liner height (in.)	2.0
L/h (ratio length/height)	2
Theta parameter	0.0346
HRR (heat loading, Btu/hr/atm/ft**3)	4.82E6
Volume (cu ft)	0.1688

temperature vulcanizing rubber (RTV), cutting the slots directly into the ceramic, or mechanical attachment of isolated segments. The study of construction techniques included work at Allison and Technetics Corporation.

The study was aimed toward determining the optimum way to manufacture a combustor composed of discrete ceramic segments. One method would be simply attach segments of strain isolator pad to the metal combustor liner, mask the gaps, and then coat the strain isolator with ceramic. The mask material could then be removed, leaving gaps for the cooling air to flow.

Another discrete segment approach, which involves mechanically attaching preceramic-coated isolator segments onto the metal combustor liner, was also considered. Rivets are inserted through the isolator pad and the ceramic coating is applied. The ceramic tile structure is now attached to the metal combustor liner via the rivet fasteners. This technique is attractive in that a damaged segment could be replaced by a new one, during full scale rig testing. However, the contact resistance between the metal substrate and isolator pad may affect the heat transfer characteristics of the CMC structure, as well as the distribution of coolant flow. In addition, high strain rates may develop locally about the rivet which could affect the ceramic coating.

Finally, the possibility of cutting through the ceramic and isolator pad was examined. Slots cut into samples of the CMC structure by different techniques were explored.

Experimental work at Allison and mechanical difficulties with the other two techniques lead to the decision to pursue the RTV rubber masking technique as the choice for forming the cooling air exit slots.

## V. TASK 3—FINAL COMBUSTOR DESIGN

Following selection of the final cycle (design) conditions (Table I), Task 3 effort focused on completing the final design of the CMC combustor. The result of this effort was the generation of detailed blueprint drawings used for fabrication of the combustor. Final design work was comprised of aerothermal design analysis concurrent with the detailed mechanical design. This effort included the following:

- selection of gross flowpath features of the combustion system derived from an existing design
- simple 1-D and empirical analysis based on gross features of the flowpath
- design analysis of CMC wall cooling distribution using micro design codes (CMFLO3 and 2-D finite difference heat transfer EJ8D)
- overall combustor airflow distribution and orifice sizing for desired stoichiometry and pressure loss (ANNLOSS)
- macro 1-D heat transfer analysis and verification of micro-macro model correspondence (WALLTEMP)
- 3-D aerothermal design optimization and hybrid performance predictions (COM3D and WALL3D)
- completion of mechanical design and generation of detailed drawings

### 5.1 EMPIRICAL DESIGN

The CMC combustor was a derivative configuration patterned after an existing Allison design. The combustor selected for the program was a compact annular reverse-flow design incorporating a single row of primary holes and a single row of dilution holes on both the inner and outer liners. The CMC concept was used in construction of the inner and outer liner walls as well as the outer transition liner (OTL). The dome was effusion-cooled and contained 12 piloted airblast fuel nozzles each surrounded by an axial swirler.

Based on the past successful testing experience of the existing Allison combustor, a number of the CMC combustor features were empirically based on the existing design. These basic design constraints included retention of the axial location, circumferential spacing, and total number of primary and dilution holes. The fuel nozzle was also similar, a piloted airblast design surrounded by a 60 deg vane angle axial swirler. However, to provide the proper primary zone stoichiometry for the growth, 3000°F BOT cycle conditions, the effective area of the axial swirlers was increased. Other derived design features included an outer-to-inner primary jet mass flow rate ratio of 1, outer-to-inner dilution jet mass flow rate ratio of 2.5 (for outlet temperature profile trimming), and a slightly higher primary zone equivalence ratio of 1. An overall combustor effective area was maintained to obtain the required 5% combustion system pressure drop. The ignitor type and location were also borrowed from the existing design, and since the CMC combustor would be tested in the existing single burner rig facility, all test facility-to-combustor mechanical engagement features were determined. However, due to the required thickness of the CMC wall structure and the requirement to accommodate the wall in the existing flow path, the total combustor volume was slightly decreased from the baseline.

A summary of the empirically determined design features and combustor cross section are given in Figure 18. Table IV provides details of the fundamental design parameters based on the simple 1-D and empirical design analysis.

With many of the basic geometric dimensions and features of the CMC combustor set, it remained to design the details of the CMC wall structure, optimize the cooling circuit airflow distribution, determine the overall airflow distribution, and perform the detailed 3-D aerothermal design verification.

Table IV.  
Fundamental parameters for final design.

Design point parameters	
Wa (liner flow, lb/s)	7.940
P3 (inlet pressure, psi)	271
T3 (inlet temperature, °F)	895
Wf (fuel flow, lb/hr)	1008
F/A (fuel/air ratio)	0.0353
Wcorr (corrected flow, lb/s)	0.696
Temperature rise (°F)	2105
Burner outlet temperature (°F)	3000
Liner pressure drop (%)	5.0
Vref (reference velocity, ft/s)	30.93
Tau (residence time, msec)	10.78
Aref (liner reference area, sq in.)	68.5
L/H (liner aspect ratio)	2.13
Theta (aerodynamic loading parameter, lb/sec-cu ft)	0.0248
HRR (heat release rate, Btu/hr-cu ft-atm)	6.45E6
Vol (combustor volume, cu ft)	0.159
Combustor geometric parameters	
Liner O.D. (in.)	13.48
Liner I.D. (in.)	9.71
Liner length (in.)	3.96
Liner height (at prim holes, in.)	1.88
Liner x-sect area (at prim holes, in. <sup>2</sup> )	68.5
Liner surface area (in. <sup>2</sup> )	558
Liner volume (in. <sup>3</sup> )	443
Transition surface area (in. <sup>2</sup> )	168
Transition volume (in. <sup>3</sup> )	155
Transition equivalent length (in.)	2.12
Casing O.D. (in.)	15
Casing I.D. (in.)	8.64
Annulus area, outer (in. <sup>2</sup> )	31.66
Annulus area, inner (in. <sup>2</sup> )	13.6
Fuel nozzle parameters	
Injector type	Piloted air blast
Number of nozzles	12
Nozzle spacing, S/H	1.52
Primary flow number, FN, lb/hr(psi) <sup>0.5</sup>	0.45
Nozzle "cracking" pressure, psid	156
Secondary flow number, FN, lb/hr(psi) <sup>0.5</sup>	2.5
Nozzle cone angle, deg	60, max power
Nozzle hydraulic diameter, in.	0.25
Nozzle filmer diameter, in.	0.145
Air entry configuration	
Axial swirler, swirl angle (deg)	60
Axial swirler, geometric area (sq in.)	0.0851/swirler
Axial swirler, effective area (sq in.)	0.0511/swirler
Fuel nozzle air, geometric area (sq in.)	0.0707/nozzle
Fuel nozzle air, effective area (sq in.)	0.0424/nozzle

Table IV (cont).

	Number of holes		Location/configuration
	Inner	Outer	
Primary orifices	24	24	Eq spaced, in-line with nozzle, opposed jets
Dilution orifices	36	36	Eq spaced, in-line with nozzle, opposed jets
Dome, number of effusion holes			2592
Dome, diameter of effusion holes			0.015
Dome, effective area, $C_d \approx 1$ (sq in.)			0.458
Outer liner seal, geometric area (sq in.)			0.129
Outer liner seal, effective area (sq in.)			0.093
Inner liner seal, geometric area (sq in.)			0.129
Inner liner seal, effective area (sq in.)			0.110

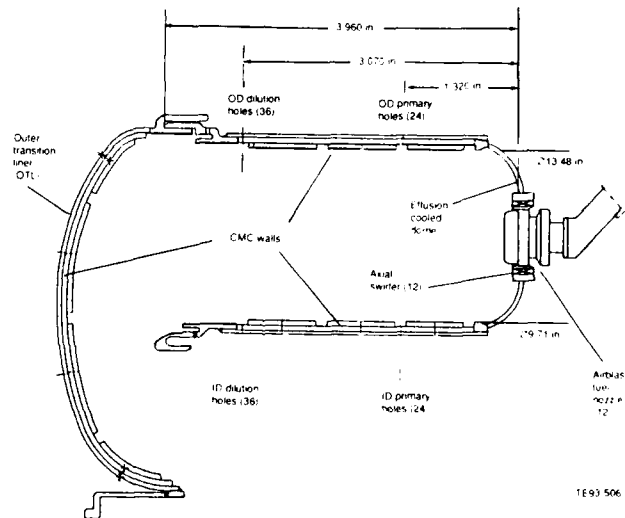


Figure 18. Basic design features.

## 5.2 MICRO DESIGN OF THE CMC WALL AND DETERMINATION OF THE OVERALL COOLANT DISTRIBUTION

The coolant orifice diameter and spacing, ceramic "tile" side length, exit slot width, and ceramic thickness (refer to Figure 2) were the critical CMC wall design parameters requiring optimization for the combustor application. A tile consists of a single square element of ceramic fed by cooling air through a single orifice through the substrate. The air enters the porous pad through the orifice and

flows around the backside of the ceramic and exits through slots between the tiles. The cooling circuit design was based on a 1750°F design limit for the critical ceramic-Brunsbond interface.

Sizing and placement of the ceramic tile pattern assumed a single continuous layer of Brunsbond porous pad would be bonded to the substrate. Dimensions of the ceramic tiles were dictated by the desire to minimize the total number of tiles and place primary and dilution combustion air orifices, which penetrate all layers of the CMC wall, centered on the hot-side coolant air exit slots. This design ensures a desirable, uniform airflow distribution and minimizes mechanical/structural disturbances to the ceramic tiles. Another consideration was staggering the coolant exit slots by offsetting the pattern of ceramic tiles and the desire to use nominally square ceramic segments with the coolant air fed by a single orifice through the substrate, again to ensure uniform coolant flow. Following determination of these basic design constraints and choosing an exit slot gap of 0.125 in., it remained only to fit the number of ceramic tiles to the circumferential and axial dimensions of the inner and outer liners.

Two identical size rows of tiles between the primary and dilution holes were chosen to minimize the total number of required ceramic tiles yet achieve desirable wall temperature distribution. For the outer transition liner, major considerations beyond appropriate wall temperatures included minimizing the number of tiles and obtaining a good fit of tiles to the complex half toroidal geometry. To obtain this fit, the tiles have been designed in a slightly pie-shaped geometry. Again, a single cooling orifice feeds air to each ceramic segment.

Once a geometric design was reached, work centered on calculating an appropriate airflow distribution through the liner orifices. As the critical design limit is a 1750°F porous pad/ceramic layer interface temperature, it was decided to scale cooling hole diameters (or airflow) for the first iteration. Heat transfer analyses (details of the method were given in Section III. B, 2-D finite difference model for an isolated segment of the wall, EJ8D) were used to verify the appropriateness of the selected nominal ceramic tile side lengths and optimize the cooling orifice sizing and final airflow distribution for the cooling circuit. Figure 19 is a plot of results from EJ8D for segment side length versus wall temperature for a 0.188 in. hole diameter. This was used to scale hole diameters for segments with a given side length to achieve the selected porous pad/ceramic interface temperature. As shown in Figure 19, the design goal was selected as a 1625°F pad/ceramic interface temperature. This value was selected to gain some margin over the 1750°F limit yet minimize cooling airflow as much as possible.

Using the Figure 19 curves for a 0.188 in. diameter hole, the required hole diameter was calculated having chosen the combustor tile segment side lengths. This first estimate of hole diameter allows calculation of the flow through a single material segment. Mass flow rate calculations were carried out using the isolated segment flow program (CMFLO3) described earlier in Section III, which is based on Green's equation for flow through compact porous media. The mass rate is then summed for all tiles in the circumferential direction at given axial locations and gives the total cooling flow rates. The summary of cooling airflow distribution and geometric parameters for the final design are given in Figure 20.

Validation of the CMC cooling circuit design was carried out by use of heat transfer analysis models for an isolated wall segment (micro model) and 1-D and pseudo 3-D models for the whole combustor (macro models) using a design limit for the critical Brunsbond/ceramic interface of 1750°F.

Results of 2-D finite difference heat transfer analyses (EJ8D) are given in Figures 21 through 29. Referring to Figures 2 and 13 helps clarify that the EJ8D results provide CMC wall temperatures at the critical surface and interface locations in the wall as a function of edgewise (i.e., radial) location for an isolated segment of the wall. Hence zero location is the center of the coolant orifice and the last radial station is the edge of the coolant exit slot in the ceramic.

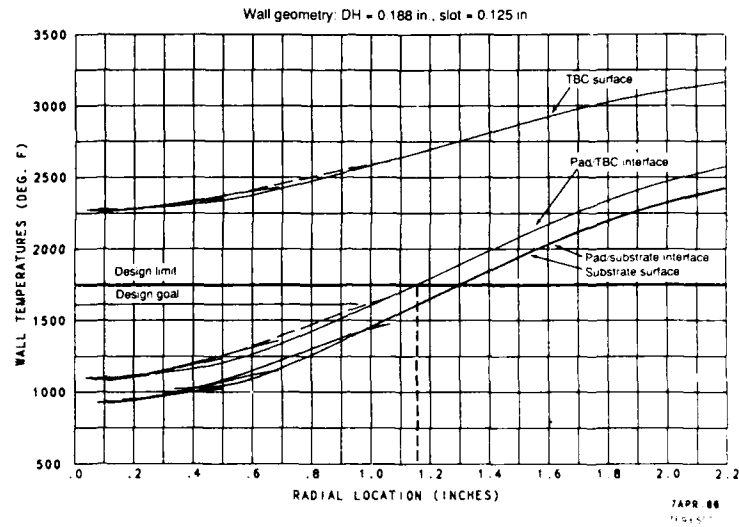


Figure 19. CMC material temperature versus radius from 2-D finite difference heat transfer analysis.

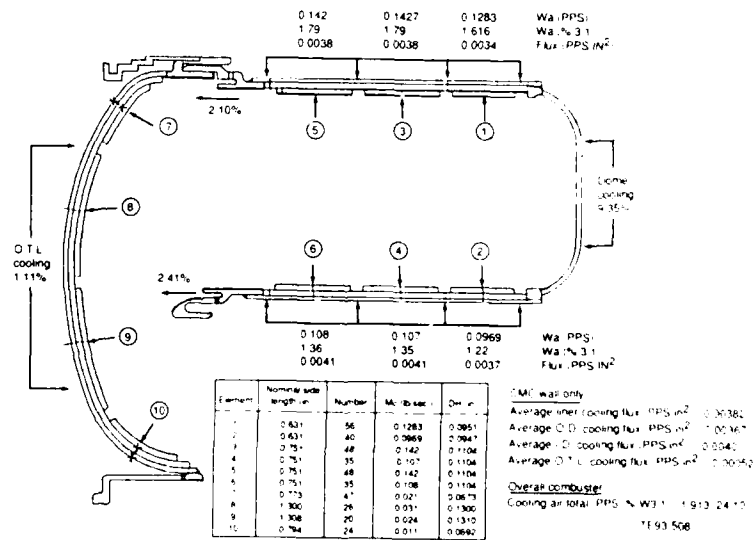


Figure 20. CMC combustor cooling circuit design and cooling airflow distribution.

Wall geometry DH = 1104 in., slot = 0.131 in., Wa = 0.0028 lb/sec

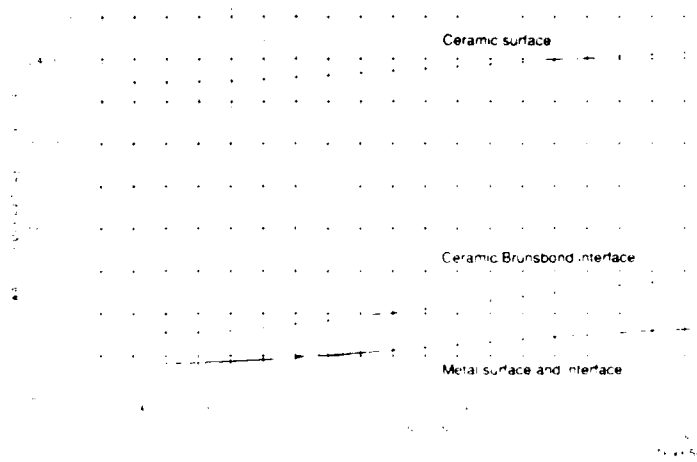


Figure 21. Micro heat transfer model predictions for a single segment - tile #5, outer liner

Wall geometry DH = 1000 in., slot = 0.123 in., Wa = 0.0025 lb/sec

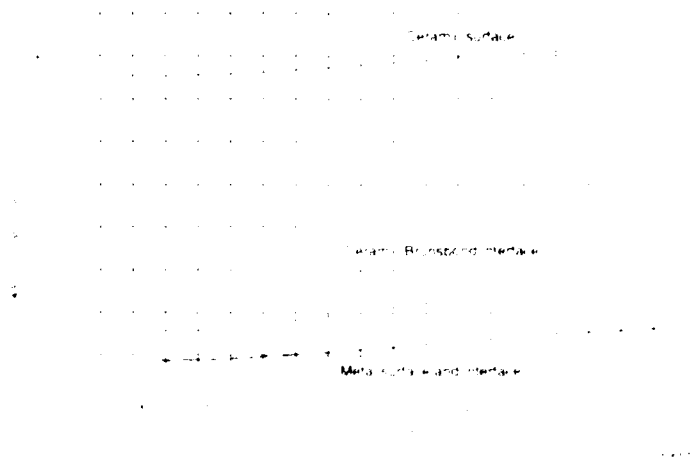


Figure 22. Micro heat transfer model predictions for a single segment - tile #1, outer liner

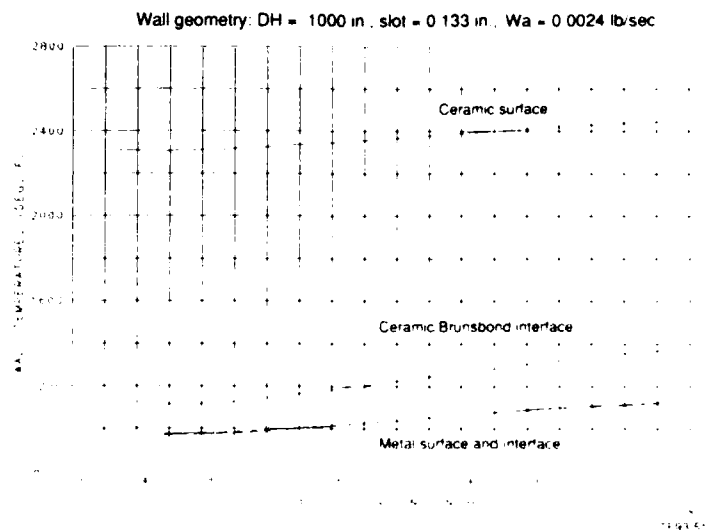


Figure 23. Micro heat transfer model predictions for a single segment—tile #2 inner liner

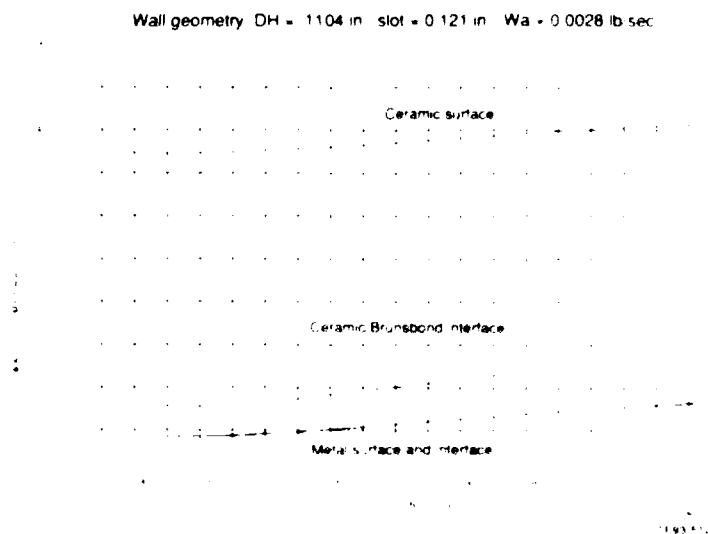


Figure 24. Micro heat transfer model predictions for a single segment—tile #6 inner liner



Wall geometry DH = 0.673 in. side = 0.773 in. Wa = 0.0013 lb/sec

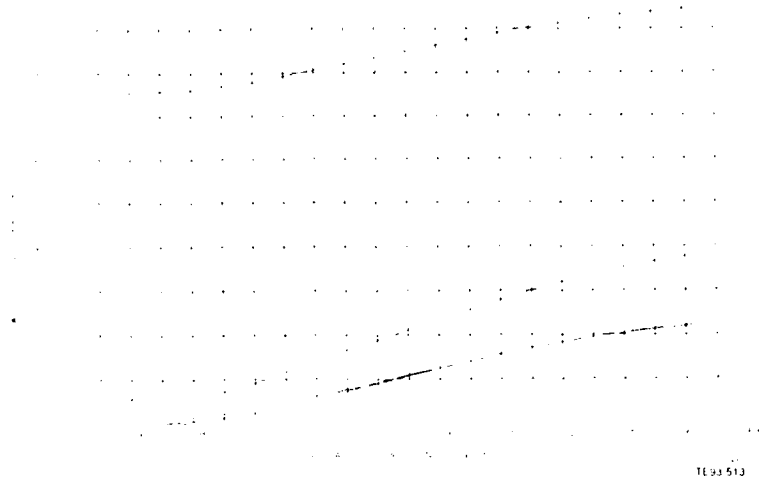


Figure 25. Micro heat transfer model predictions for a single segment—row #7 at transition inlet.

Wall geometry DH = 1.269 in. side = 1.300 in. Wa = 0.0034 lb/sec

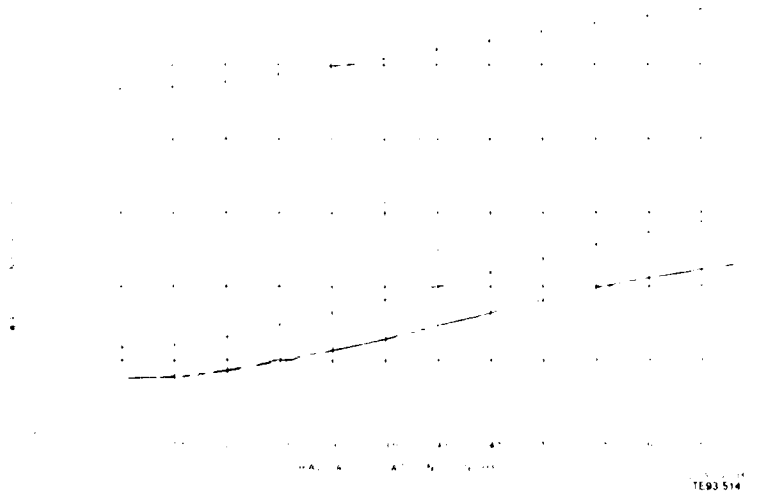


Figure 26. Micro heat transfer model predictions for a single segment—row #8 at transition upper center.

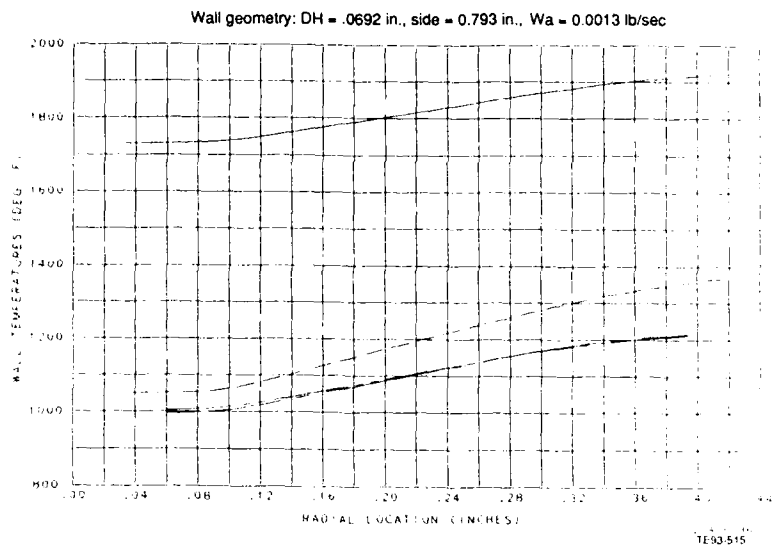


Figure 27. Micro heat transfer model predictions for a single segment—row #10 at transition outlet.

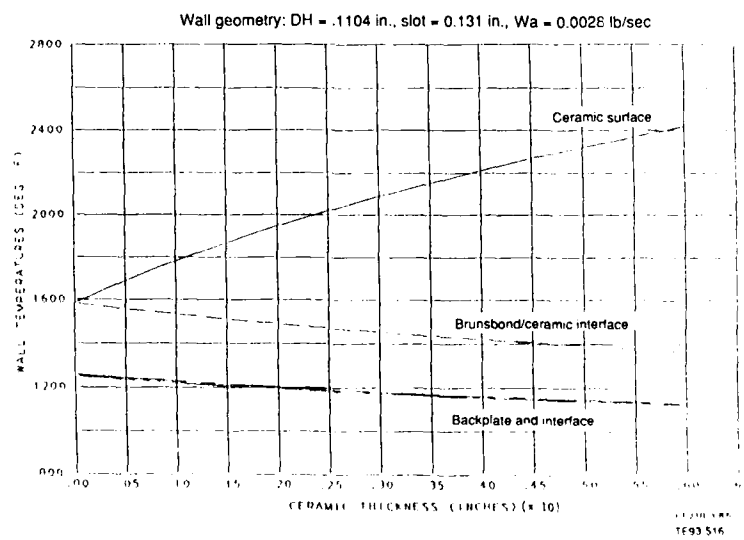


Figure 28. CMC segment temperature versus ceramic thickness—tile #3: outer liner.

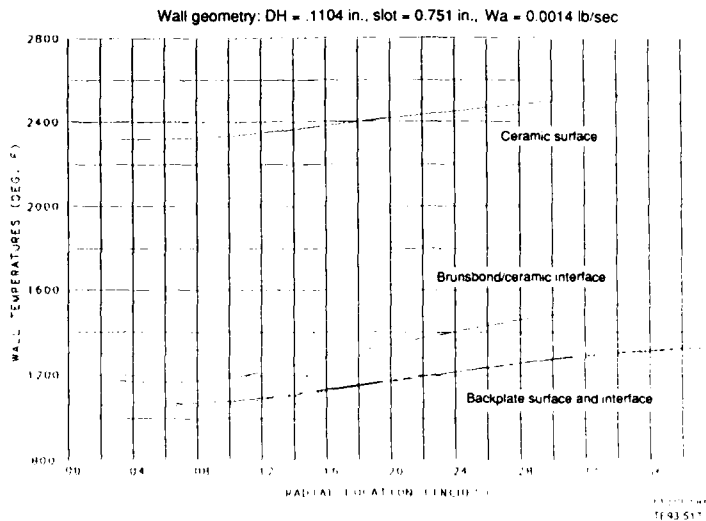


Figure 29. CMC liner tile #3 temperature versus radius—restricted flow scenario: 50% blockage.

Figures 21 and 22 are for wall segments on the outer liner of the combustor. The reader is referred to Figure 20 where identification of tiles or wall segments are provided. For example, tile No. 5 wall temperature predictions are given in Figure 21. Figure 20 shows tile No. 5 is located on the combustor outer wall, at the aft end of the liner or near the transition section inlet. Figures 23 and 24 are for inner wall tiles. It should be noted that stoichiometric gas temperatures were assumed to drive the convective and radiative heat loads to the wall. This was a conservative assumption and should yield maximum wall temperatures. Figures 22 and 23 are for tile Nos. 1 and 2, which correspond to axial locations in the combustor from 0.0 in. (dome face) to 1.32 in. Figures 21 and 24 are for tile Nos. 5 and 6, which correspond to axial locations in the combustor ranging from 2.20 to 3.07 in. (center of dilution orifices). Since tiles 3, 4, 5, and 6 are geometrically equivalent and stoichiometric streak gas temperatures were assumed, wall temperature predictions are also similar, and results for tiles 3 and 4 are omitted.

Examination of Figures 21 to 24 leads to several conclusions. First, the micro model predictions for a single compliant matrix wall segment for both inner and outer liner reveals that at the critical ceramic/Brunsbond interface peak temperatures uniformly reach about 1400°F, well below the 1750°F limit. The radial gradient at the interface for all tiles is about 200°F and demonstrates the dependence of temperature on the segment side length. These plots also show a thermal gradient across the ceramic coating of 1000°F and essentially no gradient across the metal substrate, indicating the excellent insulating qualities of the ceramic and Brunsbond layers.

The previous discussion centered on heat transfer analysis of the combustion system inner and outer liner. The outer transition liner was also analyzed during the design effort and the results using the 2-D finite difference micro code are given in Figures 25 to 27. Figure 25 is for a typical segment in the row of tiles at the transition inlet. Figure 26 is for the row of tiles at the upper center of the transition and adjacent to the row of tiles given in Figure 25. The row of tiles at the transition outlet is given in Figure 27. Examination of the plots show interface temperatures ranging from 1050°F at the segment inlet to about 1375°F at the edge of the segment, again with good margin under the 1750°F limit. The ceramic surface temperature ranges from 1750°F to 1950°F and reflects the cooler gas temperatures in the OTL. Also, essentially zero gradient is observed across the metal substrate wall.

Two additional heat transfer analyses were carried out for the combustor liner. Tile No. 3, centered near the primary zone on the outer liner, was used for both analyses as representative of a thermally critical location in the combustor. Stoichiometric streak conditions were the conservative assumptions for both studies. Figure 28 illustrates the results for investigating the fate of the exposed portions of the Brunsbond located just below the cooling air exit slots on the hot-side of the combustor. The question had arisen whether this exposed, air-cooled Brunsbond could survive exposure to the severe primary zone environment. Note that Figure 28 provides wall temperatures for the various locations in the CMC system as a function of ceramic thickness. As the ceramic thermal barrier coating thins out, its surface temperature diminishes and the Brunsbond pad and metal backing plate temperature increase. When the ceramic decreases to zero thickness, the critical interface has reached 1590°F, still below the limit. Figure 29 was generated to investigate a scenario where 50% flow blockage (beyond the 50% blockage already assumed in sizing the cooling air orifices) was incurred in the Brunsbond pad by some unexpected means. The results of this analysis also show interface temperatures approaching 1600°F but not exceeding the limit. These studies again tend to support and lend confidence to the combustor cooling circuit design.

In summary, the micro heat transfer analysis verified the acceptability of the cooling flow distribution, as selected, and shown in Figure 20. The results presented show the maximum interface temperature, assuming stoichiometric streak conditions, is approximately 400°F below the 1750°F design limit.

Hence it was felt enough margin was available to proceed with combustor front-end and secondary zone design using the selected cooling circuit geometry and airflow distribution along with the selected primary zone stoichiometry. The balance of aerothermal design effort during Task III then centered on sizing primary and dilution orifices to optimize the combustor's overall airflow distribution. Having determined the overall combustor design, it was then possible to run the 1-D and 3-D aerothermal and heat transfer analysis codes and verify the micro-macro design correspondence.

### 5.3 DETERMINATION OF OVERALL COMBUSTOR AEROTHERMAL DESIGN

The front-end design and overall flow split calculation was carried out using two computer programs, one FLSPLT2 for the front-end and ANNLOSS (see Appendix B) for the overall airflow distribution. An iterative design process was carried out as described in the following paragraph.

Known values required as input were first calculated. Fuel flow necessary to achieve a 3000°F burner outlet temperature (BOT) cycle was determined using a chemical equilibrium program. Also required was a larger area swirler to obtain more flow in the front-end. The baseline 0.064 in.<sup>2</sup> swirler was replaced with a 0.0851 in.<sup>2</sup> design. The primary zone equivalence ratio was set at unity and, knowing the fuel flow, an estimate of primary zone airflow was calculated. A discharge coefficient for the dome effusion holes was based on empirical data and used for input to the ANNLOSS flow model. Other calculations included modifying ANNLOSS input data for the geometry of the CMC combustor and its unique cooling scheme. Following this, the input data set for FLSPLT2 was generated and the first run carried out to determine the required primary orifice diameters. These values were used as input to ANNLOSS to get the overall flow distribution. From this point an iterative process was required to obtain agreement between the two models for primary zone stoichiometry and cooling flows. Dilution zone orifices were sized, again through iteration, with the ANNLOSS model to set the overall system pressure drop at 5% and to obtain an outer liner dilution air to inner liner dilution airflow rate of 2.5 for proper outlet temperature profiling. The final overall airflow distribution for the CMC combustor is given in Figure 30.

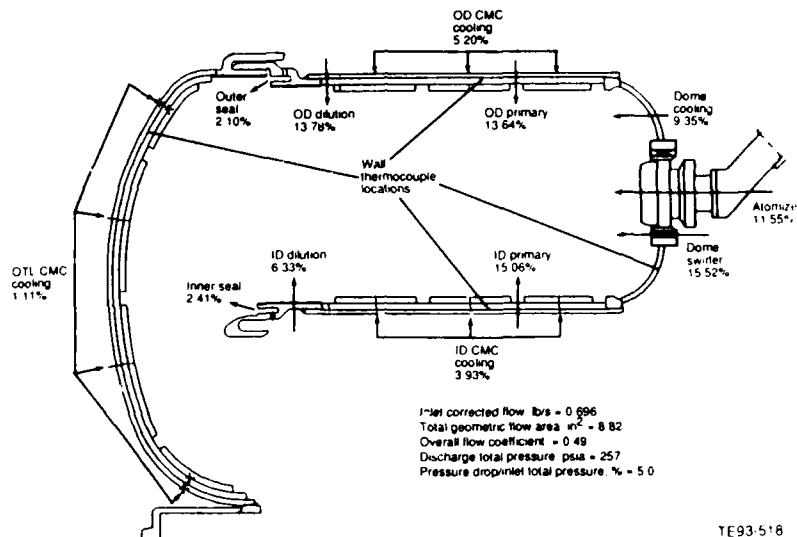


Figure 30. CMC combustor predicted airflow distribution at design point, before rework.

#### 5.4 MICRO-MACRO HEAT TRANSFER CORRESPONDENCES

Having established the overall combustor aerothermal design, it was now possible to run the 1-D macro heat transfer analysis (WALLTEMP, described in Appendix B). Input to WALLTEMP includes basic geometric constraints as well as airflow distribution and gas temperature distribution as a function of axial location in the combustor. In addition to geometry and gas properties, inputs such as wall emissivity and thermal conductivities are also required. The purpose of this analysis was to verify the micro-macro heat transfer model correspondence.

It should be recalled that the micro 2-D finite difference model, described previously, predicts the various wall temperatures as a function of isolated segment edgewise distance, while the micro 1-D model provides the various wall temperatures as a function of axial location in the combustor. Therefore direct comparison of the abscissae is not possible. To compare the results, a peak value from the micro model prediction is plotted on the curves for the entire combustor at their corresponding axial locations.

Initially, an investigation of the degree of axial temperature gradient was carried out by determining a F/A-ratio distribution and then calculating the corresponding adiabatic flame temperatures using a chemical equilibrium code. Referring to the results given in Figures 31 for the outer wall and 32 for the inner wall, it should be noted that the first axial location, at the point where the curves begin, is located just beyond the dome and in the primary zone. The final axial location is beyond the dilution holes but prior to the transition section inlet start. The ceramic surface temperature reaches a peak in the primary zone at about 2370°F and decreases to 1800°F as dilution air is injected into the system. The critical ceramic/porous pad interface temperature peaks and remains at 1400°F until the dilution air cools the pad interface to about 1200°F. Finally, both the inner and outer metal substrates reach temperatures of around 1075°F trailing off to less than 1000°F. No temperature gradient is observed across the thickness of the metal shell. Similar results are predicted for both inner and outer liner, and indicate relatively uniform axial temperature gradients.

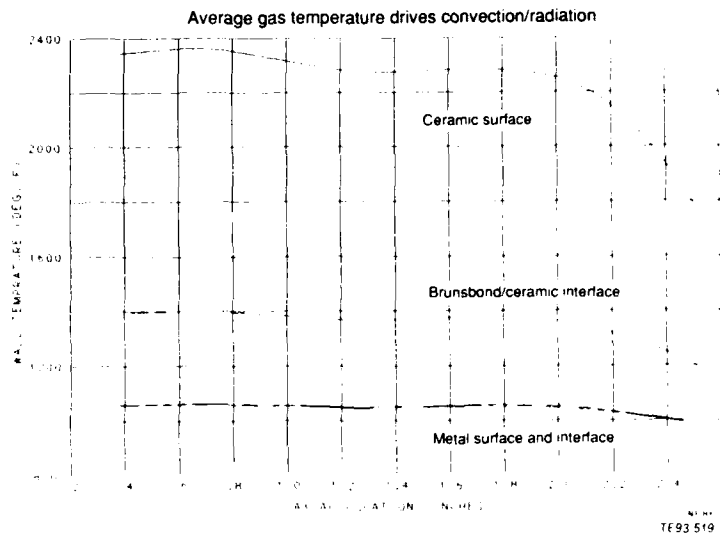


Figure 31. Macro heat transfer model predictions for wall temperatures—outer liner.

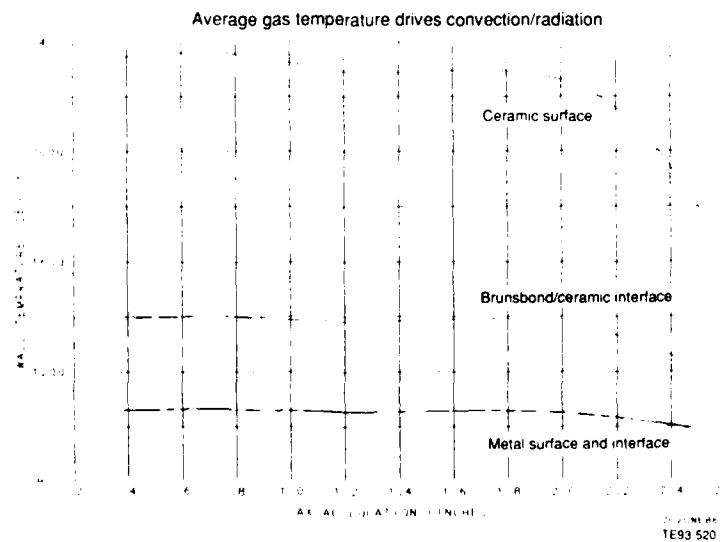


Figure 32. Macro heat transfer model predictions for wall temperatures—inner liner.

To indicate the level of micro-macro model correspondence, it was necessary to rerun the macro 1-D heat transfer code assuming stoichiometric gas temperatures. This allows direct comparison of the models. Peak wall temperature values from Figures 21 and 22 are overlayed on Figure 33 for the outer wall. Likewise, peak wall temperatures from Figures 23 and 24 are plotted on Figure 34 for the inner wall.

The absence of significant variation in axial temperature gradient for the full combustor is due to some extent from the assumption of stoichiometric temperatures through the length of the combustor. However, as Figures 33 and 34 reveal, good agreement is observed between the two independently developed models for predicted wall temperatures in the CMC wall structure. This level of agreement lends confidence to the design method and selected final design of the combustor. Based on these results, final verification of the CMC combustor design was carried out using the 3-D aerothermal analysis codes, COM3D and WALL3D.

##### 5.5 FINAL VERIFICATION: 3-D AEROTHERMAL AND HEAT TRANSFER ANALYSIS

Final verification was carried out with the 3-D combustor performance analysis model, COM3D. Output from this program includes velocity vectors, contours of gas temperature, fuel-air ratio, mass fraction unburned fuel as well as average gas temperatures and  $f/a$  ratios over user defined combustor subvolumes. These provide input to the pseudo 3-D heat transfer code, WALL3D, which gives wall temperature predictions as a function of axial and circumferential location. A description of COM3D and WALL3D is provided in Appendix B.

The pseudo 3-D heat transfer code is similar to a 1-D analysis (i.e., WALLTEMP) for an energy balance on a point of the wall with the exception that the heat transfer calculation procedure incorporates the variation in combustor operating conditions in the three dimensions provided by the subvolume analysis. In addition, the radiative flux components are calculated through a view factor which considers effects from the rest of the combustor volume in all three directions.

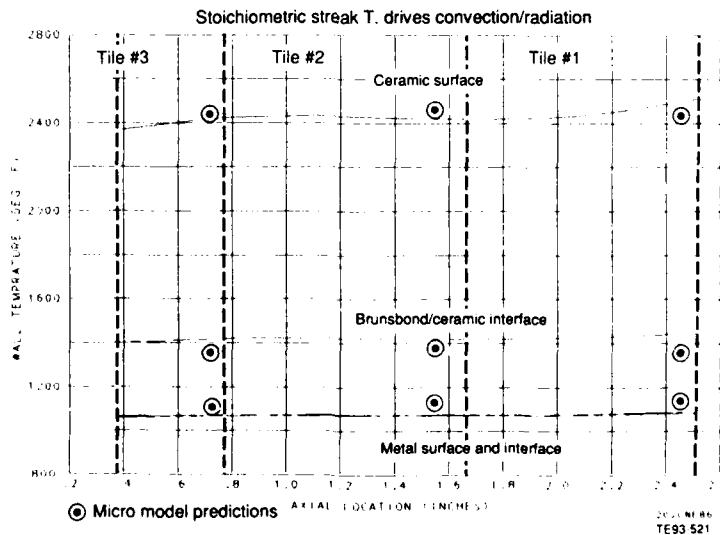


Figure 33. Macro-micro heat transfer model predictions—outer liner.

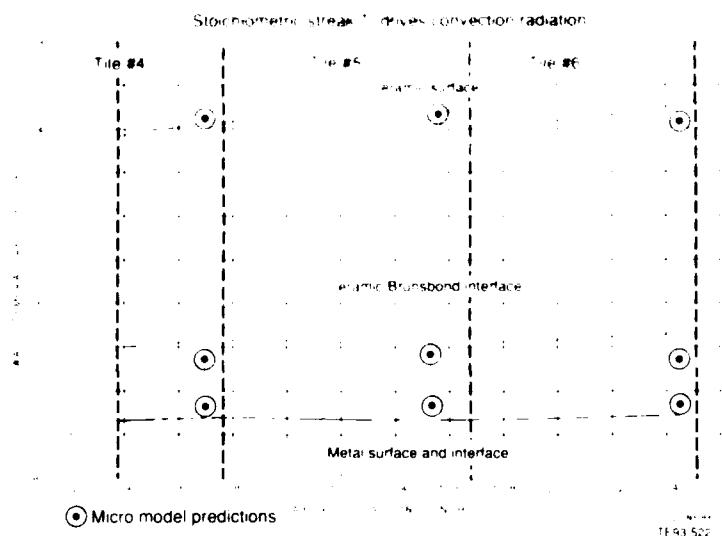


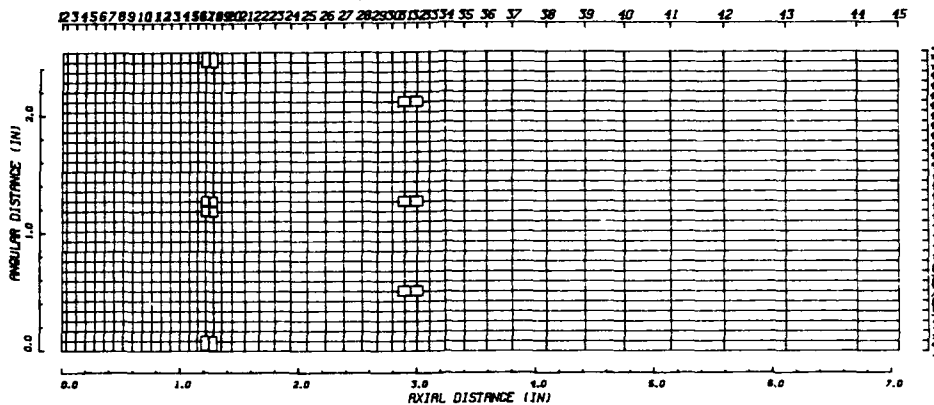
Figure 34. Macro-micro heat transfer model for wall temperatures—inner liner.

The combustor is modeled by a single fuel nozzle or 30 deg sector. Figures 35 and 36 are plots of the inner and outer wall x-y grid, along with the air injection node arrangement. Figure 37 gives the grid in the y-z plane. To represent the fuel nozzle-swirler boundary condition of the dome, a three swirler arrangement was used. The first swirler was placed as an air source near the center of the fuel nozzle to better represent the nozzle inner fuel-sheet sweep air. The second swirler input represents a combination of outer sweep air, nozzle tip sweep air, and axial injection (to prevent carbon build-up) with a calculated (based on equivalent momentum) swirl angle of 14 deg. The third swirler lies concentrically outside the first two swirlers and represents the 60 deg main axial swirler. Other boundary conditions included the specification of operating conditions and airflow distribution as well as the two- or four-step reaction mechanism for the kinetics model. Control parameters, convergence criteria, parameters for the turbulence submodel, and input for subvolume, hybrid empirical performance, and 3-D heat transfer model make up the balance of the required input dataset.

Results from the 3-D aerothermal analysis of the final design are shown in Figures 38 through 48. Figures 38, 39, and 40 are velocity vector plots in the i-j plane at K=16, which is through the fuel nozzle centerline, the j-k plane at i=17 through the plane of the primary jets, and the j-k plane at i=31 through the plane of the dilution jets, respectively. A well balanced recirculation zone and well behaved, radially oriented primary jets impinging near the center of the combustor are observed. The effects of this flowfield on temperature contours are shown in Figures 41 to 45. These plots show temperature fields corresponding to the vector plots of Figures 38 to 40 with the addition of contours in the j-k plane at i=2 through the dome face and in the j-k plane at i=24 in the primary combustion zone.

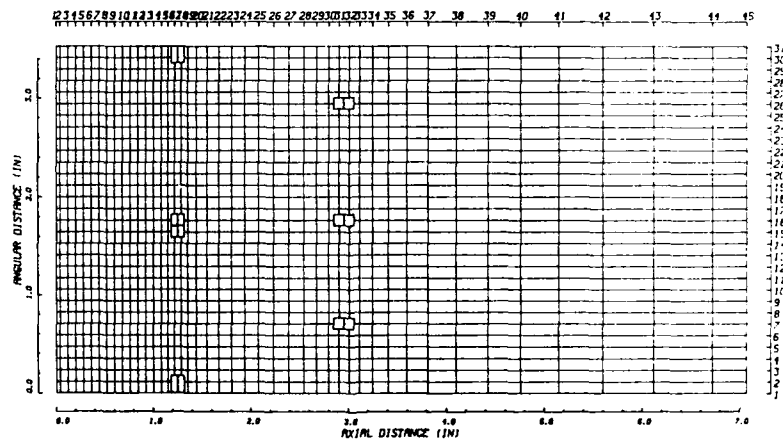
In general, the temperature contours reveal a well behaved primary zone with the hottest gases contained in the interior between the dome and primary jets, where the recirculation zone is well defined. The temperature fields also indicate good uniformity of the gas temperatures downstream of the dilution jets where rapid quenching of the hot primary zone gases occurs due to the evidence of uniform mixing. Figures 46 and 47 are fuel-air ratio contours corresponding to the i-j plane at K=16, fuel nozzle centerline and the j-k plane at i=17 through the plane of the primary air jets. Finally, Figure 48 provides a contour of mass fraction unburned fuel in the fuel nozzle centerline plane at K=16.





TE93-523

Figure 35. Inner wall grid and orifice arrangement, i-k plane.



TE93-524

Figure 36. Outer wall grid and orifice arrangement, i-k plane.

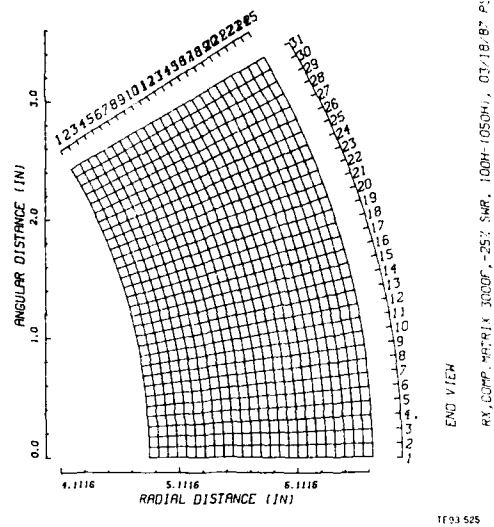


Figure 37. Dome grid in the j-k plane.

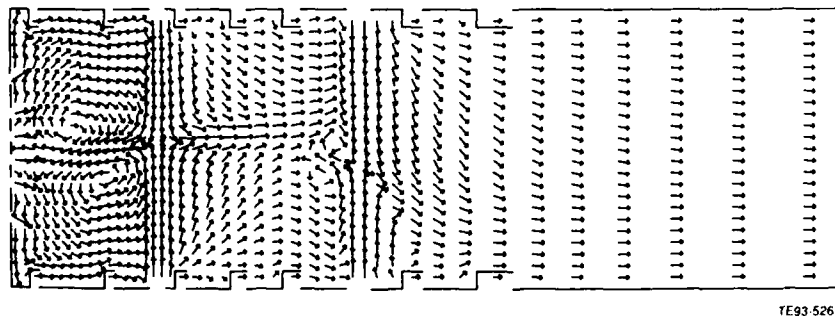


Figure 38. COM3D velocity vectors, i-j plane, k=16, fuel nozzle centerline.

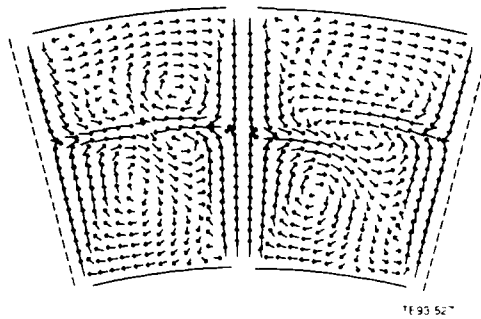


Figure 39. COM3D velocity vectors, j-k plane,  $i=17$ , primary jets.

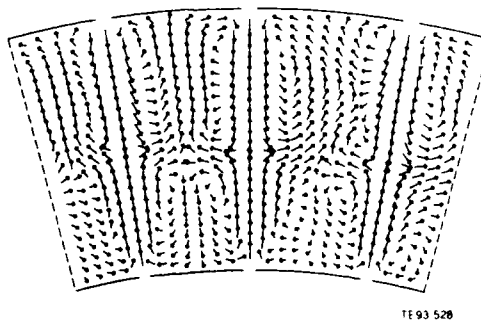


Figure 40. COM3D velocity vectors, j-k plane,  $i=31$ , dilution jets.

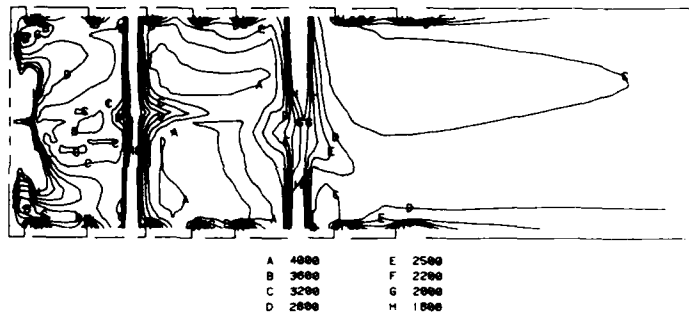


Figure 41. Temperature contours from COM3D, i-j plane, k=16, fuel nozzle centerline.

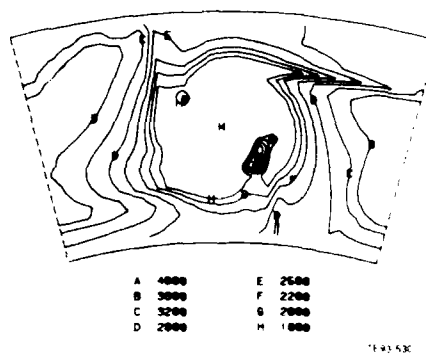
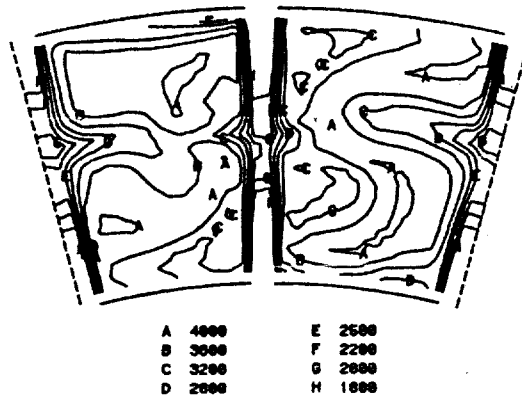
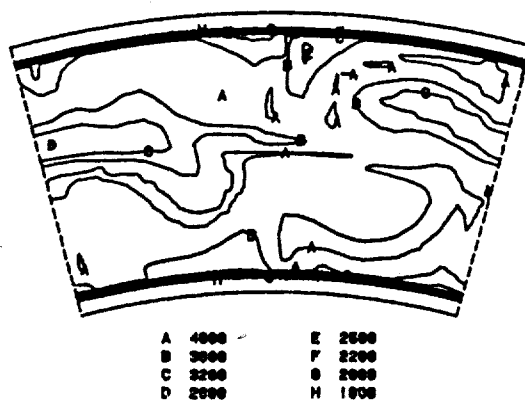


Figure 42. Temperature contours from COM3D, j-k plane, i=2, dome



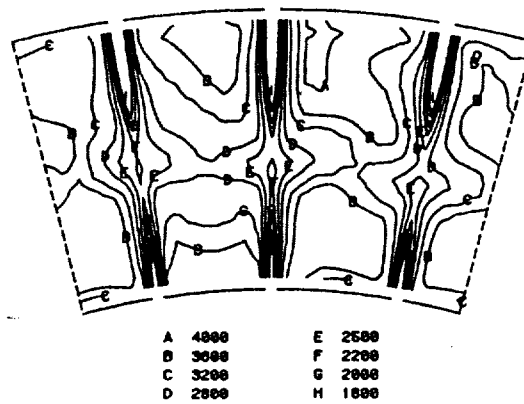
TE93-531

Figure 43. Temperature contours from COM3D, j-k plane i=17, primary jets.



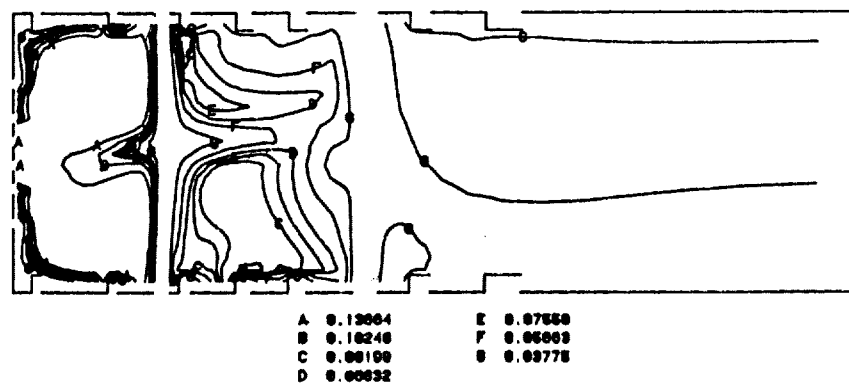
TE93-532

Figure 44. Temperature contours from COM3D, j-k plane, l=24, primary zone.



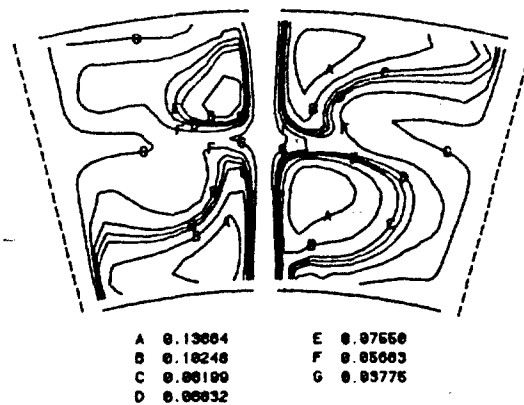
TE93-533

Figure 45. Temperature contours from COM3D, j-k plane, i=31, dilution zone.



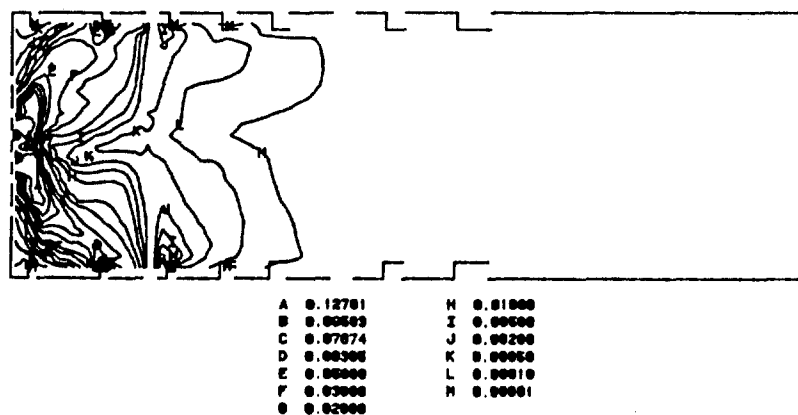
TE93-534

Figure 46. Fuel-air ratio contours from COM3D, i-j plane, k=16, fuel nozzle centerline.



TE93 535

Figure 47. Fuel-air ratio contours from COM3D, j-k plane i=17, primary jets.



TE93 536

Figure 48. Unburned fuel contours from COM3D, i-j plane, k=16, fuel nozzle centerline.

General conclusions from the 3-D modeling are that the combustor exhibits good aerothermal behavior with a well defined recirculation zone. Temperature patterns reveal most of the hottest gases are contained toward the center of the combustion volume with some fingers of hot gas being entrained toward primary and dilution jets. The mass fraction unburned fuel contour, Figure 48, shows excellent fuel burnout prior to the dilution jets.

The subvolume averaged data from the completed 3-D aerothermal analysis was subsequently used to run the pseudo 3-D heat transfer model (WALL3D) and provide input for the Allison empirical correlation analysis for combustor performance prediction.

Predicted 3-D wall temperatures are shown in the color contour plot of Figure 49 for both the inner and outer walls of the CMC combustor. The substrate surface temperatures range from 1100°F to around 1300°F. The results also reveal that the combustor meets the design 1750°F ceramic-Brunsbond interface temperature goal.

The predicted interface temperatures peak at just over 1550°F near the entrance to the outer transition liner. Most other axial locations on both the inner and outer walls range from 1430 to 1480°F and agree acceptably well with the past 2-D finite difference and 1-D macro heat transfer analyses, as discussed earlier.

The final analysis of the CMC combustor used the Allison empirical correlation code to predict performance based on the subvolume averaged data from the COM3D 3-D simulation. Table V gives these results.

Results show high combustion efficiency, good pattern factor, low UHC and CO, but high smoke and NO<sub>x</sub>. As smoke and NO<sub>x</sub> were low for testing of the similar Allison baseline combustor, it is suspected these predictions are related to the density of specified subvolumes in the COM3D input or to inaccuracy in the correlation constants for these parameters.

In summary, the design described in the previous pages has been rigorously analyzed with 1-D, 2-D, and pseudo 3-D heat transfer codes resulting in wall temperature predictions with good margin under the 1750°F design limit for the ceramic/Brunsbond interface. In addition all heat transfer codes have yielded similar predictions for analyses using different assumptions and methods for setting up physical boundary conditions. Further, aerothermal analysis using 3-D combustor modeling with the COM3D code reveals a satisfactory flowfield and gas temperature contours. Results of the 3-D analysis were used to predict performance parameters for the combustor and, with the exception of NO<sub>x</sub> and smoke emissions, the predicted performance was considered acceptable. With completion of the final aerothermal design, details of the mechanical design were selected and a detailed blueprint drawing prepared.

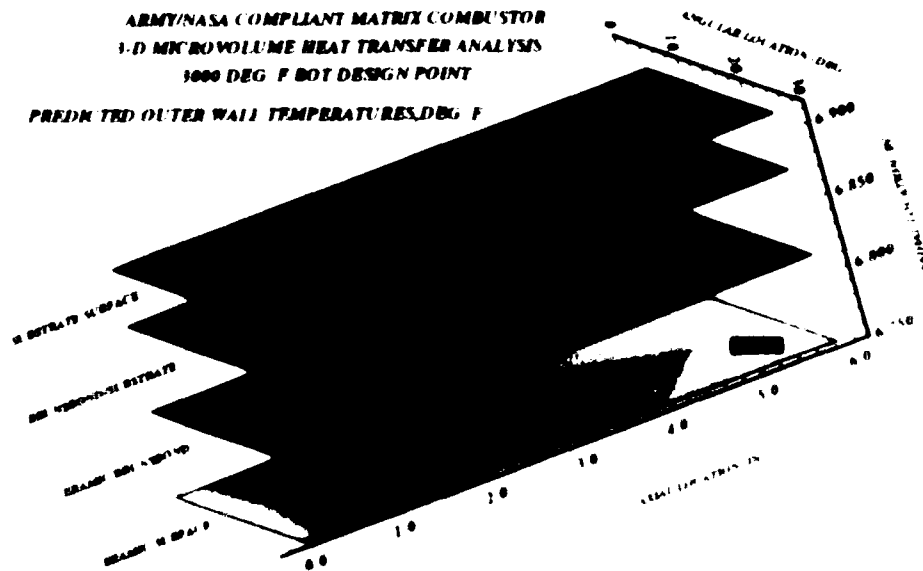
---

Table V.  
Summary of results from 3-D performance code prediction.

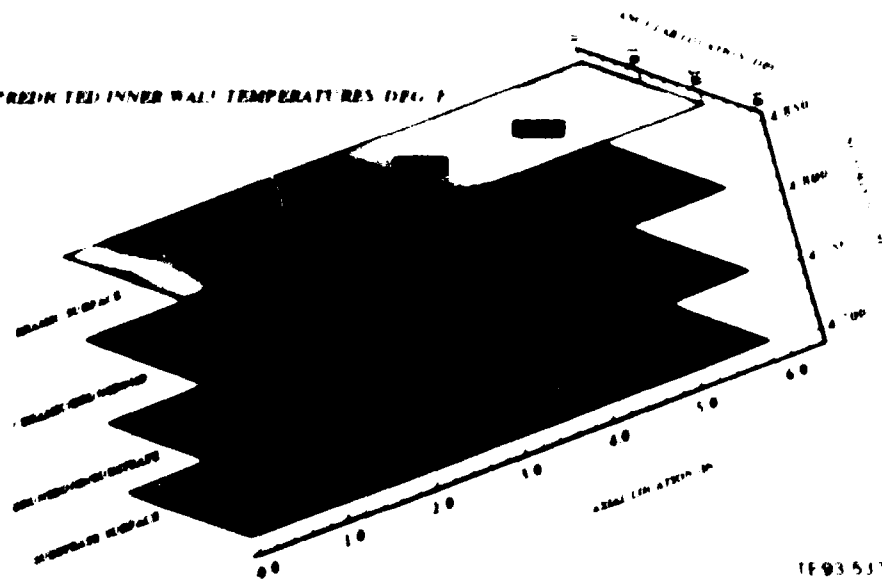
NO <sub>x</sub> (EI)	39
CO (EI)	0.41
UHC (EI)	0.16
Smoke No. (SAE)	26
Combustor efficiency, $\eta_c$ (%)	99.4
Pattern factor	0.176



ARMY/NASA COMPLIANT MATRIX COMBUSTOR  
 3-D MICROVOLUME HEAT TRANSFER ANALYSIS  
 3000 DEG F HOT DESIGN POINT  
 PREDICTED OUTER WALL TEMPERATURES, DEG F



PREDICTED INNER WALL TEMPERATURES, DEG F



TF93537

Figure 49 Army/NASA compliant matrix combustor 3-D microvolume heat transfer analysis 3000-1  
 HOT design point

## 5.6 FINAL MECHANICAL DESIGN AND DETAIL DRAWINGS

Detailed mechanical design of the CMC combustor resulted in the drawings provided in Figures 50 through 54 for the liner portion of the combustor which includes the inner and outer liner and dome (EX154047) and Figures 55 through 57 which describes the outer transition liner or OTL (EX155342)

A number of mechanical design challenges were encountered for the CMC combustor which included the following:

- design of mating joint between the effusion-cooled dome and the CMC wall inner and outer liners
- integration of the inner and outer liner with the OTL
- placement of discontinuities or seams in the compliant layer below the surface of the ceramic TBC
- requirement to split liner for ceramic spray access using the robotic plasma-flame method
- locating welded joints away from Brunsbond/substrate braze joints and ceramic surfaces to avoid weld embrittlement through braze wicking or cracking of the ceramic

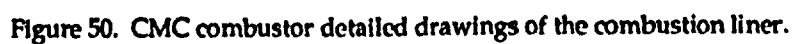
The basic geometry of the CMC combustor, including flow path features and mounting/support surfaces, is equivalent to an existing Allison design. Modifications were then required to adapt the design for the special requirements of the CMC wall structure.

Four approaches to designing the dome to barrel connection were studied and a method chosen. The methods investigated included an overlapping slip fit and weld, formed lips and fastening rivets, three flanges fastened with bolts, and the chosen design of machined rings configured to accept the CMC wall structure. The advantage of the machined ring design is that it allows minimizing effects of area reduction in the annulus and liner due to the increased wall thickness of the CMC system. This is accomplished by recessing the metal substrate such that the porous pad is flush with the dome and transition seals, allowing only the thickness of the metal backing to penetrate the annulus volume.

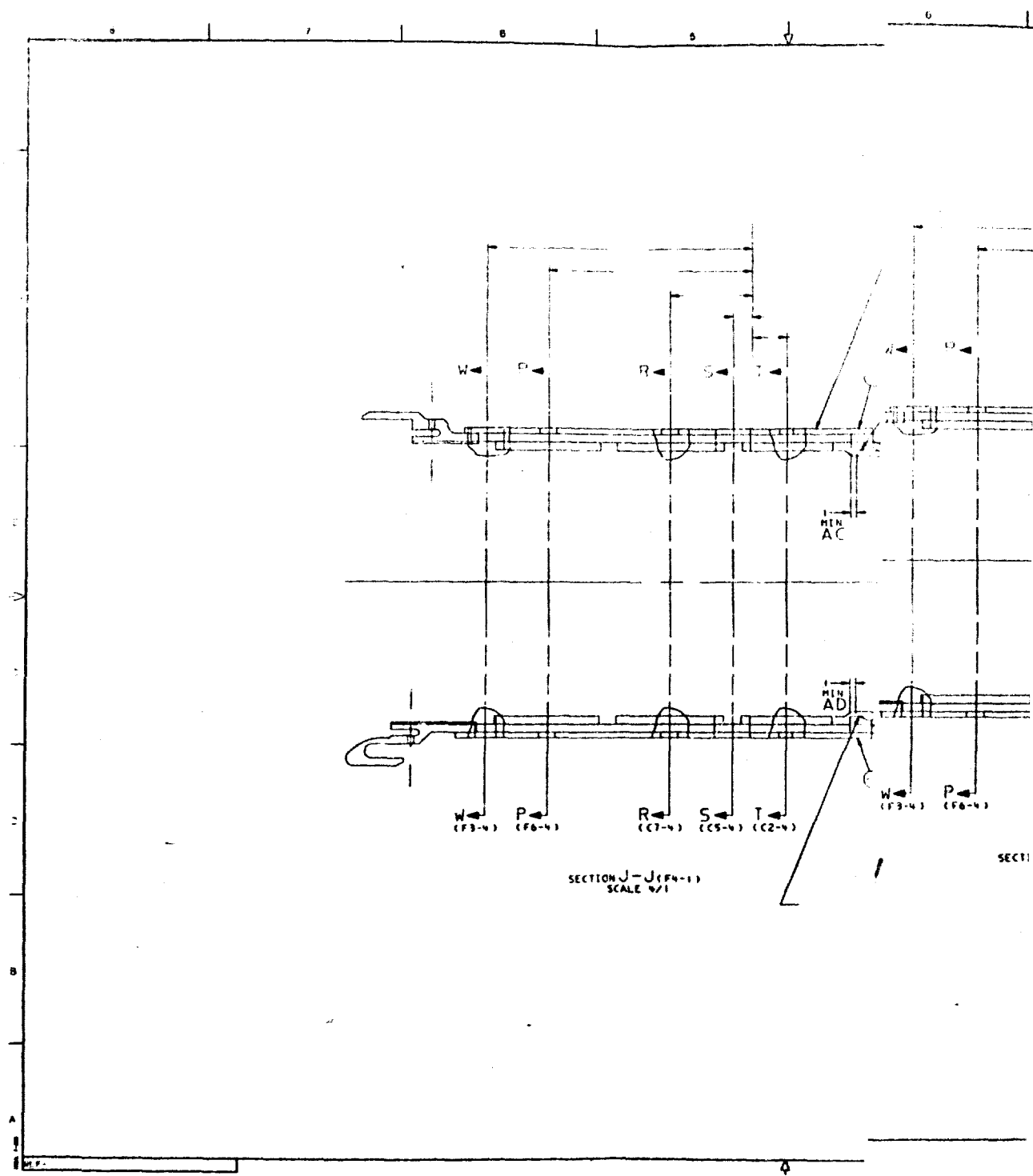
As shown in the drawings, the inner and outer liner and outer transition liner utilize the CMC wall structure. The dome is an effusion-cooled wall as the complex geometry precludes fabrication with the CMC wall concept. Radii of structural supports such as locating pin brackets, igniter boss, and forged rings are all equivalent to the existing design as the completed CMC combustor was tested in the existing, single burner test rig.

Significant design input was required for the mechanical incorporation of the CMC wall structure into the inner and outer liners and outer transition liner. Further, processing modifications are required so the inner and outer liners can be separated at the appropriate time during the fabrication phase to allow access for robotic application of the ceramic surface. The baseline combustor has inner and outer liners welded to the dome. For the CMC combustor, application of the ceramic tiles requires splitting the dome through its circumferential centerline, following the welding of the liner barrel to the dome. This will allow separation of the inner and outer liner and access for ceramic plasma spray coating. In addition, weld locations for inner and outer liner attachment to the fore and aft machined rings requires the weld locations to be at least 0.1 in. from the braze joint between the Hastelloy-X substrate and Brunsbond pad. This would avoid melting the braze and separation of Brunsbond from substrate and also avoid embrittlement of the weld caused by wicking braze material into the weld. To accomplish the CMC wall attachment, two new machined rings were designed for liner attachment to the dome, and the pre-existing machined rings used for attachment to the OTL were slightly modified. The pre-existing machined rings on the OTL have been modified to accommodate the CMC wall and move the weld joint location for attachment of substrate to ring away from the braze joint between substrate and Brunsbond. The redesign of the machined rings and the addition of the two new rings also serve to minimize area reduction in the combustor annulus and inside the barrel due to the increased thickness of the CMC wall, 0.16 in. The rings accommodate the wall by placing the middle Brunsbond layer at the same radius as the existing combustor's wall, hence the substrate layer slightly reduces the annulus area and the liner volume is reduced by the volume the ceramic tiles occupy. This feature avoids restricting the





57B



59 A





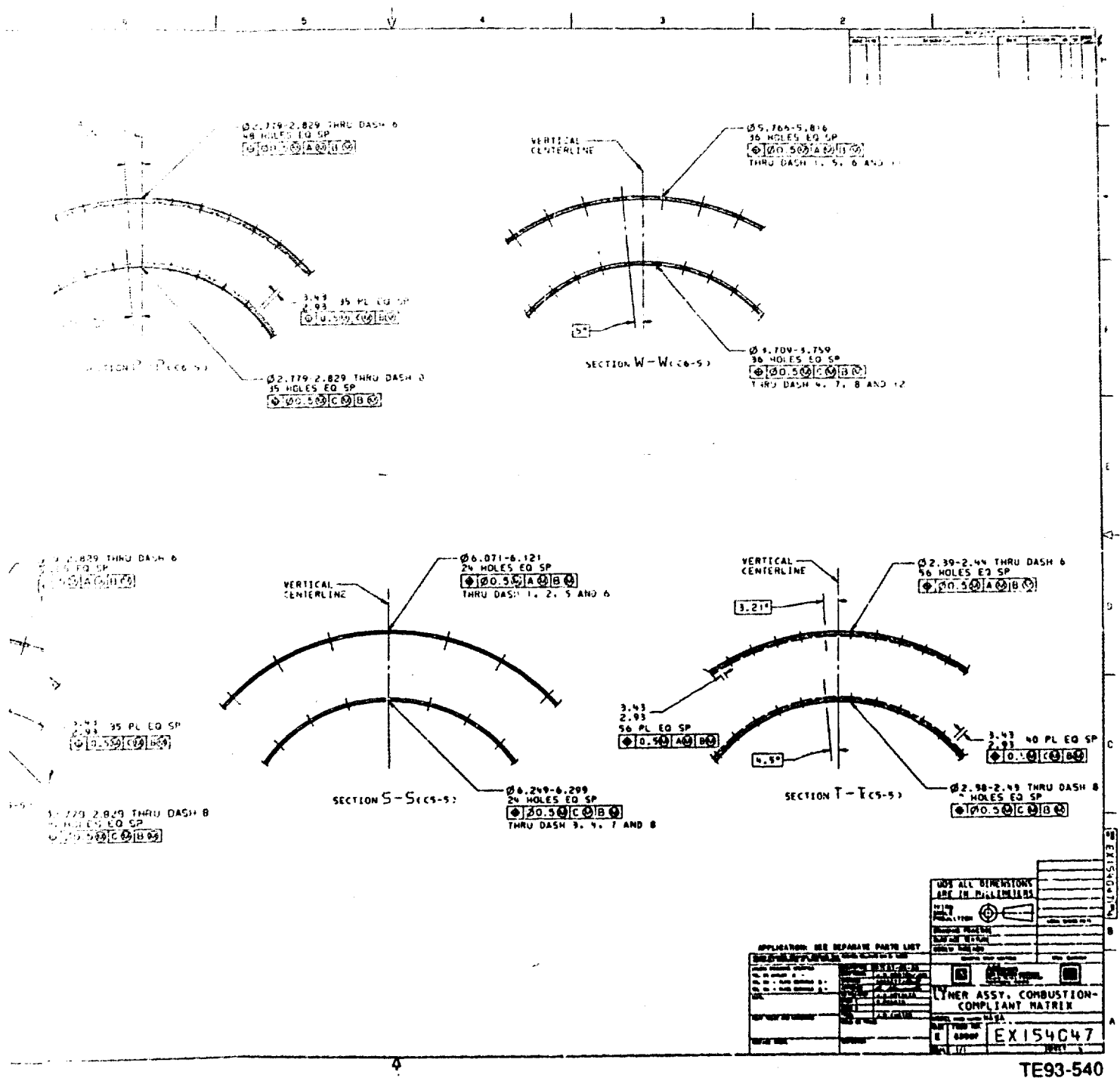
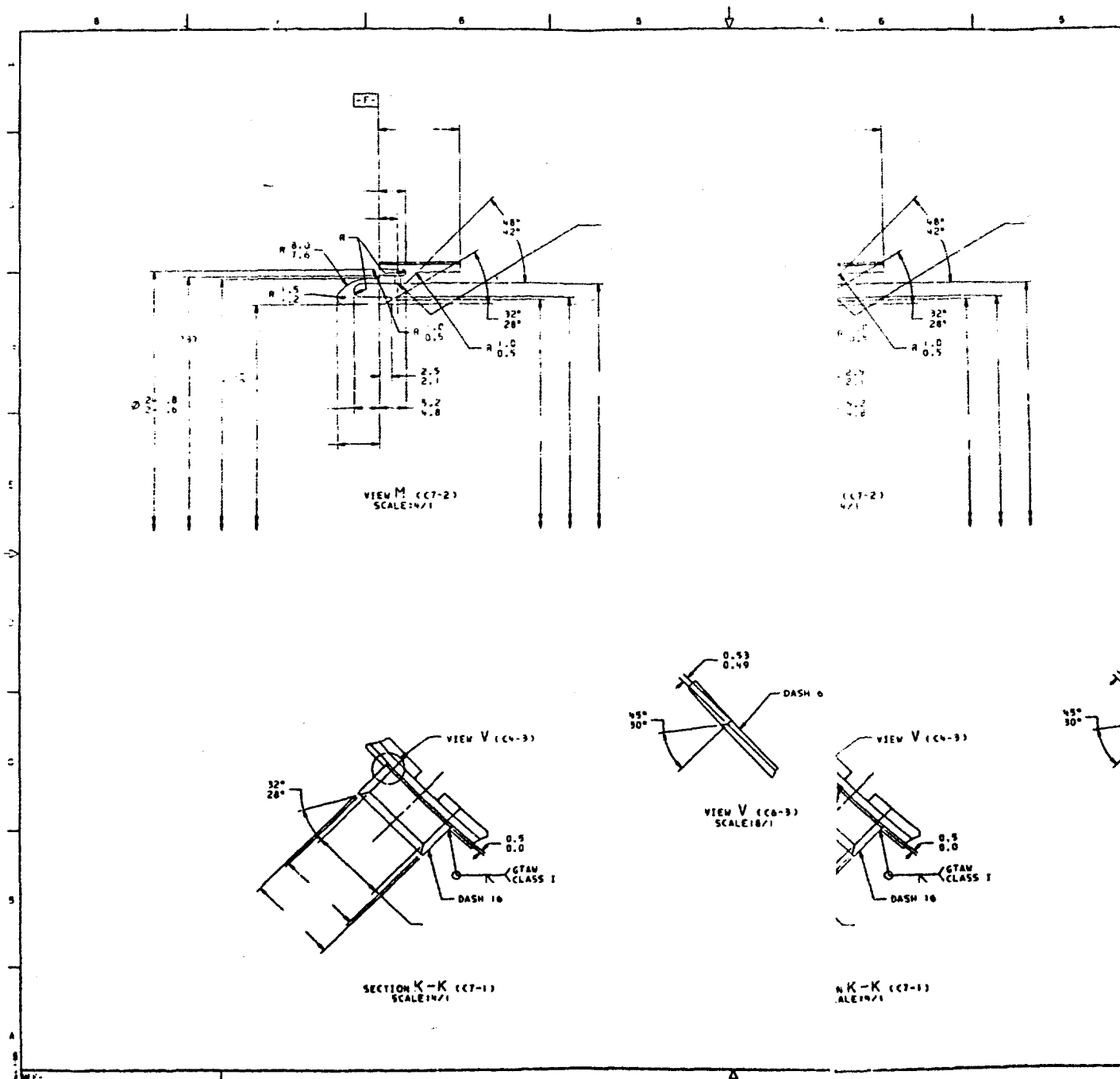


Figure 52. CMC combustor detailed drawings of the combustion liner.









①

65A



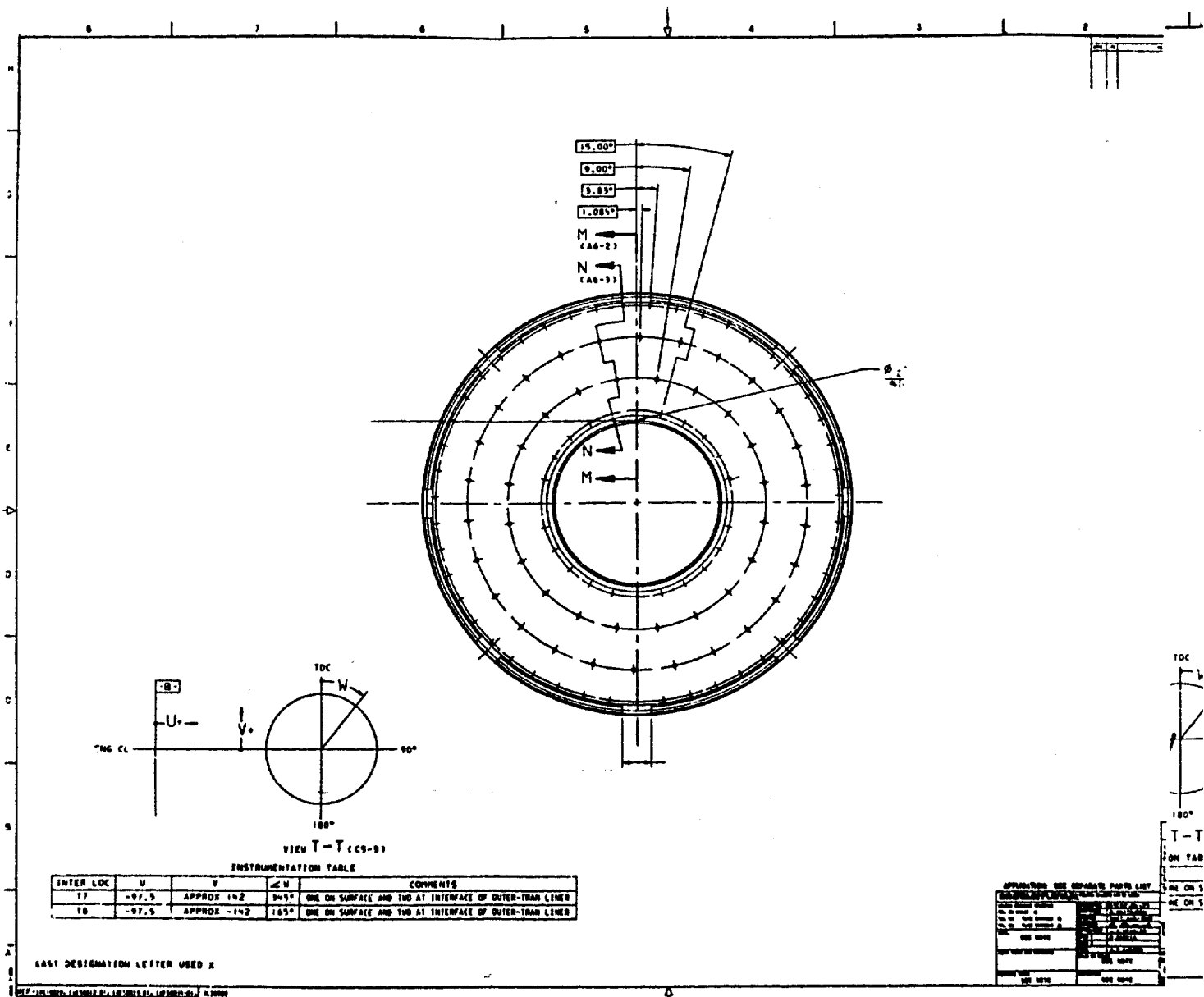
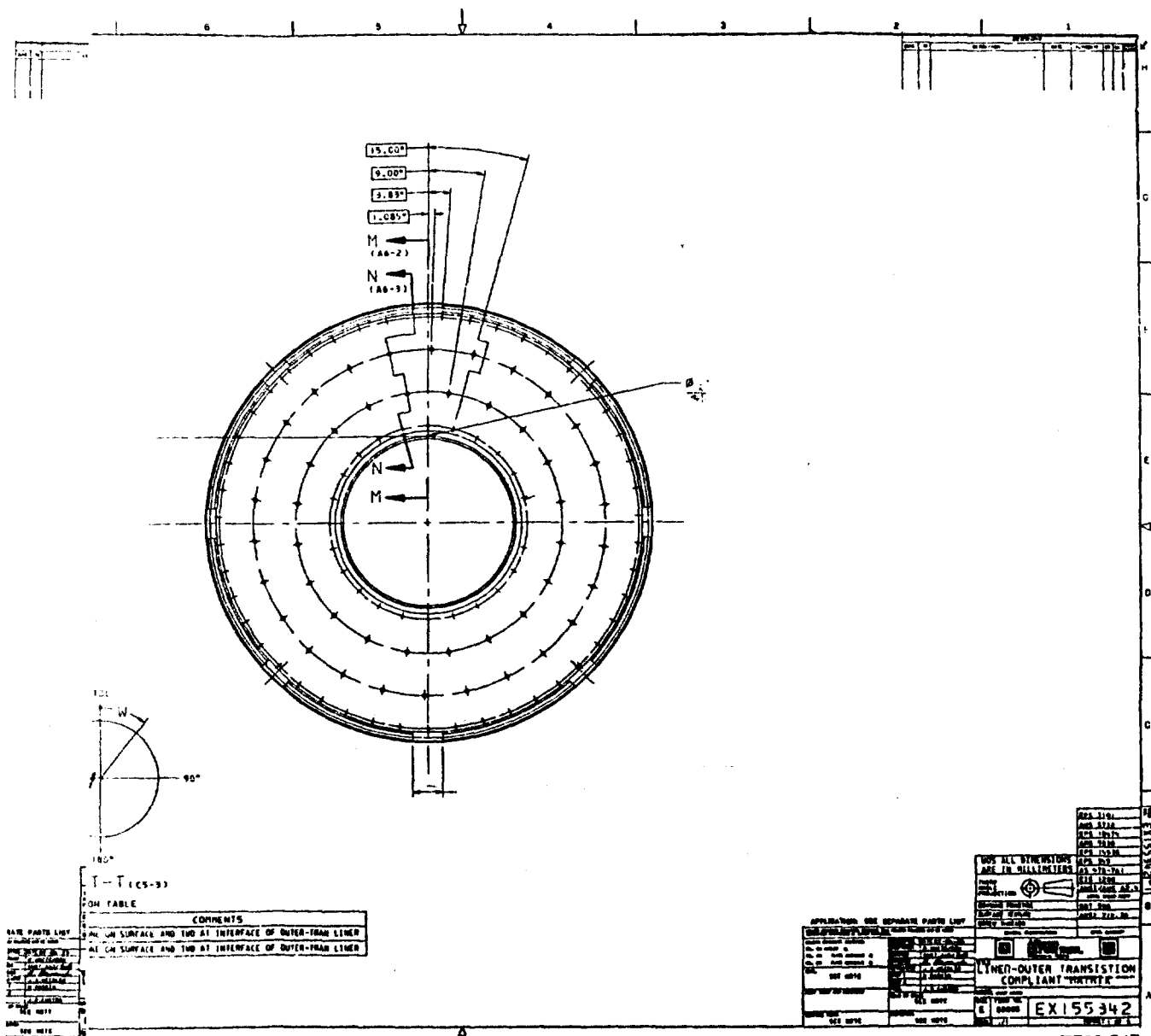


Figure 55. CMC combustor detailed drawings of the outer t

U

67A

2



TE93-547

Figure 55. CMC combustor detailed drawings of the outer transition liner (OTL).

the outer t

67B

①

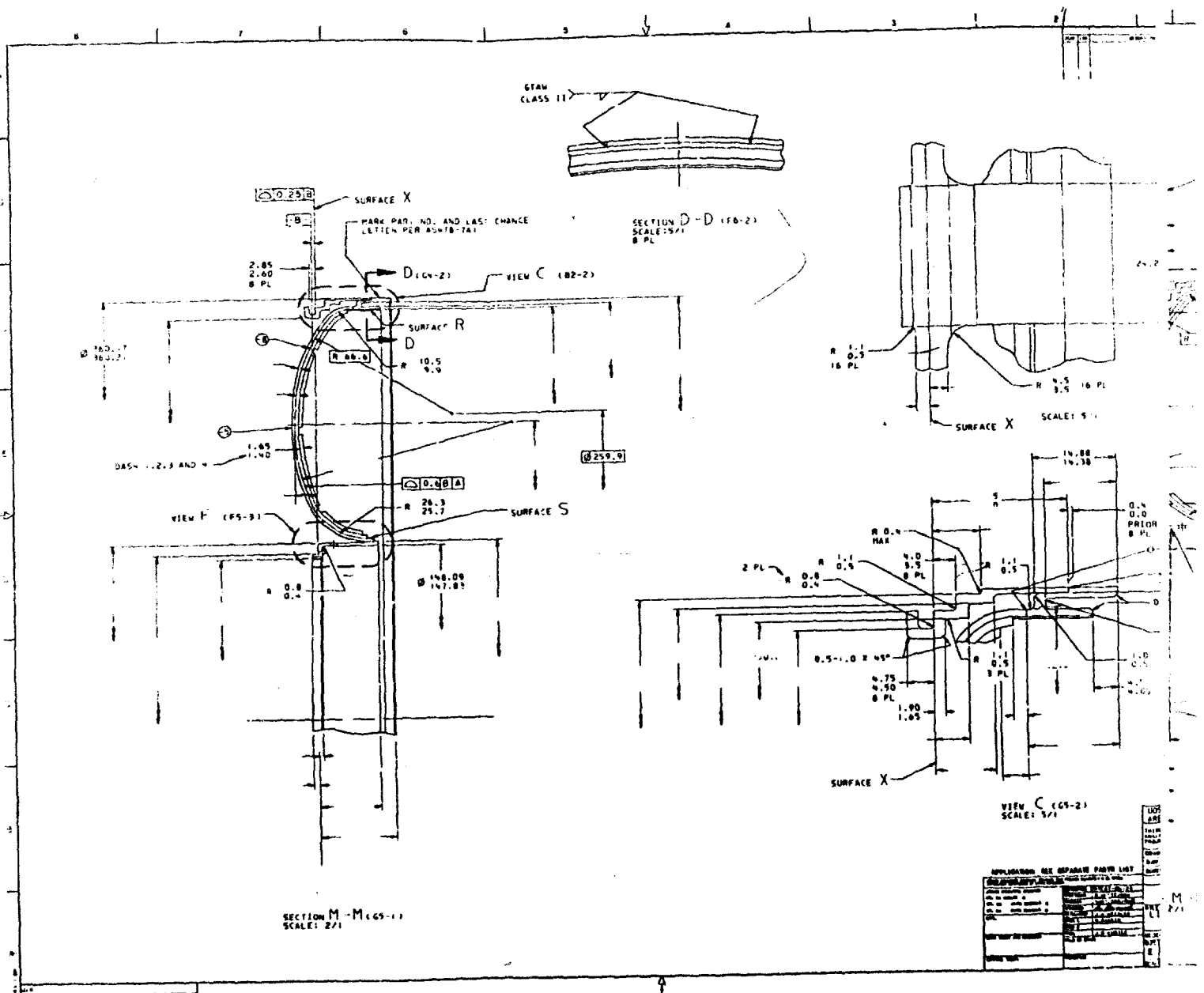
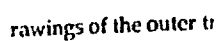


Figure 56. CMC combustor detailed drawings of the outer ti

69 A



69B







liner volume by both Brunsbond and ceramic if the substrate layer were located at the same radius as the wall of the existing design. Following completion of the detailed mechanical design and drawings, fabrication and testing was carried out as described in Section VI.

## VI. TASK 1: FABRICATION AND TESTING

Fabrication of the CMC combustor was based on the final detailed drawings as provided in Figures 50 through 54 for the main combustion liner and 55 through 57 for the outer transition liner (OTL). The experimental nature of the fabrication of the CMC combustor and its complex wall structure was a critical task with potential for major influence on the success or failure of the program. The fabrication effort was carried out jointly between Allison Gas Turbine Experimental Model Shop and Technetics Corporation, located in Deland, FL. Close coordination was required between the participants and resulted in a successful fabrication phase of the program. Following fabrication, five rig builds and combustor tests were carried out. Extensive steady-state and transient performance mapping was carried out along with a final series of cyclic, thermal shock tests to investigate the durability of the CMC concept. Details of the fabrication and testing effort are provided in the following sections.

### 6.1 FABRICATION

Fabrication and processing of the CMC combustor encompassed a number of challenges which included, in addition to processing methodology, development of a processing specification for quality control and close coordination of processing steps carried out alternately between Technetics Corporation and Allison.

Due to the uncertainty in developing the manufacturing processes for the CMC combustor, it was desired to establish a quality control specification to monitor the quality of individual processing operations and their outcome and thus set a minimum required quality standard for the complete combustor. It was important to achieve precise location of the sections of compliant layer, as well as a strong bond between the compliant layer and outer metal shell (substrate). Since air was to flow through holes in the solid metal substrate, turn and flow through the porous Brunsbond pad and then exit through slots in the ceramic that form the individual tiles, it was also critical that the feed hole pattern be uniform and that bonding and coating techniques be refined to ensure minimum deposition or distortion within the compliant layer that could lead to restriction of cooling air flow. Braze material bridging an internal or exposed gap would also cause unacceptable perturbations in the flow of cooling air. Therefore, to monitor the quality of the CMC wall during fabrication, a modified version of Allison EPS (Engineering Process Specification) 7101 was implemented after coordination and acceptance by Technetics Corporation.

EPS 7101 has a current application for Allison production engine abradable blade tracks that employ a concept similar to the CMC technology. The specification serves to control quality on production lots of the blade tracks. Allison's original specification applies to production parts and, as a result, requires expensive quality control and monitoring steps that are not appropriate for a research effort. Hence, a modified specification was written with the approval of Allison's ceramic materials group that minimizes costs but maintains the quality of data to be obtained during the fabrication process. Technetics treated EPS 7101 as a process specification and avoided the costly involvement of their production quality control process. Hence a record of the fabrication steps was obtained along with assurance of a minimum acceptable level of quality for the parts received. EPS 7101 achieves these objectives as described in the following. The Technical Requirements section of EPS 7101 describes equipment, materials, and the preparation and application of the CMC system. To obtain process quality records, the Process Control section of the specification describes quality/record specimens (coupons) and various metallographic exams and inspections. The required quality/record coupons are described in the following matrix, Table VI.

The braze coupon was used to determine the quality of the braze joint between Brunsbond and substrate by visual and metallographic examination and was required for all subassemblies of the combustor. The total coupon was processed through all operations and helped determine the quality of the ceramic layers and also was required for all subassemblies. A single electric discharge machining (EDM) coupon

Table VI.  
EPS 7101 required wall coupons for fabrication quality control.

Coupon	Braze furnace load		
	1. Inner Liner	2. Outer Liner	3. OTL
Braze	X	X	X
EDM	X		
Total	X	X	X
Flow	X		

determined the effects of submerging Brunsbond parts in EDM oil and the effectiveness of the post-EDM cleaning operation. Braze, EDM, and total coupons are 1 in. by 3 in. rectangular segments.

Utilization of EPS 7101 during fabrication of the CMC combustor was critical in ensuring the production of a quality part. Two incidents were identified, during braze operations, using examinations of quality coupons, that led to changes in braze/material combinations.

An analysis of quality inspection coupons (per EPS 7101) revealed that the strength of the braze joint on OTL parts were unacceptable. An effort to determine the cause of the weak braze joints was subsequently carried out and resulted in the conclusion that a bad combination of materials was the problem. The material combination used included a high temperature (2150°F) braze alloy (AMS 4782) in conjunction with the Hoskins-875 Brunsbond and the Haynes-188 substrate. According to Technetics, the high temperature braze results in Aluminum diffusion from the Brunsbond pad to the braze joint and in addition, the AMS 4782 braze alloy does not wet the surface of the Haynes-188 substrate. This resulted in two effects—a weak braze joint and a decrease in the oxidation temperature limit of the Brunsbond pad. Also, since the inner and outer liners were brazed with the AMS 4782 alloy, it was suspected the oxidation temperature limit of the Brunsbond on the liners may also be decreased due to the Aluminum diffusion. The inner and outer liners use a Hast-X substrate and the braze joints were determined to be acceptable. The resulting impact on the quality of these parts resulted in the necessity to use a set of materials within the experience base of Technetics. Hence, to avoid the problems identified, Hastelloy-X was used for all sheetstock (OTL as well as inner and outer liners) in combination with a lower temperature (1950°F) braze alloy, AMS 4777.

The experimental nature of processing the CMC combustor to meet the special requirements of the wall structure presented several process methodology challenges summarized as follows:

- roll- and hydroforming the brazed (i.e. prejoined) Brunsbond/substrate structure, required for the inner, outer, and transition liners, had to be accomplished without tearing or crushing the porous Brunsbond layer. Crushing could effect the blockage in the compliant layer and restrict the rate of cooling airflow. This effort was particularly challenging for the OTL, which contains complex curvature features and required hydroforming to process.
- avoiding excessive braze wicking and ceramic seepage into the Brunsbond layer, which would also impact blockage in the compliant layer
- to avoid relieving the as-sprayed stresses in the robotically applied ceramic (TBC) layer, heat work of the substrate layer (i.e. welding or machining) was not allowed. Therefore, robotic plasma-flame application of the ceramic coating could only be carried out after completion of most machining and welding operations. In addition, stress relief operations carried out on metal parts after weld operations were not allowed after application of the ceramic tiles.

- discontinuities in the Brunsbond layer below the ceramic surface had to be avoided to avoid the potential of the discontinuities causing stress regions and cracking in the ceramic during combustor operation. Therefore, the seams of the Brunsbond layer were staggered on the inner and outer liner to correspond with the cooling air exit slots between the ceramic tiles.
- to allow access for the robotically applied ceramic tiles, the combustor was designed for division into three sections: inner, outer, and transition liner. Therefore, a weld seam was required through the dome centerline to allow final assembly of the inner and outer liners in addition to gaining as much distance as possible between the weld joint and ceramic tiles.
- weld joints between the CMC wall structures and the machined rings also required placement away from heat affected zones to avoid substrate/Brunsbond braze joints to melt and cause delamination or embrittlement of the weld joint from braze wicking to the weld location
- machining operations that required liquid coolant or flushes or solvent degreasing operations required careful scheduling to avoid operations of this type following TBC application. Liquid flushes or solvents will soak into the Brunsbond pad (as well as the ceramic) and possibly carry contaminants into the pad which would be impossible to remove, hence compromising the open area of the Brunsbond. After ceramic application, only dry processing operations were allowed.
- significant process development effort was required before a suitable technique, using thin metal wire and RTV rubber, was identified to produce the pattern of coolant air exit slots in the ceramic layer, thus forming the individual ceramic tiles.
- care in handling of the combustor assembly was critical during processing to avoid damaging the relatively brittle ceramic tiles.
- finally, wall temperature thermocouple instrumentation (to measure temperatures at the interface between substrate and Brunsbond and the interface between Brunsbond and ceramic) required installation before the application of the TBC.

The CMC combustor is basically comprised of four sheet metal pieces welded to machined forgings which establish the support structure and sealing surfaces for the fishmouth seal between the OTL and main combustion liner and seals for engine or rig installation. The four pieces are the hydroformed, annular sheet metal dome (effusion cooled), the hydroformed annular outer transition liner (OTL), and the two rolled cylindrical liners (inner and outer). The balance of combustor hardware consists of locating brackets, ignitor boss, swirler/fuel nozzle ferrules, and thermocouple instrumentation. Table VII is a detailed breakdown of the fabrication effort, as split between Allison and Technetics. Table VII also provides the processing sequence that was needed to meet the special requirements of the CMC wall structure.

As previously described, the OTL and two cylindrical liners are comprised of the CMC structure. The Brunsbond was brazed in flat form to the flat sheet stock (Hast-X) that comprises the three liners. For the inner and outer liners, the Hastelloy-X sheet stock was predrilled in the flat to create the coolant feed orifices. The layout of the coolant orifices was calculated so the holes would properly locate (one orifice per ceramic tile, six (6) rows of tiles) following the roll forming process that produces the cylindrical inner and outer liner. The completed liners are shown in Figure 64 as they looked following the roll forming, welding, and finish trim operations at Technetics. Figure 65 is a view of the Brunsbond surface showing the staggered seam (and substrate weld joint) that coincides with the location of coolant air slots between tiles. The OTL, however, failed during hydroforming when the coolant air feed orifices were predrilled in the flat sheet stock. Failure occurred via cracking in the substrate between the predrilled cooling air holes at the smallest diameter row of holes. Examination of the parts determined that cracking occurred as a result of the high stress zones concentrated around the cooling holes during hydroform. An attempt to stress relieve the OTL during the forming process offered no help. To correct the problem of tearing, cooling air holes were not predrilled as in previous attempts. The solid, flat sheet stock was brazed to the Brunsbond pad and then hydroformed into the shape of the OTL. The four rows of cooling air holes were electric discharges machined (EDM) in the formed part rather than in the flat sheet stock. A previous investigation had explored and determined the viability of EDMing the small diameter cooling holes through the substrate layer only of the brazed substrate/Brunsbond assemblies. Results from test pieces, shipped to Allison for assessment, revealed that

Table VII.  
CMC combustor fabrication effort: description, sequence, and split of processing operations.

Step Number	Allison Fab Effort	Step Number	Technetics Fab Effort
1.	Provide flat sheet stock with predrilled cooling holes positioned such that they locate properly when formed to shape, ship sheet stock to Technetics for the inner, outer, and OTL liners. Hydroform the dome.	1.	Braze Brunsbond pad to flat Hast-X sheet stock and form to shape (for 3 liners), ensuring proper location of cooling holes and minimizing restriction of Brunsbond cooling air passages. Voids or openings between layers to be avoided.
2.	Rough machine modified OTL forgings (3), inner and outer rear liner forgings (2), and new inner and outer forward liner forgings (2).	2.	Transmit to Allison the completed, formed inner and outer liner and OTL. The liners at this point having only substrate and Brunsbond attached and finished trimmed.
3.	To the formed liners weld ignitor boss, locating brackets, and all forgings (7). Finish machining carried out on forgings. Drill primary and dilution and thermocouple holes through substrate and Brunsbond. Attach thermocouple at interface locations. Drill cooling and nozzle/swirler holes in the formed, effusion cooled dome. Trim and attach dome to inner and outer liner. Then cut dome through pitchline to separate inner and outer combustion liners. Ship to Technetics along with OTL for ceramic application.	3.	Technetics creates thin wire/RTV slot/tile gridwork as specified and robotically applies ceramic plasma spray to form ceramic tiles and coolant exit slots. Slots are cleaned up with machining to ensure free area. Technetics ships the (3) liner pieces back to Allison for final assembly.
4.	Weld dome through pitchline to reattach inner and outer liners. Tack weld swirler/fuel nozzle ferrules in place on dome. Finish parts as necessary, inspect dimensionality.		

the process, by proper control of the depth of cut into the Brunsbond layer, provides cooling holes which are not obviously blocked by braze alloy or other debris from the EDM process. After completion of the braze and finish trim operations at Technetics, the liners were shipped to Allison for attachment of the machined forging support rings, dome, miscellaneous hardware, and thermocouple instrumentation. Figure 66 shows the inner liner after completion of these operations at Allison while Figure 67 shows the outer liner. As seen in these figures, half of the effusion cooled dome is attached to the inner liner and half of the dome is attached to the outer liner. Thermocouple instrumentation (20 total, 14 on the liners and 6 on the OTL) are also installed and shown in these figures.

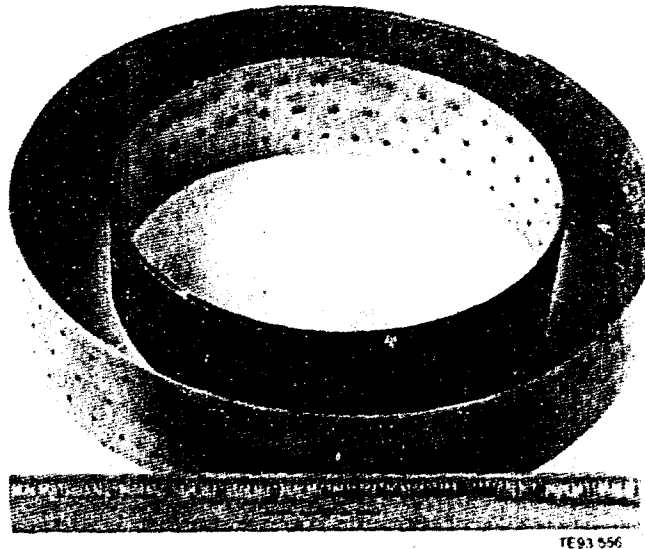


Figure 64. Inner and outer liner—substrate and Brunsbond only.

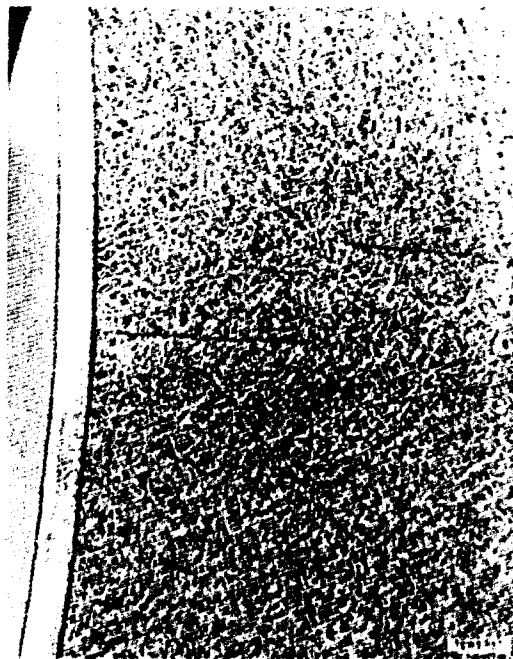


Figure 65. Brunsbond surface and staggered seam.



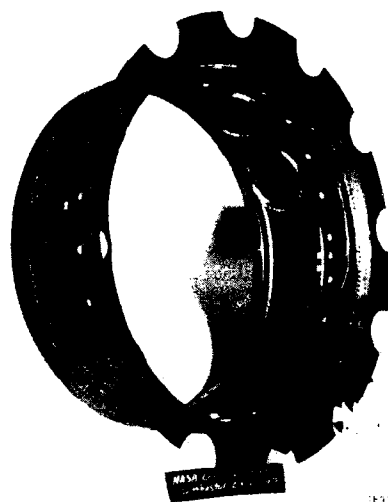


Figure 66. Inner liner—ready for TBC application.



Figure 67. Outer liner—ready for TBC application.

The thermocouple used at the interface locations between Brunsbond and ceramic and Brunsbond and substrate required a novel design. Development was required to produce a design that would be rugged enough and yet not upset local heat transfer rates by providing conduction paths which will also lead to erroneous readings. An investigation of sample thermocouples examined such types as 0.010 in. diameter swaged stock with closed tip grounded junction as well as larger diameter, both open and closed tip designs up to 0.060 in. diameter with bore wire designs using ceramic tubes attached to the substrate and Brunsbond walls. The final selected thermocouples were 0.020 in. diameter chrome-alumae (CA) closed or opened tip thermocouples imbedded in the ceramic tubes. Figure 68 shows a close-up of an installed thermocouple located at the critical ceramic-Brunsbond interface. As shown, the ceramic tube minimizes conduction errors and the vertically installed design minimizes the cross-sectional area and, as a result, reduces the potential for damaging the ceramic tile during combustor operation from the existence of a discontinuity below the ceramic surface.

Technetics subsequently fabricated the thin wire/RTV network required to form the tile pattern and coolant exit slots. Considerable development was required to perfect this process to form the excellent quality tile pattern in the final product. Figure 69 is a photo of the inner liner as received at Allison following application of the TBC. Allison carried out the final assembly processing to complete the combustor liner and OTL. The completed combustor (inner and outer liner and dome) are shown in Figure 70. The complete combustion system, with OTL slip fitted to the liner, is shown in the photo of Figure 71.

## 6.2 TESTING

### 6.2.1 Description of Test Facility and Capability

Full-scale rig tests were performed to determine combustion system steady-state performance, ignition and lean stability limits, exhaust emissions, temperature levels and gradients, and resistance to cyclic, thermal shock tests to assess combustor structural durability.

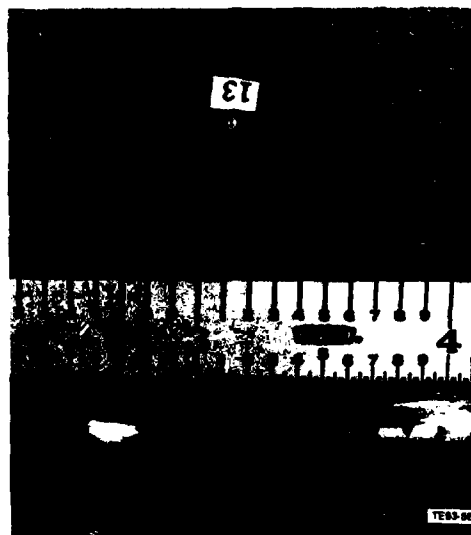


Figure 68. Detail of thermocouple installation at critical ceramic/Brunsbond interface.

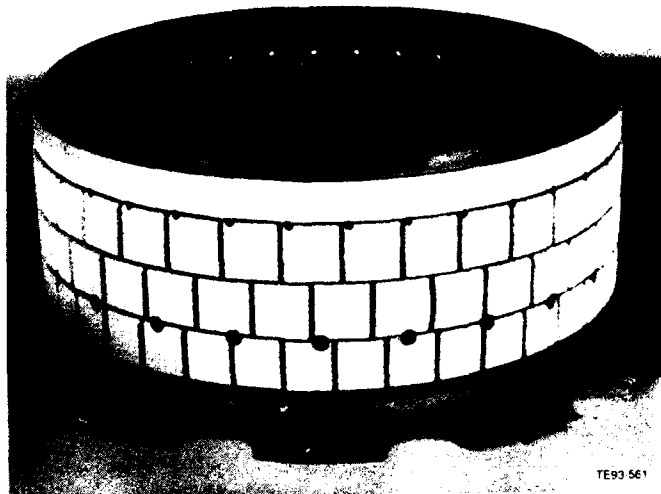


Figure 69. Inner liner—after TBC application.

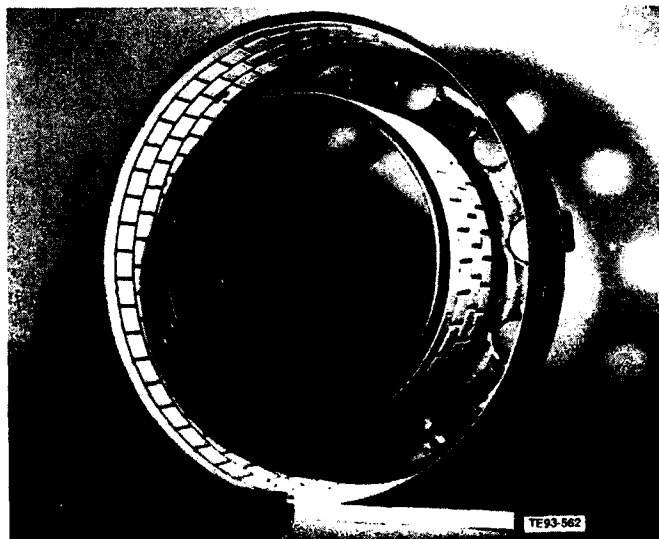


Figure 70. Completed CMC combustor—before test.



Figure 71. Completed CMC combustor with OTL—before test.

Combustor component rig tests were performed in the Allison combustion facility, which contains a fully instrumented combustor rig for advanced, small reverse-flow combustors. The full annular rig simulates compressor discharge geometry and aerodynamic conditions of Mach number, swirl angle, and temperature. Pressures were limited to 250 psia. A schematic and photo of the advanced, full-scale small combustor test rig is shown in Figure 72.

The rig and instrumentation consisted of the advanced, reverse-flow combustor rig equipment, burner inlet and outlet total pressure rakes, the rotating, air-cooled BOT rake, emissions probes and sampling system, as well as wall thermocouples and various static pressure taps.

The combustor rig simulates an engine flow path from compressor diffuser to the inlet of the gasifier turbine. The rig has provision to extract bleed air to simulate engine operation. Rig airflow is measured with a 3 in. thin plate orifice located within the test cell. Combustor bleed air was measured with ASME thin plate orifices. Instrumentation throughout the rig provides overall performance measurements of the test combustor. A main feature of the rig is the rotating probe for measuring burner outlet temperature. Eight platinum-platinum-rhodium thermocouples are air-cooled and mounted on four air-cooled platinum bodied rakes offset 90 degrees. Temperatures are correlated with uncooled, reference thermocouples which provide the approximate 3100°F bulk average BOT capability of the rig. A platinum bodied total pressure rake along with a static pressure tap are also mounted in the vicinity of the rotating probe at the combustor exit plane. There are four stationary emissions probes at the exit of the combustor. Each probe has four individual sampling lines manifolded together after exit from the rig. Twenty chrome-alumel (CA) thermocouples are attached to the combustor to measure wall temperatures throughout the CMC wall. As shown in Figures 2 and 30, the thermocouples were placed on the effusion-cooled dome, on the substrate surface (cold side), on the interfaces between ceramic and compliant layer, and compliant layer and substrate for both the inner and outer liners and OTL. Combustor inlet air conditions were measured with 14 total pressure rakes. Each rake contains three measurement elements. The rakes are spaced circumferentially in the exit of the inlet diffuser. In addition to total pressure rakes, there are 16 static pressure taps throughout the combustor rig. They are placed in the deswirl vanes, combustor plenum, and bleed air paths. Two Flotron transducers were

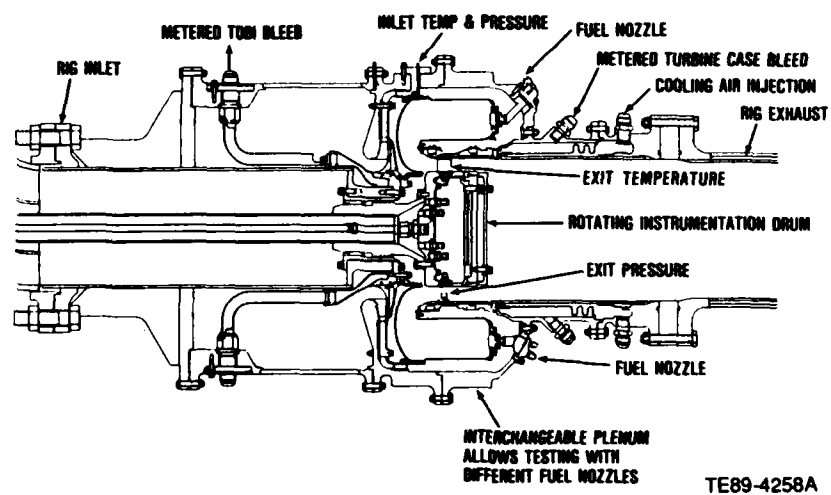
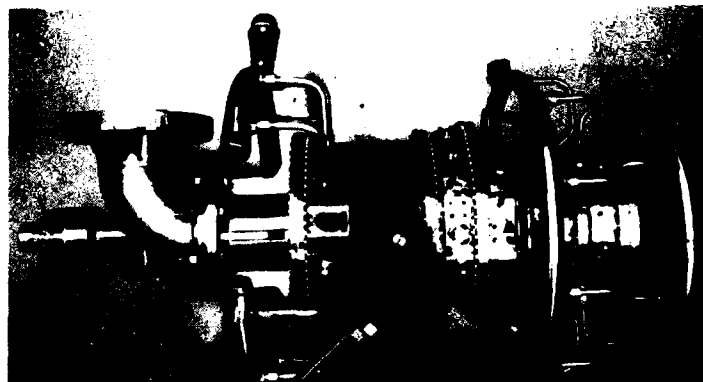


Figure 72. Advanced reverse-flow full-scale small combustor test rig.

installed in series with a boosted, high pressure fuel pump to provide and measure fuel flow. The cooling water system features high pressure water used to cool the exhaust gases upstream of the exhaust valve. The exhaust spool was also water-cooled with the high pressure water supply.

The test articles consisted of the following:

- CMC combustor liner
- OTL (transition)
- swirlers (12) and retaining rings
- piloted airblast fuel nozzles (12)
- pilot and main fuel manifolds
- external fuel nozzle flow divider valve
- ignitor plug
- excitor box
- JP-4 fuel

The test measurements included:

- BOT traverse temperatures
- liner static pressure drop
- liner total pressure drop
- total rig airflow
- bleed airflows
- burner inlet temperature (BIT)
- burner inlet pressure (BIP) static
- BIP total
- burner outlet pressure (BOP) static
- BOP total
- liner wall temperature
- exhaust emissions
- fuel flow
- fuel temperature
- fuel pressure

A brief description of the test procedures used during the program are provided in the next section.

#### 6.2.2 Test Procedures

Combustor rig assembly and system checkout is carried out first before initiating high pressure combustion tests for a given build. To avoid damage to the combustor during mating of the rig halves, a procedure was devised using a borescope to guide alignment of the OTL and combustor barrel. Instrumentation lines were routed out as the two halves to the rig were mated together. Before the cold flow pressure tests, the rig system was pressurized and deadheaded. All splitlines, fittings, nozzles, etc, were physically checked for leaks. Pressure measuring devices were checked for agreement. Fuel nozzle immersion depth, defined as the distance between the nozzle face and inside (hot side) swirler face, was also measured at this time for possible correlation with performance results. Immersion depth may be positive (immersed into combustor) or negative (recessed).

Cold flow pressure drop characteristics were determined next by setting the rig to a given pressure, temperature, and airflow and then recording the pressure drop.

High pressure combustion tests were carried out after cold flow pressure evaluation. The combustor was fired and stabilized at simulated engine power conditions from idle to maximum power. For each condition the rig operating parameters (i.e., airflow, pressure, temperature, emissions, and BOT) were mea-

sured. The BOT and pattern were measured by rotating the BOT probe while continuously recording thermocouple output. The probe was rotated at approximately 0.4 in./sec. This speed allows the thermocouple elements to fully respond to the gas path temperature. At the conclusion of each combustion test, the fuel nozzles were purged with high-pressure nitrogen to prevent fuel carboning in the nozzle passages.

Performance measurements are derived quantities obtained from basic measurements made during the steady-state combustion tests. Included are liner total pressure drop, chemical combustion efficiency, radial burner outlet profile (defined as the circumferential BOT average at various radial locations divided by the overall average BOT), and pattern factor (defined as the difference between the maximum recorded BOT and average BOT divided by the average burner temperature rise). Ignition and lean blowout (LBO) fuel-air ratios were determined over the range of the start and flight envelopes, respectively. Ignition and LBO data were correlated versus corrected reference velocity.

Ignition tests were performed by setting flow conditions for a given operating point and then initiating a preset fuel flow. Ignition must be obtained within one or two seconds of reaching full fuel manifold pressures. The test was repeated at the same flow condition until the minimum fuel flow for a successful ignition was obtained.

Lean blowout fuel/air ratios were determined by setting flow conditions for a given operating point and slowly reducing fuel flow until no flame can be detected by outlet thermocouples. Fuel flow was then increased to ensure that the combustor has blown out and would not relight.

Smoke and gaseous exhaust emissions were measured at SLS standard day steady-state operating conditions from idle to maximum power. Smoke is important for visibility considerations and the gaseous emissions CO, UHC, and NO<sub>x</sub> are important for calculating combustion efficiency and for air pollution considerations. Smoke was measured in accordance with SAE ARP1179 and gaseous emissions in accordance with SAE ARP1256.

As previously mentioned, liner and OTL wall temperature levels and gradients were continuously monitored using 14 CA thermocouples on the liner and 6 CA thermocouples on the OTL. In addition, further insight was provided by the application of thermal indicating paint to the metal substrate surface.

Finally, to assess the durability of the CMC combustor, cyclic thermal shock tests were performed. Cyclic testing was carried out by holding burner inlet conditions of pressure, temperature, and airflow constant while repeating fuel flow excursions between a minimum, determined to avoid flameout, and a maximum to achieve a BOT of either 2700°F (initial tests) or 3000°F (final test).

### 6.2.3 Test Plan

The overall objective of the test plan was to establish the cooling effectiveness, performance, and durability of the CMC combustor concept. Testing consisted of cold flow pressure drop, lean stability and ignition mapping, steady-state performance throughout the operational range including the milestone 3000°F BOT design condition, as well as two series of cyclic thermal shock tests at high point BOT conditions of 2700°F and 3000°F. Five test builds and approximately thirty (30) hours of combustion testing were planned. Characterization of wall temperatures through thermal paint tests and wall thermocouple measurements would be used in the decision to adjust local coolant flux, if necessary. Analytical calculations using the flow and heat transfer models were used to correlate empirical results and provide specifications for rework of the OTL and effusion-cooled dome.

The test program matrix of test conditions is given in Table VIII. Lean blowout points are designated LBO, ignition points are designated IGN, and steady-state points, SS. All cold flow testing was performed at ambient conditions over a range of corrected flows from 0.5 to 0.9 lb/s with bleed air off.

Table VIII.  
Matrix of test conditions for CMC combustor.

Point	Condition*	BIP (psia)	BIT (°F)	Rig flow (lbm/s)	Blade bleed (lbm/s)	Vane bleed (lbm/s)	Liner airflow (lbm/s)	Fuel flow	F/A	BOT (°F)	Vr, corr (ft/s)	Wcorr (lbm/s)
1 (LBO)	6 KM 72.5 KCAS Cold day idle	35.9	229	1.73	0.07	0.14	1.52	68.5	0.0125	1112	73.7	0.717
2 (LBO)	6 KM 0.6 MN Cold day idle	41.2	259	2.08	0.09	0.16	1.83	65.6	0.01	973	96.6	0.768
3 (LBO)	3 KM 0.3 MN ISA idle	46.3	370	2.10	0.09	0.17	1.84	89.9	0.0136	1307	129.4	0.739
4 (LBO)	SLS ISAA idle	61.8	414	2.70	0.12	0.21	2.37	127	0.0149	1460	184.8	0.731
5 (LBO)	6 KM 0.3 MN Cold day decel	68.7	468	3.22	0.14	0.25	2.83	85.6	0.0084	1056	248.8	0.810
6 (IGN)	SLS 59°F day 10% NGG	14.9	65	0.27	0	0	0.27	--	--	--	7.6	0.268
7 (IGN)	SLS 59°F day 15% NGG	15.3	69	0.41	0	0	0.41	--	--	--	11.7	0.398
8 (IGN)	SLS 59°F day 20% NGG	15.6	74	0.54	0	0	0.54	--	--	--	15.7	0.516
9 (IGN)	SLS 59°F day 25% NGG	16.0	78	0.68	0	0	0.68	--	--	--	20.1	0.636
10 (IGN)	SLS 59°F day 30% NGG	16.3	83	0.81	0	0	0.81	--	--	--	24.4	0.747
11 (SS)	50% IRP	181.3	717	6.73	0.29	0.53	5.91	494	0.0232	2148	836	0.722
12 (SS)	MCP	235	819	8.21	0.35	0.65	7.21	720	0.0277	2475	1204	0.708
13 (Cyclic)	IRP	261	873	8.82	0.38	0.70	7.74	831	0.0298	2701	1404	0.699
14 (SS)	TP1 (thermal paint)	272	895	9.04	0.39	0.71	7.94	927	0.0324	2800	1488	0.693
15 (SS, cyclic)	TP2 (thermal paint-max power)	272	895	9.04	0.39	0.71	7.94	1008	0.0353	3000	1488	0.693

\* KM = altitude in kilometers  
MN = Mach number  
SLS = sea level, static condition  
NGG = gas generator speed  
IRP = intermediate rated power  
MCP = maximum continuous power

Steady-state performance and thermal paint signatures were obtained at test points 4, 11, 12, 13, 14, and 15 using JP-4 as the fuel. During each test, a complete survey of the burner exit was made to determine exit temperature pattern, pressure loss, and exhaust emissions. Wall temperatures were measured using TP-8 thermal paint and 20 wall thermocouples located as shown in Figure 30 and as described in Table IX.

Ignition data was obtained at test points 6 through 10 and lean blowout mapping was obtained at test points 1 to 5 using JP-4 as the test fuel. The complete steady-state, thermal paint, ignition, and LBO testing plan is defined in Table X.

The durability of the CMC combustor structure was assessed by subjecting the combustor to cyclic variations in fuel flow and maximum burner exit temperature. The burner inlet conditions were held constant and throttle excursions between minimum fuel flow (above blowout) and the maximum fuel flow were



Table IX.  
Burner wall temperature thermocouple locations.

<u>Thermocouple number</u>	<u>Location</u>
1	Barrel, bottom, outer, metal cold side
2	Barrel, bottom, outer, ceramic/Brunsbond interface
3	Barrel, bottom, outer, metal/Brunsbond interface
4	Dome, bottom, metal cold side
5	Barrel, top, outer, metal cold side
6	Barrel, top, outer, ceramic/Brunsbond interface
7	Barrel, top, outer, metal/Brunsbond interface
8	Dome, top, metal cold side
9	Barrel, top, inner, metal cold side
10	Barrel, top, inner, ceramic/Brunsbond interface
11	Barrel, top, inner, metal/Brunsbond interface
12	Barrel, bottom, inner, metal cold side
13	Barrel, bottom, inner, ceramic/Brunsbond interface
14	Barrel, bottom, inner, metal/Brunsbond interface
15	OTL, top, Brunsbond/ceramic interface
16	OTL, top, metal/Brunsbond interface
17	OTL, top, metal cold side
18	OTL, bottom, Brunsbond/ceramic interface
19	OTL, bottom, metal/Brunsbond interface
20	OTL, bottom, metal cold side

Table X.  
Steady-state, thermal paint, ignition, and LBO performance measurements for CMC combustor.

<u>Condition</u>	<u>Cycle point number</u>	<u>Burning hours</u>	<u>Teardown/inspection rebuild</u>
Idle	4	0.75	No
50% IRP	11	0.75	No
MCP	12	0.75	Yes
IRP	13	0.75	Yes
Thermal paint 1	14	0.75	Yes
Thermal paint 2	15	0.75	Yes
Ignition	6-10	1.5	No
LBO	1-5	1.5	No

Photograph liner and OTL after each teardown

repeated. The burner inlet conditions were those of test points 13 and 15 given in Table VIII. Table XI describes the cyclic testing program.

Figure 73 provides a single-cycle illustration for the throttle excursions of cyclic tests 1 through 3. The fuel flows shown are approximately 30% above idle fuel flow and are chosen to avoid flameout. During

Table XI.  
Cyclic testing program for CMC combustor.

Condition	Point number	Burn hours	Number of cycle	Approximate average		Teardown/inspection rebuild
				Max (°F) BOT	Min (°F) BOT	
IRP (1)	13	3.0	32	2700	1300	Yes
TP2 (2)	15	6.5	92	3000	1300	No
TP2 (3)	15	6.5	91	3000	1300	No

the test program, the minimum fuel flow was experimentally determined by decreasing the fuel rate from a stable operating condition to a point just above flameout. On each day of cyclic testing, a complete burner exit survey was performed during steady-state operation to establish the location of the maximum temperature. The rotating probe was left in this position during the cyclic testing. Wall temperature and pressure drop histories were monitored and recorded to evaluate potential problems or failures. Emissions and burner exit temperature patterns were measured at the start and end of each day's cyclic tests.

#### 6.2.4 Test Results and Analysis

The test program was accomplished in five rig builds (BU 1 through BU5). A build is defined as a combustion test involving assembly of the combustor/instrumentation and rig followed by teardown inspection of the combustor and rig to assess condition. The five builds are summarized as follows:

- BU1—Initial steady-state (SS) performance evaluation covering idle condition (point 4 in Table VIII) through MCP (operating point 12 in Table VIII). Although thermal paint was applied to the combustor, the test was not a dedicated thermal paint run as several hours (7:14 hours burn time) were accumulated and the paint was expected to "wash" out. However, qualitative temperature distribution data and identification of hot spots were obtained to support wall thermocouple temperature measurements.
- BU2—Dedicated 2800°F BOT thermal paint test. This test verified the necessity to adjust local coolant flux on the dome and OTL. BU2 was followed by rework of the liner dome and OTL.
- BU3—Ignition/lean blowout (LBO) mapping, SS performance up to the milestone 3000°F BOT condition. Demonstrated excellent SS performance and consistency of results with BU1 data.
- BU4—Cyclic thermal shock testing at high point BOT of 2700°F (32 total cycles).
- BU5—Cyclic thermal shock testing at high point BOT of 3000°F (68 total cycles).

Test results obtained during BU1 indicated the need to perform a component cold flow-pressure drop test of the OTL. The OTL thermocouples revealed approximately 200 degree higher wall temperatures relative to the inner and outer liners of the combustor. The OTL was flowed and, as expected, demonstrated a much lower coolant flow area than the design value. In addition, BU1 wall thermocouple temperature results, at the MCP test condition of 2475°F, were correlated using the 3-D (COM3D) flow-field model and heat transfer analysis. Good agreement between measured and predicted wall temperatures provided empirical validation of the design system.

The dedicated thermal paint test of BU2 provided wall temperature data with poor resolution of isotherms due to the extended length of the combustion test. However, the thermal paint revealed and verified hot spots on the dome and OTL. Rework of the liner dome and OTL was carried out to adjust local coolant flux by the addition of effusion cooling holes on the dome and several additional coolant orifices on the OTL. Subsequently, BU3 through BU5 testing completed SS performance evaluation,

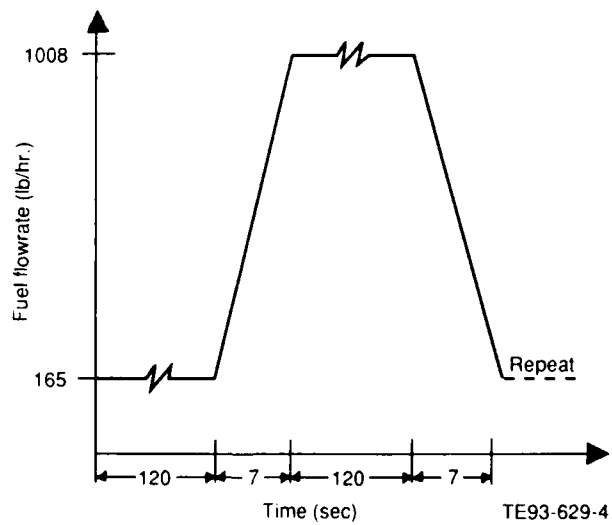
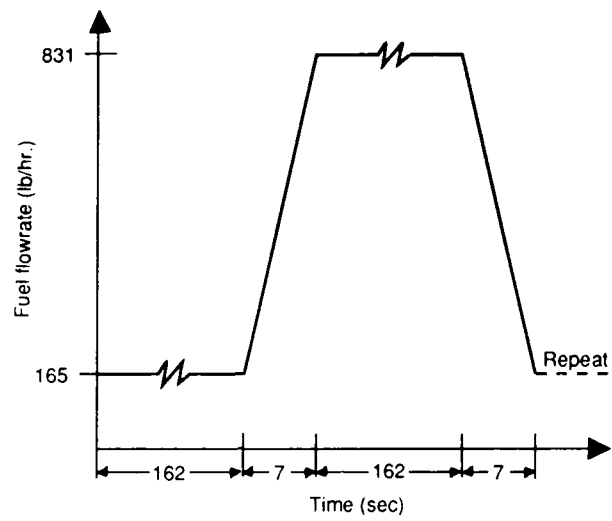


Figure 73. Single-cycle illustration for throttle excursions of cyclic tests 1 to 3.

transient performance mapping, and finally, cyclic durability testing. Unfortunately, due to a failure of one axial swirler during the 68th cycle of the 3000°F cyclic testing of BU5, which was unrelated to the structural design of the CMC wall, damage was incurred that forced completion of the test program. A detailed presentation of the test results and analysis of the five builds is provided in the following sections of the report.

#### 6.2.4.1 BU1

For the initial testing of BU1, thermal paint was applied to the liner and OTL. BU1 testing was not intended to be a dedicated thermal paint run and wall temperature data were expected to be of marginal quality as our initial tests would accumulate 5-6 hours before teardown. Normal thermal paint runs require a rig teardown after a 5-10 minute steady-state run at design point operation. The data generated would be most useful for finding the hottest wall locations, where hot spots blacken the paint in locations exceeding 1600°F.

The swirlers were installed in the liner and a build-up initiated to check fuel nozzle immersion depth. Immersion/recession depth measurement results are given in Table XII. Immersion depth was found to be -0.06 in. (distance between nozzle and swirler face) on the average, which could potentially affect pattern factor and limit our overall BOT, based on previous combustor experience. Options to resolve this situation either by testing "as-is" or through mods to fix immersion depth were investigated. The problem was resolved by picking the best combination of 24 available nozzles and 12 swirlers. After the completion of steady-state burn time and the first teardown, a decision to rework hardware was considered based on performance results. Rework was never required.

Subsequent to immersion depth measurements, the combustor liner and OTL were installed and the rig assembled. Fuel flow calibrations, final instrumentation hook-up, electrical troubleshooting, and initial cold flow testing were then completed.

A complete summary of steady-state performance data for all builds is given in Table XIII and will be referred to throughout the discussion of performance results. Likewise, all cold and hot flow combustor pressure drop data are summarized in Figure 74 and will be referred to during discussion of results for BU1 through BU5.

---

Table XII.  
Fuel nozzle location\* and immersion depths.

<u>Position</u>	<u>Immersion depth--in.</u>
1	-0.071
2	-0.069
3	-0.080
4	-0.074
5	-0.061
6	-0.064
7	-0.063
8	-0.034
9	-0.052
10	-0.045
11	-0.048
12	-0.057

- \* Fuel nozzle location, starting at position 1, is referenced to a view of the combustor standing aft looking forward to the rig inlet and starting at TDC and counting clockwise.

Table XIII.  
Summary of Army/NASA CMC combustor steady-state performance.

BUILD NUMBER	BU1	BU1	BU1	BU1	BU2	BU3	BU3	BU3	BU3	BU3	BU3	BU4	BU4	BU5	BU5
TEST CONDITION	4	11	12	12	14	12	12	14	15	15	15	13	13	15	15
YEAR OF TEST	1989	1989	1989	1989	1992	1992	1992	1992	1992	1992	1992	1992	1992	1992	1992
RECORD #	271	294	76	88	34, 8/27	67, 9/25	80, 9/25	93, 9/25	106, 9/25	119, 9/25	58, 9/29	362, 9/29	36, 10/2	207, 10/2	
BIP (PSIA)	63.1	185.2	237.8	240.4	246.6	243.4	241	250.6	250	252.3	255	253.2	252.9	248.4	
BIT (F)	402.8	715.2	842.3	814.5	914.2	805.3	824.6	892.1	866	900.9	876.2	876.7	891.2	905.1	
WA (LB/SEC)	2.31	5.68	7.46	7.28	7.26	7.49	7.61	7.27	7.67	7.27	7.39	7.15	7.31	7.11	
DELTA PP (%)	5.14	4.84	5.16	4.67	4.22	4.49	4.93	4.33	4.78	4.39	4.16	4.02	5.11	3.98	
BOT (F)	1372	2208	2379	2458	2807	2366	2222	2780	2874	3017	2649	2691	3023	3105	
F/A	0.0151	0.0239	0.0266	0.0278	0.0325	0.026	0.0255	0.0327	0.0346	0.0369	0.03	0.0307	0.0344	0.0377	
PATTERN FACTOR	0.228	0.189	0.153	0.15	0.217	0.15	0.144	0.13	0.148	0.156	0.197	0.226	0.265	0.247	
CHEM. EFFICIENCY (%)	98.81	99.94	99.82	99.85	99.86	99.89	99.91	99.85	99.84	99.82	99.86	99.86	99.84	99.85	
NOR (EI)	3.1	13.05	23.02	25	27	17.65	16.59	29.23	31.81	36.09	27.21	28.63	32.79	29.95	
CO (EI)	34.8	0	0	0	0.41	0.21	0.17	0.27	0.31	0.35	0.29	0.26	0.39	0.44	
UHC (EI)	3.7	0.038	0.74	0.331	0.037	0.261	0.131	0.053	0.039	0.04	0.093	0.064	0.039	0.064	
SMOKE (SAR)	1.3	0.7	3.9	5.3	0.7	0	0	0	1.3	1.3	0	0	0	0	
WALL T/C'S (F):															
1 OUTER BARREL, BOT., METAL COLD SIDE	610	908	1011	999	1158	984	981	1099	1081	1132	1077	1079	1136	1156	
2 OUTER BARREL, BOT., CERAMIC/BRUNS INTER.	660	986	1083	1070	1258	1072	1069	1195	1175	1232	1176	1180	1224	1281	
3 OUTER BARREL, BOT., METAL/BRUNS INTER.	572	847	949	931	1065	929	928	1031	1014	1054	1015	1017	1059	1083	
4 DOME, BOT. COLD SIDE	799	1253	1388	1361	1666	0	0	0	0	0	0	0	0	0	
5 OUTER BARREL, TOP, METAL COLD SIDE	581	865	1023	1019	1116	980	970	1089	1083	1116	1060	1070	1112	1135	
6 OUTER BARREL, TOP, CERAMIC/BRUN INTER.	668	982	1183	1186	1264	1118	1100	1251	1262	1295	1220	1245	1317	1340	
7 OUTER BARREL, TOP, METAL/BRUNS INTER.	581	848	987	972	1075	0	0	0	0	0	0	0	0	0	
8 DOME, TOP, COLD SIDE	762	1063	1278	1335	1601	1373	1354	1557	1558	1642	1533	1296	1419	1343	
9 INNER BARREL, TOP, METAL COLD SIDE	714	1012	1004	978	1295	1348	1346	1482	1480	1558	1431	1412	1478	1560	
10 INNER BARREL, TOP, CERAMIC/BRUNS INTER.	878	1232	1176	1152	1588	1711	1709	1891	1911	2034	1942	1919	2054	1117	
11 INNER BARREL, TOP, METAL/BRUNS INTER.	594	865	931	909	1095	1000	0	0	1119	1355	1272	1245	1307	1306	
12 INNER BARREL, BOT., METAL COLD SIDE	718	1036	1128	1121	1351	999	988	1153	1161	1217	1101	1108	1193	1238	
13 INNER BARREL, BOT., CERAMIC/BRUNS INTER.	0	0	0	0	1634	1712	1695	1886	1900	1960	1858	1849	1999	0	
14 INNER BARREL, BOT., METAL/BRUNS INTER.	634	895	988	973	1127	1128	1189	1327	1317	1361	1285	1248	1312	1275	
15 OTL, TOP, CERAMIC/BRUNS INTER.	795	1217	1408	1408	1772	1050	1044	1207	1214	1257	1163	1197	1306	1386	
16 OTL, TOP, METAL/BRUNS INTER.	713	1080	1210	1208	1593	1252	1244	1457	1481	1521	1383	1445	1612	1739	
17 OTL, TOP, METAL COLD SIDE	708	1072	1201	1196	1596	1061	1055	1215	1220	1261	1171	1200	1306	1381	
18 OTL, BOTTOM, CERAMIC/BRUNS INTER.	1007	1435	1384	1359	1776	1051	1033	1223	1239	1299	1165	1175	1270	1318	
19 OTL, BOTTOM, METAL/BRUNS INTER.	862	1221	1215	1194	1539	1149	1129	1377	1415	1496	1275	1295	1441	1501	
20 OTL, BOTTOM, METAL COLD SIDE	868	1231	1212	1192	1562	1423	1406	1529	1517	1552	1448	1407	1478	1517	

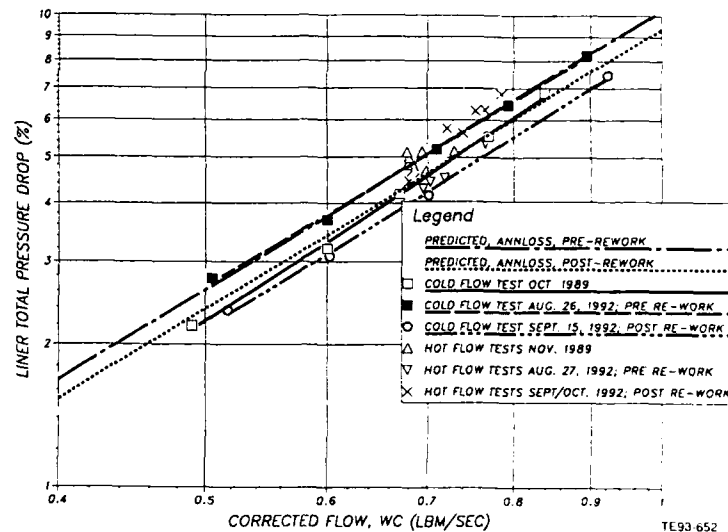


Figure 74. Army/NASA CMC combustor predicted and measured pressure drop versus corrected flow.

BU1 measured cold flow pressure drop was 4.5% at the design point corrected flow (0.696 lb/sec) compared to a predicted value of 5%, as shown in Figure 74. With good agreement from the cold flow tests, combustion tests were initiated. Photographs of the liner and OTL showing the after-test condition and thermal paint results are given in Figures 75, 76, and 77. As shown, no damage was sustained to the combustor hardware, and ceramic tiles were in place with no spalling or delamination noted. The only noticeable change, other than discoloration, from the new ceramic condition were small hairline cracks on the OTL innermost two rows of tiles. Although a dedicated thermal paint test was not part of the test plan, the liner was painted to help locate areas of extreme temperature. No hot spots were found on the CMC wall portions of the liner with the exception of a small, 0.75 in. diameter spot located on the OTL. The paint did indicate some areas  $>1600^{\circ}\text{F}$  occurring on the effusion cooled dome. Steady-state operating performance was measured at idle through maximum continuous power conditions (points 4, 11, and 12 in Table VIII) and the test results are provided in Table XIII. As shown in Table XIII, efficiency and smoke performance was excellent. Chemical combustion efficiency at the MCP condition was measured as 99.9% and hot pressure drop was 4.68%. Emissions at this point, compared to similar engine requirements for maximum power operation, were below the requirements with the exception of unburned hydrocarbons (UHC), 0.3 EI versus the  $<0.1$  goal. Smoke was an extremely low SAE 5.3.

Pattern factor and radial profile results compared favorably with results from similar combustion systems. Pattern factor as a function of burner temperature rise is given in Figure 78 while radial profile measurements are given in Figure 79. The circumferential BOT trace is provided for the idle condition (test point 4) in Figure 80 and for the MCP condition (test point 12) in Figure 81.

The outlet temperature distribution is observed to be relatively flat over the range of conditions tested in BU1 providing the low values of pattern factor (0.186 to 0.150) calculated. In addition, the radial profiles are also consistent across the range of operation with a peak around 50% span.

Results of thermocouple wall temperature measurements and their comparison with predicted results are presented in Table XIV. Table XIII provides absolute values for all 20 wall thermocouples. No measured wall temperatures at the critical ceramic/compliant layer interface exceeded the  $1750^{\circ}\text{F}$ .



Figure 75. CMC combustor after 1989 BU1 thermal paint test.

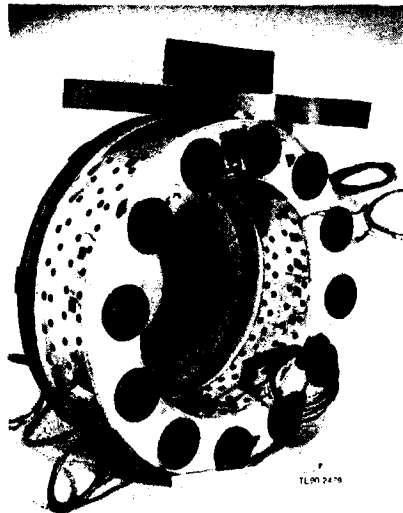


Figure 76. CMC combustor after 1989 BU1 thermal paint test, view of dome.

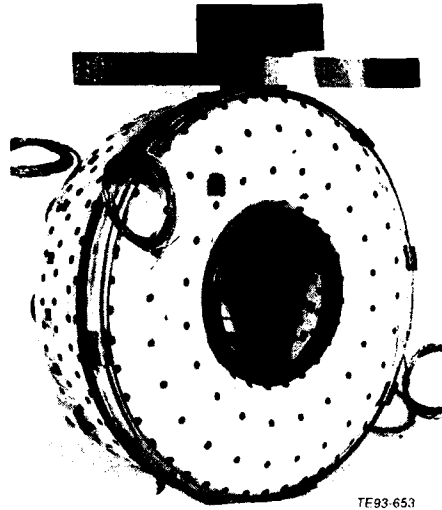


Figure 77. CMC combustor after 1989 BU1 thermal paint test—view of OTL.

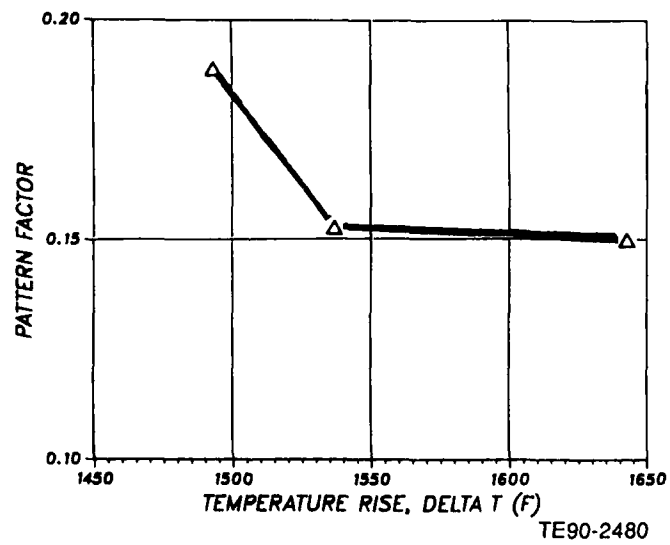


Figure 78. Measured pattern factor as a function of temperature rise—BU1.



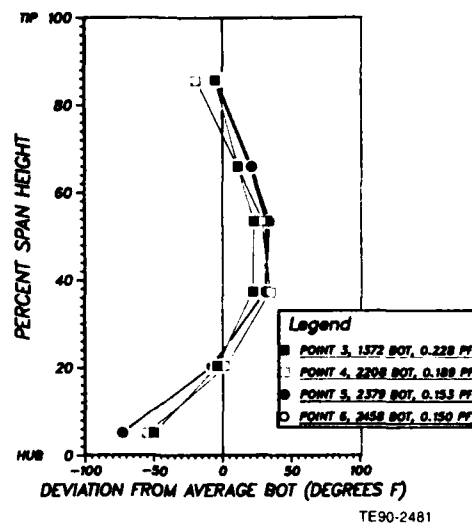


Figure 79. Measured radial profile—BU1.

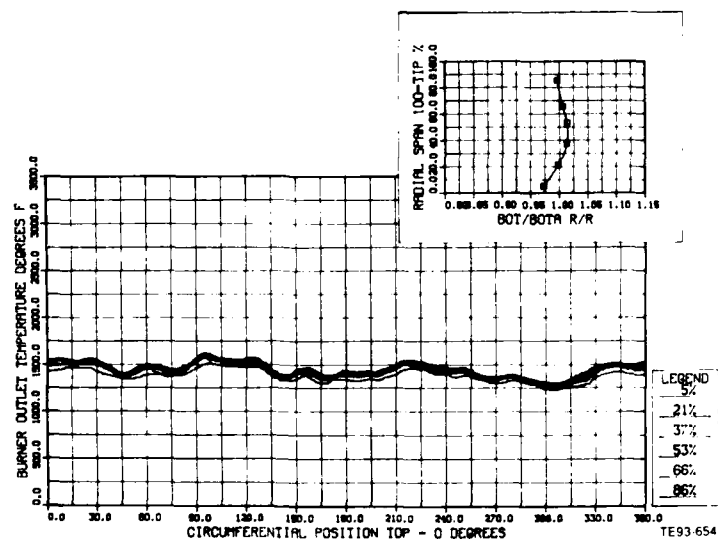


Figure 80. CMC combustor—BU1 idle point circumferential temperature trace.

Table XIV.  
Comparison between measured and predicted wall temperature levels (°F), MCP operating condition.

	<u>Ceramic</u>	<u>Ceramic/ Bruns- bond</u>	<u>Bruns- bond/ metal</u>	<u>Metal</u>
<u>Inner wall temperatures</u>				
Average				
Predicted	1763	1210	1009	1006
Measured	N/A	1152	941	1050
Minimum				
Predicted	1266	1056	933	930
Measured	N/A	1152	909	978
Maximum				
Predicted	2239	1399	1118	1113
Measured	N/A	1152	973	1121
<u>Outer wall temperatures</u>				
Average				
Predicted	1671	1165	983	980
Measured	N/A	1128	952	1009
Minimum				
Predicted	1324	1040	893	890
Measured	N/A	1070	931	999
Maximum				
Predicted	2154	1339	1076	1070
Measured	N/A	1186	972	1019
<u>Outer transition liner (ITL) temperatures</u>				
Average				
Measured	N/A	1384	1201	1194
Minimum				
Measured	N/A	1359	1194	1192
Maximum				
Measured	N/A	1408	1208	1196

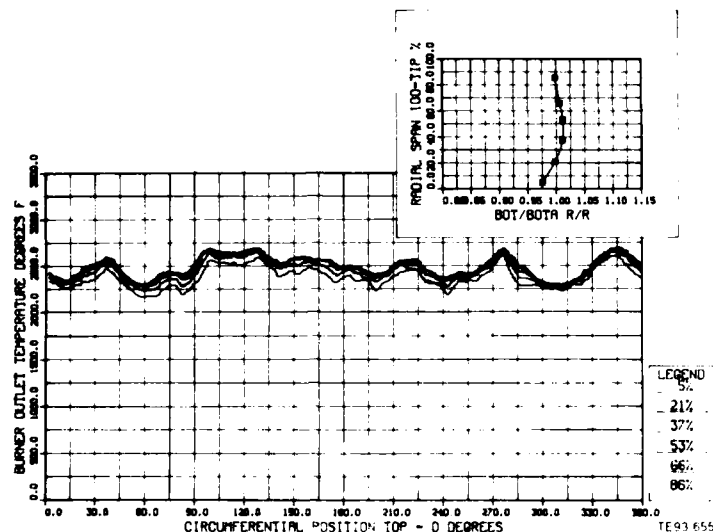


Figure 81. CMC combustor—BU1 MCP point circumferential temperature trace.

design limit. The maximum recorded wall temperature of 1408°F occurred at the ceramic/compliant layer interface on the outer transition liner (OTL). The maximum recorded temperature of 1360°F on the liner barrel occurred on the effusion-cooled dome. For the CMC wall inner and outer liner, the maximum temperature was 1186°F on the outer liner and 1152°F on the inner liner, both at the ceramic/compliant layer interface. Measured wall temperatures indicated the OTL runs approximately 200°F hotter than the liner and, as noted earlier, the hottest indicated wall temperature occurred on the OTL. Hence, it was suspected the OTL cooling flow was restricted to some extent and was most likely related to the hydroform process and EDMed cooling holes, both processes unique to the OTL. As described later, verification was obtained through cold flow analysis of the OTL. Due to the difficulty of analyzing the OTL geometry, predicted 3-D heat transfer results for the inner and outer liners only are compared to measured wall temperature data.

Excellent agreement between predicted and measured temperature is evident from Table XIV. The results of the wall temperature predictions were generated using the COM3D aerothermal analysis code and the 3-D heat transfer analysis. A similar analysis, presented as a color contour plot in Figure 49, was carried out during the design phase of the program for the 3000°F BOT design point condition. To illustrate the results from the 3-D wall temperature predictions for the 2458°F test condition, predicted results are presented as temperature contours for the "unwrapped" outer and inner liners. Figures 82 and 83 presents the ceramic surface predicted wall contours, contours at the ceramic/compliant layer interface, and compliant layer/substrate interface for the outer and inner walls, respectively. The absence of large axial gradients is noted for all three layers.

For the purpose of comparing measured data to predicted, the predicted data were reduced to obtain maximum, minimum, and average values which are presented in Table XIV. Results for the substrate surface were not plotted as they were nearly identical to the results for the compliant layer/substrate location, indicating essentially zero temperature gradient across the substrate layer, which was verified by the measured results. Since good agreement between predicted and measured wall temperatures were obtained for the 2458°F BOT condition, it was felt predictions for the 3000°F BOT condition would be acceptably accurate for the inner and outer liner. However, since the measured OTL wall

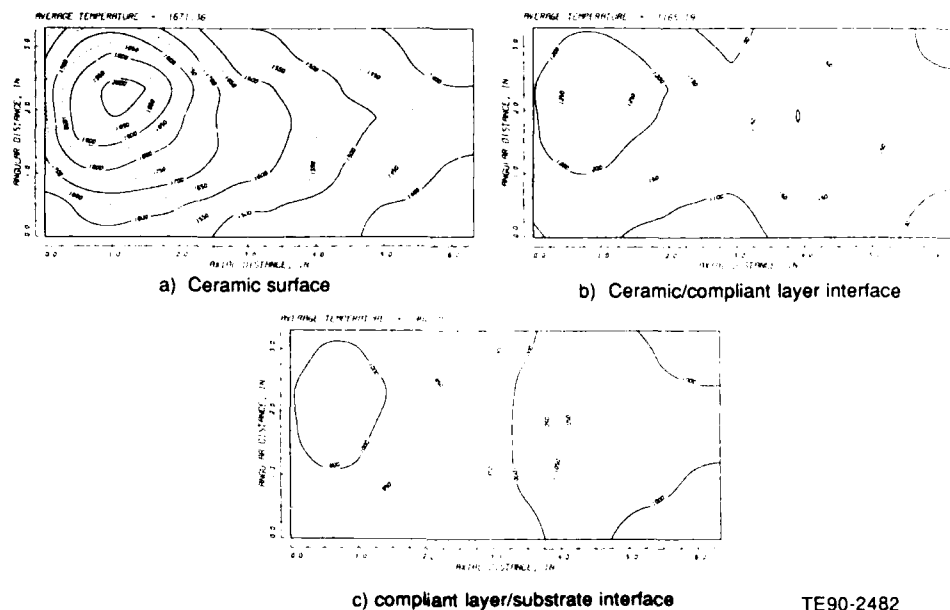


Figure 82. Predicted wall temperature contours for CMC 2458°F BOT test point—outer wall.

temperatures ran higher than the liner, it was decided component cold flow analysis of the OTL would be appropriate to quantify the coolant flow area.

Coordination with the Allison Research Lab resulted in fabrication of a fixture to cold flow the outer transition liner (OTL). Subsequently, the flow-pressure drop relation was determined. A curve of predicted flow versus pressure drop was generated for the OTL using the CMC wall flow model (CMFLO3, used in the combustor design) and compared with the measured data. Figure 84 provides a comparison of the predicted and measured OTL pressure drop-flow relationship. The results indicate severe blockage in the OTL cooling air circuit. The measured ACd (i.e., effective flow area,  $0.047 \text{ in.}^2$ ) was 65% less than the design value ( $0.130 \text{ in.}^2$ ) at the design point corrected flow. These results provide an explanation for the high wall temperatures (relative to the inner and outer walls of the liner) measured on the OTL during the BU1 combustion tests. It is expected the blockage is a direct result of the manufacturing processes used in the fabrication of the OTL. To predict the wall temperatures the OTL will experience at the 3000°F maximum operating condition, BU1 measured wall temperatures were correlated with the known coolant flux using the 1-D heat transfer model and then predictions were made for the conditions of the 3000°F tests.

The purpose of this analysis was to predict the wall temperatures for the upcoming 3000°F BOT combustor tests, and if necessary, determine the requirements for making modifications to the OTL to bring wall temperatures down to acceptable levels. The Allison Research Lab cold flow measurements indicated that OTL flow blockage amounts to a 65% reduction in coolant flux relative to the design value. Since wall temperature measurements were previously obtained at BOTs up to 2458°F, it was possible to compare the heat transfer model with measured data. With acceptable agreement, the model was then used to predict the wall temperature levels for the maximum power condition and 3000°F BOT. Results from the analysis are given in Table XV.

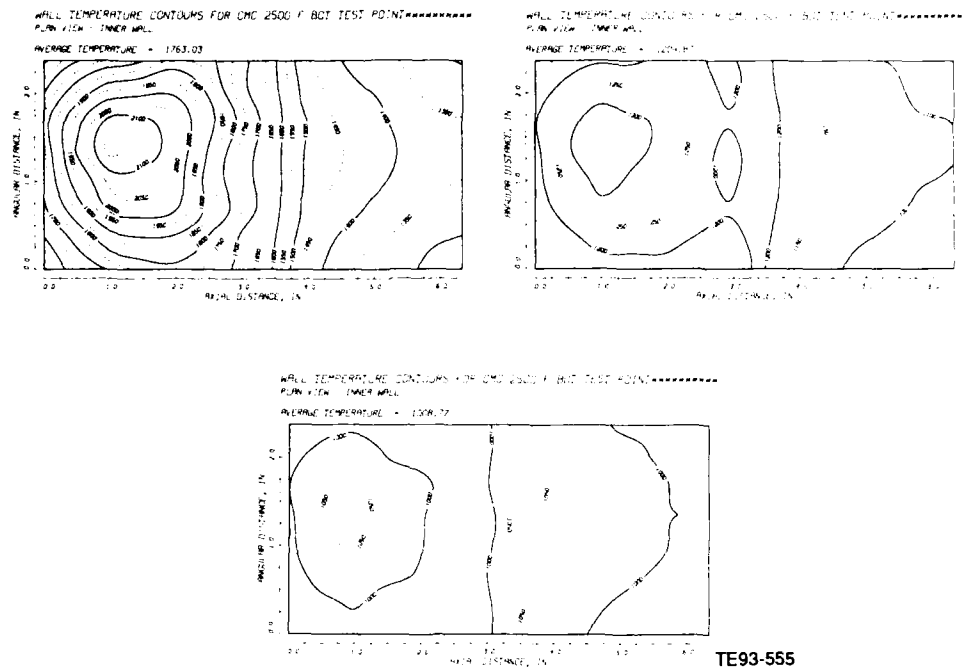


Figure 83. Predicted wall temperature contours for CMC 2458°F BOT test point—inner wall.

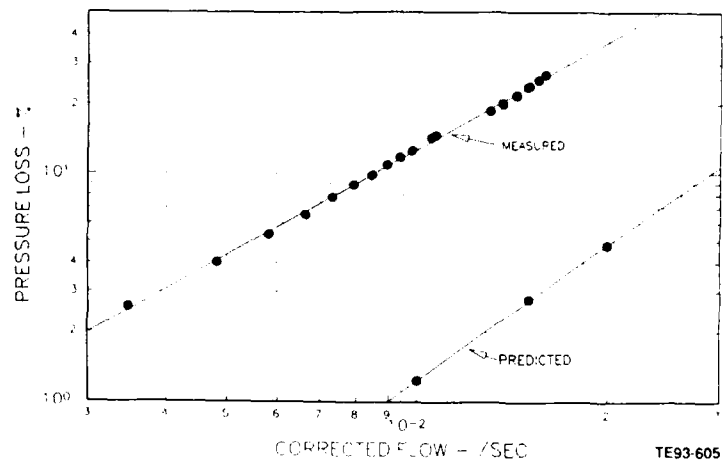


Figure 84. CMC OTL—pressure loss versus corrected flow.

Table XV.  
Results of 1-D heat transfer analysis of outer transition liner.

	2458°F BOT		3000°F BOT
	Average measured	Predicted	predicted
Substrate (metal) surface	1194°F	1276°F	1521°F
Metal/compliant pad interface	1201°F	1278°F	1525°F
Compliant pad/ceramic interface	1384°F	1356°F	1619°F
Ceramic surface	--	1630°F	2045°F

Results of the analysis indicated the critical compliant pad/ceramic temperature will approach 1620°F, well below the 1750 to 1800°F thermal oxidation limit. The O.D. metal temperature was predicted to be 1521°F, near the maximum acceptable temperature level normally allowed for nickel-base alloy materials such as Hast-X.

Since BU2 was a dedicated thermal paint test at the intermediate condition of 2800°F BOT, it was decided to assess results from the BU2 test before making a final decision to rework the OTL to increase coolant flux.

#### 6.2.4.2 BU2

BU2 was a dedicated thermal paint test at 2800°F BOT. This test provided wall temperature data with poor resolution of isotherms due to the unexpected length of the time required to reach the operating condition (point TP1, Table VIII). However, the thermal paint revealed and verified hot spots on the dome and OTL as well as the necessity to adjust local coolant flux. Rework of the liner dome and OTL was carried out following BU2 by adding laser drilled effusion cooling holes (600 total at 50 holes per nozzle) to the dome and several additional coolant orifices (through the substrate only) on the OTL.

In preparation for the BU2 thermal paint test, the CMC fuel nozzles were bench tested to evaluate spray quality and flow rate. Review of the results showed many of the nozzles to have marginal spray quality and flow. This was attributed to possible minor blockage from carboning in the internal passages from previous tests. The nozzles were returned to the vendor for overhaul. Although 12 nozzles were needed for the test, 14 were overhauled to include spares and were received from the vendor and subsequently tested again on the Allison fuel nozzle bench test facility.

Test results indicated significant improvement in performance relative to flow rate, patternation, and visual spray quality. However, a few nozzles still exhibited patternation results outside the 30% maximum limit. Based on previous experience with these nozzles prior to their overhaul and recognizing that the nozzle's condition must be improved relative to their condition during the series of tests carried out in 1989, it was decided to use the nozzles as-is. Preparation for the 2800°F BOT thermal paint test was then initiated.

Results of the fuel nozzle patternation tests were used to specify fuel nozzle locations within the rig and combustor. This was done with the goal of minimizing variation in fuel flow distribution. A mock rig build followed and measurements of immersion/recession depth were taken. Table XVI provides results. Recession of the nozzles averaged out 0.024 in. deeper (inside the swirler) than during the last test in 1989. Spray trajectory calculations indicated the spray would not hit the edge of the swirler, so it was decided to run the test in the as-is condition. The difference in recession depth was attributed to slight changes in rig/combustor dimensions during the initial hot tests in 1989 and/or measurement technique and error. Figure 85 shows the installed combustor before final rig assembly.

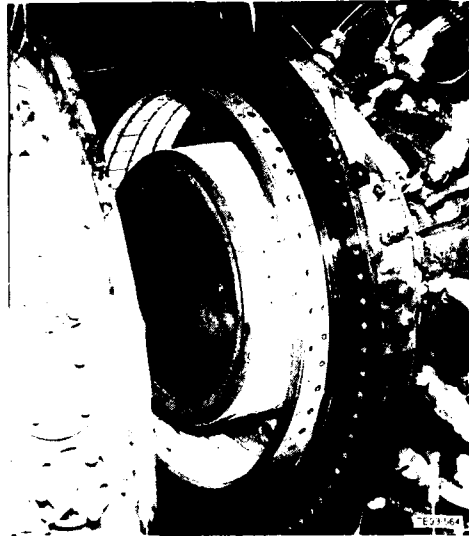


Figure 85. Installed CMC combustor pretest for 1992 series (BU2) testing.

Subsequently, cold flow pressure drop testing and the 2800°F BOT thermal paint test were completed. Overall the test went smoothly; however, the test data indicated a high pattern factor relative to the 1989 test due to a hot streak in the exhaust gas near the hub as well as high wall temperatures on the OTL and dome. However, on the inside and outside liner walls, no hot spots were observed and wall thermocouples indicated outside (cold side) metal temperatures in the 1100 to 1350°F range. Figure 86 provides the circumferential BOT data for the eight BOT thermocouples. Figure 87 shows the radial temperature distribution. Cold flow data compared to 1989 test results are provided in Figure 74. Table XIII summarizes other performance parameters of interest.

Table XVI.  
Fuel nozzle location and immersion depth, BU2.

<u>Position</u>	<u>Immersion depth--in.</u>
1	-0.067
2	-0.047
3	-0.102
4	-0.101
5	-0.092
6	-0.101
7	-0.085
8	-0.088
9	-0.059
10	-0.074
11	-0.065
12	-0.072

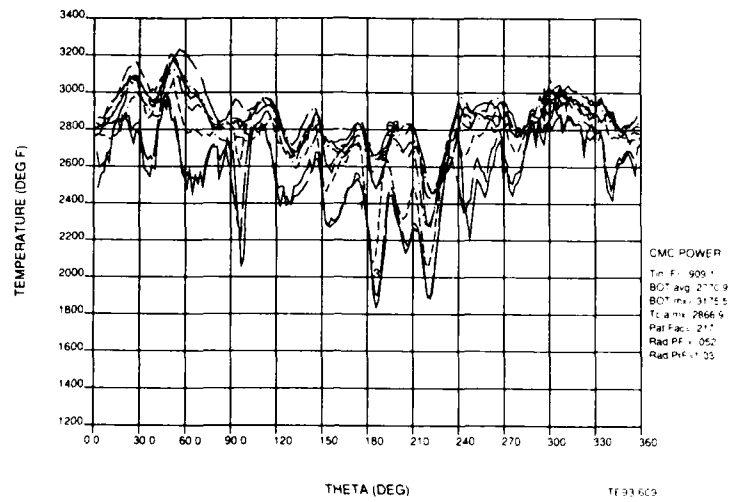


Figure 86. 2800°F BOT thermal paint test (BU2, 8/27/92)—circumferential BOT trace.

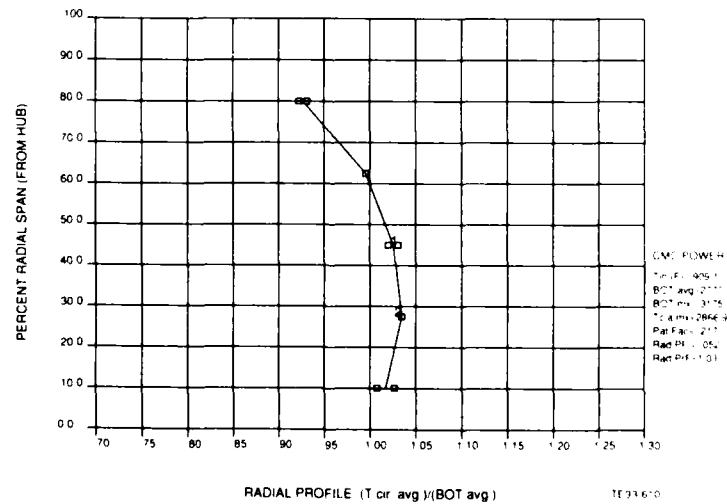


Figure 87. 2800°F BOT thermal paint test (BU2, 8/27/92)—radial temperature profile.



Photos of the liner and OTL are shown in Figures 88 and 89 for the liner/dome and Figures 90 and 91 for the OTL.

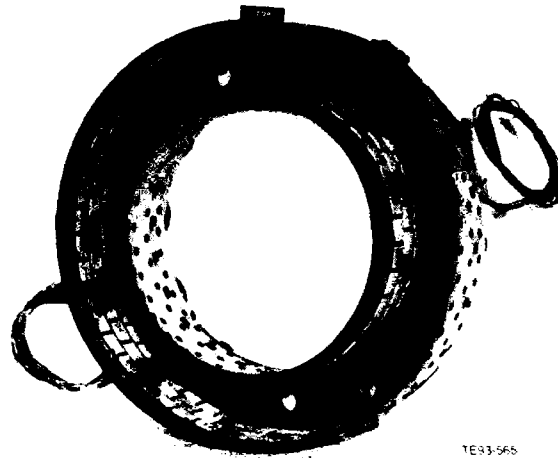


Figure 88. CMC combustor after 8/27/92, 2800°F BOT thermal paint test—liner.

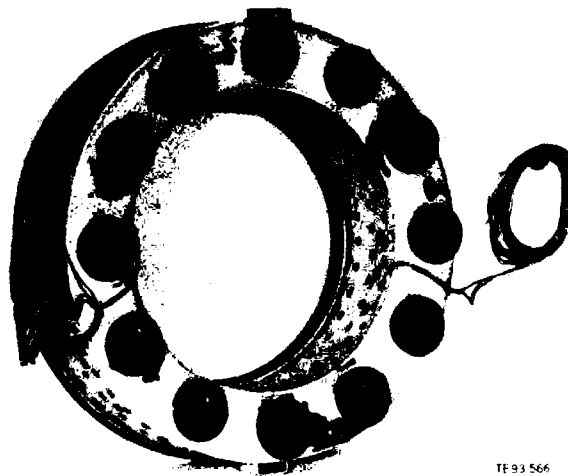


Figure 89. CMC combustor after 8/27/92, 2800°F BOT thermal paint test—liner.

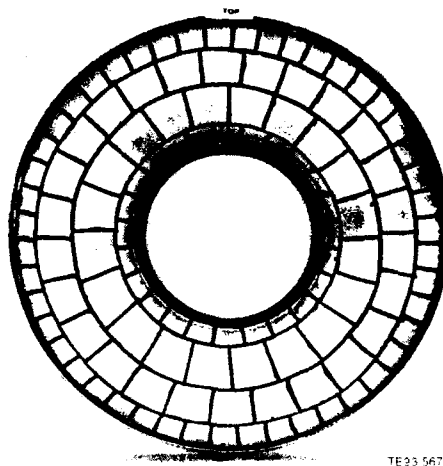


Figure 90. CMC combustor after 8/27/92, 2800°F BOT thermal paint test—outer transition liner (OTL).

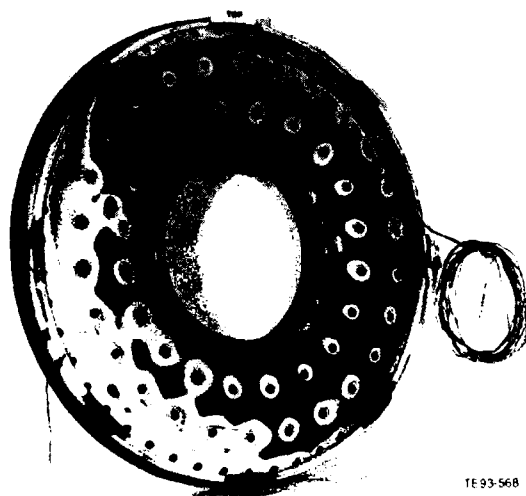


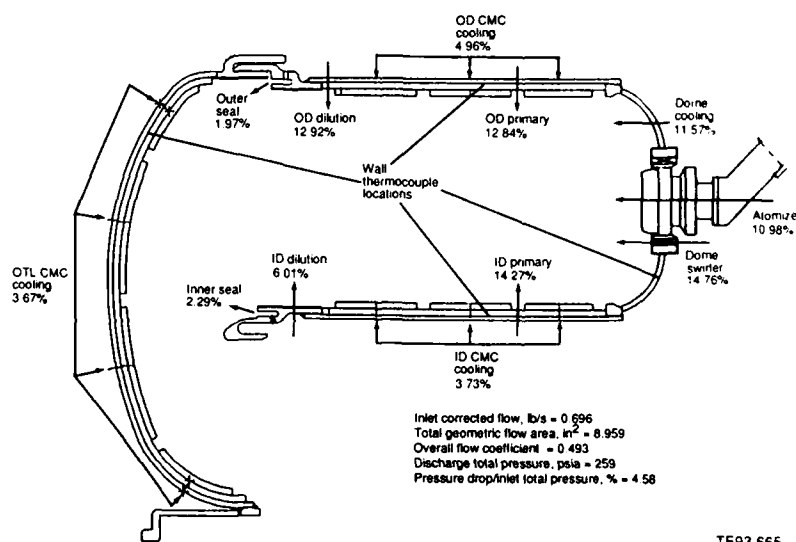
Figure 91. CMC combustor after 8/27/92, 2800°F BOT thermal paint test—outer transition liner (OTL).

As indicated by the data in Table XIII, pattern factor was measured as 0.218 compared to the 0.150 value obtained during the 1989 test. Combustion efficiency, pressure drop, and emissions were acceptable and in-line with previous measurements. The main concern with BU2 test results were the dome and OTL wall temperature measurements and the streaky condition of the circumferential BOT trace (Figure 86).

Exhaustive investigation of the cause of the hot streak and cold spikes, as indicated by the circumferential temperature traces, did not yield a conclusive cause.

An air leak at the inner liner-rig seal interface seemed possible. Dimensional checks after the rig was disassembled indicated, in the cold state, a potential hot condition increase in area of 1.68% over the predicted liner ACD. Pressure drop data for the hot test indicated a possible area increase of 5.1%, relative to the cold flow effective area. It was not possible to correlate fuel nozzle performance or recession depth to the streak locations. The best conclusion, based on review of the data, was that an air leak occurred near the inner liner-rig seal interface and was possibly related to improper rig assembly. In addition, to rule out effects from the air-cooled BOT thermocouple probes, BU3 test plans were modified to include combustor operation at the 1989 steady-state, 2450°F BOT condition, with and without thermocouple probe cooling air active. This would help rule out or enhance the plausibility of the theory. Besides rework of the OTL and dome to increase local coolant flux, no other rig/combustor modifications were specified prior to initiating the testing of BU3.

Figure 92 provides the overall CMC combustor airflow distribution following rework as predicted by ANNLOSS. Comparison with Figure 30, airflow distribution before rework, shows cooling flow for the dome and OTL was increased by more than 2% each and the total effective area of the liner (=overall flow coefficient X total liner geometric area) has been increased by nearly 0.1 in<sup>2</sup>.



TE93-665

Figure 92. CMC combustor predicted airflow distribution at design point—after rework.

#### 6.2.4.3. BU3

After rework of the combustor dome and OTL to increase local coolant flux, a modified test plan was implemented for BU3 that included additional steady-state performance conditions as well as the previously planned lean blowout, ignition, and 3000°F BOT performance points. The new steady-state points were repeats of the 1989 MCP power point, with and without cooling air to the rotating BOT probes. This test would verify consistency with the excellent performance results obtained during BU1 testing. The performance demonstrated in the 1989 tests was repeated at similar conditions of 2400°F BOT as well as BOTs beyond 3000°F. In addition, LBO and ignition data comparable to previous, similar combustor experience was demonstrated.

Modifications to the liner and OTL, identified from the BU2 2800°F BOT performance test carried out in August 1992, were specified and completed. Following the 2800°F BOT test, thermal paint results indicated adjustment to the coolant flux on the effusion-cooled dome and CMC-cooled OTL were required. Heat transfer and flow analyses were carried out to help define the increased cooling flows. For the OTL, the difficulty of dry machining the substrate, without smearing or blocking the underlying Brunsbond pad, led to the decision to overcompensate the design by adding a large number of additional cooling holes. For the effusion-cooled dome, approximately 50 holes per nozzle, adequate to cover the overtemperated area defined by the thermal paint, were laser drilled. Other effort carried out in preparation for the tests included atmospheric bench test of the 12 fuel nozzles. Test results showed essentially no change in nozzle performance relative to the bench test results carried out before the initiation of burner testing in BU2.

Cold flow pressure drop was carried out after rebuilding the rig and results were presented in Figure 74. At the design point corrected flow of 0.696 lb/sec, the measured liner pressure drop (post rework) was 4.2% versus the predicted value of 4.5%. With acceptable agreement, LBO and ignition tests were initiated.

Results of the LBO test are presented in Figure 93, and ignition test results are provided in Figure 94. For the LBO tests, a comparison is made to measured data for the combustion system from which the CMC combustor was derived. CMC combustor LBO results correlated well with the corrected reference velocity parameter,  $Vr_{88}$ . However, the data lie slightly above the stability curve for the combustion system from which the CMC combustor was derived. LBO results are still considered acceptable, ranging from 0.004 to 0.007 fuel/air ratio over the operating conditions of interest. LBO test points were previously described in Table VIII.

Ignition data presented in Figure 94, also correlated well with corrected reference velocity and is observed to closely parallel previous experience. Recorded ignition was slightly higher than expected, ranging from 0.04 at low velocity to about 0.025 at the high corrected reference velocity.

Following mapping of LBO and ignition performance for the CMC combustor, additional steady-state performance tests were completed.

As reported, the BU2 2800°F BOT performance data showed a poor pattern factor and circumferential exit temperature data indicating an air leak. Therefore, our test plan was modified to include steady-state operating points that would repeat the 1989 test condition of approximately 2400°F BOT. In addition, this point was run back-to-back with and without thermocouple probe cooling air applied. Data from the test showed the air leakage was eliminated with the new build and that performance of the CMC combustor, with the probe cooling air off, repeated the data obtained in 1989. Steady-state performance tests were also carried out at temperatures up to and including the milestone 3000°F BOT. Pattern factor at this condition was 0.15 with acceptable radial profile. Following this test build, the burner rig was split and the combustor and OTL examined and photographed, as installed. The combustor was not removed from the rig to avoid the complicated, time consuming, and costly task of tearing

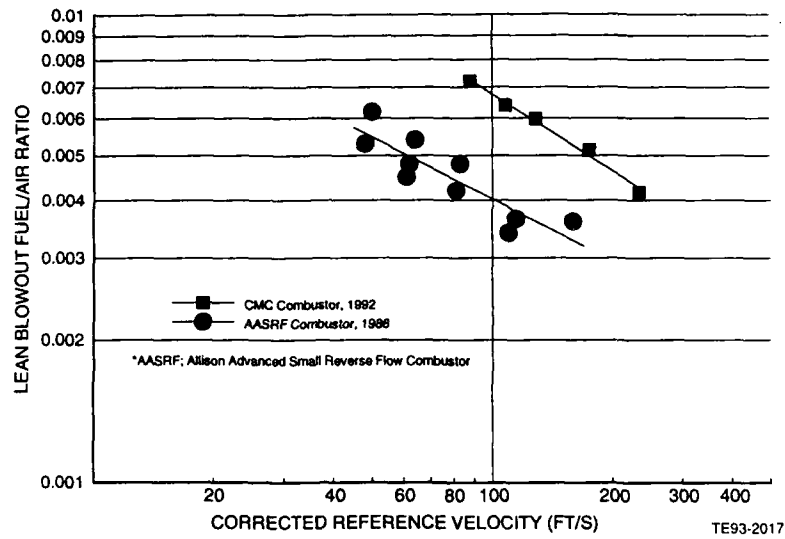


Figure 93. CMC combustor lean blowout characteristics.

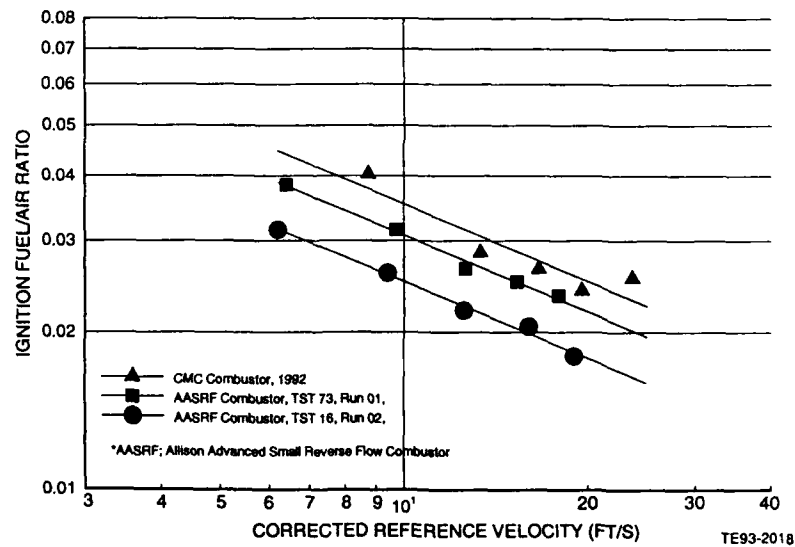


Figure 94. CMC combustor ignition characteristics.

down the exit thermocouple probes and other ancillary hardware and instrumentation. No damage or deterioration was noted in the hardware's condition, as shown in Figures 95 and 96.

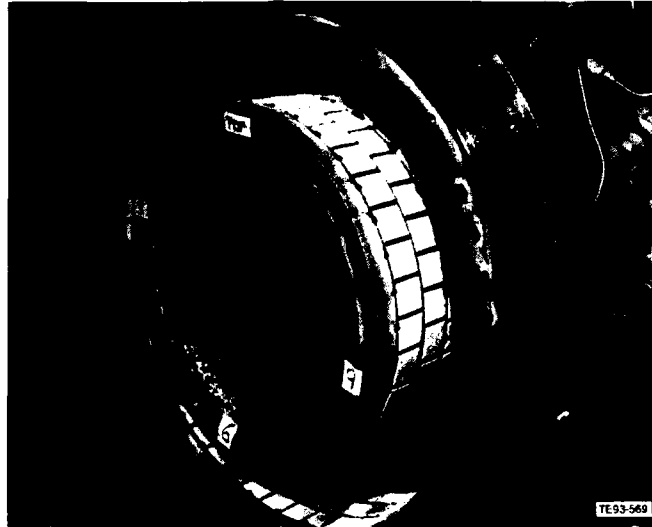


Figure 95. CMC combustor after 9/25/92 3000°F BOT steady-state performance test—liner.

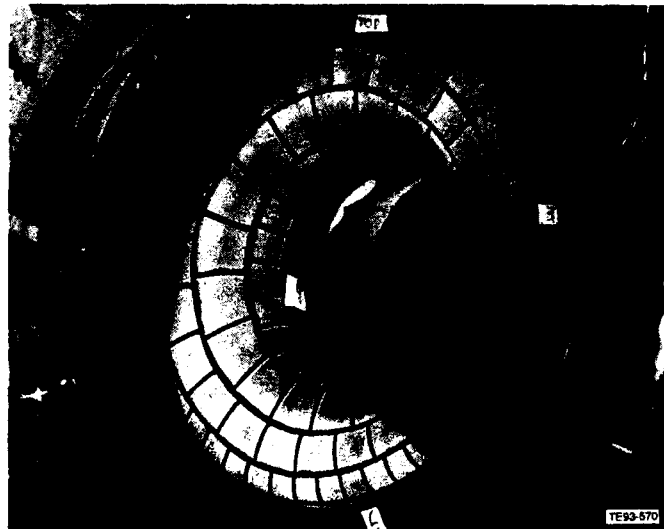


Figure 96. CMC combustor after 9/25/92 3000°F BOT steady-state performance test—OTL.

Steady-state performance results for BU3 were summarized in Table XIII for operating conditions 12, 14, and 15. Cold and hot flow liner pressure drop data were also presented in Figure 74.

For operating condition 12, the repeat MCP point, circumferential and radial BOT temperature plots are provided in Figures 97 and 98 (probe cooling air on) and Figures 99 and 100 (probe cooling air off). Examination of the data presented in these plots as well as Table XIII reveals a pattern factor of 0.150, which repeats the data of BU1. In addition, radial profile data also repeats the 1989 BU1 data, as illustrated in Figure 101. Based on these encouraging results, it was concluded the misleading BU2 temperature distributions were caused by an air leak related to rig assembly or performance problems. In addition to pattern factor and radial profile, pressure drop, combustion efficiency, emissions, and smoke results were acceptable and comparable to BU1 results. However, NO<sub>x</sub> was observed to significantly decrease relative to BU1 data (13 EI versus 23 EI for BU1) and CO was up slightly (0.3 EI versus BU1's 0 EI), and UHC decreased slightly. Part of the difference in measured emissions values at these low levels can be largely attributed to variation in the measured values due to normal uncertainty in emissions measurements.

Wall thermocouple measurements for thermocouples numbered 1 to 20 are presented in Table XIII. Wall thermocouple locations were identified in Table IX as well as Table XIII. By comparing test point 12 wall temperature results from BU3 to results from BU1, a number of conclusions can be made as follows:

- For all locations on the outer liner, close agreement was obtained between BU1 and BU3 measured temperatures.
- The dome (bottom) thermocouple and outer liner (top) thermocouple at the metal/Brunsbond interface both failed and remained inactive for all BU3 and subsequent testing.
- The dome (top) thermocouple agreed closely between BU1 and BU3 tests.
- For the inner liner, results were inconsistent; for the inner barrel (top), metal cold side, BU3 temperatures were hotter than BU1 results and for the bottom metal cold side, BU3 temperatures were cooler than BU1.

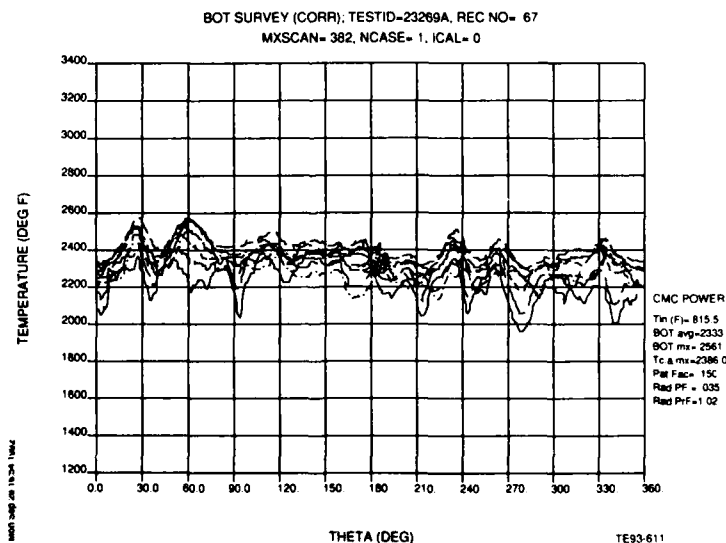


Figure 97. 2400°F BOT steady-state performance (9/25/92); circumferential temperature trace—T/C probe cooling air on.

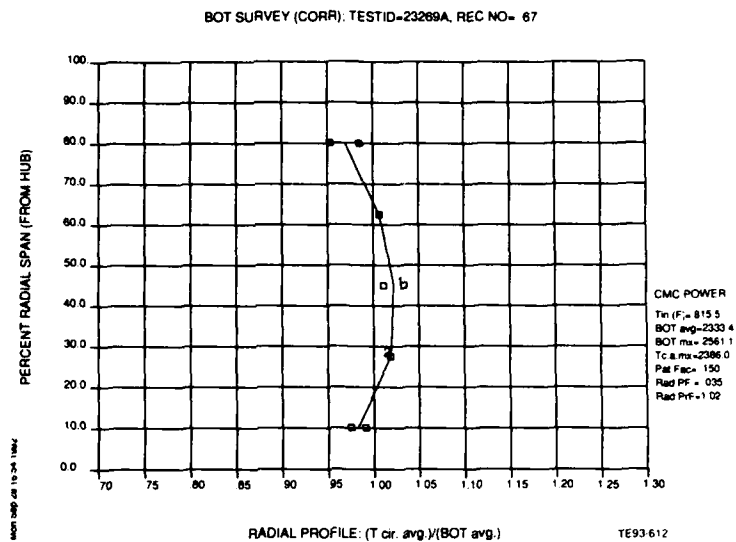


Figure 98. 2400°F BOT steady-state performance (9/25/92); radial temperature profile—T/C probe cooling air on.

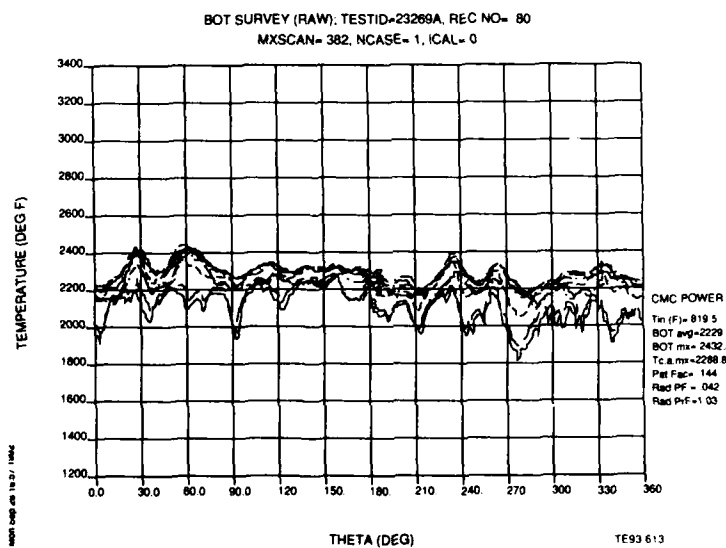


Figure 99. 2400°F BOT steady-state performance (9/25/92); circumferential temperature trace—T/C probe cooling air off.



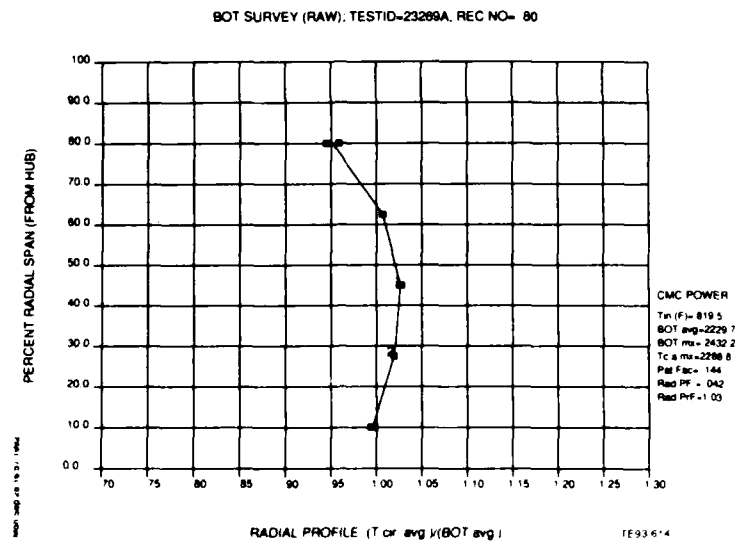


Figure 100. 2400°F BOT steady-state performance (9/25/92); radial temperature profile—T/C probe cooling air off.

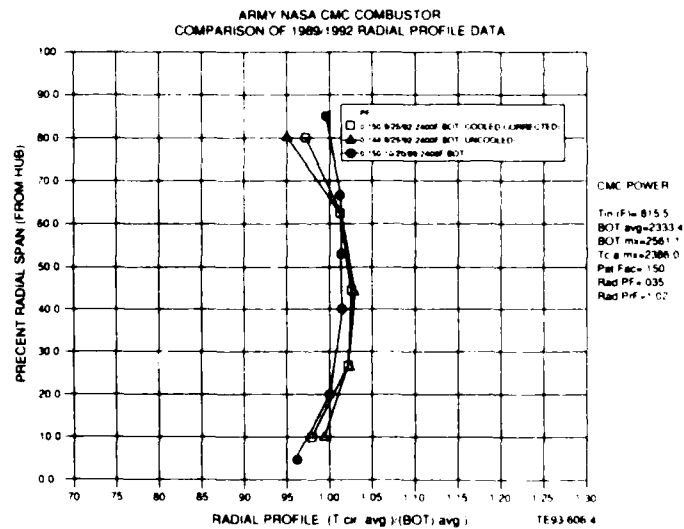


Figure 101. Comparison of 1989/1992 radial profile data.

- Both inner liner thermocouples at the ceramic/Brunsbond interface either became completely inactive or gave inaccurate readings, indicating failure.
- Overall results for the OTL indicated the effectiveness of the rework to increase coolant flux and reduce temperatures. With the exception of the OTL (bottom) metal cold side, all BU3 recorded thermocouples on the OTL were similar to or significantly less than the temperatures recorded during BU1 testing.

With the exception of failed thermocouples at locations 4, 7, 10, and 13, comparative and absolute results of test condition 12 wall thermocouple measurements were very favorable and continued to indicate the effectiveness of the CMC cooling scheme. Subsequently, BU3 explored steady-state performance of the CMC combustor in a stepwise fashion, initially repeating BU2 test point 14 (2800°F BOT) and then the milestone maximum power condition 15, first at 2900°F BOT and finally at 3000°F BOT.

Steady-state performance data are summarized for the high point BOT conditions in Table XIII and Figure 74. Circumferential and radial BOT traces for the 2800°F BOT point are provided in Figures 102 and 103, and for the 3000°F BOT condition in Figures 104 and 105. Review of the data indicates liner pressure drop falls directly on the predicted line for the post rework combustor. At the corrected flow of 0.680-0.695, the measured liner pressure drop was 4.7% to 5.0%. Pattern factor was calculated as 0.130 for the 2800°F BOT condition (compared to 0.218 for BU2) and at 3000°F BOT, pattern factor was 0.156. Radial profile was consistent with the acceptable results obtained during previous testing.

Comparison of test point 14 performance results (Table XIII) for BU3 and BU2 (pre- and post-rework) shows very similar results for all parameters with the exception of pattern factor, again indicating an abnormal rig condition during the BU2 test.

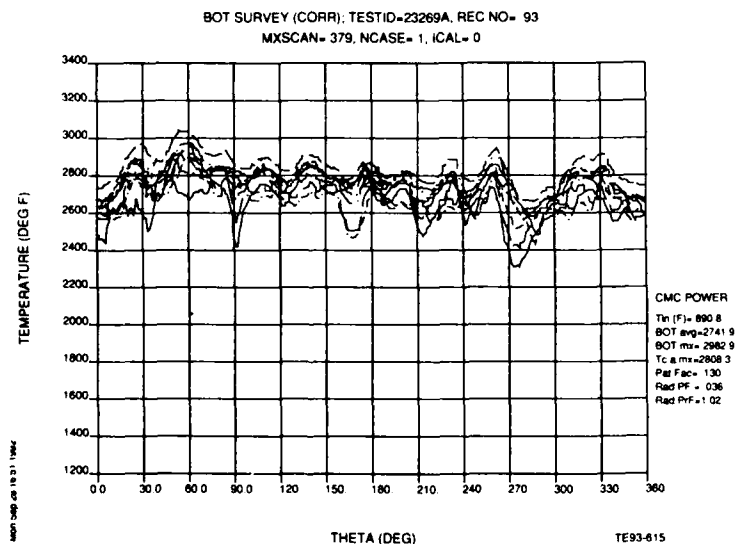


Figure 102. 2800°F BOT steady-state performance (9/25/92)—circumferential temperature trace.

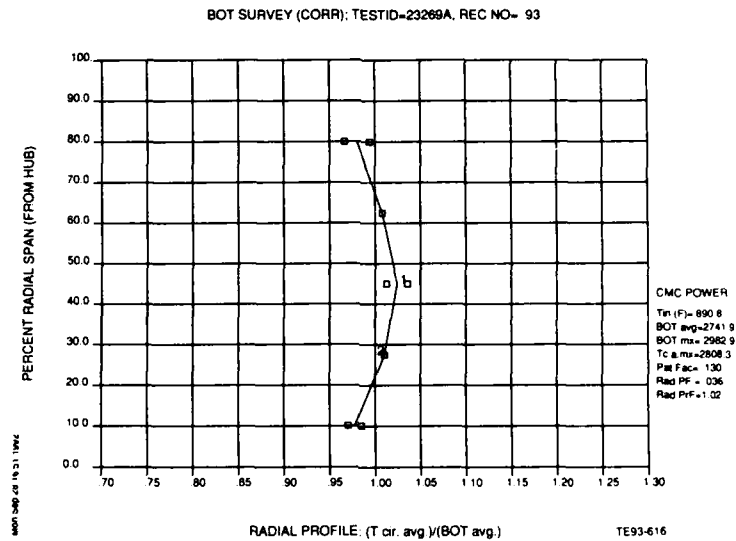


Figure 103. 2800°F BOT steady-state performance (9/25/92)—radial temperature profile.

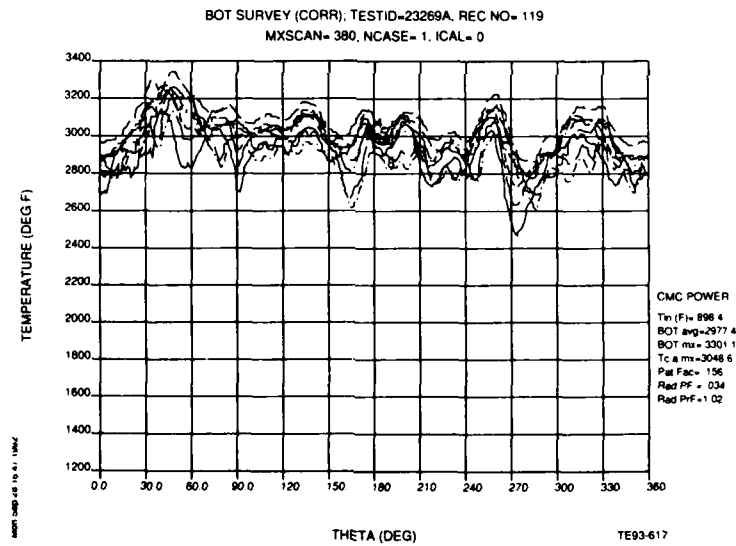


Figure 104. 3000°F BOT steady-state performance (9/25/92)—circumferential temperature trace.

BOT SURVEY (CORR): TESTID=23269A, REC NO= 119

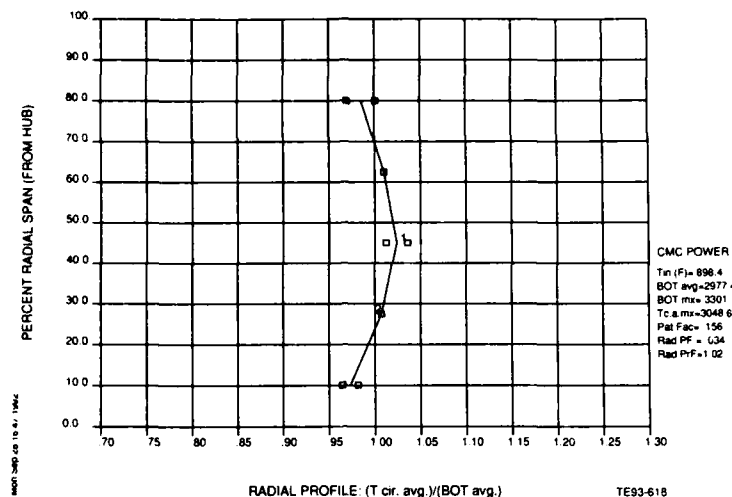


Figure 105. 3000°F BOT steady-state performance (9/25/92)—radial temperature profile.

The following conclusions can be reached by comparing test point 14 wall thermocouple measurements between BU2 and BU3:

- For the outer liner and dome, results are very comparable, within about 50°F.
- For the inner liner, results were somewhat inconsistent. On the inner liner (top) metal cold side, BU3's reading was over 180°F higher while for the inner liner (bottom) metal cold side, BU3's reading was nearly 200°F cooler. In addition, at the bottom, metal/Brunsbond interface location, BU3's wall temperature reading was 200°F higher than BU2's corresponding reading.
- On the OTL, across the board, BU3's (post rework) wall temperatures were considerably lower than BU2 temperatures. Once again, the benefits of increased coolant flux on the OTL was demonstrated.
- Overall, the critical ceramic/Brunsbond interface temperatures never exceeded the 1750°F design limit and wall temperatures were acceptable.

Referring once again to Table XIII for the maximum power condition 15, emissions and combustion efficiency results were close to expected values and in-line with the other steady-state operating points. For the 2900°F and 3000°F BOT operating conditions, wall thermocouple temperature measurements can be compared to predictions given in the color contour plot of Figure 49. Predictions given in Figure 49 are similar for both the inner and outer liner. Predicted metal surface temperatures range from 1100 to 1300°F compared to 1124°F measured average for the outer wall and 1388°F measured average for the inner wall. At the critical ceramic/Brunsbond interface, predicted temperatures range from 1430°F to about 1500°F compared to an average measured outer wall temperature of 1264°F. The average measured inner wall temperature was not available because of failed thermocouples.

In summary, the LBO, ignition, and steady-state performance mapping of BU3 provided verification of the design method and performance benefits of the CMC cooling scheme throughout the combustor's operational range and achieved performance goals at the milestone 3000°F BOT condition. Based on wall thermocouple measurements, the selected coolant flow distribution appears to be adequate. However, a number of inconsistencies in the thermocouple measurements were identified. It is hypothesized that

inconsistent wall temperature measurements, which were also observed in the subsequent cyclic tests of BU4 and BU5, may be related to the introduction of conductive and/or convective errors caused by the method interface thermocouples are mechanically attached.

Thermocouples at the ceramic/Brunsbond and Brunsbond/substrate interfaces were installed during combustor fabrication and the durability of the laser welded junction was unknown. It is possible the junction weld failed on some thermocouples during the rigorous test program, leading to totally failed thermocouples and possibly others which gave erroneous and misleading temperature readings. For example, following BU2, OTL thermocouples consistently indicated higher metal surface (cold side) temperatures than at the ceramic/Brunsbond interface. Since these results are not physically possible, a fair amount of judgment was executed in interpreting wall temperature results. For the OTL, monitoring wall temperature levels was used to follow operational trends and absolute values were treated with caution.

#### 6.2.4.4 BU4

Following teardown inspection of BU3, the rig was subsequently rebuilt and the 3-hr, 32 cycle thermal shock test initiated. For this test, the high point BOT was 2700°F. The low point BOT was selected to avoid blowout with some margin and was determined to be approximately 0.010 F/A ratio corresponding to an approximate BOT of 1300°F. The 32 cycle test was completed without incident and the rig subsequently torn down. Once again, inspection of the combustor and OTL revealed no apparent damage or deterioration.

Photos of the liner and OTL following the 2700°F BOT cyclic test are given in Figures 106 and 107, respectively. Steady-state performance measurements were obtained before initiating cyclic tests and after completion of cyclic testing. Operating condition 13/IRP steady-state performance is provided in Table XIII. Figures 108 and 109 provide the circumferential and radial BOT distribution before initiating cyclic testing, and Figures 110 and 111 correspond to the conclusion of testing for BU4.

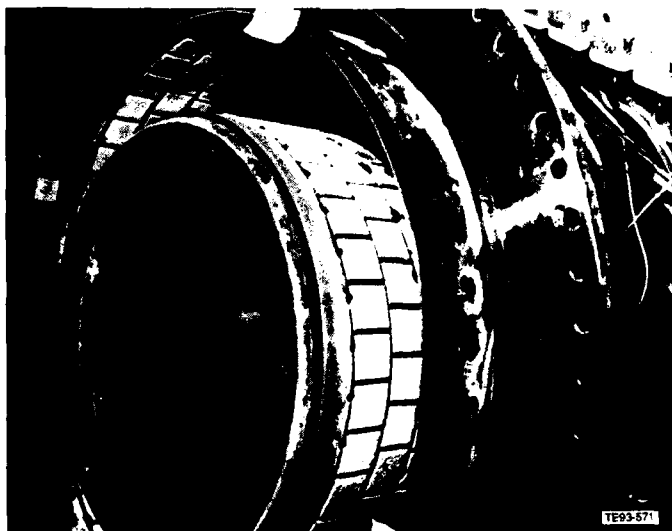


Figure 106. CMC combustor after 9/29/92 2700°F BOT cyclic shock test—liner.

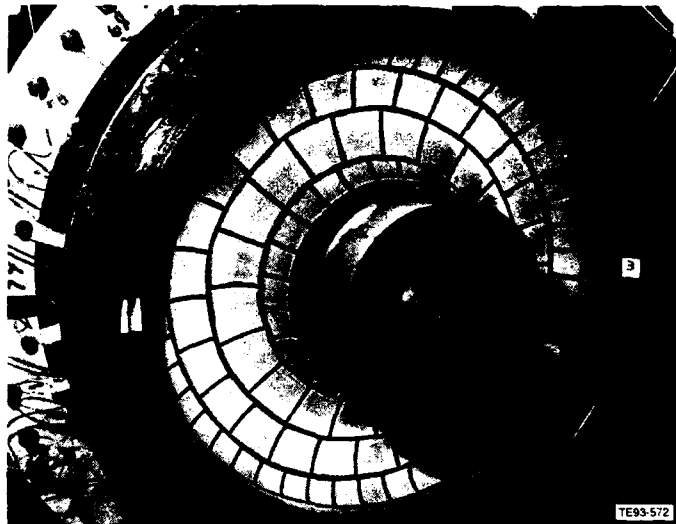


Figure 107. CMC combustor after 9/29/92 2700°F BOT cyclic shock test—OTL.

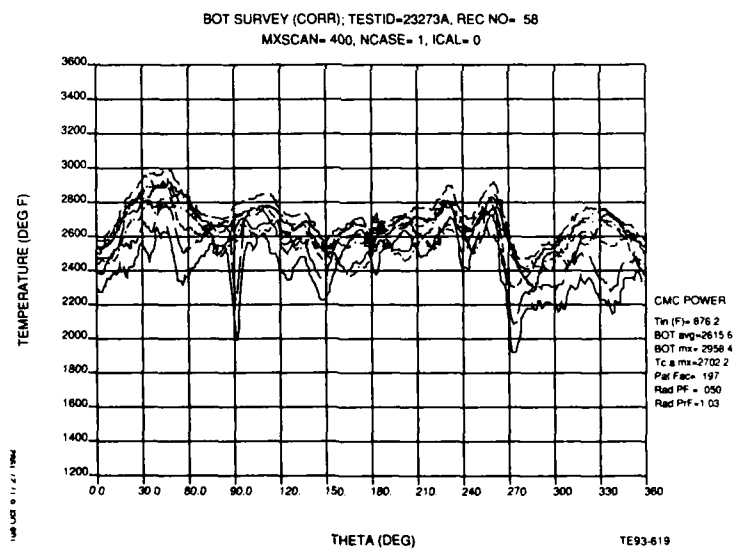


Figure 108. 2700°F cyclic testing, initial scan (9/29/92)—circumferential temperature trace.

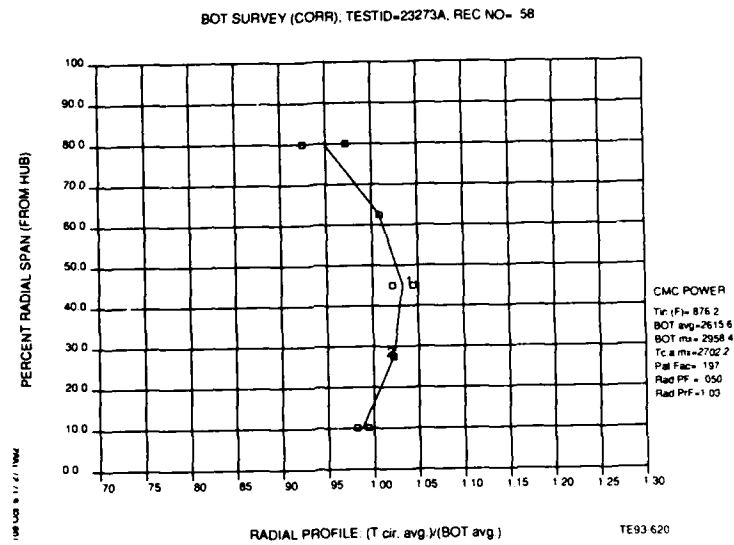


Figure 109. 2700°F cyclic testing, initial scan (9/29/92)—radial temperature profile.

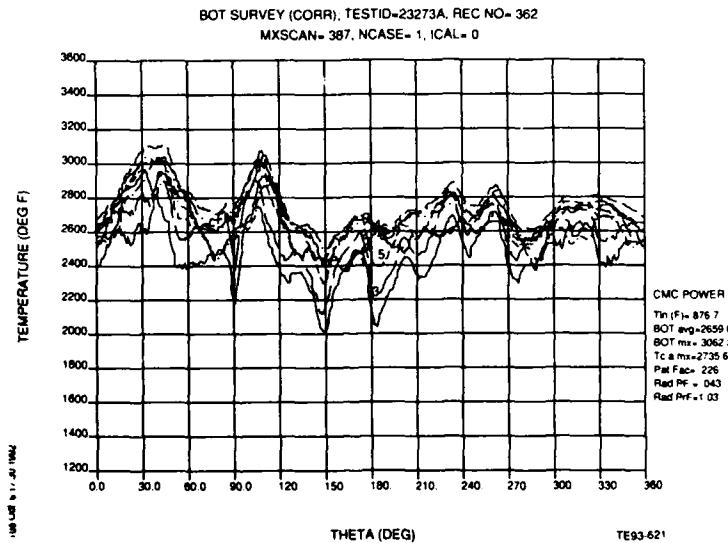


Figure 110. 2700°F cyclic testing, final scan, (9/29/92)—circumferential temperature trace.

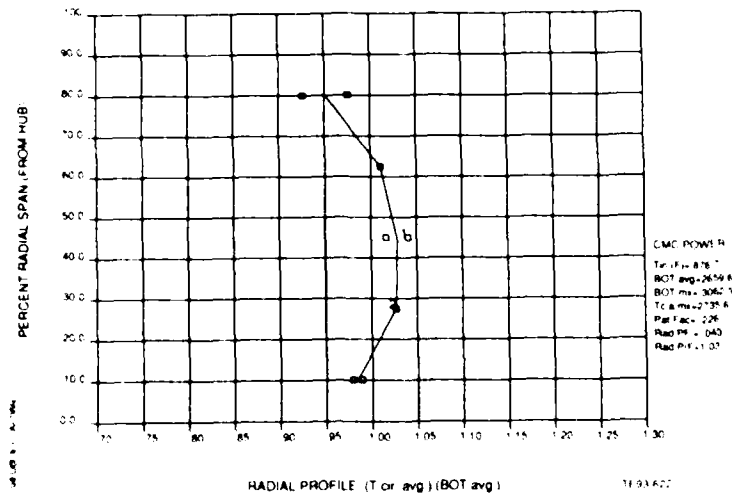


Figure 111. 2700°F cyclic testing, final scan, (9/29/92)—radial temperature profile

Overall, steady-state performance was consistent with other similar test points with the exception of pattern factor. Before initiation of cyclic testing, pattern factor was measured as 0.197 and increased to 0.226 following the 32 cycle test. Radial profile, emissions, efficiency, and wall temperature results were all similar to previous results. In addition, comparison of before and after steady-state performance, including wall temperature levels, indicated little if any change in CMC combustor performance after the 32 cycle durability test. This is evident from the data given in Table XIII for test point 13, BU4.

The increase in pattern factor from the 0.15 level to the 0.2 level can be explained by examination of the circumferential BOT traces of Figures 108 and 110 and comparing these results to the BU2 circumferential trace (Figure 86) and BU3 circumferential traces (Figures 102 and 104). As explained earlier, BU2 experienced an air leak that manifested itself as the streaks and cold spikes evident in Figure 86 and the pattern factor of 0.218. The leak resolved itself in BU3 as evident from Figures 102 and 104 and the 0.150 pattern factor. However, the leak appears to have returned in BU4. Similar peaks and valleys are observed in both Figures 86 (BU2) and 108 and 110 (BU4). Hence, a similar value of pattern factor was also obtained. The cause of the leak may be related to rig assembly or possibly mechanical distortions from the severe 3000°F average temperature of BU3.

During the course of cyclic testing, operating conditions at the high point BOT were recorded to monitor combustion system condition and the potential development of system problems or failure. In addition to operating conditions (overall fuel-air ratio and corrected flow rate), liner pressure drop and wall temperature levels were continuously monitored. Figures 112 through 124 provide a comprehensive record of these measurements. As evident from these figures, during the course of the 32 cycle durability test, combustor effective flow area (Figure 114) and all wall thermocouple readings remained steady and only fluctuated with fluctuations in operating conditions (Figure 112). With successful completion of the 32 cycle durability test, teardown inspection was initiated. No damage or deterioration was noted in the hardware's condition. The rig was subsequently reassembled for initiation of BU5 testing.



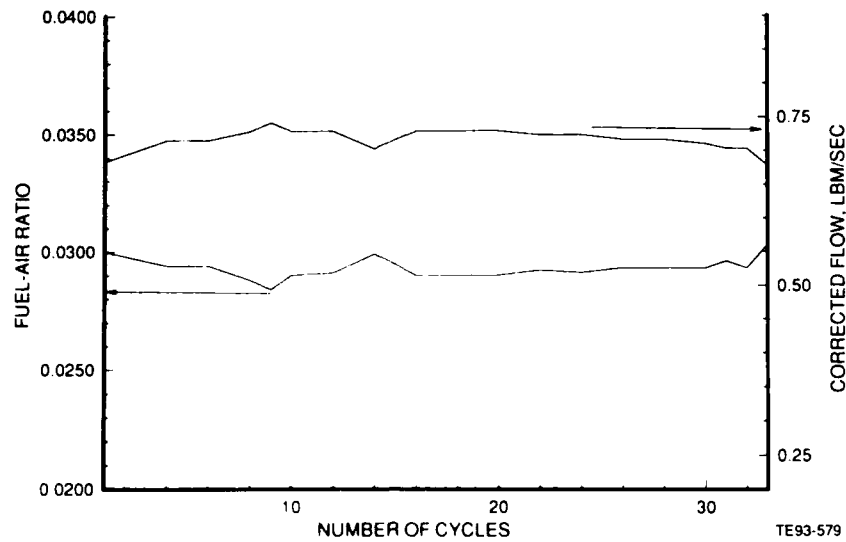


Figure 112. Army/NASA CMC combustor thermal shock test—2700°F BOT high point operating condition versus cycle.

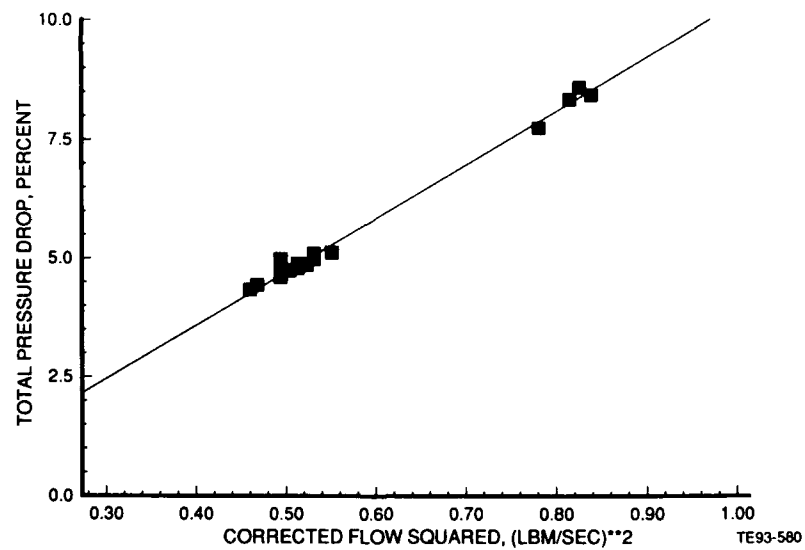


Figure 113. Army/NASA CMC combustor thermal shock test—2700°F BOT high point pressure drop versus corrected flow.

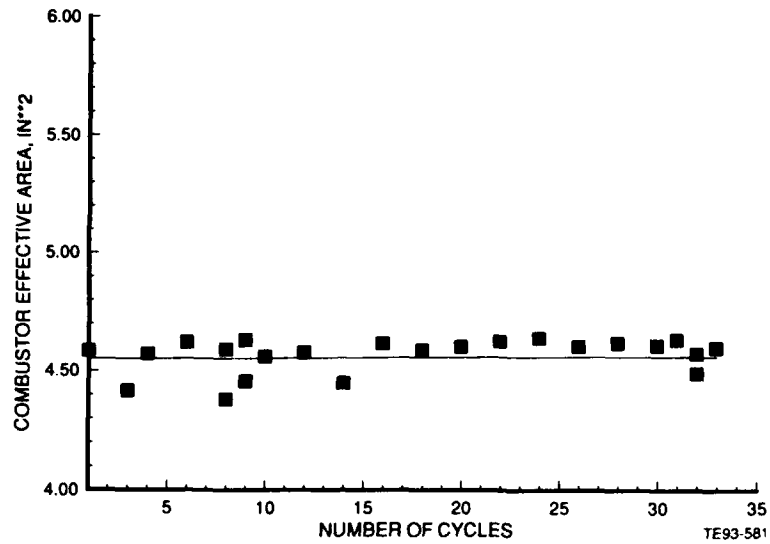


Figure 114. Army/NASA CMC combustor thermal shock test—2700°F BOT high point effective flow area versus number of cycles.

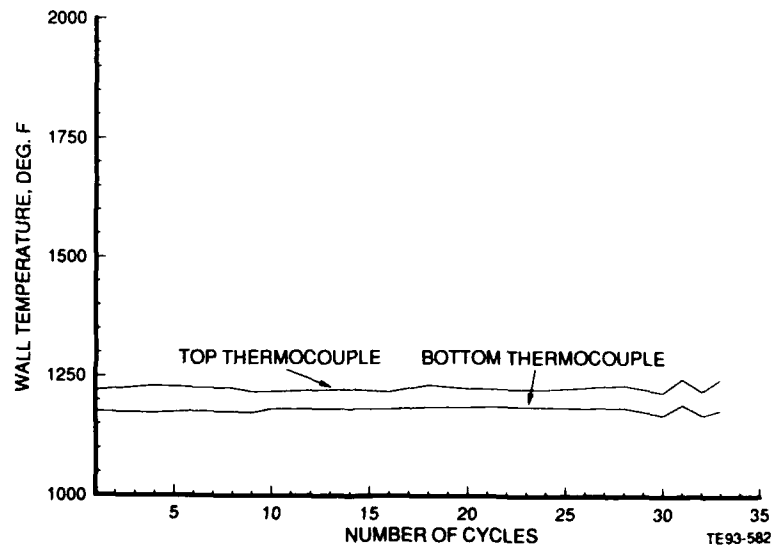


Figure 115. Army/NASA CMC combustor thermal shock test—2700°F BOT high point, ceramic/Brunsbond interface, outer barrel.

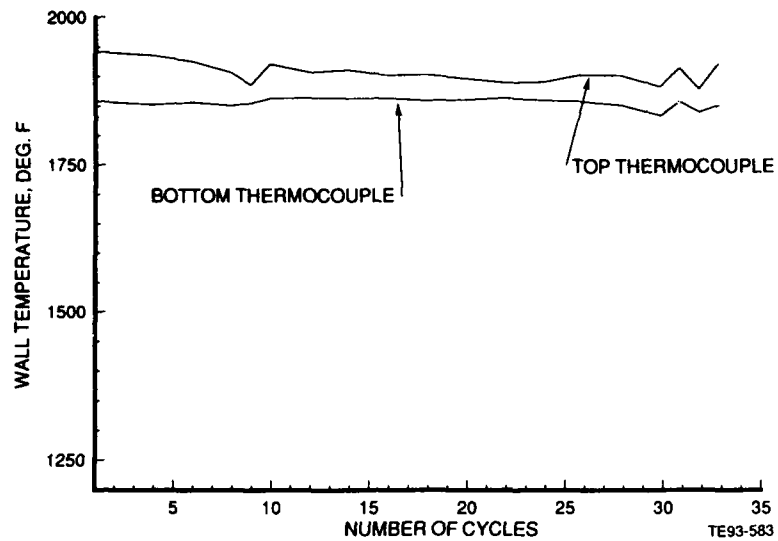


Figure 116. Army/NASA CMC combustor thermal shock test—2700°F BOT high point, ceramic/Prunsbond interface, inner barrel.

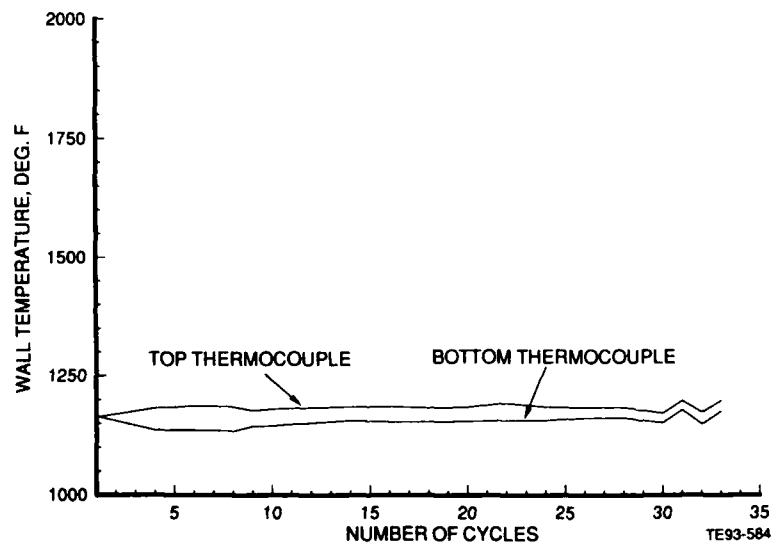


Figure 117. Army/NASA CMC combustor thermal shock test—2700°F BOT high point, ceramic/Brunsbond interface, OTL.

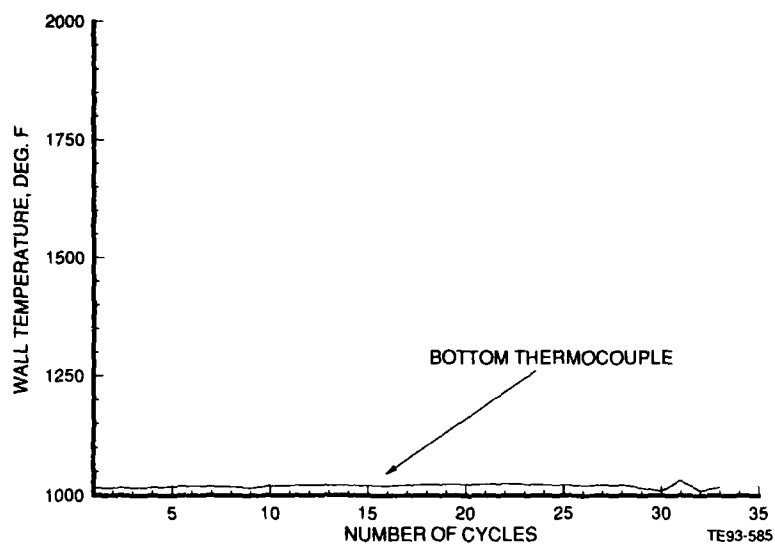


Figure 118. Army/NASA CMC combustor thermal shock test—2700°F BOT high point, metal/Brunsbond interface, outer barrel.

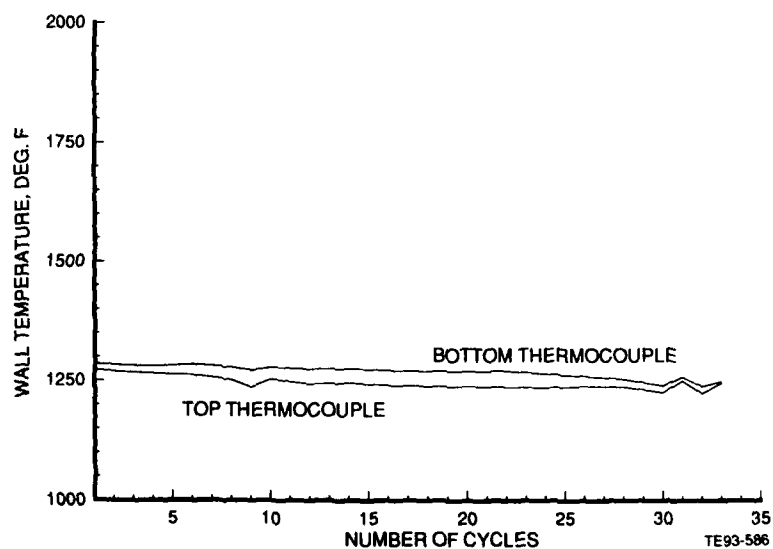


Figure 119. Army/NASA CMC combustor thermal shock test—2700°F BOT high point, metal/Brunsbond interface, inner barrel.

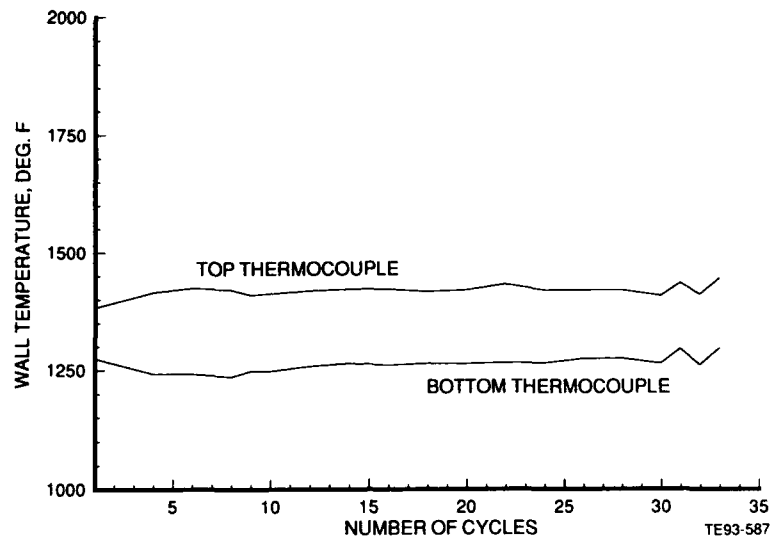


Figure 120. Army/NASA CMC combustor thermal shock test—2700°F BOT high point, metal/Brunsbond interface, OTL.

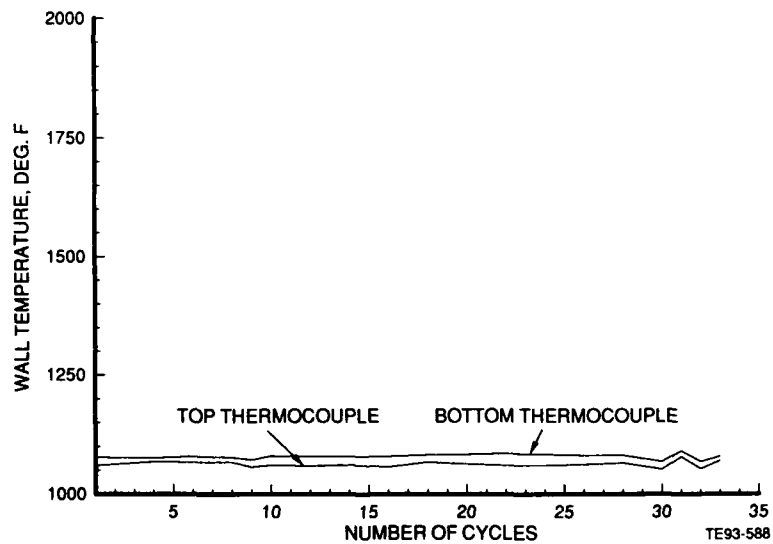


Figure 121: Army/NASA CMC combustor thermal shock test—2700°F BOT high point, metal cold side, outer barrel.

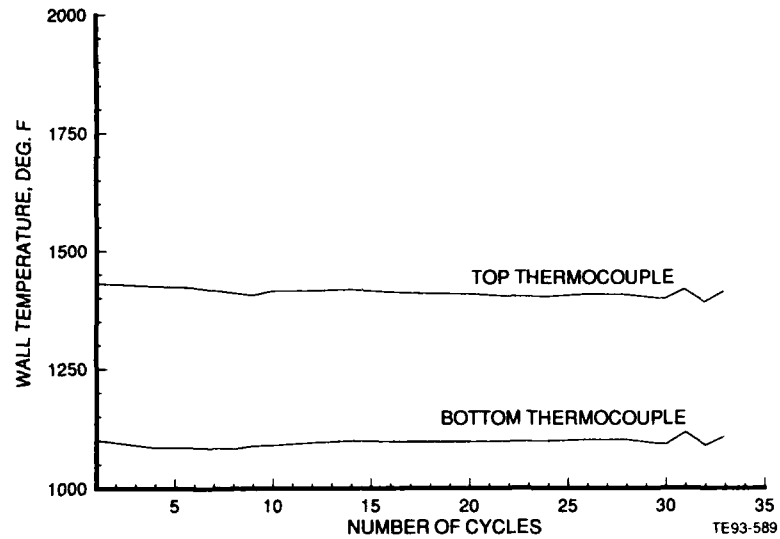


Figure 122. Army/NASA CMC combustor thermal shock test—2700°F BOT high point, metal cold side, inner barrel.

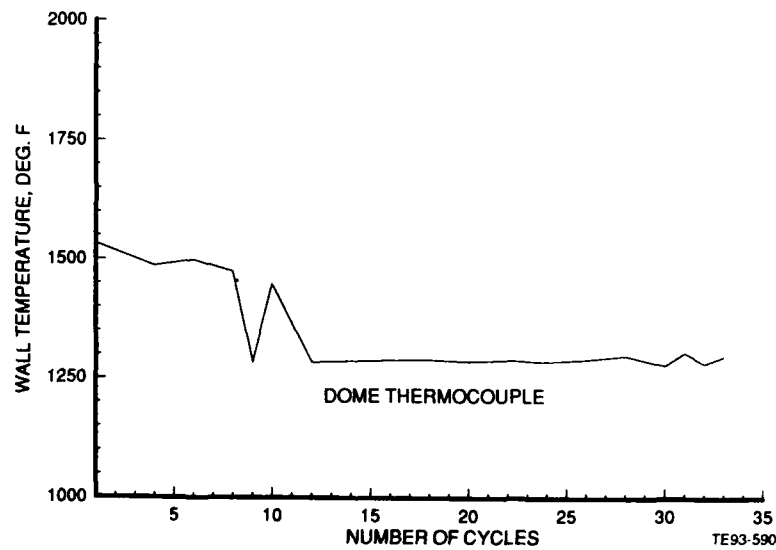


Figure 123. Army/NASA CMC combustor thermal shock test—2700°F BOT high point, metal cold side, effusion cooled dome.

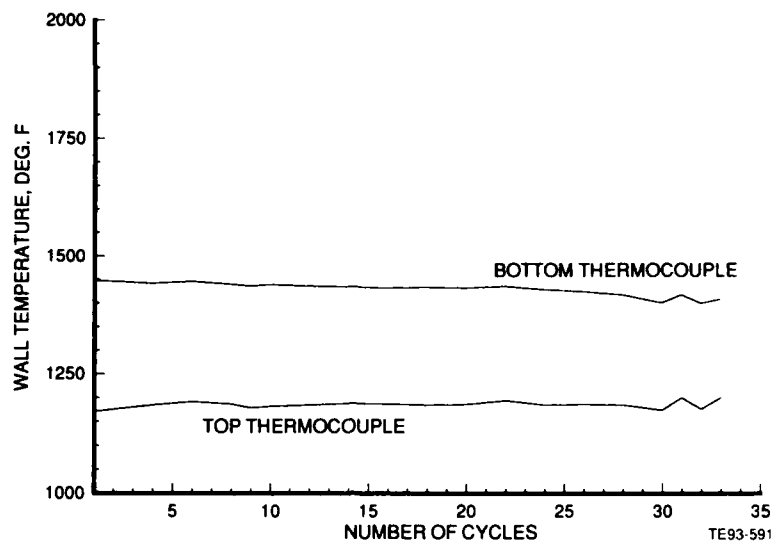


Figure 124. Army/NASA CMC combustor thermal shock test—2700°F BOT high point, metal cold side, OTL.

#### 6.2.4.5 BU5

Cyclic testing at 3000°F BOT was carried out without incident and with stable operating conditions for 68 cycles. However, during the 68th cycle, a sudden BOT and wall thermocouple temperature increase was observed. The temperature spikes were so severe the test was immediately shutdown. Rig tear-down and hardware inspection revealed the axial air swirler located at the No. 4 fuel nozzle had failed and was missing from its position. Unreparable damage was sustained to the liner barrel and seal as well as the outer transition liner (OTL). In addition, the burner rig effusion-cooled inner flow path, water spray nozzles, emission probe body, and BOT probe elements were damaged from the overtemperature.

Steady-state performance measurements were made at the beginning of the test and after 30 cycles. These data were presented in Table XIII, and circumferential and radial temperature distributions are provided in Figures 125 through 130.

Review of these data indicate, once again, the presence of air leakage which is impacting pattern factor. During BU5, pattern factor increased to the 0.25 level compared to 0.20 levels of BU4. It was suspected that the durability testing of BU4 exasperated the rig leakage problem. Figure 125 was the initial (before cyclic testing) BOT scan and Figure 127 was a repeat scan. The nonuniformity of the trace is evident in these figures and similar to the pattern observed in BU2 and BU4. After 30 cycles, a BOT scan was completed and Figure 129 presents the circumferential trace while radial profile is shown in Figure 130. One conclusion made from Figure 129 is that after 30 cycles, no significant change in combustor operation was observed. This is supported by the radial profile results as well as the combustion efficiency, emissions, smoke, and wall temperature data presented in Table XIII. Overall, steady-state performance was consistent with previous data at the 3000°F BOT condition and after 30 cycles, steady-state performance indicated insignificant changes in combustor operation.

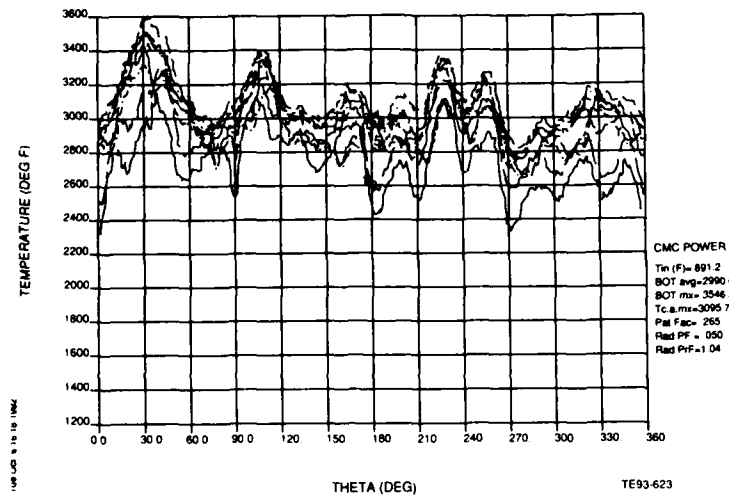


Figure 125. 3000°F BOT cyclic testing, initial scan (10/02/92)—circumferential temperature trace.

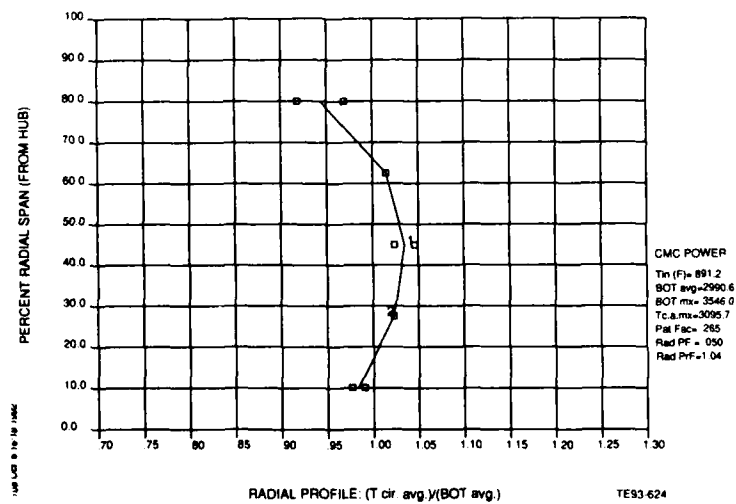


Figure 126. 3000°F BOT cyclic testing, initial scan (10/02/92)—radial temperature profile.



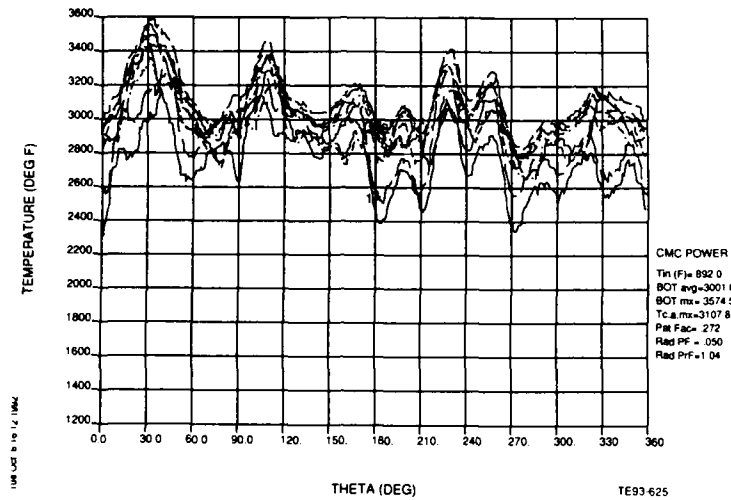


Figure 127. 3000°F BOT cyclic testing, repeat point (10/02/92)—circumferential temperature trace.

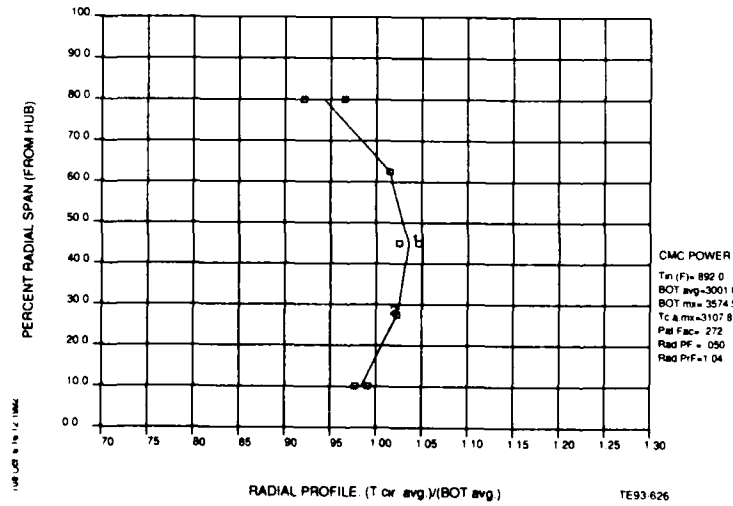


Figure 128. 3000°F BOT cyclic testing, repeat point (10/02/92)—radial temperature profile.

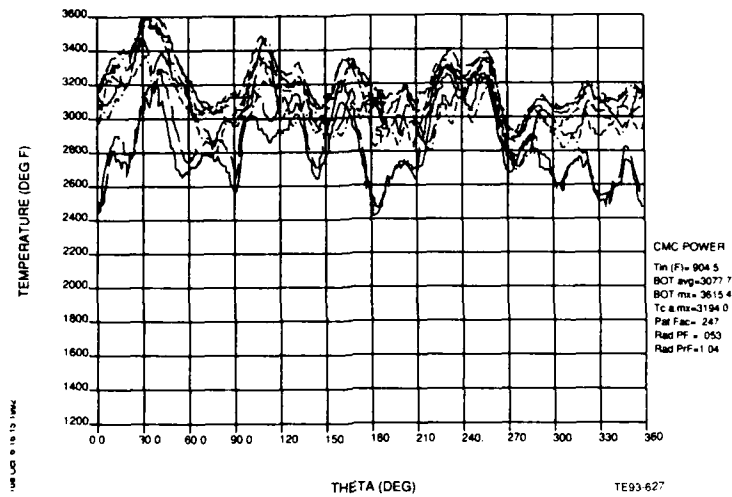


Figure 129. 3000°F BOT cyclic testing, final scan after 30 cycles (10/02/92)—circumferential temperature trace.

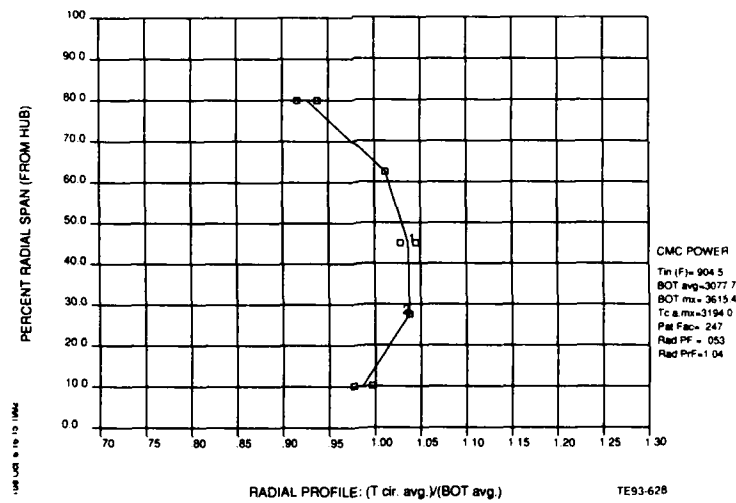


Figure 130. 3000°F BOT cyclic testing, final scan after 30 cycles (10/02/92)—radial temperature profile.

During the cyclic testing of BU5, operating conditions at the 3000°F high point condition were recorded to monitor combustion system condition and the potential development of system problems or failure. Fuel-air ratio, corrected flow rate, liner total pressure drop, and wall temperature levels were continuously monitored. In addition, the test stand display of the parked, BOT thermocouples were observed during the test but not recorded. Figures 131 through 143 provide the record of these measurements. Comparing Figure 131 to 112, it is observed that considerably more fluctuation in inlet conditions was sustained during the BU5 testing. The failure of the swirler during cycle No. 68 is evident from Figures 132 and 133. In Figure 132, liner pressure drop falls off the correlating line over a range of corrected flows, tested after the problem was identified. Figure 133 provides a clear display of the swirler failure by plotting liner effective flow area versus cycle number. A sudden increase in flow area is observed at cycle No. 68 when the failure occurred.

However, Figures 132 and 133 also indicate that up to the point of failure, no evidence of progressive deterioration was observed. Unfortunately, when the emergency shutdown procedure was carried out during the 68th cycle, data were not recorded and measurement of temperature levels and distribution at failure was not available.

Figures 134 through 143 provide wall thermocouple measurements for the first 67 cycles of the durability test. Wall temperature levels fluctuate with the fluctuation of operating conditions. Figure 135 shows thermocouples at the ceramic/Brunsbond interface on the inner liner. Both thermocouples were previously giving inaccurate readings until one of two failed completely while the other seemed to attain a level on the order of temperature readings indicated in Figure 134 for the outer liner ceramic/Brunsbond interface. All other thermocouples maintained relatively steady values up to the 68th cycle when the failure occurred. The wall thermocouple readings provided further evidence that up to the point of catastrophic failure, the CMC combustor system was in satisfactory condition and no indications of progressive failure were evident.

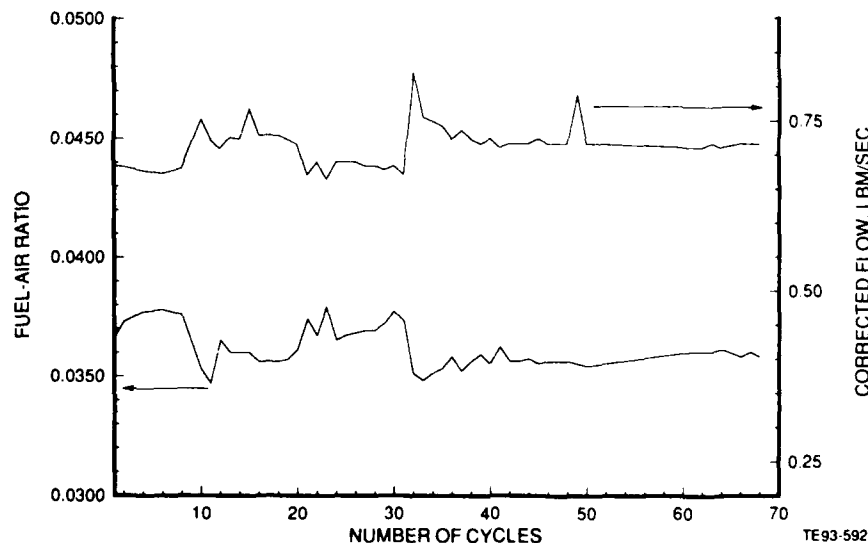


Figure 131. Army/NASA CMC combustor thermal shock test—3000°F BOT high point operating condition versus cycle.

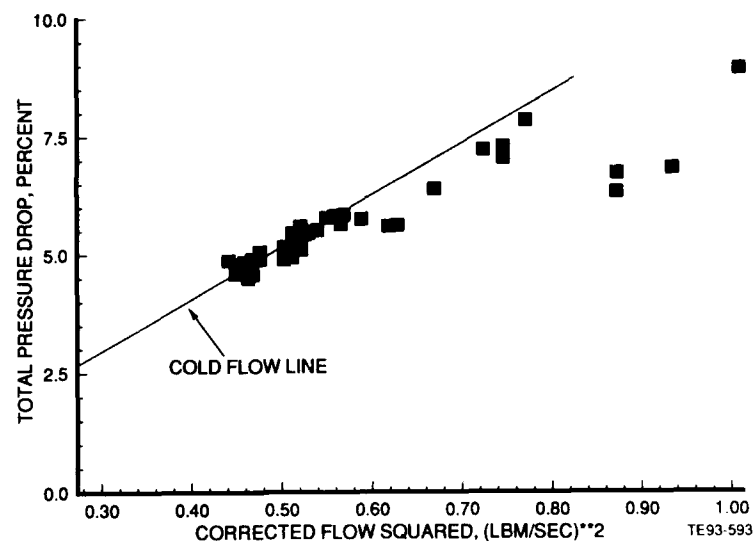


Figure 132. Army/NASA CMC combustor thermal shock test—3000°F BOT high point pressure drop versus corrected flow.

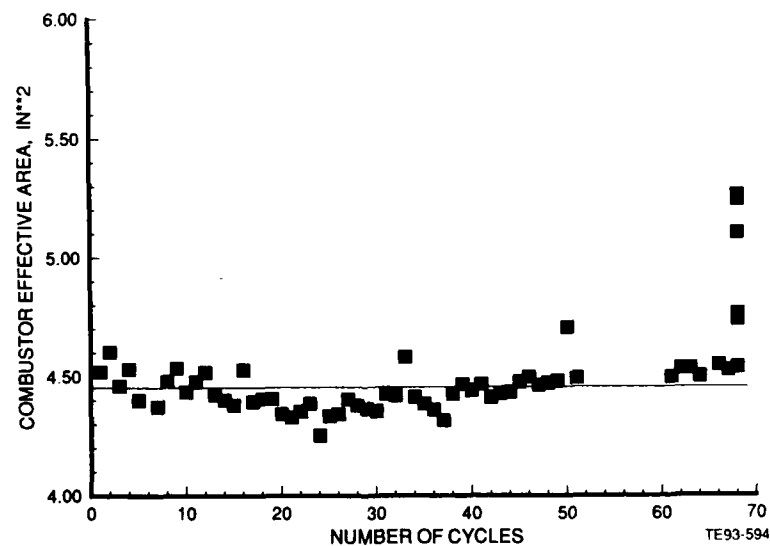


Figure 133. Army/NASA CMC combustor thermal shock test—3000°F BOT high point effective flow area versus number of cycles.

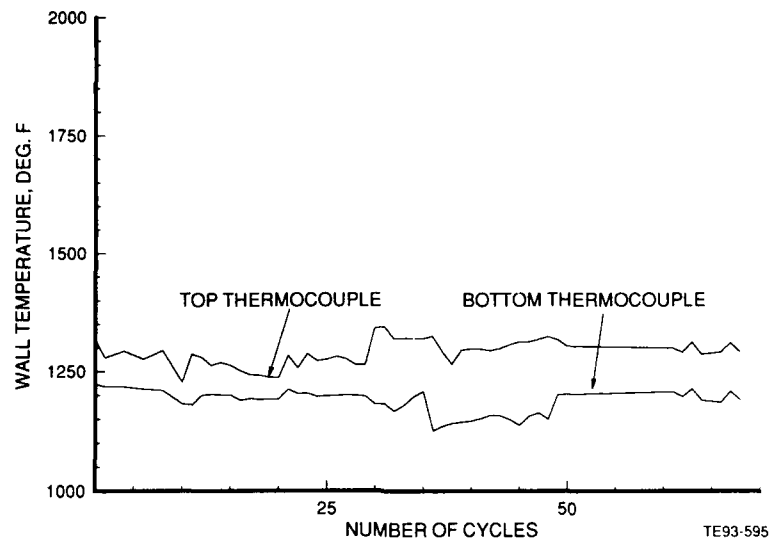


Figure 134. Army/NASA CMC combustor thermal shock test—3000°F BOT high point, ceramic/Brunsbond interface, outer barrel.

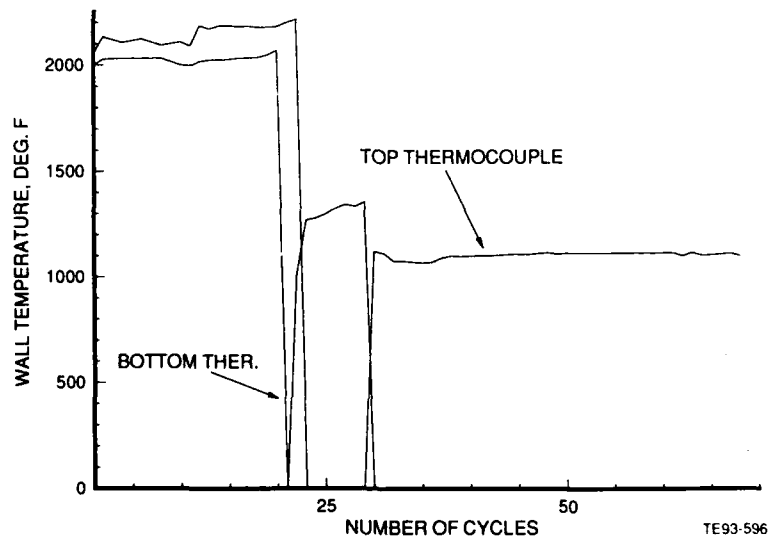


Figure 135. Army/NASA CMC combustor thermal shock test—3000°F BOT high point, ceramic/Brunsbond interface, inner barrel.

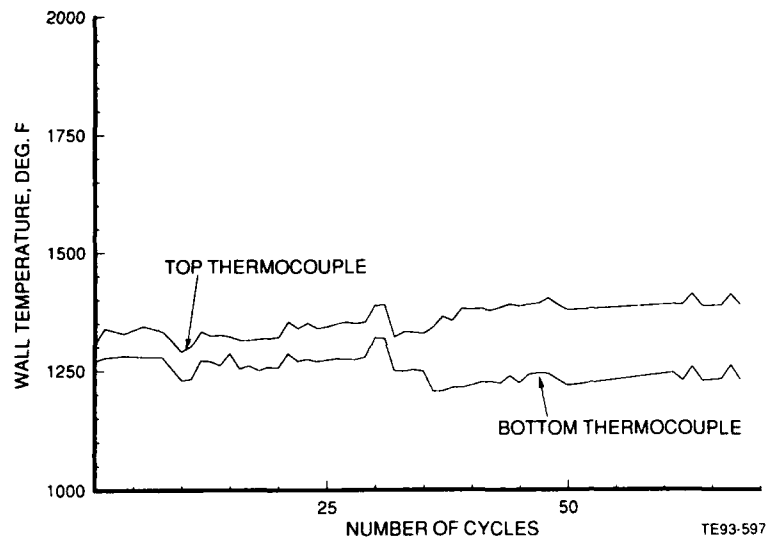


Figure 136. Army/NASA CMC combustor thermal shock test—3000°F BOT high point, ceramic/Brunsbond interface, OTL.

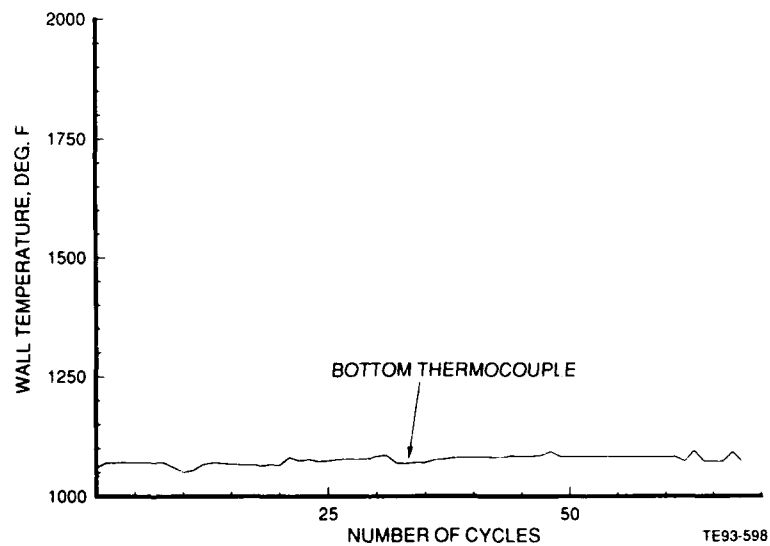


Figure 137. Army/NASA CMC combustor thermal shock test—3000°F BOT high point, metal/Brunsbond interface, outer barrel.

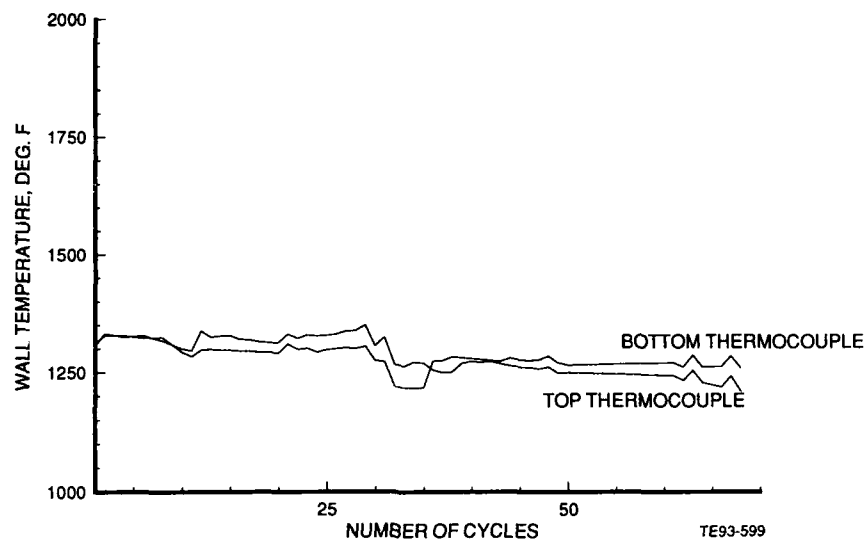


Figure 138. Army/NASA CMC combustor thermal shock test—3000°F BOT high point, metal/Brnsbond interface, inner barrel.

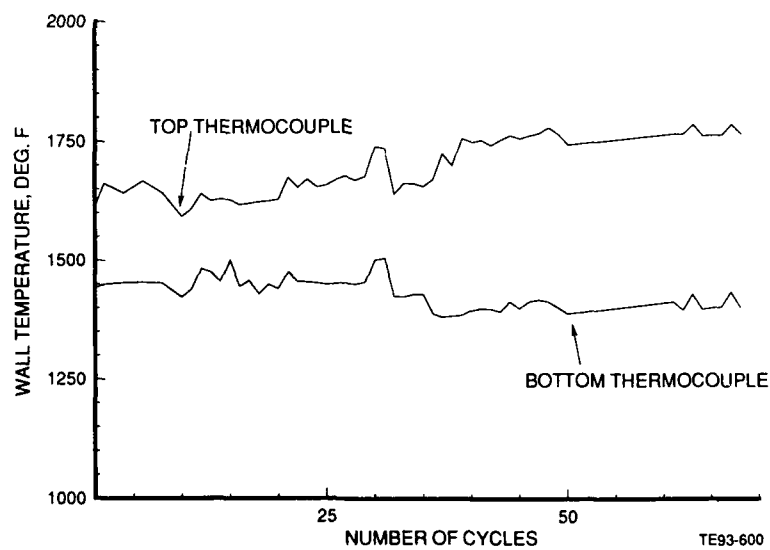


Figure 139. Army/NASA CMC combustor thermal shock test—3000°F BOT high point, metal/Brnsbond interface, OTL.

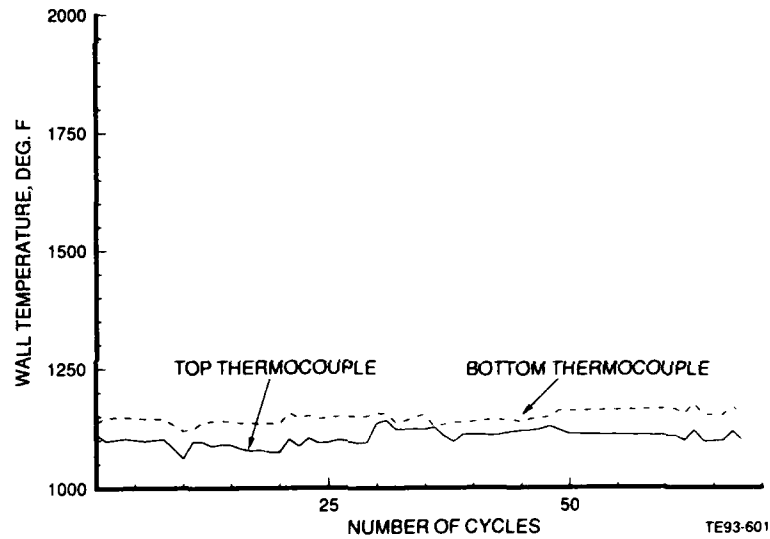


Figure 140. Army/NASA CMC combustor thermal shock test—3000°F BOT high point, metal cold side, outer barrel.

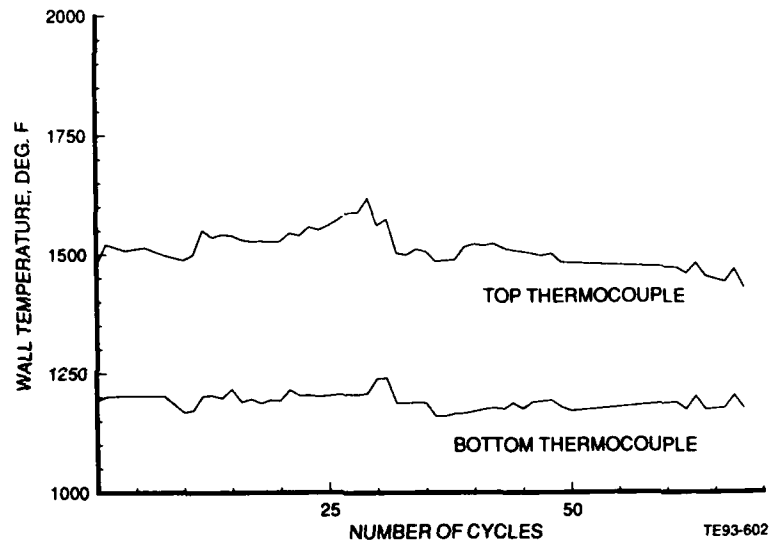


Figure 141. Army/NASA CMC combustor thermal shock test—3000°F BOT high point, metal cold side, inner barrel.



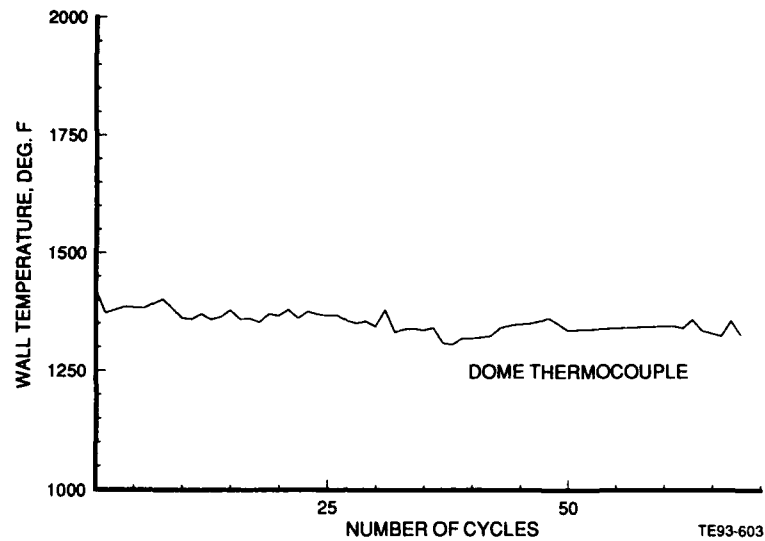


Figure 142. Army/NASA CMC combustor thermal shock test—3000°F BOT high point, metal cold side, dome.

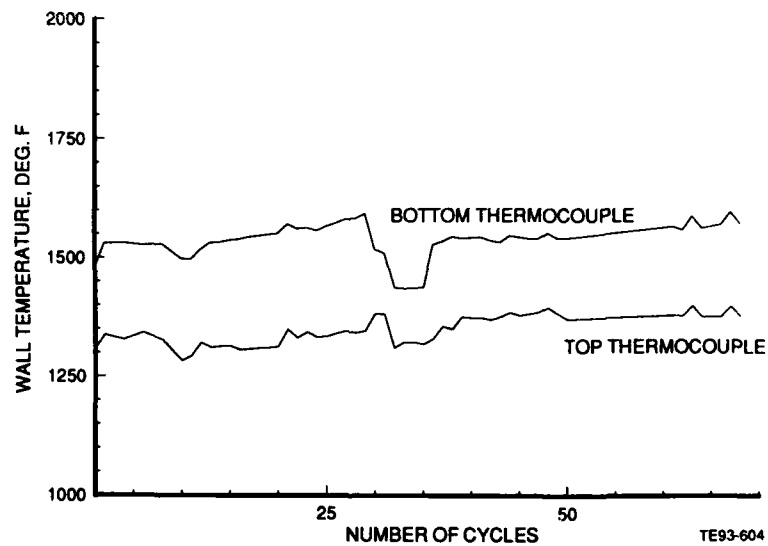


Figure 143. Army/NASA CMC combustor thermal shock test—3000°F BOT high point, metal cold side, OTL.

During the 68th cycle, as fuel flow was increased to attain the 3000°F BOT condition, a sudden overtemperature was observed in the test stand graphic displays which monitor BOT and wall thermocouples. Following shutdown and rig teardown, it was observed that the axial swirler located at the No. 4 fuel nozzle position was missing, as shown in Figure 144. The overtemperature caused the inner liner-to-rig seal to melt, which deposited on the OTL, shown in Figure 145. In spite of the severe temperature conditions, the outer liner ceramic tiles survived relatively intact. A view of the outer liner tiles, showing discoloration and through-the-plane cracking, is provided in Figure 146. On the other hand, much more damage was sustained to the inner wall tiles where a view is given in Figure 147. This was attributed to the starvation of coolant flow on the inner wall when the swirler failed. Because of the reverse-flow design, inlet air enters at the outer wall and must flow across the combustor dome before turning and entering the inner wall plenum. With the open area surrounding fuel nozzle 4, it is suspected air would preferentially enter the opening and consequently starve the inner wall of coolant air. In addition, this likely exasperated the failure of the inner seal which may have led to the type of mechanical distortion observed around the dome and shown in Figure 148. Finally, Figure 149 shows a photo of the damaged fuel nozzle from the No. 4 position.

In summary, the cause of the overtemperature condition is suspected to be related to the failure of the air swirler. The failed swirler was one of two swirlers reworked after damage inflicted during calibration of the air-cooled BOT thermocouple elements during a previous test. During rework, the damaged swirler vanes were machined away, leaving a cylinder. Another swirler vane section from a similar swirler assembly, of different mounting design but same aerodynamic characteristics, was then machined to fit the cylinder and integrated using a press fit after cooling the vane section in liquid nitrogen. In addition, tack welds were used to further reinforce the assembly. Apparently, cyclic testing at the severe conditions of the test program failed the welds and loosened the vane section sufficiently to separate from the swirler body. The other reworked swirler was still intact and undamaged at the time of the failure. With the swirler gone, a large area was opened which starved the other fuel nozzles and inner liner of air. In addition, it's likely the No. 4 fuel nozzle fuel spray suffered poor atomization. The combination of unatomized fuel spray burning downstream with attendant increase in fuel-

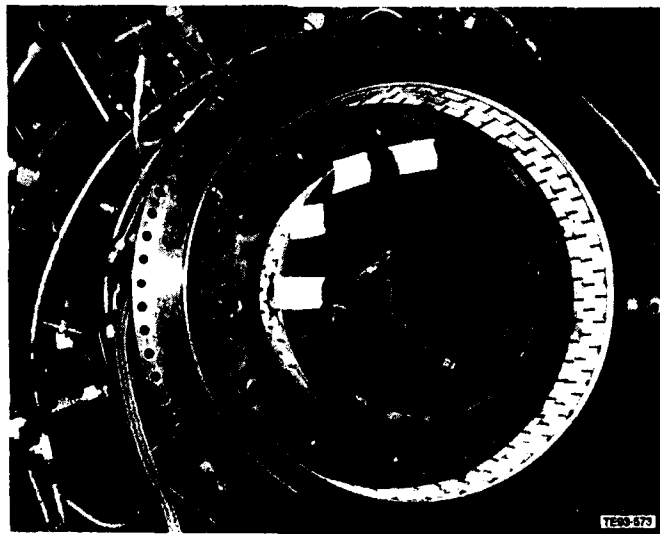


Figure 144. CMC combustor after 10/02/92 3000°F BOT cyclic shock test—liner.

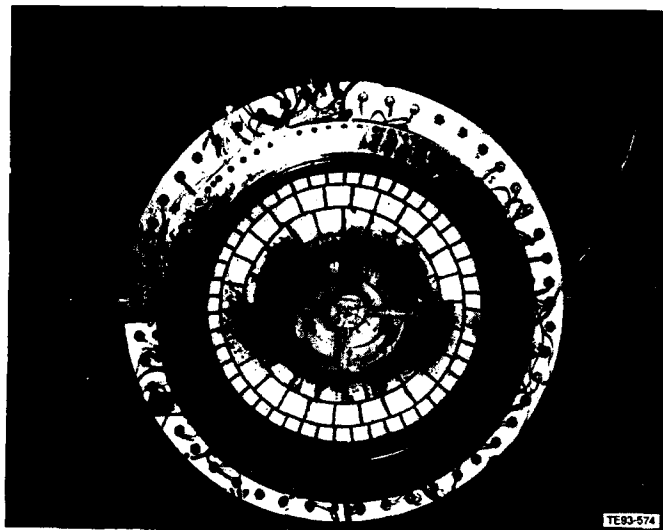


Figure 145. CMC combustor after 10/02/92 3000°F BOT cyclic shock test—OTL.

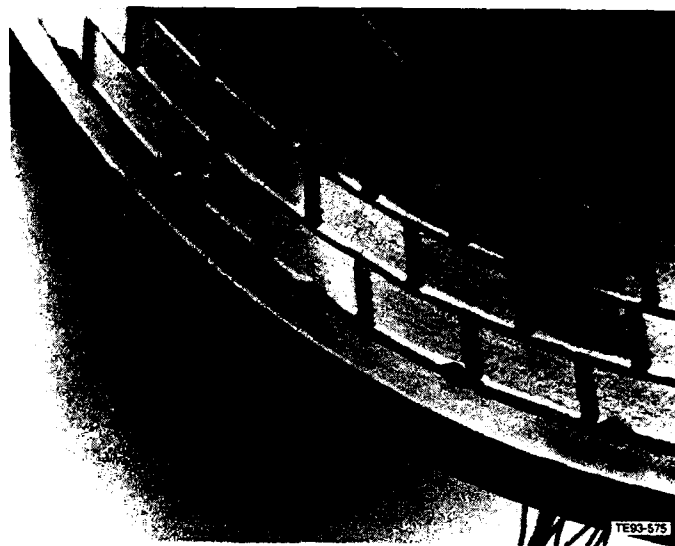


Figure 146. CMC combustor outer wall after 10/02/92 3000°F BOT cyclic shock test.

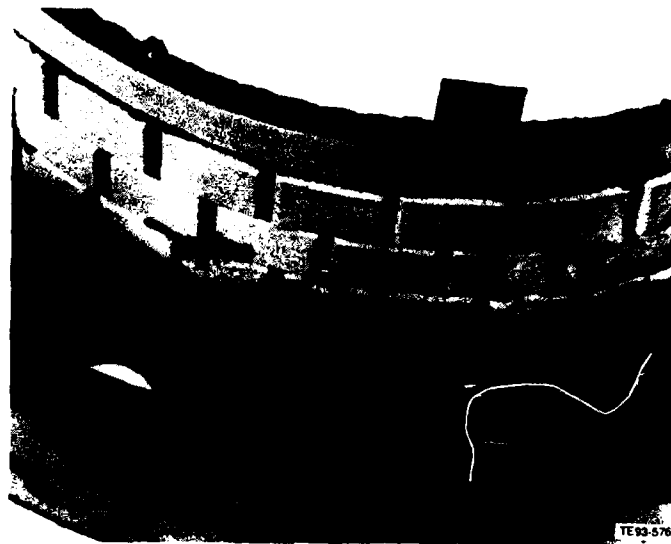


Figure 147. CMC combustor inner wall after 10/02/92 3000°F BOT cyclic shock test.



Figure 148. Post 3000°F BOT cyclic shock test—dome distortion.



TE93-578

Figure 149. Post 3000°F BOT cyclic shock test—damaged fuel nozzle.

air ratio at the other nozzles, along with the starvation of cooling air to the inner liner and seal is hypothesized as causing the observed temperature rise and hardware damage. Although failure occurred, data analysis indicates until the sudden temperature peak on the 68th cycle, the combustor performance was stable with no observable indications of progressive degradation. Therefore it is concluded from the test program that the CMC technology offers considerable combustor performance benefits and further development of the concept is recommended.

## VII. SUMMARY AND RECOMMENDATIONS

A joint Army/NASA program was conducted to design, fabricate, and test an advanced, reverse-flow, small gas turbine combustor utilizing a compliant metal/ceramic (CMC) wall cooling concept. The objectives of this effort were to develop a design method (basic data and analysis) for the CMC cooling technique and then demonstrate the application for an advanced cycle combustor with 3000°F burner outlet temperature (BOT).

The program was divided into four tasks. Task I defined component materials and localized design of the composite wall structure in conjunction with development of basic design models for the analysis of flow and heat transfer through the wall. Task II required implementation of the selected materials and validated design models during combustor preliminary design. Detail design of the selected combustor concept and its refinement with 3-D aerothermal analysis were completed in Task III. Task IV covered detail drawings, process development and fabrication, and a series of burner rig tests. Burner rig tests covered characterization of cold flow pressure drop, lean blowout and ignition mapping, steady-state performance throughout the operating range including the milestone 3000°F BOT design condition, as well as two series of cyclic thermal shock tests at high point BOT conditions of 2700°F (32 total cycles) and 3000°F (68 total cycles).

The main objectives of this program were: (1) the development of materials and design methodology, (2) full-scale design, and (3) fabrication and testing for steady-state performance and cyclic durability. As described in the report, the program's main objectives have been achieved.

The heat transfer and flow/pressure drop characterization of Brunsbond pad and subsequent verification of heat transfer performance of the micro CMC system has yielded an engineering "tool" that can be used in a full-scale combustor design using this cooling technique. Although the test data that were used to "build" the analysis model were limited, it is thought that the final model should yield realistic temperatures certainly capable of providing the required design input for the CMC combustor.

Limitations of the design methodology are related to unknown factors affecting the CMC system performance introduced by the fabrication process.

It is recommended that further development work be undertaken to ascertain the effect on flow/pressure drop of the braze wicking, pad crushing, and introduction of impurities into the porous pad. This additional work should also include the effect of flow/pressure drop of applying the TBC to the CMC structure.

The developed design methodology was applied to the full-scale design and the combustor fabricated and tested. In general, rig data were found to be consistent with the design system predictions. Rig test results have demonstrated the benefits and viability of the CMC concept meeting or exceeding the performance of similar combustors, achieving 0.15 pattern factor at 3000°F BOT while utilizing approximately 80% less cooling air than conventional, film-cooled combustion systems.

Failure of the axial swirler during cyclic durability testing and subsequent combustor damage was an isolated incident and was unrelated to the performance of the CMC wall concept. An assessment of the combustor damage may be summarized as follows:

- swirler failure related to a rework and cyclic fatigue
- overtemperature condition a result of swirler failure and redistribution of airflow and poor fuel atomization
- inner seal undercooled—possibly led to dome distortion via thermal growth and mechanical engagement
- inner seal melting exasperated by overtemperature, deposited on OTL
- inner wall damage from swirler and undercooled + overtemperature condition

It is recommended further development of the CMC wall cooling concept be carried out through design, fabrication, and testing of the CMC concept in an advanced technology combustor. The following considerations should be addressed in the new combustor design:

- dome should be film cooled to reduce potential for hot spots
- consider use of simplex airblast fuel nozzles
- increase cooling air to inner seal and inner liner
- investigate improvements in the fabrication process, specifically those used in manufacture of the OTL

## REFERENCES

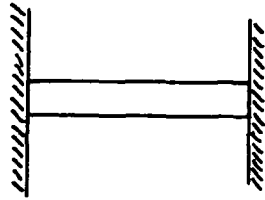
1. E. P. Demetri, R. F. Topping, and R. P. Wilson, Jr., "Study of Research and Development Requirements of Small Gas Turbine Combustors," Arthur D. Little, Inc., Cambridge, MA, ADL-83381-2, January 1980 (NASA CR-159796).
2. D. A. Nealy, S. B. Reider, H. C. Mongia, "Alternate Cooling Configurations for Gas Turbine Combustion Systems," Allison Gas Turbine Division, General Motors Corporation, Indianapolis, IN, AGARD Conference Proceedings No. 390, 1985.
3. R. R. Venkat Raman, Gerald Roffe, "Testing of Felt-Ceramic Materials for Combustor Applications," General Applied Science Laboratories, Inc., Westbury, NY, Prepared for Lewis Research Center under Contract NAS3-22775, NASA Contractor Report 168103, April 1983.
4. D. B. Ercegovic, C. L. Walker, and C. T. Norgren, "Ceramic Composite Liner Material for Gas Turbine Combustors," US Army Aviation R&D Command and NASA Lewis Research Center, Cleveland, OH, AIAA-84-0363, January 1984.
5. W. A. Acosta and C. T. Norgren, "Small Gas Turbine Combustor Experimental Study-Compliant Metal/Ceramic Liner and Performance Evaluation," U.S. Army Aviation R&D Activity (AVSCOM), NASA Lewis Research Center, Cleveland, OH, NASA Technical Memorandum 87304, USAAVSCOM Technical Report 86-C-6, June 1986.
6. T. W. Bruce, H. C. Mongia, and R. S. Reynolds, "Combustor Design Criteria Validation, Volume 1 - Element Tests and Model Validation," AiResearch Manufacturing Co., Phoenix, AZ, Final Report for U.S. Army Applied Technology Laboratories (AVRADCOM), USARTL-TR-78-55A, March 1979.
7. C. H. Liebert and R. A. Miller, "Ceramic Thermal Barrier Coatings," NASA Lewis Research Center, Cleveland, OH, Prepared for the *Journal of the American Chemical Society*, January 1984.
8. L. Green, Jr. and P. Guwez, "Fluid Flow Through Porous Metal," *Journal of Applied Mechanics*, Vol 18, No. 1, March 1951, pp 39-45.
9. J. Heberlein and E. Pfender, "Transpiration Cooling of the Constrictor Walls of an Electric High-Intensity Arc," *Journal of Heat Transfer*, May 1971, pp 146-154.
10. J. C. Y. Koh and E. delCasal, "Heat and Mass Flow Through Porous Matrixes for Transpiration Cooling," 1975 Proceedings of the Heat Transfer and Fluid Mechanics Institute, pp 263-281.
11. The Brunswick Corporation, Technetics Division, Energy Conservation Systems, TD900, 5 March 1981.
12. R. E. Chupp, "Transient-Temperature Analysis of a General Nodal-Network System: Computer Program EJ-8," Allison Gas Turbine Division of General Motors Corporation, TDR AX.0013-030, 18 April 1972.
13. R. P. Tolokan, J. B. Brady, and G. P. Janabet, "Strain Isolated Ceramic Coatings," presented at the 1983 Gas Turbine Conference and Exhibits of the American Society of Mechanical Engineers, Phoenix, AZ, 30 March 1983.
14. C. H. Liebert, "Emittance and Absorptance of NASA Ceramic Thermal Barrier Coating System," NASA Technical Paper 1190, April 1978.
15. R. W. Claus, J. D. Wear, and C. H. Liebert, "Ceramic Coating Effect on Liner Metal Temperatures of Film-Cooled Annular Combustor," NASA Technical Paper 1323, January 1979.
16. A. H. Lefebvre and M. V. Herbert, "Heat Transfer Processes in Gas Turbine Combustion Chambers," *Proc Instn Mechanical Engineers*, Vol 173, No. 12, 1960, pp 463-48.
17. J. Odgers and D. Kretschmer, "A Simple Method for the Prediction of Wall Temperatures in a Gas Turbine," ASME Paper No. 78-GT-90, April 1978.
18. W. M. Kays, *Convective Heat and Mass Transfer*, first edition, McGraw-Hill Book Company, New York, 1966, pp 269.
19. F. Kreith, *Principles of Heat Transfer*, second edition, International Textbook Company, Scranton, PA 1965, pp 379.
20. D. Fread, "Composite Segment for Combustor-Stress Analysis (Parametric Study), Allison Gas Turbine Division, GMC, TDR AK.0320-002, September 14, 1984.



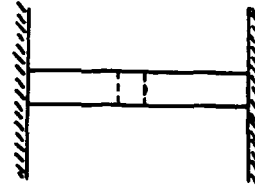
21. A. H. Shapiro, "The Dynamics and Thermodynamics of Compressible Fluid Flow, Vol. I," Chapter 8, The Ronald Press Company, New York (1953).
22. H. Mongia, R. Reynolds, E. Coleman, T. Bruce, "Combustor Design Criteria Validation, Volume III—User's Manual," Final Technical Report, USARTL-TR-78-55C, for AVRADCOM, February 1979.
23. M.I. Gurevich, "Theory of Jets in an Ideal Fluid," Pergamon Press, pp. 52-59.
24. N.K. Rizk, and H.C. Mongia, "Gas Turbine Combustor Design Methodology," AIAA paper No. 86-1531, 1986.
25. T. G. Daehler, "Flow and Heat Transfer Characteristics Study of a Composite Matrix System for Combustor Wall Cooling," Allison TDR AX.0320-016, 23 February 1987.

APPENDIX A  
COMPONENT COLD FLOW CHARACTERISTICS

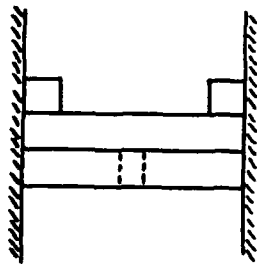
COLD FLOW SAMPLE CONFIGURATIONS



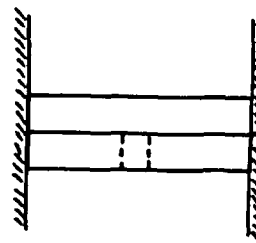
A - PAD ONLY



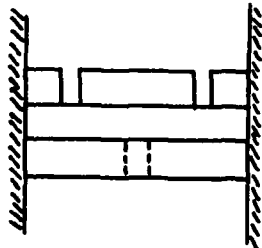
B - INLET ONLY



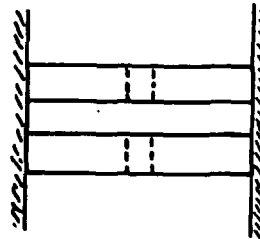
C - INLET, PAD, COVER  
OUTER BLOCKAGE



D - INLET, PAD



E - FULL COOLING UNIT



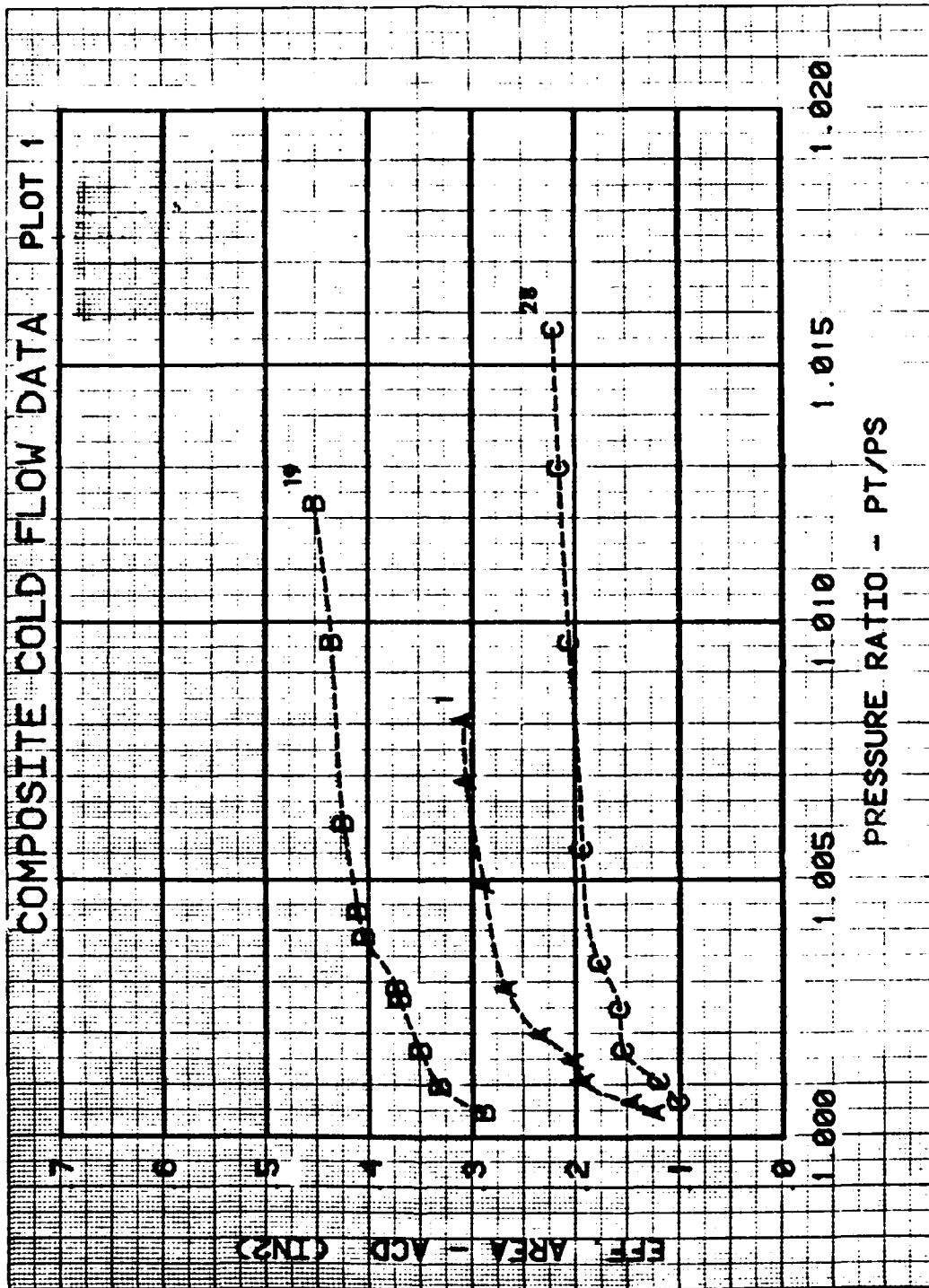
F - INLET, PAD, INLET

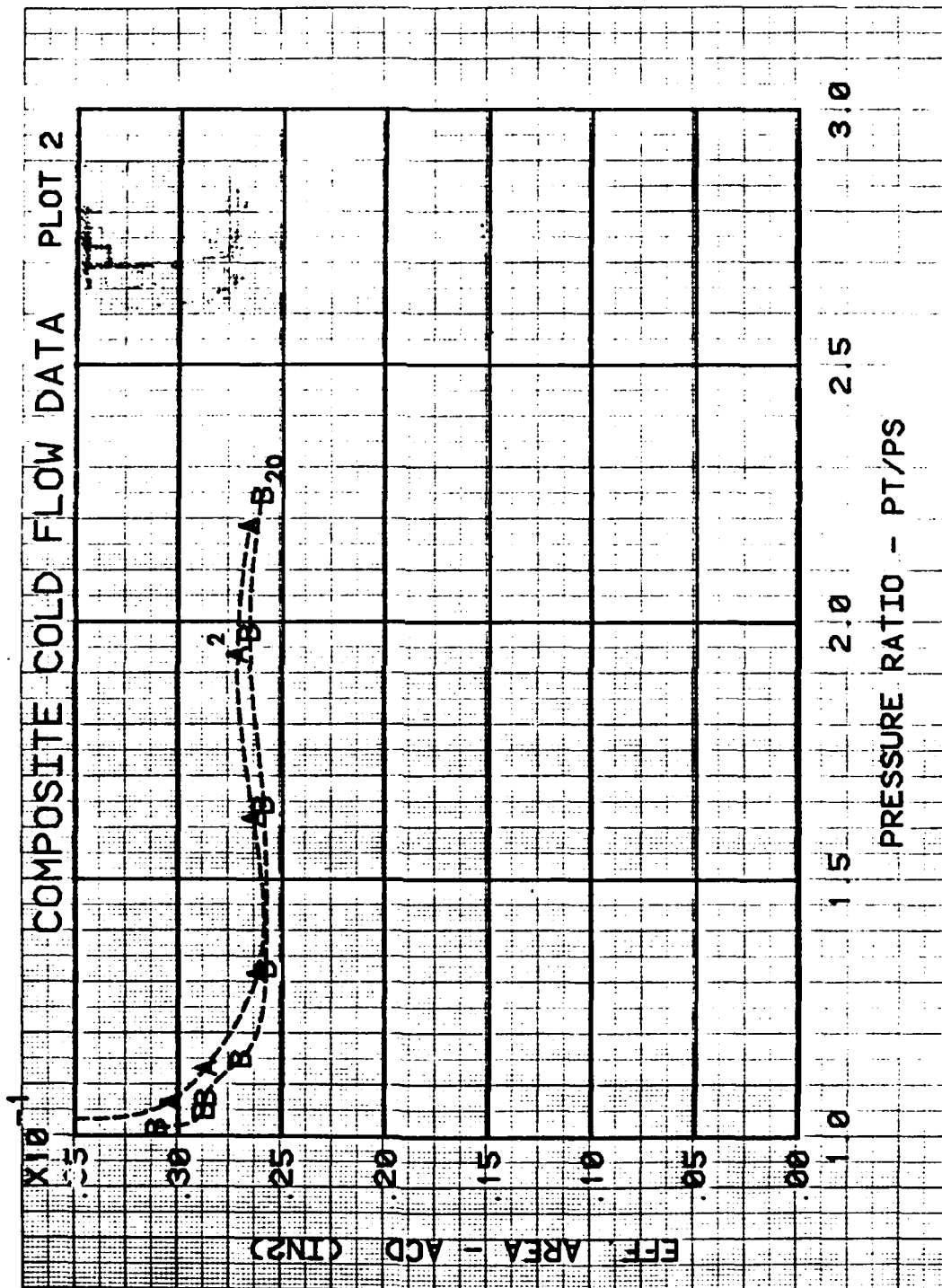
DATA CONFIGURATIONS--COLD FLOW

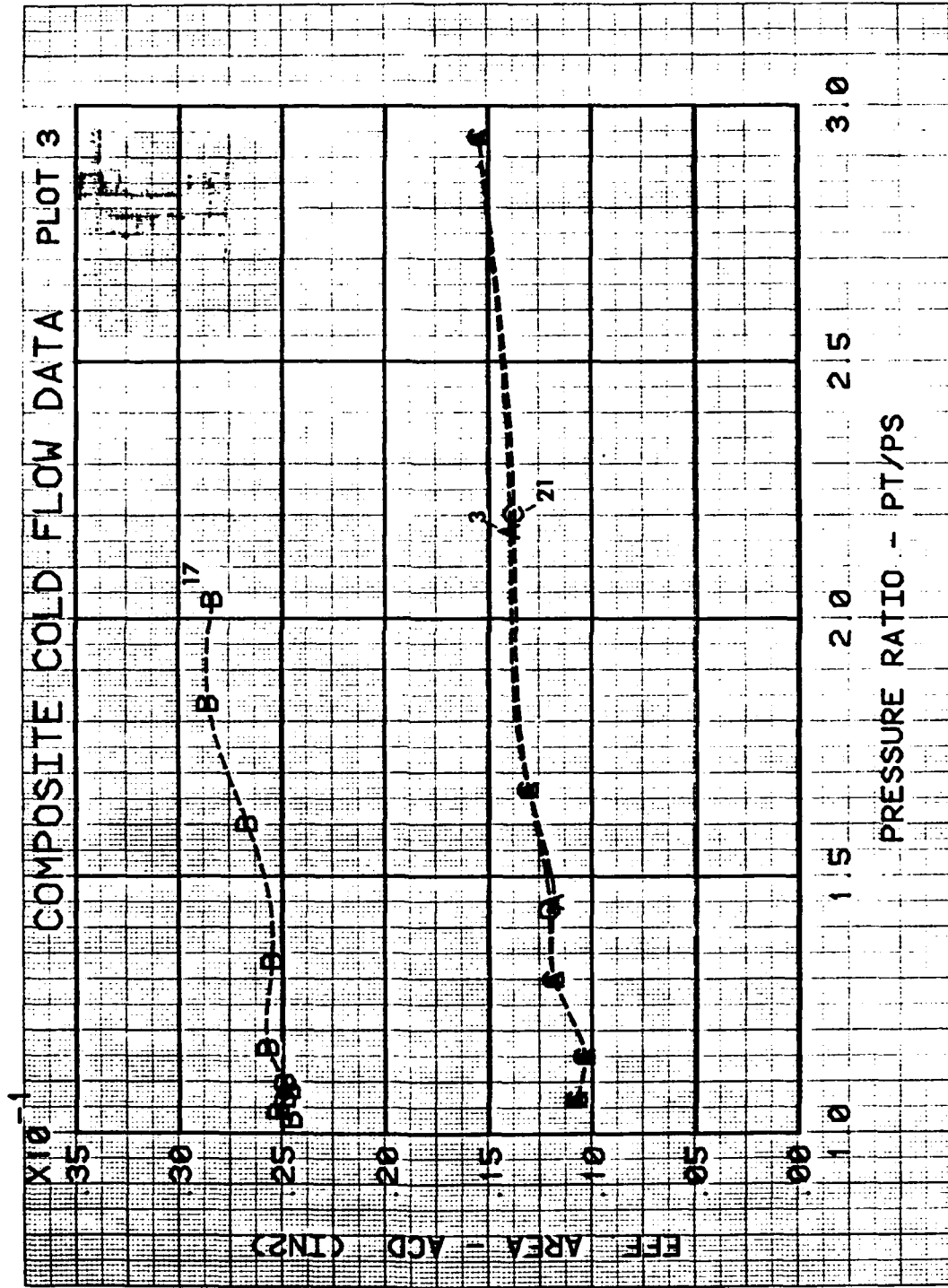
<u>Data set</u>	<u>Config. type</u>	<u>Pad dense %</u>	<u>Pad thick in.</u>	<u>D<sub>1</sub> in.</u>	<u>D<sub>2</sub> in.</u>	<u>A<sub>inlet</sub> in.<sup>2</sup></u>	<u>A<sub>outlet</sub> in.<sup>2</sup></u>
1	A	35	0.127	1.75	1.75	2.405	2.405
2	B	--	---	0.188	0.188	0.0278	0.0278
3	C	35	0.127	0.188	1.00	0.0278	0.785
4	D	35	0.127	0.188	1.75	0.0278	2.405
5	E	35	0.127	0.188	1.00	0.0278	0.344
6	F	35	0.127	0.188	0.188	0.0278	0.0278
7	D	35	0.127	0.188	1.75	0.0278	2.405
8	E	35	0.127	0.188	1.00	0.0278	0.344
9	D	35	0.127	0.188	1.75	0.0278	2.405
10	E	35	0.127	0.265	1.00	0.0552	0.344
11	D	50	0.040	0.188	1.75	0.0278	2.405
12	D	50	0.040	0.188	1.75	0.0278	2.405
13	E	50	0.040	0.188	1.00	0.0278	0.344
14	D	50	0.040	0.265	1.75	0.0552	2.405
15	E	50	0.040	0.265	1.00	0.0552	0.344
16	D	35	0.127	0.265	1.75	0.0552	2.405
17	C	35	0.127	0.265	1.00	0.0552	0.785
18	C	35	0.127	0.265	1.00	0.0552	0.785
19	A	35	0.062	1.75	1.75	2.405	2.405
20	B	--	---	0.188	0.188	0.0278	0.0278
21	C	35	0.062	0.188	1.00	0.0278	0.785
22	D	35	0.062	0.188	1.75	0.0278	2.405
23	E	35	0.062	0.188	1.00	0.0278	0.344
24	F	35	0.062	0.188	0.188	0.0278	0.0278
25	C	50	0.040	0.265	1.00	0.0552	0.785
26	C	50	0.040	0.188	1.00	0.0278	0.785
27	C	35	0.127	0.188	1.00	0.0278	0.785
28	A	50	0.040	1.75	1.75	2.405	2.405

# COLD FLOW DATA PLOT DESCRIPTION

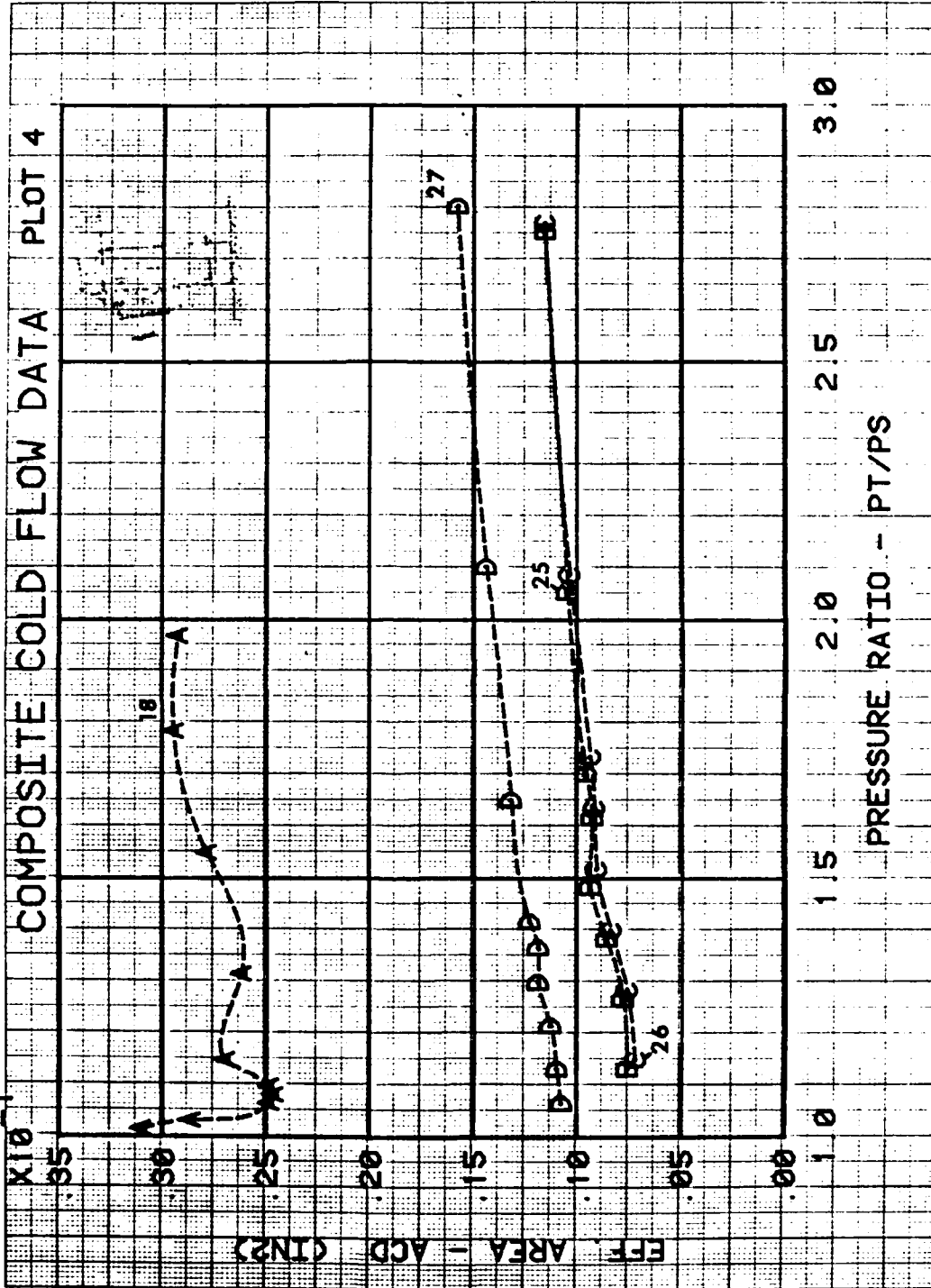
Plot No.	Inlet $\phi$	Pad density	Pad thkns.	Curve letter--data set					Flow elements inlet to outlet
				A	B	C	D	E	
1		--Parametrics--		1	19	28			A Pad only
2				2	20				B Inlet only
3				3	17	21			C Inlet, pad, outer ring
4				18	25	26	27		C Inlet, pad, outer ring
5				4	11	14	16		D Inlet, pad
6				7	12	22			D Inlet, pad
7				<u>5</u>	<u>8</u>	<u>23</u>			E Full sector
8				<u>10</u>	<u>13</u>	<u>15</u>			E Full sector
9				6	24				F Inlet, pad, inlet
10	0.188	25	0.127	3	4	<u>5</u>	6	20	F Full sector components build-up
11	0.188	50	0.040	11	12	<u>13</u>	20	26	
12	0.188	35	0.062	20	21	22	<u>23</u>	24	
13	0.265	35	0.127	<u>10</u>	16	17	18		
14	0.265	50	0.040	14	<u>15</u>	25			

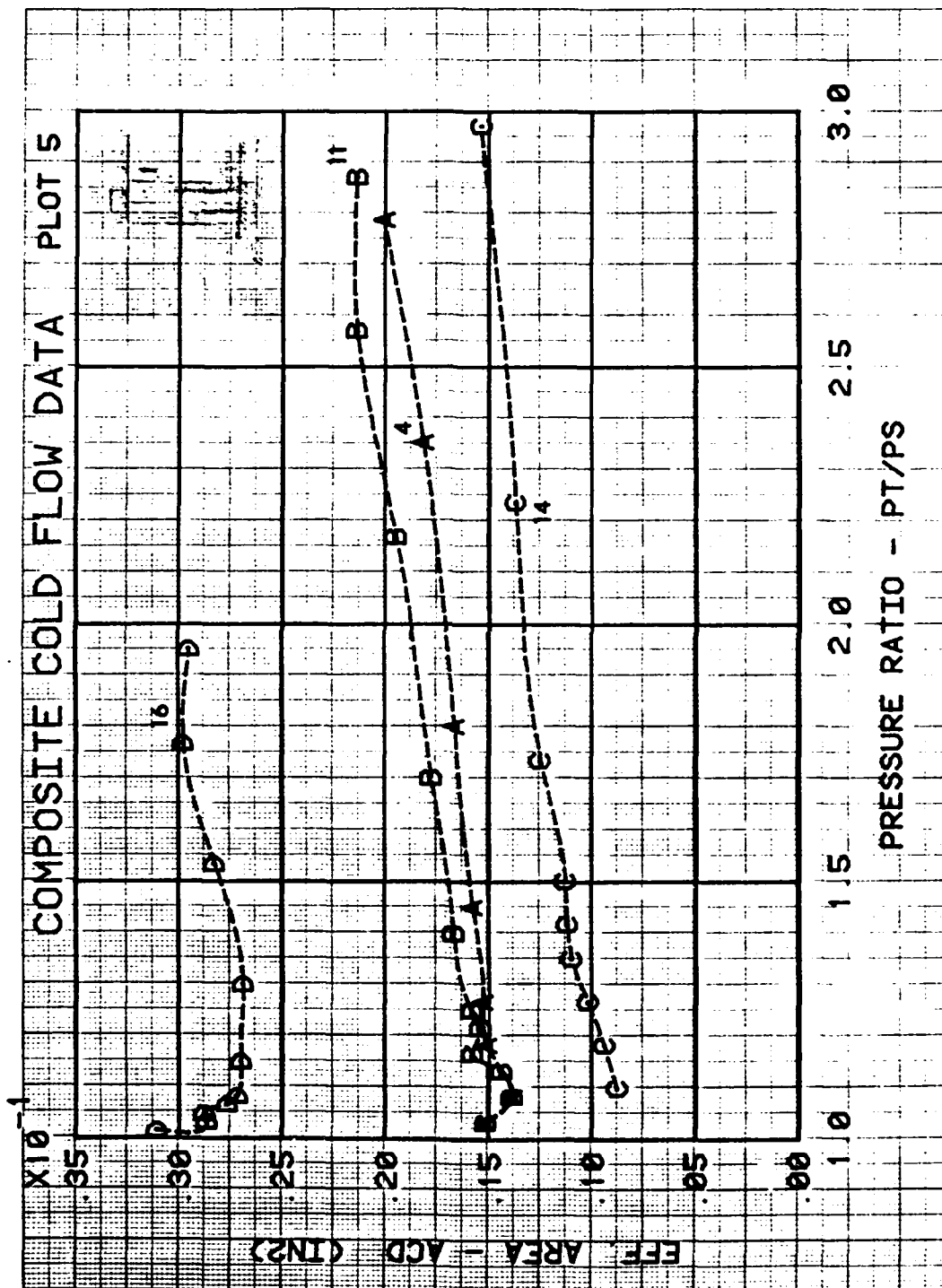


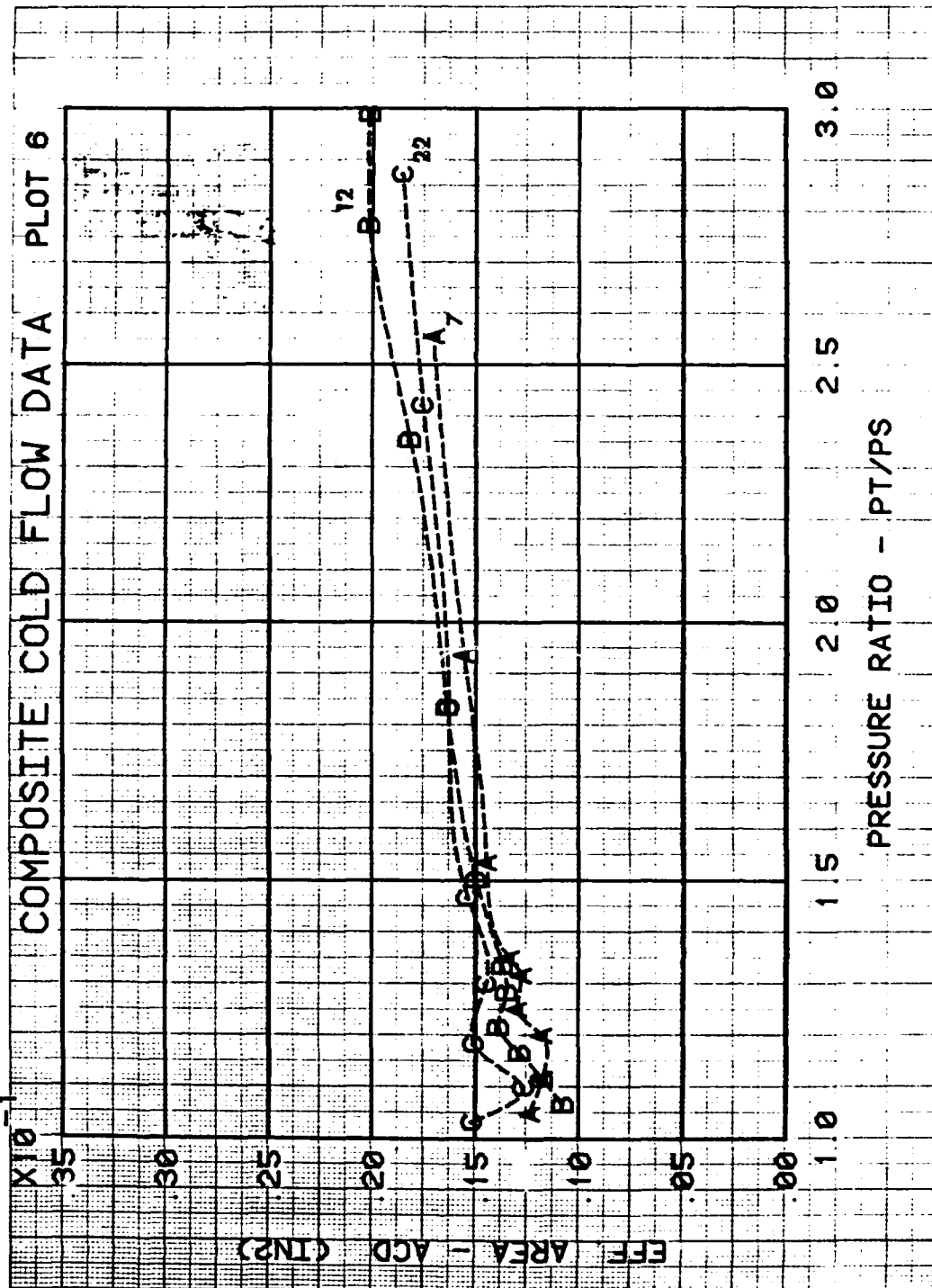


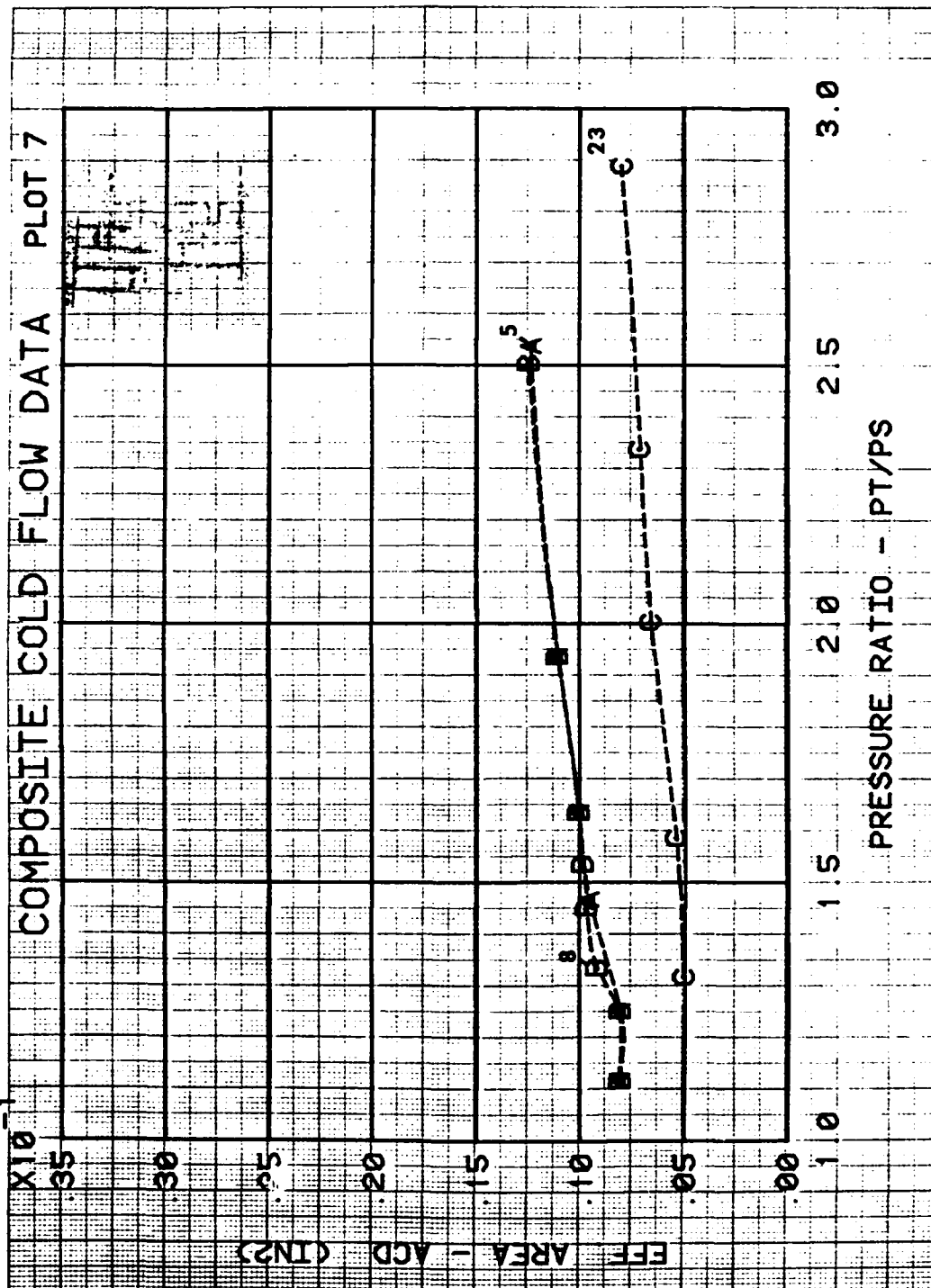


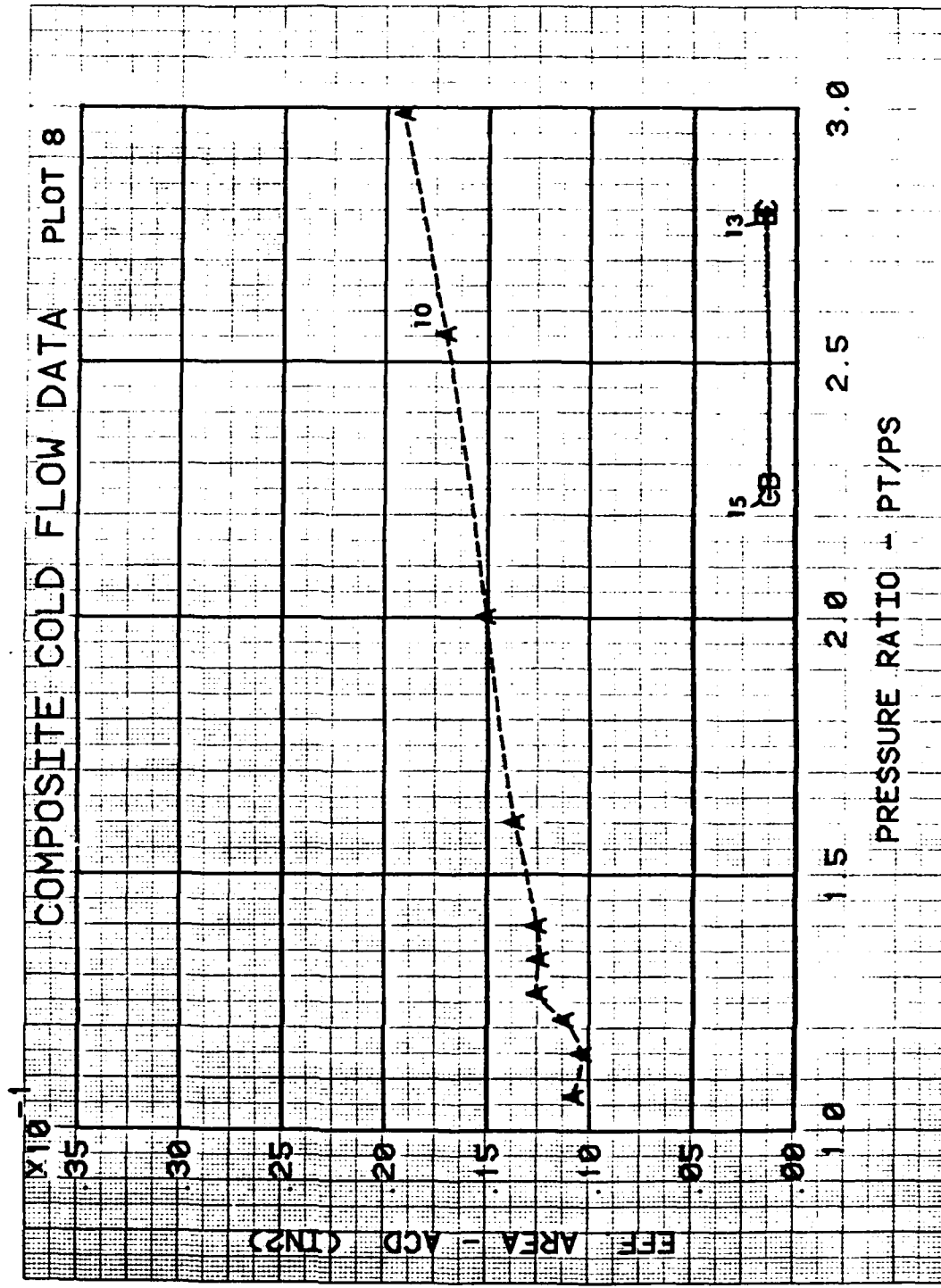


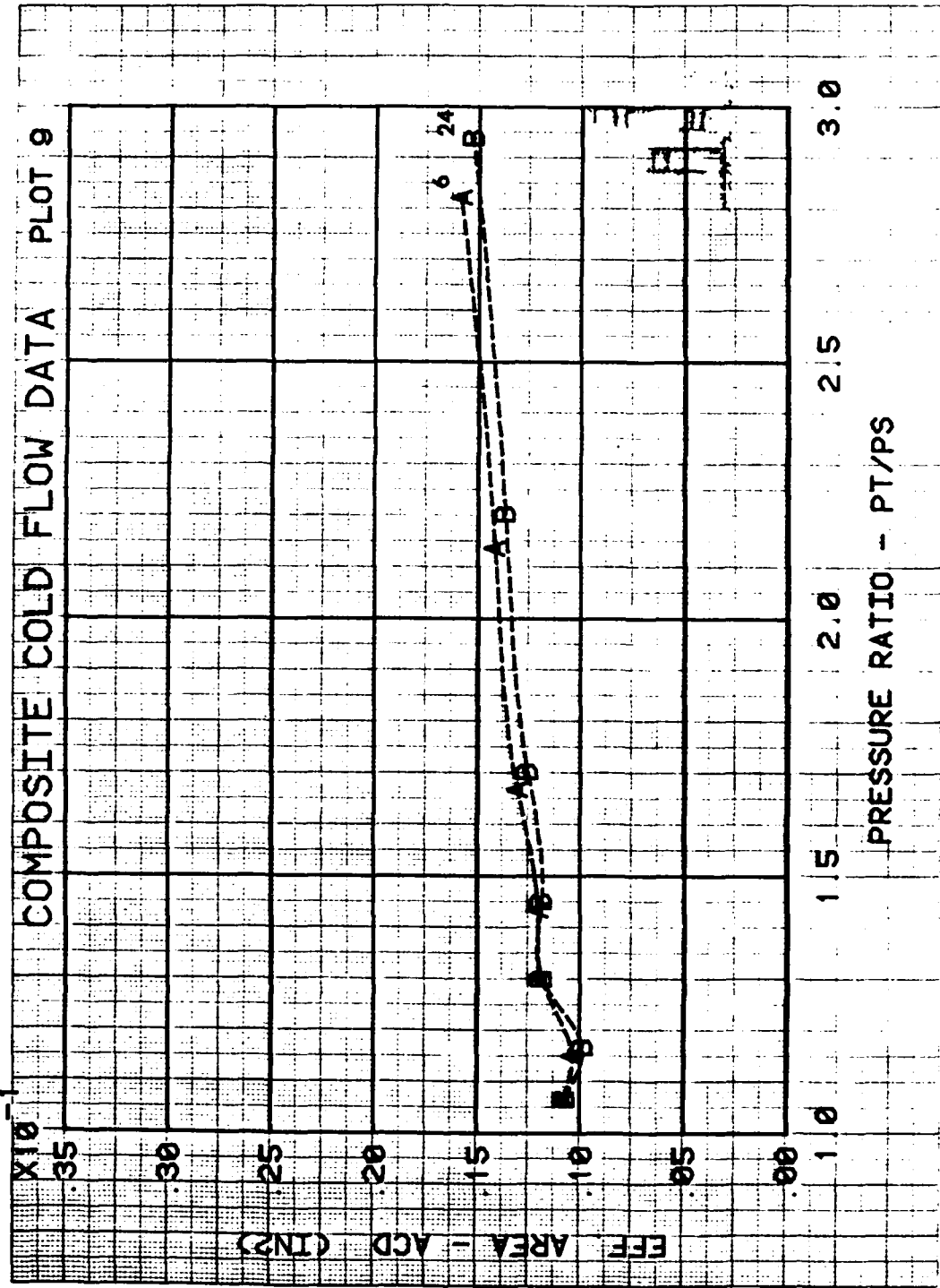


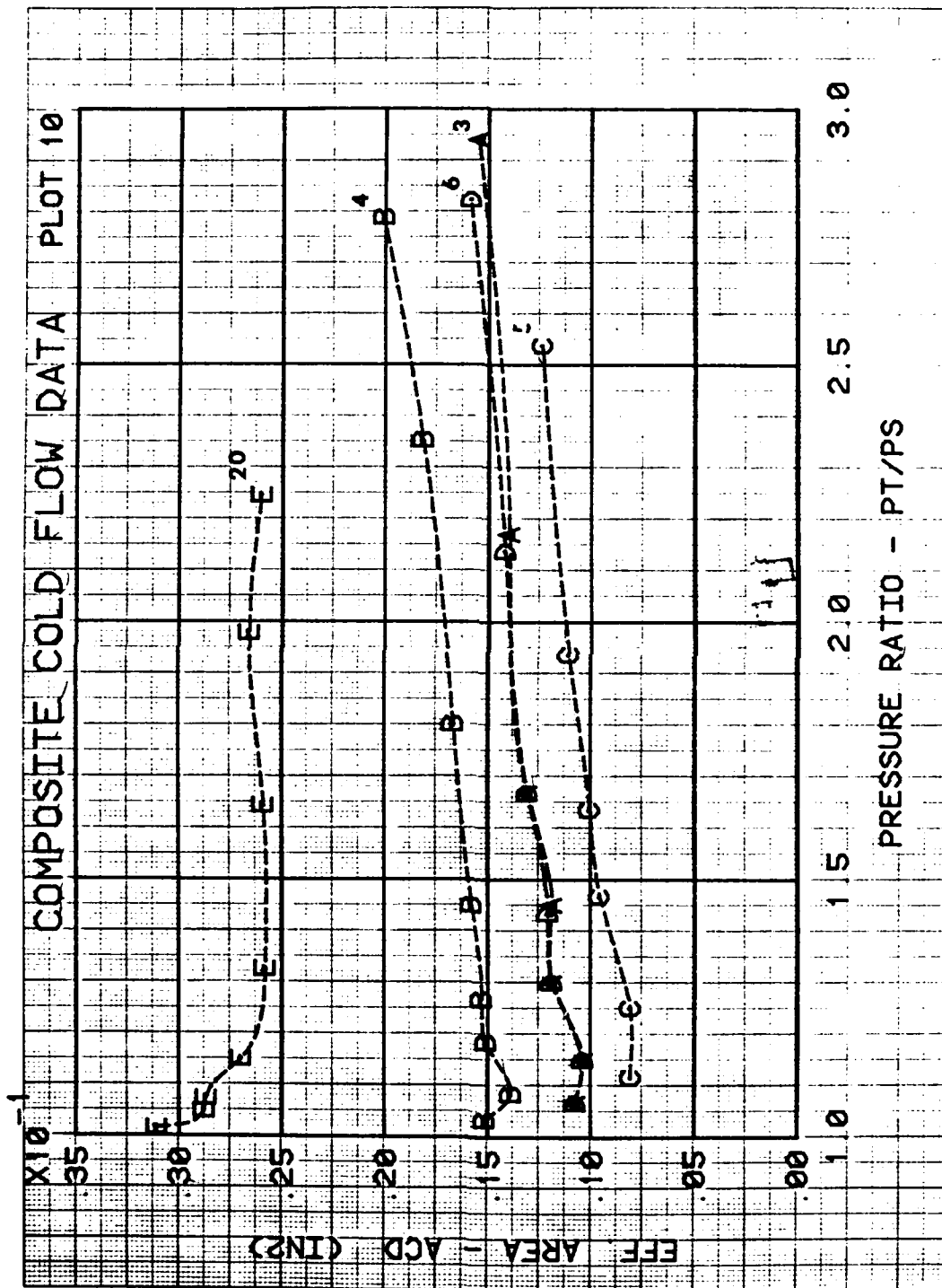


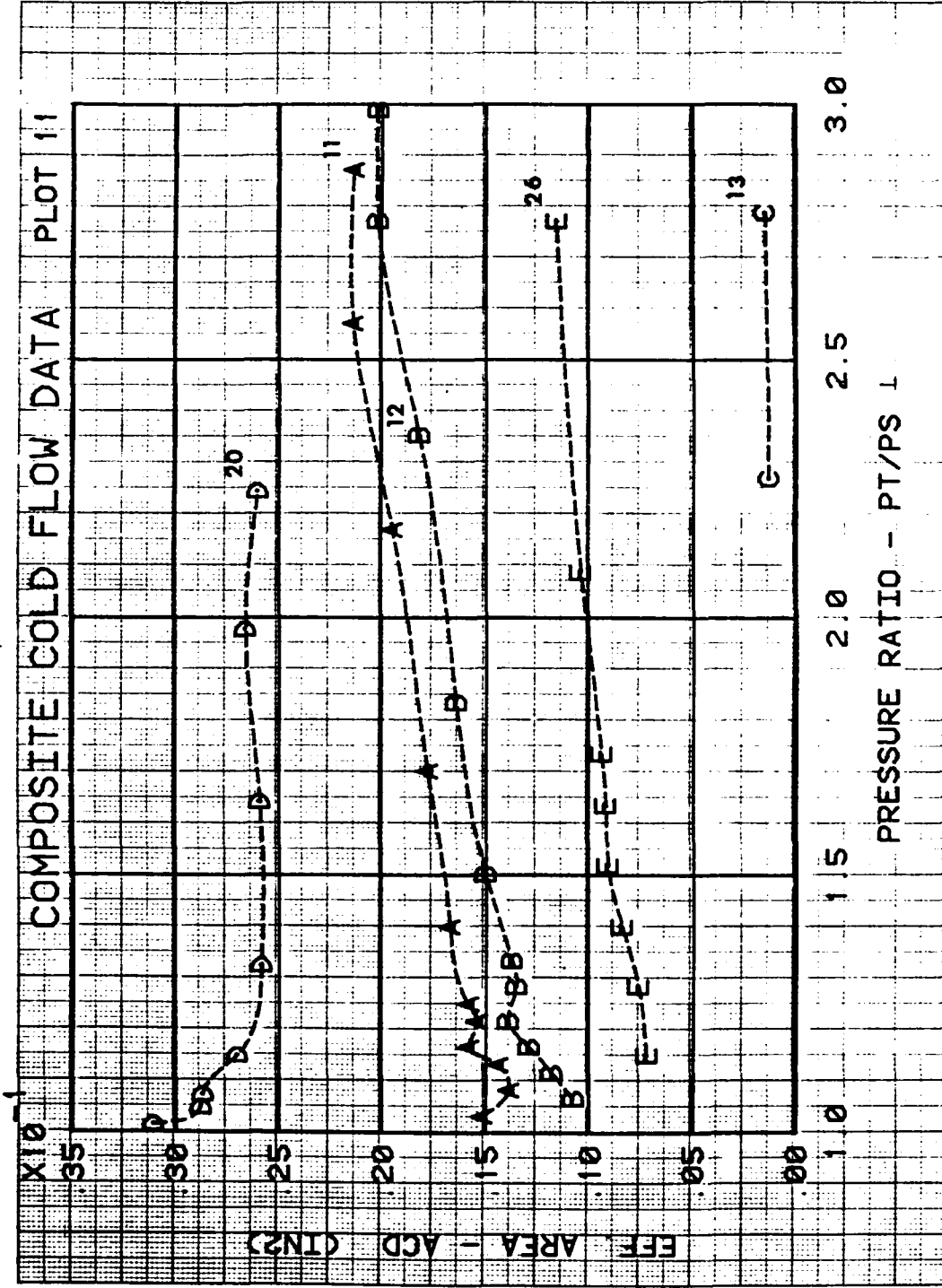




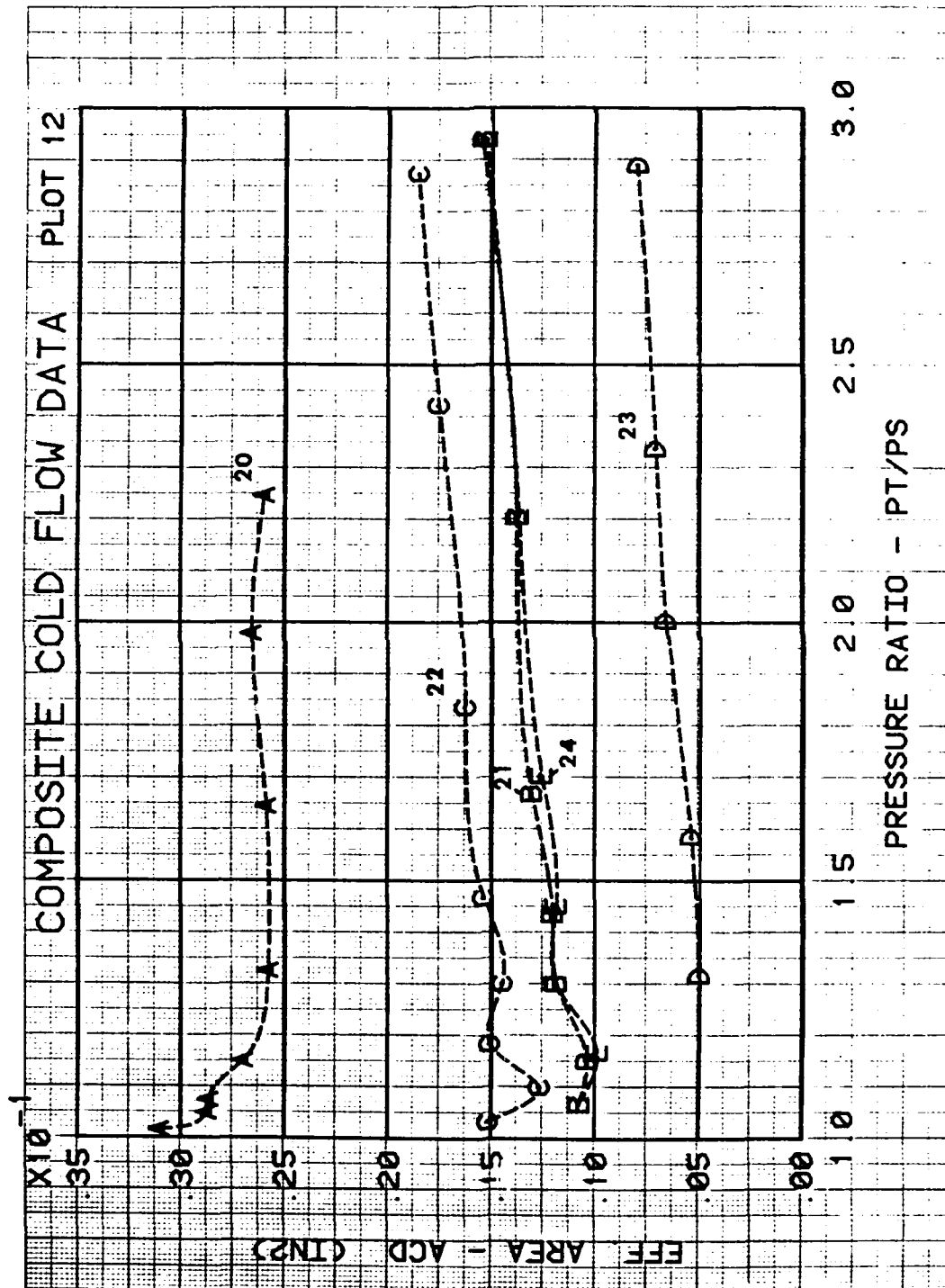


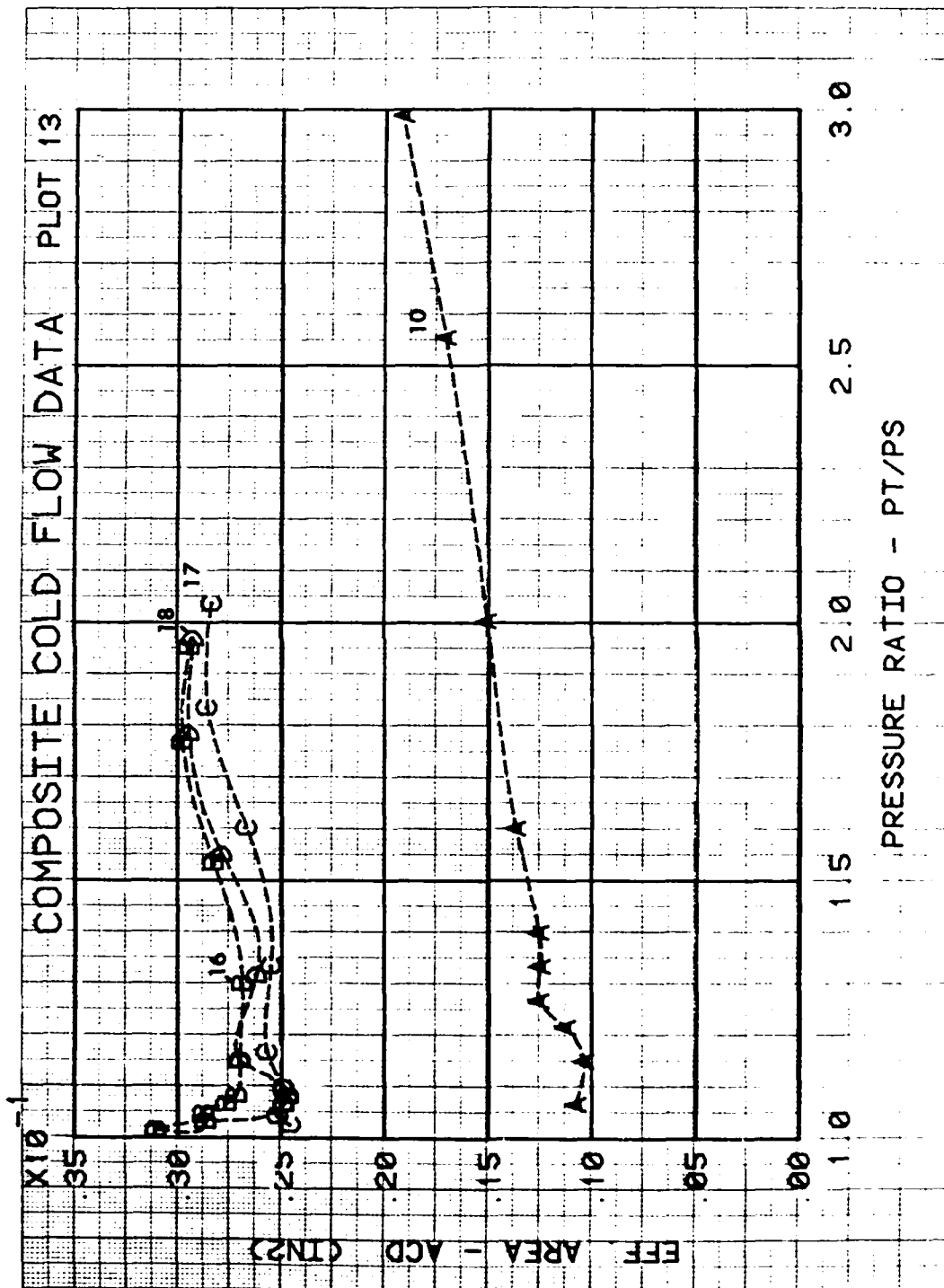


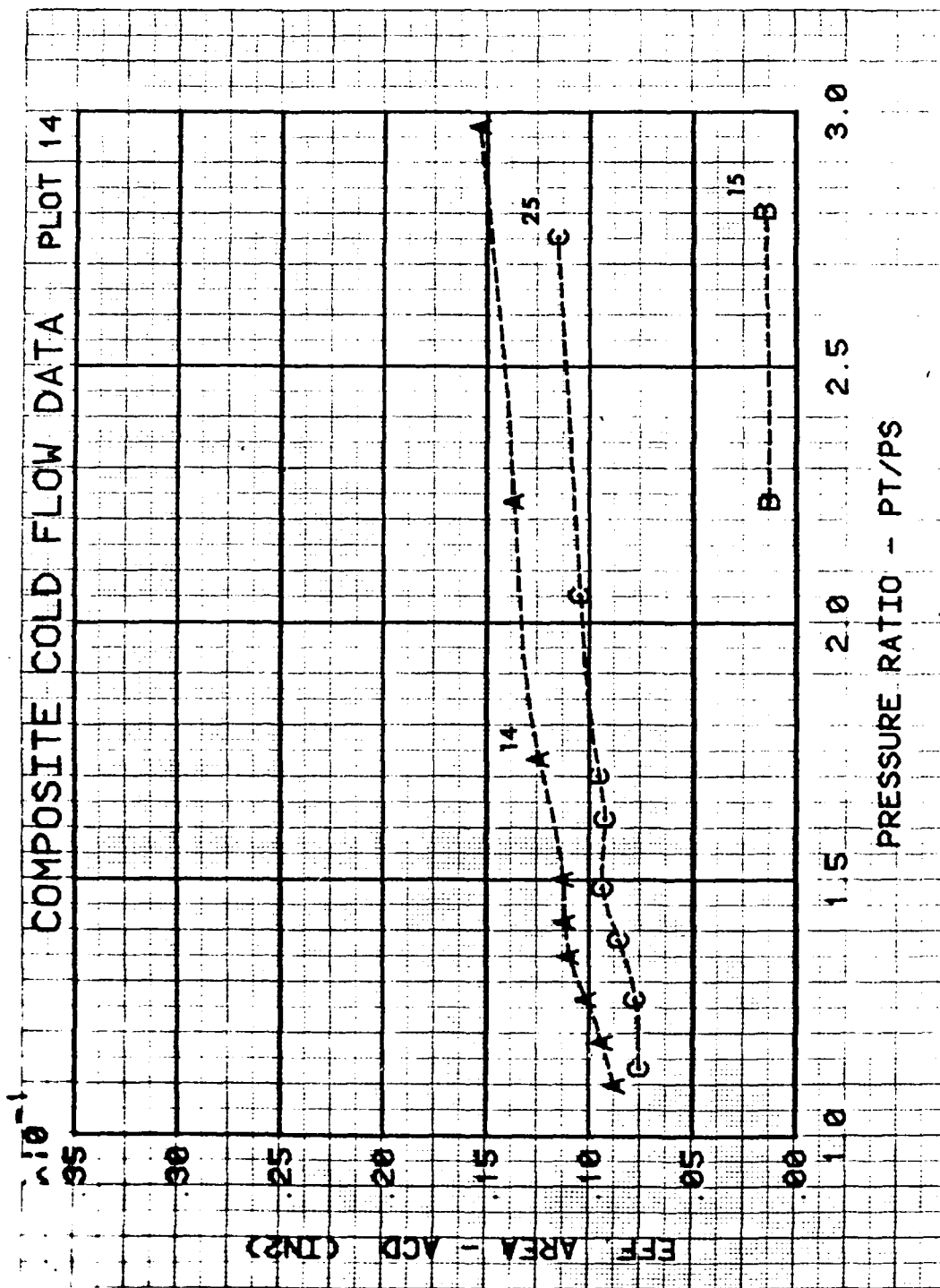












APPENDIX B  
DESCRIPTION OF MACRO DESIGN ANALYSIS CODES

## 1. ANNULUS FLOW MODEL, ANNLOSS

An annulus-flow model is used to compute pressure losses, annulus Mach number and associated air velocity, and airflow distribution around the combustor liner.

A one-dimensional analysis of the plenum annulus is conducted based upon the generalized one-dimensional continuous flow-analysis approach of Shapiro (Reference 21). The analysis considers the effect of area change, wall friction, drag introduced by inserted obstacles such as fuel nozzles and service struts, heat transfer from the liner wall, and injection or extraction of air from the annulus. The analysis is valid for constant specific heat and molecular weight.

This program was developed for reverse flow combustion systems and is based on the analytical code described in Volume III of the Army's Combustor Design Criteria Validation program (Reference 22).

Following the approach of Shapiro for a small control volume about some point located a distance from the compressor discharge, working equations are obtained for Mach number, total pressure, and static temperature. A set of equations is written for all control volumes defined by the user around the annulus. Expressions are incorporated into the code for skin friction coefficients and drag introduced by obstacles in the flowpath such as fuel nozzles. For mass addition or extraction through orifices, orifice configurations are broadly divided into two basic categories:

- Configurations such as swirlers, primary pipes, and venturi sections which are either difficult to handle analytically or their flow rates are less affected by approach conditions.
- Liner orifices, including flush port, plunged holes, and scooped ports are affected by approach conditions and are amenable to analytical approach for predicting flow rates, jet velocities, and efflux angles.

The first type of ports are handled by specifying discharge coefficients, whereas the liner orifices are handled by using a modified analytical approach described by Gurevich (Reference 23). The Gurevich approach is based upon a 2-D potential flow solution.

For a given application, the annulus upstream conditions and the static pressure inside the liner must be specified. With Gurevich equations, an orifice can be sized to pass a specified flowrate, or the flow through a specified orifice can be calculated.

With the above procedure for computing mass extraction or addition, which appears in the three working equations for Mach number, total pressure, and static temperature, it is now possible to write a set of equations for each of the control volumes around the combustor liner. These equations are solved iteratively to compute isothermal combustor-pressure drop. To this can be added pressure drop due to heat addition which gives combustor total pressure drop.

## 2. COMBUSTOR 3-D REACTING PERFORMANCE MODEL—COM3D

Extensive application of multidimensional analytical models has been used as a design aid in the development testing of combustors at Allison. These models account for the various physical/chemical processes occurring within the flow field, including turbulence and scalar transport, spray dynamics, evaporation and mixing, and hydrocarbon combustion chemistry.

Multidimensional elliptic codes that solve the Navier-Stokes equations for a 3-D reactive flow field (Reference 22) such as MARC-1 and COM3D have been adopted at Allison to evaluate combustor performance. These programs simulate turbulence by a two-equation  $k-\epsilon$  model, and combustion following vaporization is determined by either the two-step or four-step chemical reaction model based on eddy breakup concepts.

An iterative finite difference solution procedure is used to solve the resulting system of nonlinear, partial-differential equations. Extensive improvements in the codes include development of a more flexible grid system and accelerated convergence numerical techniques. Advanced spray and evaporation models also are incorporated in the 3-D codes.

To develop a combustor design method at Allison that can be intensively used in combustor development effort, the multidimensional models are combined with the predictive tool of proven empirical correlations (Reference 24). The empirical approach involves use of empirical correlations based on experimental data and simple calculation methods for combustion design criteria including combustion efficiency, lean blowout and ignition, exhaust temperature quality, and emissions. A number of empirical correlations have been developed based on loading parameters, heat release rate, combustor reference velocity and residence time, liner cooling flow requirements, and other important characteristics of flow in the combustor.

To use the detailed representation of the flow and combustion processes made available through the analytical 3-D codes, and the predictive tool of the proven empirical correlations, Allison has formulated an analytical/empirical design approach. With this approach, the impact of a systematic modification to the details of the burner is easily determined. The inclusion of improved turbulence and spray models in multidimensional combustor simulation codes will greatly enhance the analytical predictions of the design method.

To use the output data of the 3-D codes fully, a feature is introduced into the codes that allows the combustor sector to be divided into many subvolumes. The relevant combustion and flow characteristics within each microvolume are evaluated and prepared for use as an input to the performance correlations.

This Allison-developed analytical/empirical design method was verified by applying the method to a number of production combustors that varied significantly in design and concept. Typical predictions for lean blowout fuel/air ratio, smoke number,  $\text{NO}_x$  and pattern factor (PF) were compared with experimental data and the agreement observed suggests that the design method can greatly enhance the development of new and advanced combustor concepts and minimize hardware iterations.

Although the analytical models have been useful in the design of combustors, significant advances are needed in physical submodels to improve the model capability to accurately predict complex reacting flows encountered in gas turbine combustors. In addition, consideration must be given to numerical accuracy and mathematical simulation of practical gas turbine hardware. Lack of benchmark quality data in regard to combustor and cooling airflow distribution, and fuel nozzle spray characteristics is another factor that adds to the limitations of the models to provide quantitative insight of combustor performance.

### 3. 1-D AND PSEUDO 3-D HEAT TRANSFER MODELS FOR THE ENTIRE COMBUSTOR—WALLTEMP AND WALL3D

A macro or "whole" model was developed to calculate CMC wall temperatures that regards the combustor liner as a container of hot flowing gases surrounded by a casing in which air is flowing between the container and the casing. Broadly, the liner is heated by radiation and convection from the hot gases inside it, and is cooled by radiation to the outer casing and by convection to the annulus air. The relative proportions of the radiation and convection components depend upon the geometry and operating conditions of the system.

The 1-D model (WALLTEMP) uses average gas temperatures at user defined axial stations that may be generated by equilibrium temperature calculation, assumption of stoichiometric streak, or averaged temperature data from the 3-D performance model (COM3D) calculation. The major difference between the pseudo 3-D heat transfer model (WALL3D) and the 1-D model is that the heat transfer calculation proce-

ture incorporates the variation in combustor operating conditions in the three dimensions predicted by the 3-D performance code. In addition the radiative flux components are calculated through a view factor which considers effects from the rest of the combustor volume in all three directions. These programs are applicable to various cooling concepts and are a basic part of the Allison design method. A description of the models follows.

Under steady-state conditions the rate of heat transfer into a wall element must be balanced by the heat transfer out as follows:

$$K = R1 + C1 = R2 + C2 \quad (1)$$

where K is the conduction heat transfer through a solid liner wall due to a temperature gradient within the wall, R1 and R2 are the radiative heat loads into and out of the wall, and C1 and C2 are the convective loads.

In most gas turbine combustors a sizable portion of the heat transferred from the hot gases to the liner wall is by radiation. The total emitted radiation has two components; the nonluminous radiation that emanates from certain gases, notably carbon dioxide and water vapor, and the luminous radiation that depends on the number and size of the solid particles (mainly soot) in the flame. The emissivity of a luminous gas is governed by pressure through its effects on the chemistry of soot formation, the quality of atomization, the distribution of fuel in the combustion zone, and fuel-air mixing. Emissivity and radiation increase markedly with rising inlet temperature and with liner size owing to the higher beam length ( $l_b$ ), which may be thought of as the radius of gas hemisphere which will radiate to unit area at the center of its base the same as the average radiation from the actual gas mass.

Values of gas emissivity ( $\epsilon_g$ ) for  $CO_2$  and  $H_2O$  may generally be obtained from the charts that relate emissivity to gas temperature for different values of the product of partial pressure and beam length ( $l_b$ ). The beam length is determined by the size and shape of the gas volume. The nonluminous emissivity is then given by:

$$\epsilon_g = \epsilon_{CO_2} C_{CO_2} + \epsilon_{H_2O} C_{H_2O} - \Delta\epsilon \quad (2)$$

where C is a correction factor for total system pressure, and  $\Delta\epsilon$  is a correction factor for  $CO_2$  and  $H_2O$  spectral overlap.

Ideally, it should be possible to estimate the luminous emissivity from the knowledge of the size, mass concentration, and optical properties of the soot particles in the flame. However, due to the complexity involved, luminous emissivity may be obtained by introducing a luminosity factor (L) in an empirical expression for nonluminous flame as follows:

$$\epsilon_g = 1 - \exp(-290 PL (FAR \cdot l_b)^{0.5} \cdot T_g^{-1.5}) \quad (3)$$

where P is pressure and FAR is the fuel-air ratio.  $T_g$  is gas temperature.

The factor L depends largely on the carbon/hydrogen mass ratio as follows:

$$L = 0.0691 (C/H - 1.82)^{2.71} \quad (4)$$

The evaluation of the gas emissivity facilitates the calculation of the internal radiation flux, and the radiation heat transfer from the liner wall to the outer casing can be approximated by assuming gray surfaces. The components of the convection heat transfer are estimated by using the local values of gas and air properties and flow pattern, and assuming the forms of the classical heat-transfer for straight pipes.

The internal radiation may be written as:

$$R = 0.5 \sigma (1 + \epsilon_w) \epsilon_g T_g^{1.5} (T_g^{2.5} - T_w^{2.5}) \quad (5)$$

where  $\epsilon_w$  is wall emissivity that depends on material, temperature, and degree of oxidation of the wall, and  $\sigma$  is Stefan Boltzmann constant.  $T_w$  is wall temperature. The internal convection is determined using a Reynolds number index consistent with established practice for conditions of extreme turbulence. This lead to an expression of the form:

$$C = 0.017 \frac{(kg)}{D_L^{0.2}} \frac{(W_c)^{0.8}}{A_L \mu g} (T_g - T_w) \quad (6)$$

Where  $D_L$  and  $A_L$  are liner characteristic dimensions and area, respectively.  $Kg$  is gas conductivity,  $\mu g$  is gas viscosity and  $W_c$  is the cooling mass flowrate. The use of 3-D codes enables more accurate representation of hot gas flow properties to be made.

The mechanism of heat transfer for porous walls (Brunsbond) is based on the fact that heat can be removed by transfer to the coolant air during its passage through the porous wall. The actual relationship between  $T_{w1}$  and  $T_{w2}$  is given by the wall temperature ratio  $\theta t$ :

$$\theta t = (T_{w2} - T_{a2}) / (T_{w1} - T_{a2}) = \exp - (Mac \cdot C_{pa} \cdot tw / kef)$$

where  $Mac$  is cooling air flow rate per unit surface area,  $T_{a2}$  is cooling air inlet temperature,  $C_{pa}$  is the air heat capacity,  $Kef$  is the effective conductivity of the pad, and  $tw$  is wall thickness. The thermal effectiveness ( $Y$ ) is given by:

$$Y = (T_{a1} - T_{a2}) / (T_{w1} - T_{a2}) = A \cdot Mac^c \quad (8)$$

where  $A$  and  $c$  are constants. The heat flux picked by the coolant is given by:

$$Q_a = Mac \cdot C_{pa} \cdot Y \cdot (T_{w1} - T_{a2}) \quad (9)$$

and the heat balance for the porous wall is given by:

$$R1 + C1 = Q_a + R2 + C2 \quad (10)$$

Provisions are made to consider both the uncooled and cooled wall cases in the program. An iterative method is adopted to calculate the wall temperatures including temperatures on the ceramic surface, the interface between ceramic and Brunsbond, the Brunsbond/substrate interface, and the substrate (or cold side) surface.



# NOMENCLATURE-APPENDIX B

K	conduction heat transfer through solid wall
R1	radiative heat load, in
C1	convective heat load, in
R2	radiative heat load, out
C2	convective heat load, out
lb	mean beam length
eg	gas emissivity
ew	solid wall emissivity
εCO2	carbon dioxide emissivity
εH2O	water emissivity
CCO2	correction factor for pressure, carbon dioxide
CH2O	correction factor for pressure, water
Δε	correction factor for spectral overlap
L	luminosity factor
P	pressure
FAR	fuel-air ratio
Tg	gas temperature
C/H	carbon/hydrogen mass ratio
σ	stefen Boltzman constant
Tw	wall temperature
DL	combustor liner characteristic dimension
AL	area of liner
Kg	gas conductivity
μg	gas viscosity
Wc	cooling air mass flowrate
Tw1	Brunsbond wall temperature, hot side
Tw2	Brunsbond wall temperature, cold side
θt	Brunsbond dimensionless temperature gradient
Mac	cooling air flowrate per unit surface area
Ta2	cooling air inlet temperature
Ta1	cooling air exit temperature
Cpa	air heat capacity
Kel	effective thermal conductivity of Brunsbond
γ	thermal effectiveness
A	constant for thermal effectiveness equation
c	constant for thermal effectiveness equation
Qa	coolant heat flux